The Dissertation Committee for Yaser Abudllah Alzayer Certifies that this is the approved version of the following Dissertation:

Differential Compaction Fractures in Carbonate Mound Complexes: Pioneering Numerical Models Applied to Outcrops and Subsurface Reservoirs

Committee:

Charles Kerans, Supervisor

Christopher Zahm, Co-Supervisor

Xavier Janson

John Sharp, Jr.

Ronald Steel

Differential Compaction Fractures in Carbonate Mound Complexes: Pioneering Numerical Models Applied to Outcrops and Subsurface Reservoirs

by

Yaser Abdullah Alzayer

Dissertation

Presented to the Faculty of the Graduate School of

The University of Texas at Austin

in Partial Fulfillment

of the Requirements

for the Degree of

Doctor of Philosophy

The University of Texas at Austin

August 2018

Dedication

To my wife and parents

Acknowledgements

I would like to thank my advisers Dr. Chris Zahm and Dr. Charles Kerans for their supervision, guidance, and support over the past few years. I have learned a great deal of knowledge from both of them and I am a better scientist because of their feedback over the years. I thank my dissertation committee Dr. Jack Sharp, Dr. Xavier Janson, and Dr. Ronald Steel for their constructive comments and suggestions, which greatly improved this dissertation. Several other professors have helped me on the way to get to where I am today and to them I am forever grateful. Dr. Mike Taylor and Dr. Danny Stockli who gave me an opportunity to pursue research as an undergraduate and inspired me to pursue graduate studies. Dr. Peter Eichhubl and Dr. Stephen Laubach who introduced me to the world of fractures and structural diagenesis as a master's student at UT. I would like to acknowledge the staff of the Bureau of Economic Geology for their assistance and support over the years in particular Nathan Ivicic, Stephanie Lane, and Donnie Brooks. I am thankful for Philip Guerrero who went above and beyond the call of duty as a graduate coordinator to support me and my fellow graduate students whenever faced with an administrative or personal matter.

This work has benefited from research funding through the industrial associates of the Reservoir Characterization Research Laboratory (RCRL) at the Bureau of Economic Geology and the Meckel Family Named Grant of the AAPG Foundation. I am grateful for my employer Saudi Aramco and EXPEC Advanced Research Center (EXPEC ARC) management for investing in me and providing fellowship support of my graduate studies and time to pursue them. I thank several key people who have supported me throughout my career at Saudi Aramco's EXPEC ARC including Dr. Mohammad Khadrawi, Dr. Maher Almarhoon, Dr. Dave Cantrell and EXPEC ARC's manager Dr. Ali Al-Meshari.

Aramco Houston Research Center is thanked for allowing me to carry out geomechanical tests at their facilities. In particular, I would like to thank Ashraf Al-Tahini, Dan Georgi, and Bitao Lai.

I would like to thank my fellow graduate students at UT for their friendship, comradery, and peer-review. In particular, I thank Mahmoud Alnazgha for collaborating with me on the SACROC project. I would like to thank Kelly Hattori and Andrea Nolting for editing parts of this dissertation and manuscripts. I would like to thank several other fellow students who also contributed to lively scientific discussions and provided moral support during major milestones of my graduate career including Ben Smith, Greg Hurd, Nick Danger, Kris Voorhees, Taylor Canada, Ahmad Alnahawi, Nick Ettinger, Peter Schemper, Graham Soto-Kerans, Peter Soto-Kerans, Reynaldy Fifariz, Owen Callahan, Ben Rendell, Mario Guitierrez, and Nike Tokan-Lawal.

Finally, I would like to thank my parents for their endless love and support, I would not be where I am today without them. I am grateful for my wife Hadeel for her love, support, and understanding during the busy times over the past 4 years she motivated me and kept me going whenever I needed it.

Differential Compaction Fractures in Carbonate Mound Complexes: Pioneering Numerical Models Applied to Outcrops and Subsurface Reservoirs

Yaser Abdullah Alzayer, Ph.D.

The University of Texas at Austin, 2018

Supervisors: Charles Kerans and Christopher Zahm

Differential compaction is thought to be a primary driver for syndepositional fracture development in carbonate platforms. Outcrop and subsurface observations of syndepositional fractures in carbonate mound complexes and platforms cannot be used to directly identify the mechanism or controlling factors behind their formation, because these observations represents the end state of potentially long and complex stress and diagenetic history. The limitations of outcrop observations are overcome by using a finite-element and combined finite-discrete forward models to simulate differential compaction and subsequent fracture development in carbonate mound complexes. Differential compaction deformation is modeled at the mound scale (tens of meters) and at an isolated platform-scale (kilometers). Numerical models are used to (1) quantify amount of differential subsidence required to develop fractures, (2) predict areas susceptible to fracture development, and (3) identify the most critical factors controlling differential compaction fracturing.

2D and 3D models are constructed based on classic outcrops of Late Pennsylvanian carbonate mounds in the Sacramento Mountains and age-equivalent Canyon and Cisco formations in the Midland Basin, West Texas. Modeling results are consistent with fracture observations in outcrops and the subsurface. Geometry of lithified antecedent topography

and the overlying strata controls the location of differential compaction fractures. Fractures develop in strata overlying antecedent topography in transitional crest-to-off-mound/platform areas. Another location for fracture development corresponds to strata overlying the mound/platform slope-to-off-mound/basinal setting transition.

Modeling results demonstrate that only a minor amount (cm -10s cm scale) of differential subsidence is required to develop fractures in early lithified carbonates. This suggests that differential compaction fractures in carbonate systems may be generally underestimated. Fracture intensity is found to be proportional to the amount of differential subsidence. A greater control on fracture intensity is the bedding contact nature. Fracture development in strata with bedding contacts that are resistant to layer-parallel slip display almost double the fracture intensity of strata with contacts favoring slip. Layer-parallel slip is concluded to be a major mechanism for dissipating stress during compaction-driven folding. The process-based modeling approach applied by this work provides fundamental understanding of differential compaction fracture development in carbonate mound complexes, which is valuable to prediction of fractures in subsurface reservoirs.

Table of Contents

List of Tables

List of Figures

Chapter 1: Introduction

Syndepositional fracture and fault development in carbonate platform systems is a key process that controls the diagenetic, depositional, and structural evolution of the platform. Several studies have suggested that early brittle deformation in carbonate platforms is caused by differential compaction between the grain-rich platform top carbonates and the mud-rich slope and basinal sediments (Hunt et al., 1996; Saller, 1996; Hunt and Fitchen, 1999; Longley, 1999; Rusciadelli and Di Simone, 2007; Frost and Kerans, 2010; Rush and Kerans, 2010). Differential compaction has also been proposed to cause early fracture development at a smaller scale in strata overlying carbonate mounds and buildups (Davies, 1977; Mazzullo and Cys, 1979; Shinn et al., 1983; Kirkby, 1994; Gutteridge, 1995; Frost and Kerans, 2009). These postulations are difficult to confirm because the mechanisms and factors controlling syndepositional fracture development are not discernable in outcrop and subsurface data. I address this problem by 2D and 3D numerical modeling that simulates differential compaction in carbonate mound complexes at the individual mound-scale and at the platform-scale. Numerical models are based on outcrop and subsurface examples of Late-Pennsylvanian carbonate mounds. Modeling results are validated by outcrop- and subsurface-based fracture observations.

The finite-discrete element numerical models presented here are the first to model differential compaction fracture development in carbonate platforms. The evolution of the stress state during compaction is documented and the factors controlling fracture location and intensity are identified. Because the modeling approach adopted in this dissertation is process-based, it can help predict fractures in areas where direct fracture observations are not possible (e.g., inter-well areas in the subsurface). This has implications for better

characterization of subsurface permeability anisotropy and optimizing hydrocarbon reservoir development.

This dissertation consists of three self-contained manuscripts investigating field-based and model-based aspects of fracture development in carbonate mound complexes. The first manuscript (Chapter 2) is a field-based study documenting syndepositional differential compaction fractures in a classic locality for Late Penssylvnaian carbonate mounds in the Sacramento Mountains in New Mexico. The study investigates the spatial organization of syndepositional and late fractures in a carbonate mound complex and the corresponding evolution in mechanical stratigraphy.

In the second manuscript (Chapter 3), 2D finite-discrete element models of carbonate mound complexes are used to quantify and test factors controlling syndepositional fracture development. The numerical models are based on outcrops discussed in Chapter 2. In the study, numerical models are used to: (1) quantify the amount of differential compaction required to develop fractures within carbonate mound complexes, (2) determine key controls on differential compaction fracturing, and (3) determine the effect of layer-parallel slip on fracture attributes. Modeling results are compared to outcrop observations of early fracture development in carbonate mound complexes.

In the third manuscript (Chapter 4), 3D numerical models are constructed to investigate the influence of the 3D antecedent topography variability on the spatial distribution of differential compaction fractures. Finite-element models are based on the Late Pennsylvanian Canyon and Cisco isolated carbonate platforms in the SACROC unit of the giant Kelly-Snyder oil field in the Midland Basin. 3D buildup-scale models are also constructed to test the effect of 3D geometry on fracture development within the Cisco

carbonate mound complex. Modeling results are compared to subsurface based observations of fractures in the Kelly-Snyder Field.

Chapter 2: Evolving Mechanical Stratigraphy and Fracture Development in Carbonate Mound Complexes: Insight from Late Pennsylvanian Mounds in New Mexico

ABSTRACT

Syndepositional fracture development is common in mound complexes and their cover strata where marine and meteoric cementation lithify sediments prior to burial. The mechanical stratigraphy associated with early fracturing is expected to evolve with burial diagenesis. To explore this, we investigate the spatial distribution of both early-formed and late tectonic fractures and their associated mechanical stratigraphic elements in the Late Pennsylvanian-age carbonate mound complexes in Yucca Canyon, Sacramento Mountains, New Mexico. Syndepositional fractures are exclusively present in facies that underwent early cementation and are either entirely contained within a bed, or bed-bound. Mound-core facies and subaerially exposed grain-rich carbonates undergo early diagenesis in the form of marine and meteoric cementation making them competent and susceptible to brittle failure while still in the near-surface environment. In contrast, mud-rich carbonates and shale show evidence of early ductile deformation. Field characterization of stratigraphic relationships and fractures was aided by 3D digital outcrop models and revealed that syndepositional sediment-filled fracture orientation and locations are consistent with fracturing during differential compaction in a shallow burial setting. We interpret calcite-filled fractures that are present in all facies and commonly throughgoing (i.e., not bed-bound) to be of later tectonic origin (Laramide and Rio Grande Rift). Field measurements of present-day unconfined compressive strength revealed strength homogenization across mud-rich and grain-rich carbonates. The late fractures most likely post-dated strength homogenization as evidenced by their throughgoing nature and the power law/exponential relationship between height and

spacing regardless of lithology. The maximum fracture height in this evolved mechanical stratigraphy is influenced by the bedding styles of mechanical units. The highest intensities for late fractures are coincident with locations of early fracture systems, highlighting the potential of early-formed fractures to reactivate. This relationship between early and late fracture systems underscores the importance of constraining the spatial distribution of early-formed fractures, as well as an understanding of the heterogeneous pattern of early-formed mechanical stratigraphic units.

1. INTRODUCTION

Fractures and faults that develop soon after deposition in carbonate systems can create long-lived conduits for fluid flow and can influence subsequent fracture pattern (Cozzi, 2000; Narr et al., 2004; Kosa and Hunt, 2006; Frost et al., 2012; Budd et al., 2013). The spatial distribution of syndepositional fractures (also referred to as early-formed fractures hereafter) and faults in carbonate systems has been mainly studied in shelf margin settings of high-relief carbonate platforms (Playford, 1980; Hunt et al., 2003; Collins et al., 2006; Frost and Kerans, 2009; Frost and Kerans, 2010; Bud et al., 2013). Early mechanical units differentiation associated with early fracturing in high-relief carbonate platforms has been shown to be tied to the distribution of early cementation and lithification (Frost and Kerans, 2010). Several mechanisms for the generation of syndepositional fractures and faults in carbonate platforms were proposed including, differential compaction, synsedimentary tectonism, and gravitational collapse (e.g., Hunt and Fitchen, 1999; Vahrenkamp et al., 2004; Frost and Kerans, 2009). Less is known about the spatial distribution and mechanical stratigraphy associated with local syndepositional deformation in carbonate mounds and buildups. The early fractures and faults in carbonate mounds have been attributed to differential compaction (Shinn et al.,

1983; Kirkby, 1994), gravitational slope instability (Gutteridge, 1995), and synsedimentary tectonism (Bourrouilh et al., 1998).

Mechanical stratigraphy imposes a control on fracture height and intensity in layered carbonates (Corbett et al., 1987; Underwood et al., 2003). Previous studies suggested that mechanical stratigraphy can change temporally as evidenced by variable degree of fracture height confinement within the same strata (Shackleton et al., 2005; Hayes and Hanks, 2008; Laubach et al., 2009; Frost and Kerans, 2010). Such studies focused on mechanical stratigraphy evolution in either siliciclastic successions or relatively uniform carbonate successions. Carbonate mound complexes (i.e., mound core, flank, and cover strata) have high potential for displaying a strong contrast in mechanical stratigraphic properties (Young's Modulus, Poisson's ratio, and strength) over time that has not been investigated systematically. Early differential diagenesis across carbonate mound complexes is expected to produce high initial contrast between mechanical units. Carbonate mounds and reef facies have been documented to experience in situ marine cementation and organic binding throughout most of the Phanerozoic (Cross and Klosterman, 1981; Webb, 1996). Cover strata, such as the grain-rich facies occurring at the top of depositional cycles capping the mounds described in this study experience rapid, pre-burial cementation associated with both marine and meteoric vadose cementation (Goldstein, 1988b; Dravis, 1996). Early cemented facies such as mound core and grainy strata above are expected to be brittle, competent, and susceptible to fracturing prior to any significant burial. Mound flank and mud-rich cover strata are incompetent and susceptible to compaction in the near-surface setting. We hypothesize that the initial mechanical units' differentiation corresponding with early fracturing evolves with burial diagenesis such that mechanical contrast between strata decreases. Eventually all mechanical units become susceptible to fracturing with tectonism.

In this study, we use the Holder Formation outcrops in Yucca Canyon in the Sacramento Mountains of New Mexico to investigate the evolution in mechanical stratigraphy and the corresponding fracture development in carbonate mound complexes. In effort to characterize early and late fractures and infer the associated mechanical stratigraphy, we employ several methods including field investigation, Schmidt hammer measurements, high-resolution photographs, thin sections, and a 3D digital outcrop model.

2. GEOLOGIC SETTING

The present day geomorphology of the Sacramento Mountains, bordered to the west by the Tularosa Basin and the Pecos River valley to the east, formed as a result of slip along a west-dipping high-angle normal fault located along the western boundary of the range (Figure 1) (Bartsch-Winkler and Donatich, 1995; Brown and Phillips, 1999; Pray, 1961). The minimum estimated displacement along the bounding normal fault of the Sacramento Mountains is approximately 2.1 km in the central region and 1.2 km to the north and south (Pray, 1961). This is part of series of north-south trending basins with horst and graben structures associated with the Rio Grande Rift (Chapin, 1979; Seager and Morgan, 1979). Precambrian through Cretaceous-age rocks are exposed within the Sacramento Mountains. Our study, focuses on the Late-Pennsylvanian Holder Formation exposed in Dry and Yucca Canyons near Alamogordo, New Mexico. In the following, we elaborate on the stratigraphic framework and the tectonic setting relevant to the Holder Formation.

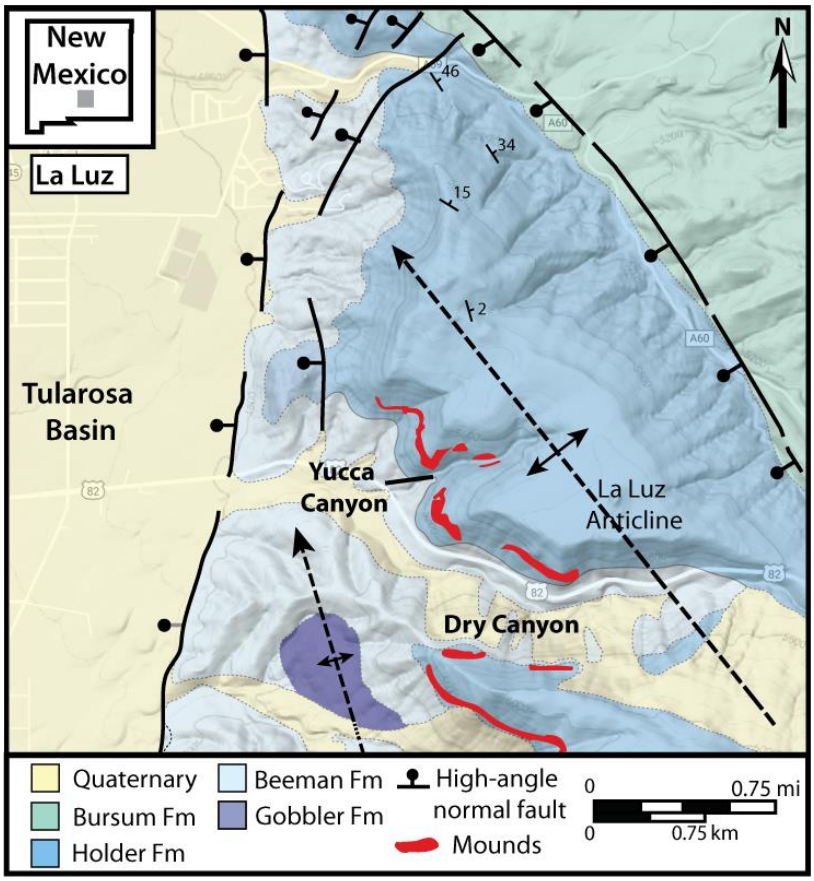

Figure 2.1: Map showing the study area (Yucca and Dry Canyons) and the distribution of phylloid mounds within the Pennsylvanian Holder Formation. Compiled from Pray (1961), Janson and Madriz (2012), and Google Terrain Maps. (Center coordinates [latitude, longtitude]: $32^{0}57'33.41"N$, $105^{0}55'13.63"W$)

2.1 Stratigraphic Framework

The Late Pennsylvanian Holder Formation is a prime example for phylloid mound complexes in a mixed carbonate-siliciclastic system with an established stratigraphic framework (Otte, 1959; Pray, 1961; Wilson, 1967; Wilson, 1972; Toomey et al., 1977; Goldstein, 1988b; Rankey et al., 1999; Janson and Kerans, 2011). The Holder Formation was deposited on a tectonically active narrow shelf between the western margin of the

Pedernal Uplift and the Orogrande Basin during Late Pennsylvanian (Virgilian) time (Pray, 1961; Wilson, 1972). The Holder Formation is characterized by massive mound cores constructed primarily by phylloid algae with flank and cover beds of skeletal wackestone to packstone, and oolitic to skeletal grainstone, as well as fossiliferous shale, sandstone and siltstone. Cyclicity was primarily controlled by eustatic sea level changes with some local influence of the syndepositional northwest-trending La Luz anticline (Goldstein, 1988b; Pray, 1961; Rankey et al., 1999; Wilson, 1967). The Holder Formation consists of 22 high-frequency sequences (6-30 m thick) each bounded by a subaerial exposure surface or its correlative conformity (Wilson, 1967; Rankey et al., 1999). Evidence of subaerial exposure includes rhizoliths, laminated crusts, and desiccation cracks (Goldstein, 1988a, b). The high-frequency sequences can be bundled into 4 third-order composite sequences (Figure 2) (Janson and Kerans, 2011). Phylloid mounds with up to 30 m of synoptic relief (i.e., depositional relief from sea floor) are present within the transgressive system tracts of the first two composite sequences, while the younger sequences are dominated by interbedded thin carbonates and siliciclastics. The focus of this study is on first two composite sequences. Facies offset, lack of tidal-flat caps (i.e., discontinuous cycles) , and frequent subaerial exposure of subtidal strata most likely at the 4^{th} order sequence level in the Holder Formation are consistent with high-amplitude, high-frequency changes in sea level as is characteristic of icehouse conditions (Wilson, 1967; Goldstein, 1988a; Kerans, 1995; Read, 1998; Rankey et al., 1999). The variability in the volume of polar ice caps generated eustatic amplitudes as high as 100 m (Soreghan and Giles, 1999). The heterogeneous nature of the mixed carbonate-siliciclastic system is expected to affect mechanical stratigraphy and fracturing. The focus herein is on Yucca Canyon near the paleo-shelf margin, where there is a concentration of carbonate mounds (Toomey et al, 1977). Dissecting the sequence of

depositional events is important to identify beds with contrasting compaction potential (Figure 3). The first composite sequence in this locality has a series of meter-scale plumose digitate algal microbial mounds ("Leopard Rock", Wilson, 1975) at its base. Beds overlying the leopard rock mounds can have extreme dip variation from 0 to upward of 60 degrees within 1 meter distance. Wackestone and shale beds are present in the inter-mound area and have high potential for compaction. Soft sediment deformation features observed in these beds further support their ductile deformation and compaction potential. This is followed by the growth of large scale phylloid mounds (up to 30 m thick). Toomey et al. (1977) described two growth stages in these large-scale mounds that is interrupted by subaerial exposure event and ended with another subaerial exposure exposing the mounds. Locally at the middle mound (Figure 2) a lowstand wedge onlaps the mound, which is dominated by mud-rich carbonates and grades to cm-scale layers of phylloid grainstones near the mound crest. Lowstand conditions is inferred given that phylloid mound deposition occurs in a moderate water depth (estimated 7-40 m) (Stevens, 1971; Schatzinger, 1983; Soreghan and Giles, 1999) while the skeletal grainstones that onlap near the mound crest require high energy (i.e., few meters of water depth). These lowstand wedge strata are observed to be dipping up to 25 degrees and had early high compaction potential. Overlying the mounds and the inter-mound fill are two shallowing up cycles from mud-rich carbonates to grainstones capped by a subaerial exposure surface. Furthermore, grainstone dips vary depending on their location relative to the mound crest from horizontal on top of the mound to up to 20 degrees dip overlying the flank of the mound. Both the mounds and the exposed grainstones were subjected to early cementation (Goldstein, 1988b) and therefore expected to be resistant to compaction.

2.2 Tectonic History

During the Late Pennsylvanian, the Pedernal Uplift to the east of the study area was active as part of the Ancestral Rocky Mountains tectonic province (Pray, 1961; Wilson, 1967; Wilson, 1972; Kluth and Coney, 1981). The paleotopography and subsequent facies distribution of the Holder Formation strata was locally influenced by the open and broad northwest-plunging La Luz anticline (active during Pennsylvanian-Early Permian) and the Pedernal shelf-edge geometry (Pray, 1949; Rankey et al., 1999; Wilson, 1972). After the deposition of the Holder Formation (275 m), the unit was subjected to pre-Laborcita erosion in some areas (~ 30 m eroded in Dry and Beeman canyons) and then overburden stress from the overlying Permian strata (762 m) and an unknown thickness of Mesozoic and Cenozoic strata (Figure 3) (Pray, 1961; Rankey et al., 1999). Post-Paleozoic deformation occurs within the Sacramento Mountains during the Laramide Orogeny (late Cretaceous to early Paleogene) (Dickinson et al., 1978; Seager, 1983). No uplift is attributed to the Laramide Orogeny in the Sacramento Mountains (Kelley and Chapin, 1997). This was followed by subjecting the rocks to extensional stresses and exhumation along the eastern flank of the Rio Grande Rift during the Eocene to present (Brown and Phillips, 1999; Berglund et al., 2012). This is evidenced by the dominance of Neogene sediment filling the adjacent Tularosa Basin (Lozinsky and Bauer, 1991), Holocene fault scarps along the basin margins (Machette, 1987), and the 35-41 Ma apatite fission track dating of metasedimentary rocks at the base of the Sacramento Mountains scarp (Kelley and Chapin, 1997). All aforementioned stress regimes may have contributed to the present day fracture population.

3. METHODS

Several methods are utilized to characterize fractures and the strength of different strata in Yucca Canyon. In the following field and remote-sensing methods utilized for fracture and strength characterization are described.

3.1 Fracture Characterization

High-resolution photographs that were taken approximately perpendicular to Yucca Canyon walls were obtained for the purpose of constraining the spatial distribution of fractures and to conduct fracture intensity analyses in phylloid mound complexes and their cover strata. Fracture orientation, aperture, fill, and relative timing cannot be determined from the photographs. Therefore, fracture fill, aperture, host lithology, orientation, GPS location, vertical continuity, and cross-cutting relationships -if present- for ~300 fractures were documented in the field in Yucca Canyon. Fracture fills for different types of fractures were also investigated at the microscale from 35 thin sections. Thin sections were imaged using Axio Imager 2 system, which produces high-resolution full-slide photomosaics. Full slide perspective is useful for a continuous view of microfractures and deformation features in thin sections, especially in mound facies where large cavities can be greater in size than the standard microscope field of view. Distinguishing early and late fractures in the field is not always clear-cut. However, some fractures can be convincingly ruled as early in origin. These are fractures that underwent solution-widening and concurrent or subsequent sedimentary fill. The trace and aperture of these fractures are irregular compared to the planar trace of the calcite-filled fractures. Also syndepostional fractures can be identified from observation of marine cement or sedimentary fill often associated with subaerial exposure (Meyers, 1974; Walls et al., 1975). Approximately 90% of fractures observed in the field are filled or partially filled

with coarse crystalline white to transparent calcite spar. Few of these fractures have red staining and others display both red stained cement and white crystalline calcite cement. This is most likely a byproduct of oxidizing of iron present within the cement rather than a caliche fill. Previous cement stratigraphy work has demonstrated that early cements in the Holder Formation are nonferroan, while late cements can be both ferroan and nonferroan (Goldstein, 1988b). Also, the majority of fractures with red staining have similar orientation and linear trace as adjacent unstained calcite-filled fractures. Calcite-filled fractures have persistent orientations within our study area, present in all facies, and often observed to cut across beddings; thus are assumed to be of late tectonic origin. Some fractures are barren of fill and are most likely a byproduct of outcrop weathering. These were a minority of the fracture population and were discarded from analyses to the best of our ability.

We utilized ArcGIS software to map ~1000 fractures that are spatially referenced relative to each other on the high resolution photograph of the northern wall of Yucca Canyon. A limitation of the high-resolution photographs is that they cannot reliably detect all fractures less than 0.25 m in height and cannot capture fractures in recessive beds. Therefore, fracture interpretation was limited to the grain-rich benches and phylloid mounds. Furthermore, bedding planes were mapped on the photo-panoramas to determine fracture vertical continuity through bedding planes (i.e., bed-bound or through-going). An unmanned aerial vehicle (UAV) with an onboard camera and GPS unit was used to capture 1200 photographs of Yucca and Dry Canyons at variable angles. The UAV was flown at an altitude of 1720 m (above sea level) in Yucca Canyon and 1790 m (above sea level) in Dry Canyon. Each photo is tagged with latitude, longitude, and altitude. Using 800 selected images in a photogrammetry software we constructed a 3D digital outcrop model (Figure 2A) (See Zahm et al. (2016) for more details).

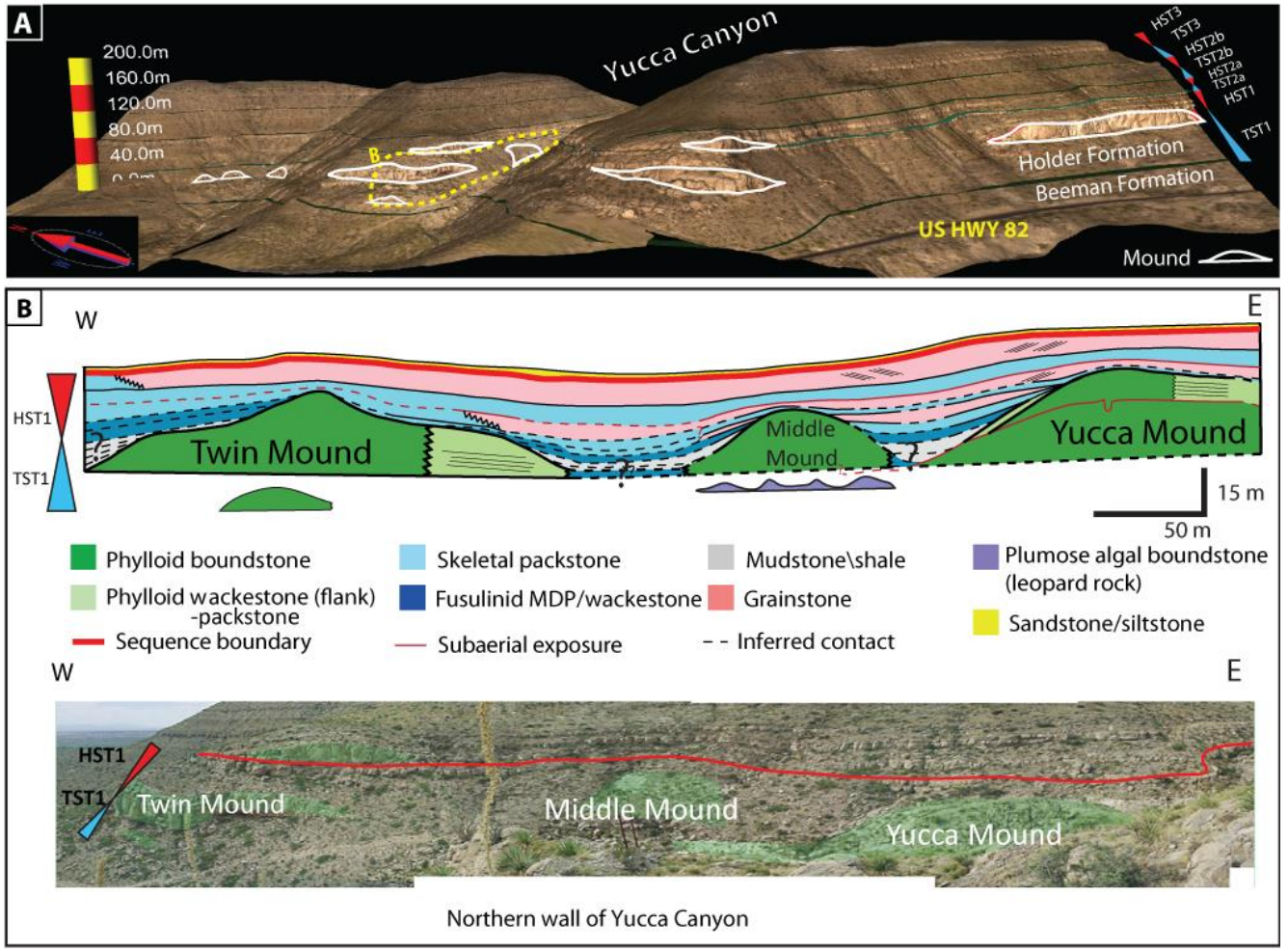

Figure 2.2: (A) 3D digital outcrop model of Yucca Canyon and part of Dry Canyon with interpretation of phylloid mounds and composite sequences extrapolated from Janson and Kerans (2011) interpretation. (B) Interpretation of the Holder Formation first composite sequence in Yucca Canyon showing the high vertical and lateral facies variability.

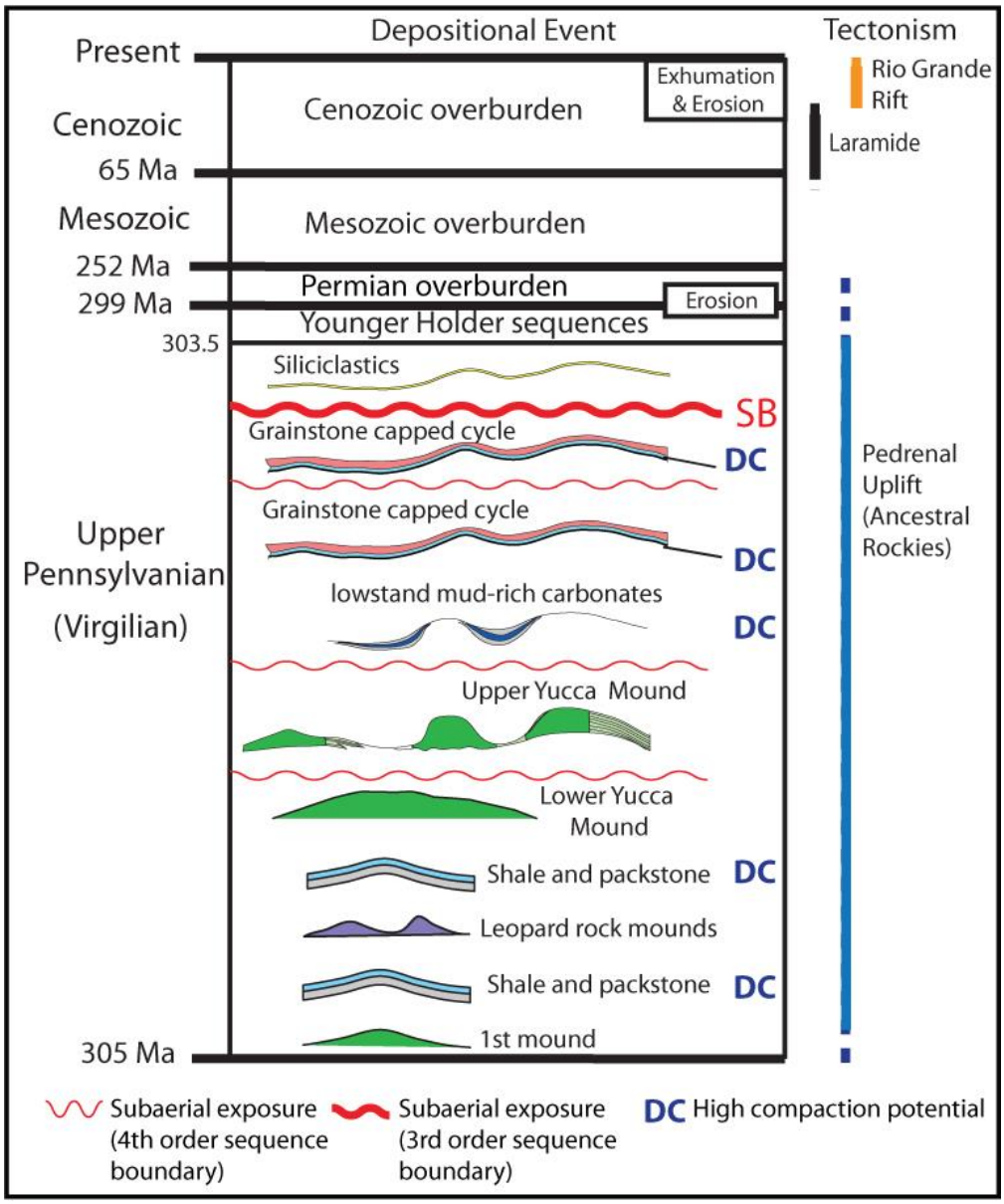

Figure 2.3: Dissection of the depositional events of the first composite sequence of the Holder Formation in a tectonic and chronological context.

Taking into consideration that the majority of fractures are less than 5 m in height and have less than 5 m average spacing, a graph of number of fractures present within each 5-meter distance along an interpreted layer was used as a measure of fracture intensity. Based on fracture height distribution, fractures were also grouped into 0.5 m height bins to investigate relationship between average fracture intensity/spacing and height. The location of early fractures with sedimentary-fill in grainstones overlying phylloid mounds in Yucca Canyon was constrained using a hand-held GPS in the field and was incorporated into the 3D digital outcrop model to visualize their location relative to the mounds.

3.2 Schmidt Hammer

A total of 296 unconfined compressive strength (UCS) values were recorded for the main facies present in the Holder Formation using N-type Schmidt hammer. The Schmidt hammer is a non-destructive test for rock hardness, which can be empirically related to several petrophysical and mechanical properties including UCS, Young's modulus, and porosity (Haramy and DeMarco, 1985; Aydin and Basu, 2005; Yagiz, 2009). Each UCS value is derived from the average of at least 10 hardness measurements in the field following ASTM (2014). The following empirical relationship is used to derive UCS value from hardness measurement: $UCS = 2.77e^{0.051*R}$, where R is the hammer rebound value (Aydin and Basu, 2005). The Schmidt hammer UCS measurements is valid for material with UCS between 20 and 150 MPa (Aydin, 2008). Some of the UCS values were recorded in a stratigraphic section representative of the first two composite sequences of the Holder Formation to document vertical variability. The majority of measured UCS values (n =266) are of wackestones, mud- and grain-dominated packstones, grainstones, and boundstones. Fewer values are measured for siliciclastics (n

= 29), because they are typically poorly exposed. UCS measurements give insight into the current mechanical stratigraphy.

4. RESULTS

4.1 Early-Formed Fractures

Field investigation in Yucca Canyon revealed the presence of early fractures in the Holder Formation, which are characterized by an irregular trace, large aperture (1-10 cm), and sedimentary fill (Figure 4 A, B). Early fracture fill consists of limonite cement/caliche fabric, altered ooids and foraminifera. Early fracture fill is often cross-cut by calcite veins (Figure 4B). The early macrofractures are subvertical and observed at subaerial exposure surfaces and must have been open during the time of exposure to be filled with sediments (i.e., approximately syndepositional). All early fractures are either bed-bound or terminate within a bed. The majority of the early macrofractures were observed in grainstones overlying phylloid mounds and only a few were observed within phylloid mound core facies (boundstone/bafflestone). The irregular trace and large aperture are consistent with solution-widening associated with vadose diagenesis. Thin section observations of isopachous calcite rims, equant pore-filling calcite, and moldic porosity indicate that grainstones containing early fractures underwent meteoric and/or marine cementation. This is consistent with findings of previous cement stratigraphy studies in the Holder Formation (Goldstein, 1988b). As a result of early cementation, grainstones and boundstones were able to deform in a brittle fashion with little to no burial and no compaction. The orientation of early fractures varies throughout Yucca Canyon from striking roughly N-S and E-W toward the east of the canyon to N-S and NW-SE toward the west. Early-formed fractures were determined in the field and their location on the 3D digital outcrop model shows them to be concentrated in grainstones

overlying phylloid mound crest-to-flank-transitions. This is especially noticeable in grainstone overlying the middle mound (Figure 5). The observed early macrofracture population is minor (10s of fractures) compared to the later tectonic fractures (1000s of fractures), however, it is conceivable that some early fractures did not experience solution-widening and cannot be conclusively characterized as early fractures in the field (e.g., Figure 4C).

Thin section investigation of phylloid mound facies reveals the presence of fractures filled or partially-filled with calcite cement (Figure 4 C, D). These fractures are distinct from the aforementioned sub-vertical fractures in that they are smaller in size and not filled with sediments. Fracture traces are often observed to be jagged and walls do not appear to be able to join back perfectly. They have many different orientations including being sub-horizontal in instances. These fractures preferentially occur in the clotted peloidal mud matrix of the mound core and were absent from mound flank facies.

4.2 Late Fractures

All partially or fully mineralized macrofractures that do not have sedimentary fill are considered to be "late" fractures. The term "late" fractures refers to all fractures that occurred during or after burial (50+ m) in response to tectonic stresses. These are widespread features that are observed to be present in all facies of the Holder Formation including proximal siliciclastics located in Dry Canyon. Late fractures are often observed to be cutting through bedding planes (i.e., through-going) and have linear traces with coarse blocky calcite fill (Figure 4 E, F). Fractures vary greatly in aperture (1 mm- 10s cm) and height (<5 cm - >10 m). Field documentation of orientations of ~300 fractures from various locations in Yucca and Dry canyons reveals that there is a major fracture set that strikes N-NE (015°-030°) and a minor set with a NW strike and wide azimuthal range

(Figure 7). Some of these fractures were observed to cross-cut vertical stylolites and in other instances horizontal stylolites indicating they post-dated some compression and overburden loading respectively (Figure 4 E).

Interpretation of fractures on high-resolution photographs in three grainstone layers that cap high frequency sequences and a phylloid mound layer from the northern wall of Yucca Canyon show a strong relationship between fracture height and intensity as well as spacing (Figure 6). The majority of fractures are equal or less than 1 m in height and decrease in abundance with increasing height following a power law curve with a negative exponent ($y = 653.2x^{-2.613}, R^2 = 0.9$) (Figure 6E). Fracture height and average spacing/intensity relationship is best described by a power law and exponential curves with exponents ranging between 0.92 and 2.3 (Figure 6D). The largest (i.e., tallest) fractures are present within the mound facies, which has the thickest and most massive bedding (Figure 6B). Fractures were noted to be most abundant within phylloid mound core and at inflection points in grainstones layers caused by the underlying transition from mound top to mound flank or intermound areas (Figure 6C). Refer to Appendix B for raw fracture data and additional results.

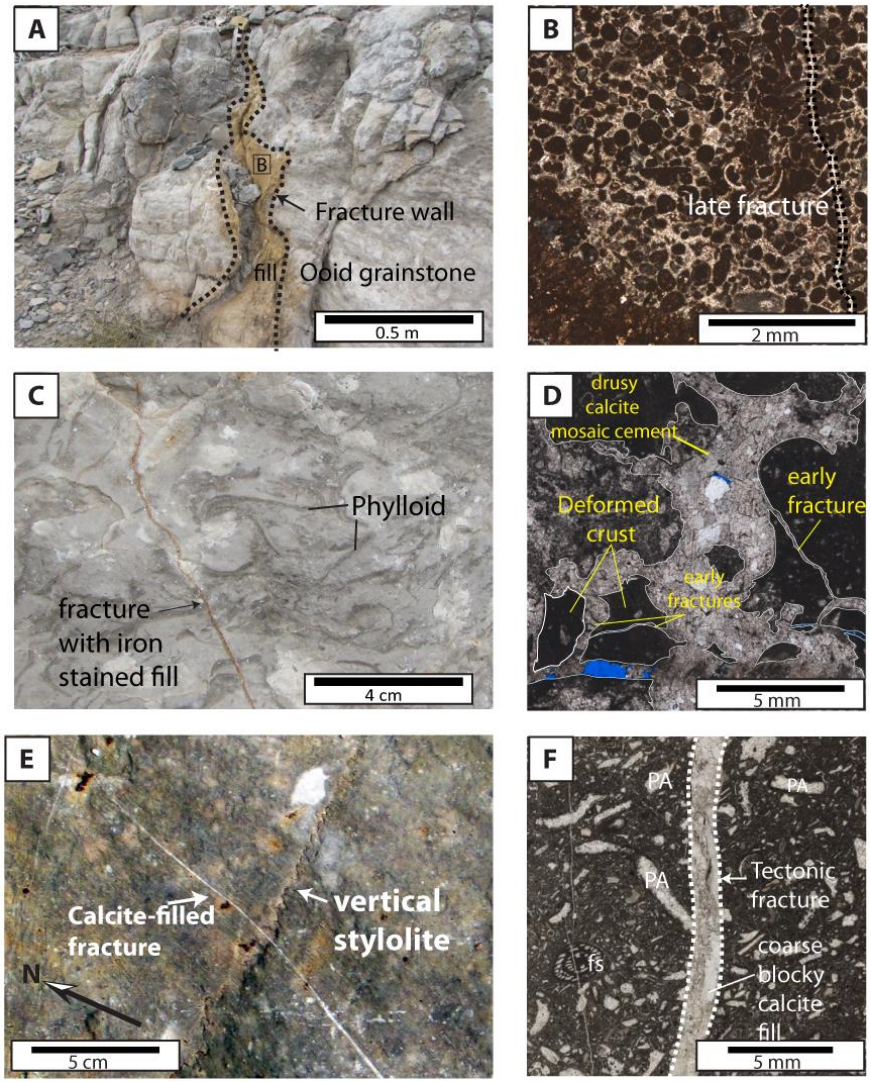

Figure 2.4: Fractures in outcrops and thin sections. (A) Solution-widened (early) fracture with sedimentary fill in an ooilitic grainstone below a subaerial exposure surface. (B) Photomicrograph of the fracture fill in A with limonite/caliche fabric, altered ooids, and microspar cement. Fracture fill is cross-cut by a later calcite-filled microfracture. (C) Phylloid mound core facies with iron-stained fracture fill. (D) Photomicrograph of mound core facies with partially filled to cemented fractures with variable orientations and irregular trace preferentially present within the mud matrix. Large cavities are filled by drusy mosaic calcite cement. (E) Calcite-filled fracture cross-cutting a vertical stylolite (photo of bedding plane). (F) Photomicrograph of phylloid algae mud-dominated packstone with a (tectonic) macrofracture with calcite fill. Fracture cross-cuts grains and matrix (fs = fusulinid, PA = phylloid algae).

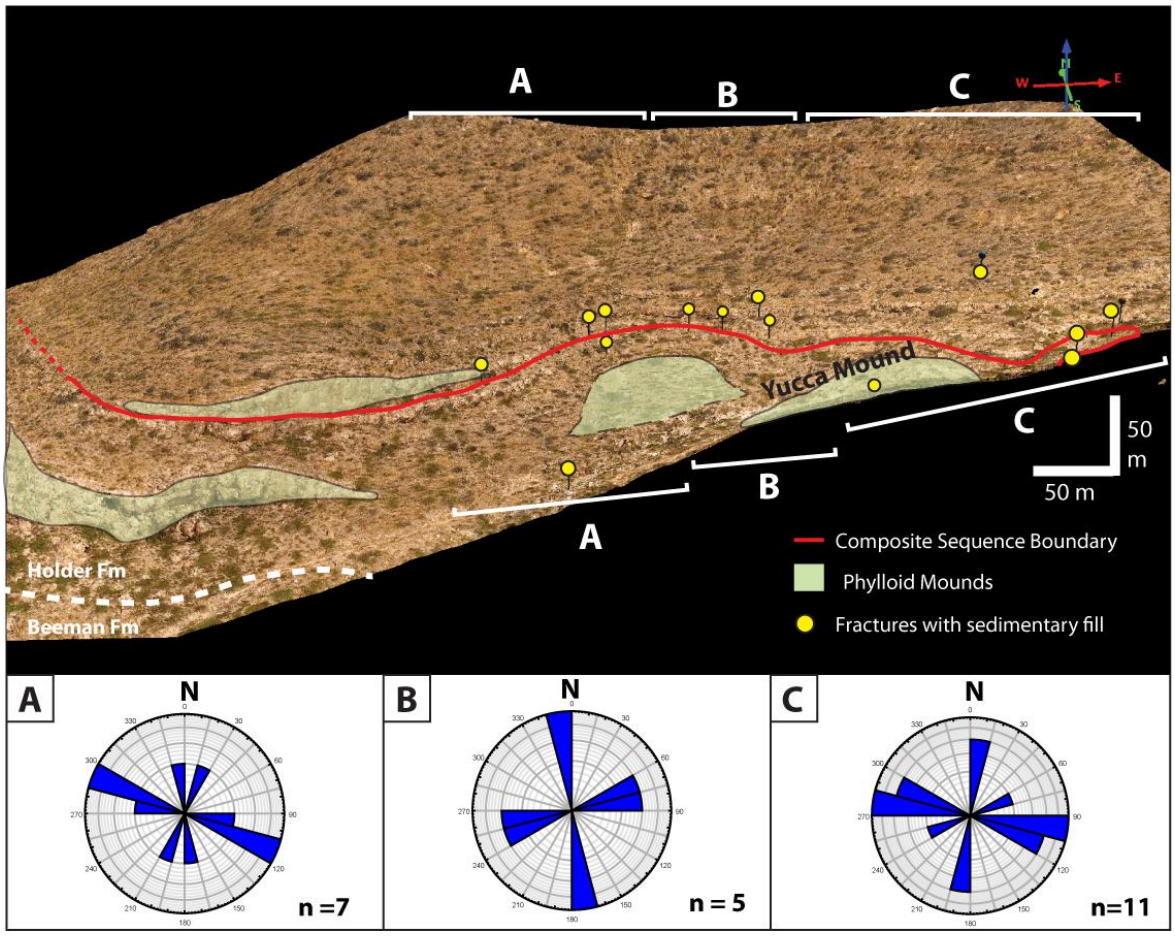

Figure 2.5: GPS Location of early sediment-filled fractures in Yucca Canyon superimposed on the 3D Digital outcrop model of Yucca Canyon. The majority of the fractures are concentrated in the grainstones overlying the flanks of phylloid mounds. (A-C) rose diagrams showing the strike of sediment-filled fractures across Yucca Canyon (n = 23).

4.3 Unconfined Compressive Strength & Mechanical Stratigraphy

Compilation of all Schmidt hammer measurements from the different facies present in the Holder Formation reveal that wackestones, packstones, and grainstones have similar median UCS values (44-50 MPa). Boundstones and sandstones are characteristically stronger than other carbonate facies with a median UCS of approximately 67 and 65 MPa respectively. Schmidt hammer measurements on shale are characteristically low (median

UCS = 20 MPa), but that might be a by-product of inherently poor exposure and small number of measurements. Comparison between the ranges of values measured for the different facies shows significant overlap (Figure 8). UCS measurements using the Schmidt hammer records a somewhat homogenized rock strength and reflects the late-stage rock strength. We discuss later in this paper how rock strength evolves from the time of deposition to present.

A stratigraphic section representative of facies present within the first two composite sequences of the Holder Formation in Yucca Canyon with matching UCS measurements was constructed to examine the vertical variation in strength (Figure 9). Plumose algal microbial boundstones (leopard rocks) are meter-scale mounds present in the base of first sequence of the Holder Formation and are the mechanically strongest mound facies. The alternating mud-dominated packstones and shale overlying these small-scale mounds show significant UCS variation. Phylloid mounds and facies in the upper sequences have minor variations in UCS with mud-rich facies and the directly overlying grain-rich facies having similar UCS in some instances.

Fracture height and terminations observations reveal variable fracturing behavior in the different facies packages of the Holder Formation indicating variability in mechanical behavior (Figure 10). Maximum fracture height varies with different facies and bedding thicknesses from cm-scale height in thin-bedded wackestone and shale to up to 10 meters high in massive phylloid boundstones. Grainstones and packstones fall between the two aforementioned fracture height extremes.

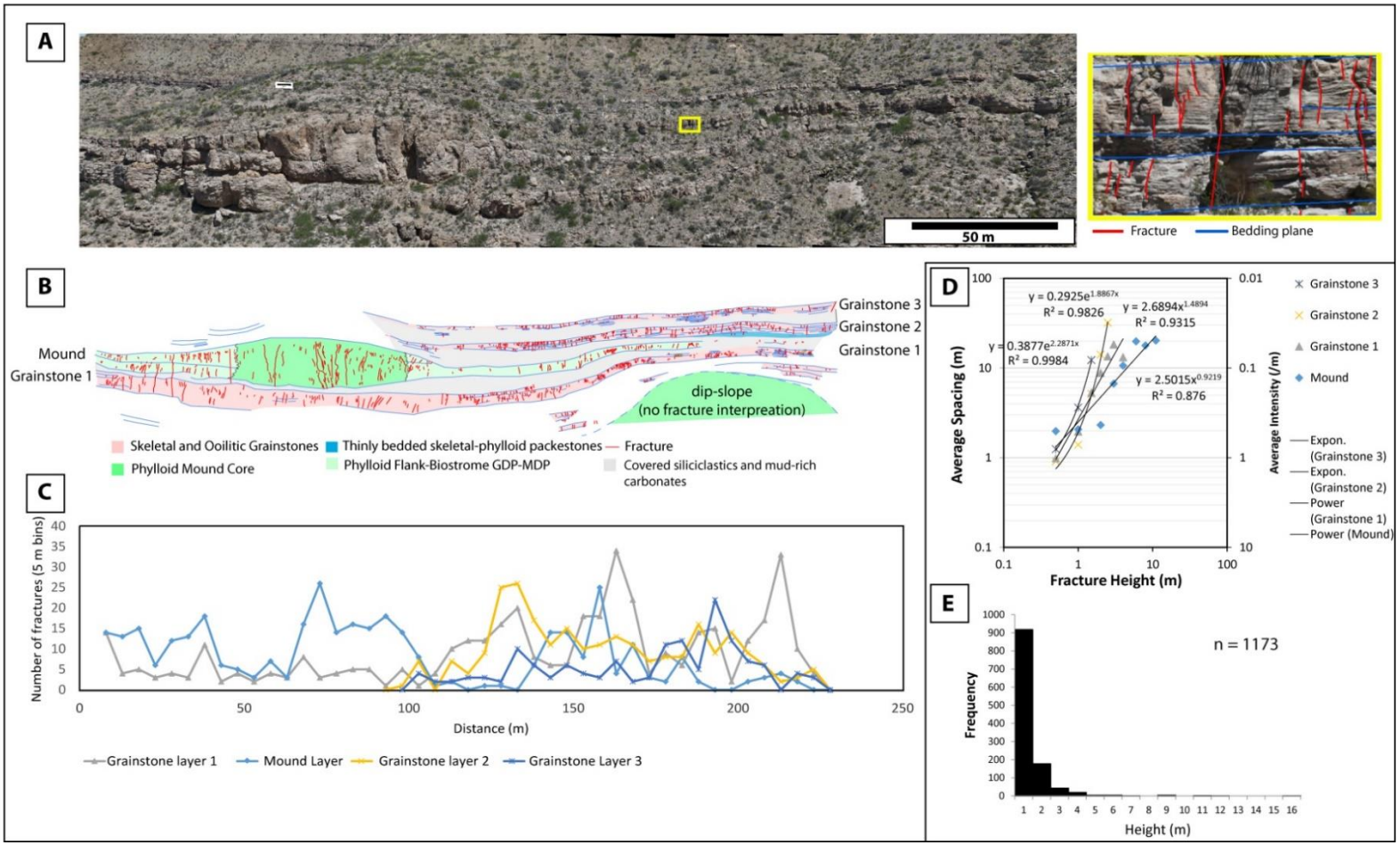

Figure 2.6: (A) High-resolution photo-panorama of northern Yucca Canyon (Yellow window shows 100% zoom of a 2 m thick grainstone). (B) Fracture, bedding, and facies mapping. (C) Number of fractures in a 5-meter distance bins as a measure of fracture intensity along beds in B. (D) Relationship between fracture height and its average spacing for the different layers. (E) Total fracture population height distribution.

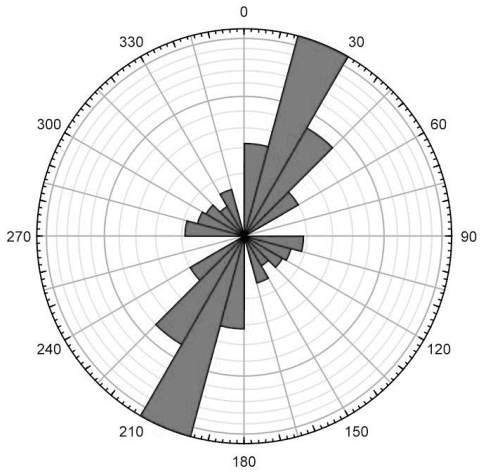

Figure 7: Rose diagram of calcite-filled fracture orientations in Yucca Canyon (n = 267).

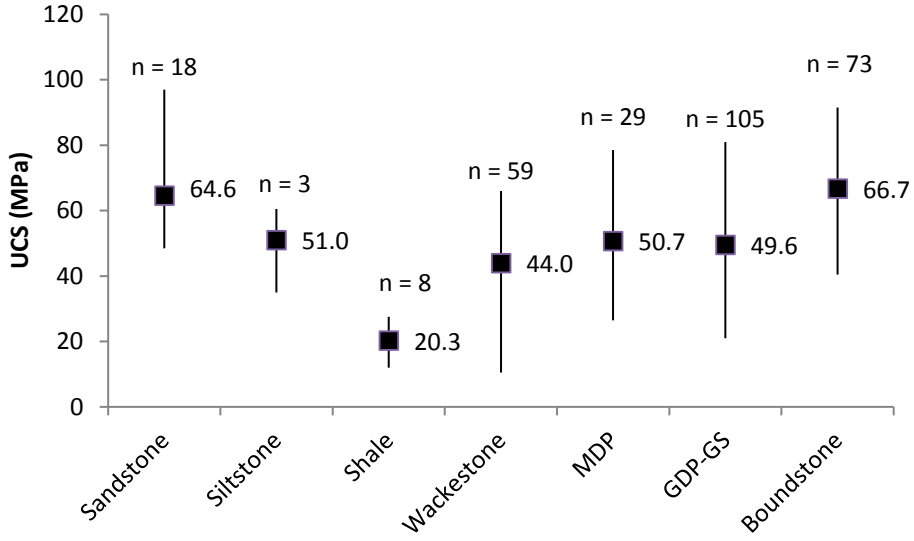

Figure 2.8: Unconfined compressive strength measurements using a Schmidt hammer for the various facies present in the Holder Formation. MDP = mud-dominated packstone, GDP = grain-dominated packstone, GS = grainstone, n = number of measurements, box = median, bars = range.

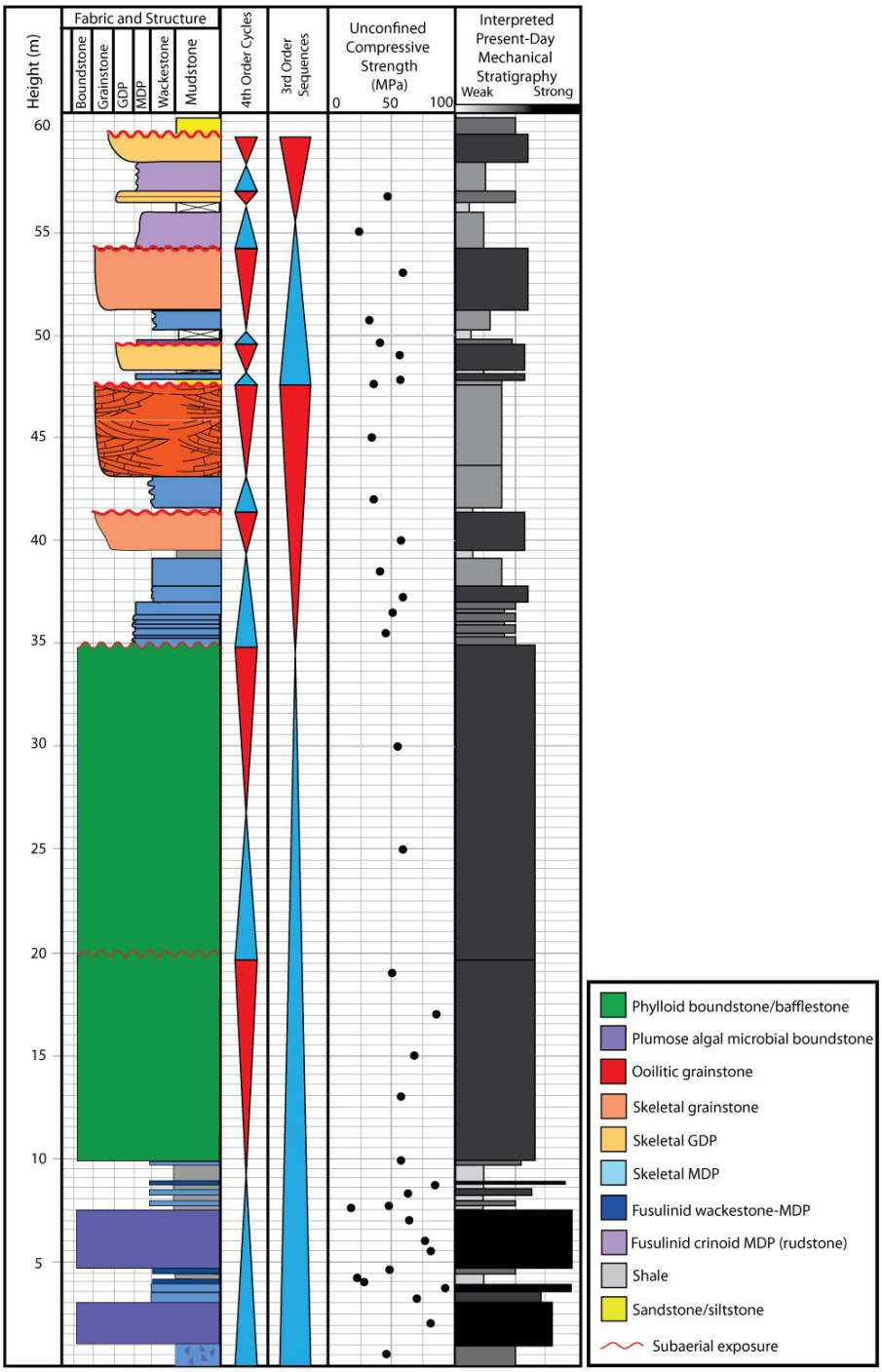

Figure 2.9: A representative stratigraphic section of the first two composite sequences of the Holder Formation in Yucca Canyon with corresponding UCS measurements and interpreted mechanical stratigraphy. Location of the section can be seen in figure 5. (GDP = grain-dominated packstone, MDP = mud-dominated packst

5. DISCUSSION

5.1 Early Fracturing Origin and Organization

Two possible mechanisms for early fracturing in the Holder Formation are considered. The first mechanism is bending of brittle early-cemented grainstones in response to differential compaction of the underlying strata. The second is fracturing in response to the development of the northwest plunging La Luz anticline, which was most active during the first two composite sequences of the Holder Formation (Wilson, 1972; Rankey et al., 1999).

Differential compaction has been recognized to occur in carbonate platforms and around carbonate buildups and reefs causing ductile and brittle deformation (Davies, 1977; Mazzullo and Cys, 1979; Shinn et al., 1983; Kerans, 1988; Kirkby, 1994; Gutteridge, 1995; Goldhammer, 1997; Hunt and Fitchen, 1999). Evidence of differential compaction in the Holder Formation includes warping of beds overlying carbonate mounds in Yucca and Dry canyons and variation in grainstone thickness (up to 30% change) (Figure 11). Dips of strata overlying the meter-scale leopard rocks can change from nearly horizontal to up to 60 degrees within 10s of centimeters (Figure 11B). Similarly, dips of grainstones overlying phylloid mounds can change from near horizontal to upward of 20 degrees when transitioning from the top of a mound crest to the inter-mound areas (Figure 11A). These extreme dips decrease gradually stratigraphically upward. Thickening of grainstone beds overlying the intermound areas and the upward decreasing dips suggest that differential compaction has initiated soon after deposition. Strata that are likely to have experienced differential compaction in the first composite sequence of the Holder Formation were identified in Yucca Canyon (Figure 3). Frost and Kerans (2009) suggested that such differential compaction can result in fracturing of strata overlying

carbonate buildups. Observations of early fractures concentrated in grainstones overlying phylloid mound crest to flank transition in Yucca Canyon are consistent with differential compaction fracturing (Figures 5 and 12). Given that these fractures are mainly identified using their solution-widened trace with sedimentary fill and the variable outcrop quality, it is conceivable that we only recognize a subset of the early fracture population. This subset of fractures would have the largest primary aperture and thus preferentially underwent solution-widening and concurrent or subsequent sediment fill (Siemers and Dreybrodt, 1998).

Yucca Canyon and the early fractures observed within it are located on the western limb of the broad northwest-plunging syndepositional La Luz anticline (Figure 1). At the time of early fracture development in grainstones and boundstones, overburden was negligible. Therefore, the minimum principle stress is vertical and the maximum principle stress is horizontal and perpendicular to the La Luz anticline axis (i.e. due NE). Given the inferred principle stress orientations, fracture sets that are consistent with folding and this particular stress configuration should be striking parallel or perpendicular to the anticline axis (i.e., due NW or NE) (Stearns, 1968). The measured strikes of early fractures are variable and the vast majority of them are not consistent with the expected fracture orientation related to La Luz anticline development (Figure 5). Therefore, the origin of the majority of observed early fractures is more consistent with differential compaction. Carbonate mounds are known to experience marine cementation and development of marine cemented cavities with geopetal fabric (Meyers, 1974; Davies, 1977; Mazzullo and Cys, 1979). Bathurst (1982) attributed microfractures within carbonate mounds to desiccation and fracturing of cemented crusts as well as deformation related to collapse of primary cavities. This is syndepositional differential compaction related to the nature of variable degree of cementation and lithification within carbonate mounds (Shinn et al.,

1983; Kirkby, 1994). This mechanism can explain the observed cemented and partially-cemented microfractures within phylloid mound cores and explains their absence from mound flanks that do not experience pervasive early cementation and lack primary cavities. This is further supported by the lack of consistent orientation of mound core microfratures and the irregular fracture traces. The degree of fracture trace irregularity could be indicative of the degree of lithification at the time of fracturing (Gutteridge, 1995).

5.2 Late Fracturing Origin and Organization

Two stress regimes are potentially responsible for the generation of late fractures in the Holder Formation including Laramide compression and exhumation related to the opening of the Tularosa Basin – part of the Rio Grande Rift. During the Laramide compression the maximum principle stress orientation was striking N-NE as evidenced from vertical stylolite orientation (015^0) observed in the field as well as previous regional work on Laramide structures (Seager, 1983). Fractures consistent with Laramide compression should be oriented parallel to the maximum principle stress. Given that some late fractures were observed to crosscut vertical stylolites (i.e., post-dated Laramide compression), not all late fractures can be attributed to Laramide stresses. The least principle stress direction associated with Rio Grande Rift was found to have rotated clockwise from NW-SE during the early development of the rift near the study area to E-W during recent to present time (Aldrich et al., 1986; Wilson et al., 2003). Fractures that are consistent with Rio Grande rifting are expected to be striking perpendicular to the least principle stress direction. However, given the stress rotation over time, a range of fracture orientations is possible from NE to N. This happens to overlap with fractures orientation consistent with Laramide stresses and therefore it is challenging to distinguish

between fractures related to these two stress regimes without clear cross-cutting relationships with vertical stylolites. Observations of late fractures present within early fracture fill indicates that early fractures are susceptible to reactivation by later tectonism. The highest fracture intensity of late fractures coincides with location of early fractures in the grainstone immediately overlying mound crest-to-flank transition as well as mound core facies (Figure 6 C). This suggests that early fractures potentially influence the spatial distribution of subsequent tectonic fractures.

5.3 Evolution of Mechanical Rock Properties through Time

The mechanical stratigraphy of phylloid mound complexes is variable both laterally and vertically reflecting the lateral and vertical stratigraphic complexity. The marine cementation of carbonate buildups makes them rigid and brittle and mechanically competent to experience syndepositional fracturing. Similarly, meteoric cementation and dissolution processes associated with subaerial exposure events allow grainstones and grain-dominated packstones, capping shoaling upward sequences, to be lithified and competent soon after deposition. In contrast, the underlying mud-rich facies (mud-dominated packstones, wackestones, and lime mudstones) are likely to experience less pervasive meteoric cementation because of their inherently low primary permeability (Enos and Sawatsky, 1981). This is consistent with observations of vertically discontinuous meteoric cement lenses in the Holder Formation (Goldstein, 1988b). Consequently, mud-rich facies within the Holder Formation are expected to be mechanically incompetent soon after deposition and are more prone to compaction than grain-rich facies. Given the early differential diagenesis, the greatest mechanical contrast between facies is expected to be present soon after deposition (Figure 12).

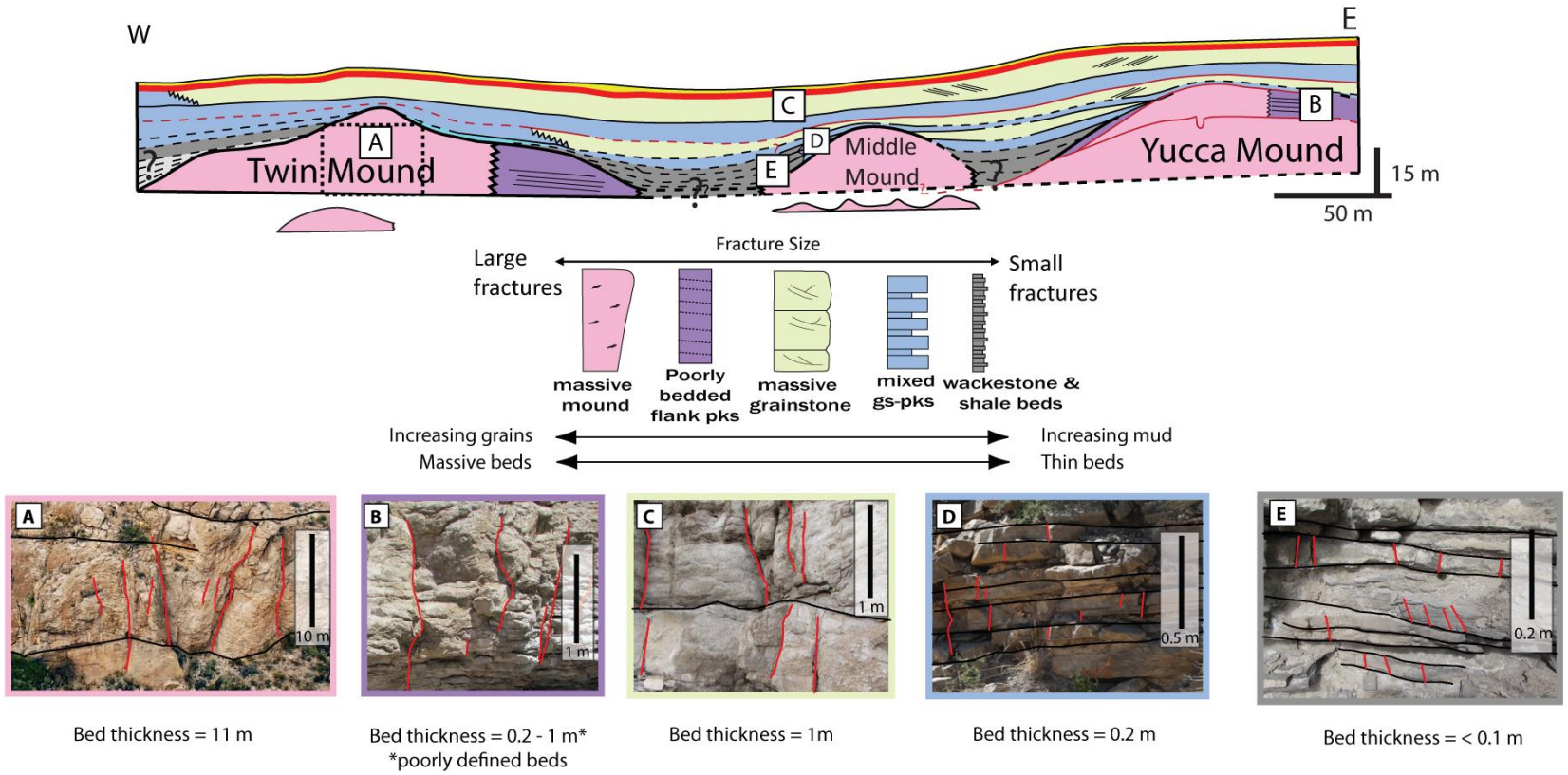

Figure 2.10: Mechanical stratigraphy scheme for the facies present within Yucca Canyon with illustrative examples of how bedding style and facies can control late fractures vertical extent. Scheme is modified from (Zahm et al. (2009)). (gs = grainstone, gdp = grain-dominated packstone, pks = packstone, ws = wackestone).

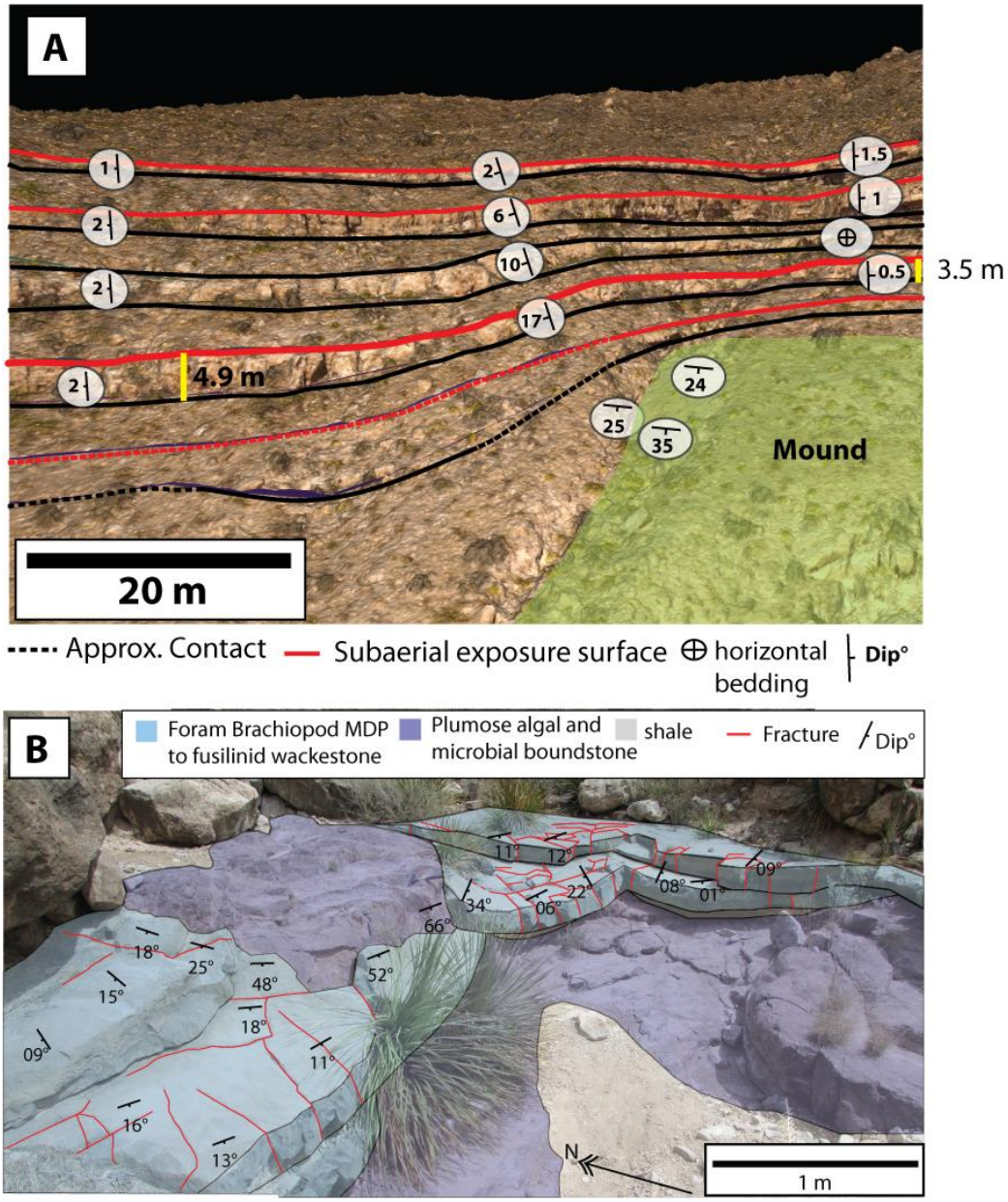

Figure 2.11: (A) 3D digital outcrop model of the middle mound in Yucca Canyon where grainstones overlying a phylloid mound are warped in response to underlying differential compaction. Degree of strata warping (dips) decreases upward. Grainstone thickness vary by up to 30%. (B) Meter-scale plumose algal microbial mound (leopard rock) with overlying shale and warped mud-rich packstones. Dips change radically in short distances in response to differential compaction.

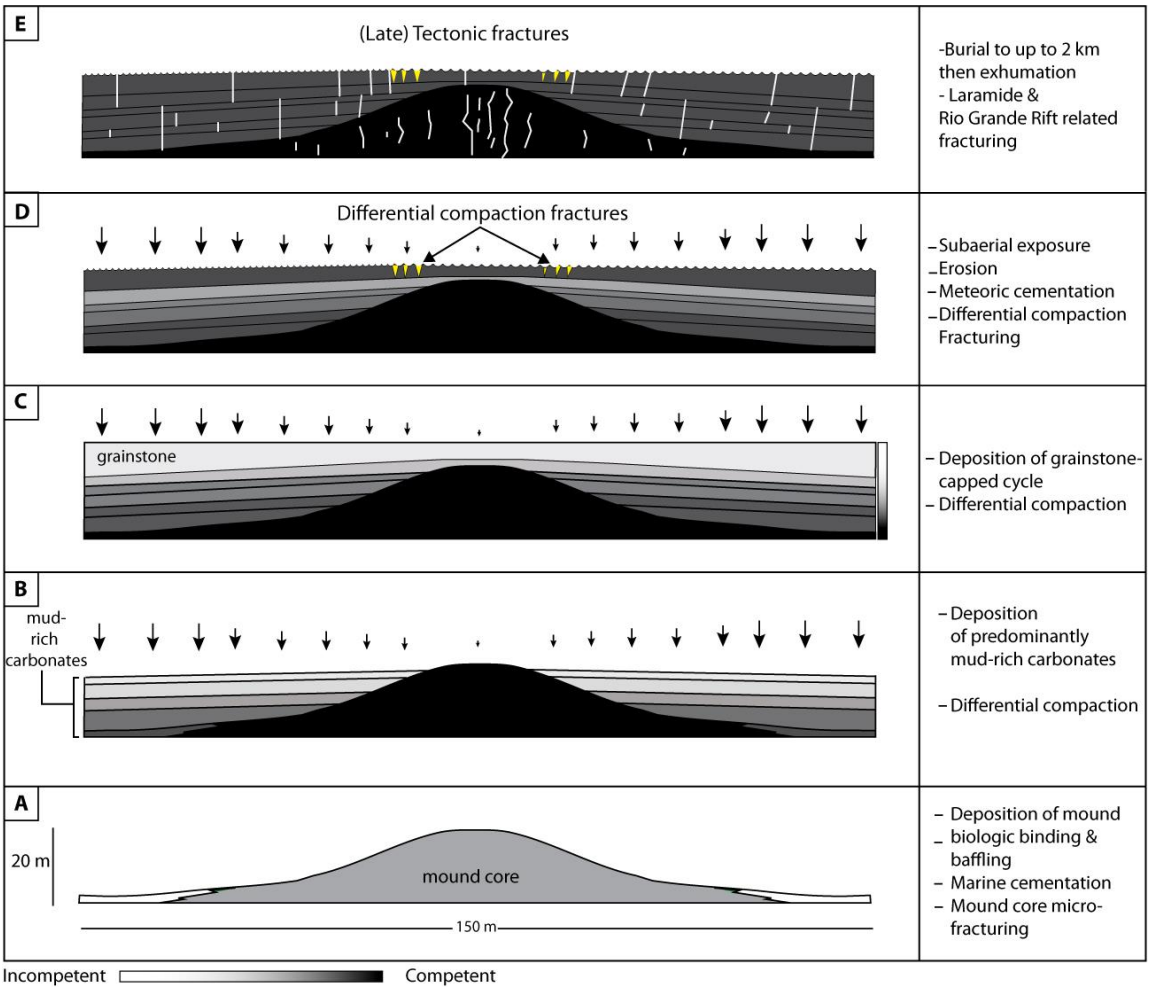

Figure 2.12: Chronological schematics of processes leading to fracture development in carbonate mounds with expected mechanical competence evolution. Black arrow sizes are relative to the amount of expected compaction.

The pervasive early marine and meteoric cementation of carbonate mounds and grain-rich facies suggests that they reach near-maximum strength prior to burial. Young grainstones (< 500 ka) that underwent early cementation prior to burial were observed to obtain strength comparable to grainstones in the Holder Formation, which allowed them to experience brittle failure (Guidry et al., 2007; Nolting et al., 2016). Conversely, the strength of mud-rich facies strength is expected to increase with burial diagenesis. Eventually, mud-rich carbonate facies could reach strengths similar or even greater than their grainy counterparts (Figure 8). This explains the minor differences in present-day UCS observed between the mud-rich and grain rich facies. Additionally, the pervasive cementation of shelter cavities within carbonate mounds (up to 40-50% of rock volume) potentially contribute to the additional strength that these facies exhibit (Figures 4D, 8). Late fracturing in the Holder Formation has occurred after significant burial diagenesis and most likely occurred after the homogenization of strength between facies. However, there are still differences in the fracturing behavior among the different facies. This could be result of variability in bedding size and style. For example, the phylloid mounds cores are massive and lack internal bedding and that allows for some late fractures to propagate unimpeded, which results in having the largest (i.e. tallest) fractures in the mound core facies. In contrast, mud-rich successions have many internal bedding planes and thus greater number of mechanical interfaces, which increases the likelihood of a fracture being terminated (Cooke and Underwood, 2001; Underwood et al., 2003; Cooke et al., 2006). Therefore, fractures in thin bedded mud-rich successions are typically shorter in height.

6. CONCLUSIONS

Examination of syndepositional and late tectonic fractures at a classic carbonate mound complex locality yields important insight into the evolution of mechanical stratigraphy

with respect to fracture development. Syndepositional fractures are limited to the early-cemented mound core and grainstone facies, suggesting that mechanical differentiation was initially high. Fractures are preferentially located in early-cemented strata overlying the flanks of the mound core and are not consistently oriented with respect to the La Luz anticline, which indicates that their origination is more consistent with differential compaction. This supports earlier work postulating that differential compaction can be a major process driving early deformation in carbonate mound complexes and in carbonate systems in general.

Highest intensities of late tectonic fractures are coincident with locations of early fractures, highlighting early fractures potential for reactivation and the significance of constraining their spatial distribution. Field measurements of rock strength –reflecting rock terminal strength– suggest that burial diagenesis obscured the early mechanical contrast and homogenized rock strength across grain-rich and mud-rich lithologies. Late tectonic fractures have consistent orientation with both Laramide and Rio Grande rift stresses and are commonly throughgoing (i.e., not bed-bound) indicating that they post-dated strength homogenization. However, bedding style and primary depositional fabric still imposed a control on maximum fracture height. The results of this study show that fracture development in carbonate mounds is affected by an evolving mechanical stratigraphy reflective of early and late diagenetic processes.

ACKNOWLEDGEMENTS

The work has benefited from discussions with Dr. Xavier Janson and Dr. Steve Bachtel. Dr. Rowan Martindale is thanked for facilitating high-resolution thin section imaging. Virtual Reality Geological Studio (VRGS) is thanked for providing free research license.

Chapter 3: Numerical Modeling of Differential Compaction Fractures in Carbonate Mound Complexes

ABSTRACT

Differential compaction has been proposed as a mechanism for early fracture development in carbonate systems with implications on fluid flow and subsequent deformation pattern. Carbonate mound complexes experience differential compaction due to differences in (lithology, early cementation, and strength) between mound core, flank, and cover strata, which promotes development of early fractures. Observations of early fractures in outcrops and core are often overprinted by subsequent diagenetic events, which impedes determination of key parameters that control their development. To address this problem, we use finite-discrete element mechanical models to simulate differential compaction fracturing in strata overlying carbonate mounds. Modeling results suggest that fracture development is influenced mainly by: (1) mound geometry and stratal architecture; (2) magnitude of differential subsidence; (3) bedding contact type; and (4) tensile strength of early-cemented strata. Mound geometry controls the location and spatial extent of fractures in the overlying strata. Fractures develop at hinges of forced folds mimicking the geometry of the underlying mound. The width of resulting fracture clusters are directly related to the shape and dimensions of the mounds. Tensile strength and magnitude of differential subsidence have inversely proportional and directly proportional relationships, respectively, to fracture intensity. The amount of differential subsidence required to initiate fractures is small relative to the mound height (as low as 1% of mound height). Through a series of forward geomechanical models we find that the amount of differential subsidence required to develop fractures is linearly related to the tensile strength of cemented strata. Comparison between a model with

layer-parallel slip and one without it reveals that layer-parallel slip has significant control on fracture intensity and style. The consistency of modeling results with outcrop observations illustrates the utility of a process-based modeling approach in predicting and quantifying early fracture development and factors that controls it.

1. INTRODUCTION

Syndepositional fracture and fault development in carbonate systems determines early permeability pathways and can influence subsequent deformation and diagenetic patterns. Compaction within and over marine-cemented carbonate mounds has been postulated to cause syndepositional fracture development (Davies, 1977; Mazzullo and Cys, 1979; Shinn et al., 1983; Kirkby, 1994; Gutteridge, 1995; Frost and Kerans, 2009). Given that differential compaction takes place early in the history of strata before subsequent overprinting by deformation and/or burial diagenesis, determining the parameters and features that are only relevant to the early fracturing process from outcrop or core observations is challenging. Here we use numerical models simulating differential compaction fracturing to overcome the complexity of present day rock observations and quantify key parameters that are otherwise indiscernible.

Forward numerical models can provide fundamental understanding of stress and strain evolution during geologic processes that occur at a large timescale (i.e., thousands-millions of years), which cannot be obtained from outcrop observations. Recent studies used modeling techniques based on the finite element method (FEM) to understand processes such as salt tectonics (Nikolinakou et al., 2014; Heidari et al., 2016) and thrust belt development (Albertz and Sanz, 2012; Thigpen et al., 2017). More appropriate to fracture modeling is the combined finite-discrete element (FDEM) technique that supports simulating fracture growth by transitioning from continuum to discontinuum.

Such a technique is useful for its ability to predict failure during an evolving stress state and continuously dissipate stress through fracturing (Klerck et al., 2004). Previous work used FDEM to model fracturing and collapse for geotechnical purposes including block-cave and open-pit mining (Elmo et al., 2007; Vyazmensky et al., 2010), tunnel excavation (Stefanizzi et al., 2007), and rock slope stability (Eberhardt et al., 2004; Stead et al., 2006). To the best of our knowledge prior to this study this modeling technique has not been applied to syndepositional fracturing in a depositional context except for fracturing by gravitational loading of steep-walled carbonate platforms (Nolting, 2017; Nolting et al., in review).

Layer-parallel slip (LPS) is another elusive process that is difficult to quantify and understand from outcrop observations. Quantifying LPS is hindered by lack of slip markers and the presence of slickenline evidence within bedding planes. Previous modeling efforts of LPS focused on quantifying amount and location of slip along bedding planes during the development of monoclines (Cooke et al., 1999; Smart et al., 2009). While it is known that LPS can create wide fracture aperture at slipping mechanical interfaces (Cooke and Underwood, 2001) the effect of LPS on the overall spatial distribution and intensity of the fracture population has not been demonstrated prior to this study.

Here we employ FDEM modeling to: (1) quantify the amount of differential compaction required to develop fractures within carbonate mound complexes, (2) determine key controls on differential compaction fracturing, and (3) determine the effect of layer-parallel slip on fracture attributes. Models initial geometry are based on the Late Pennsylvanian phylloid mound complex of the Holder Formation in the Sacramento Mountains in New Mexico (Pray, 1961; Wilson, 1967; Rankey et al., 1999). Modeling

results are compared to the distribution of early fractures observed in outcrops (refer to Chapter 2).

2. FINITE-DISCRETE ELEMENT NUMERICAL MODELING

Numerical modeling was conducted using the finite-discrete element software ELFEN®, which was chosen for its ability to model the transition of rock from continuum mass (FEM) to discontinuum (DEM) (Rockfield, 2014). This allows for the dissipation of stress in the modeled domain by simulating brittle fractures in the form of intra-element or inter-element discrete contacts (Klerck et al., 2004). Additionally, adaptive remeshing capability allows for fractures to be tracked as they grow and interact with each other as the stress conditions evolve. The modeling solution follows an explicit quasi-static plane strain formulation, where values for quantities such as stress, strain, and displacement are evaluated at each node of the meshed domain at each time step. Stress conditions are checked against the specified failure criteria at each time step and discrete contacts are formed if the brittle failure criteria are met. The following sections describe model setup and key inputs.

2.1 Model Geometry

A triangular mesh was used to construct 2D geomechanical models that simulated differential compaction and associated fracture development of strata overlying carbonate mounds. The geometry and dimensions of the modeled mounds were guided by 3D digital outcrop models of Late Pennsylvanian phylloid mounds in Yucca and Dry canyons in the Sacramento Mountains of New Mexico, USA. The 3D digital outcrop models were generated using photogrammetry software from 800 georeferenced photographs captured by an unmanned aerial vehicle and consists of 35 million points

each with x, y, z values (i.e., longitude, latitude, and elevation), and RGB color designation (See Zahm et al. (2016) for further details). Two mounds exposed along dip-oriented cliffs were chosen to be used for modeling representing two end-members of carbonate mound shapes: convex and tabular. The mounds were traced on the 3D model and their geometries were projected to a 2D plane and simplified by smoothing to enhance computation efficiency (Figure 1). The preserved mound geometry was retained as it is thought to have changed little from original deposition owing to pervasive marine cementation (Soreghan and Giles, 1999).

Mound flanks and intermound areas are overlain by mud-rich strata and shale shallowing upwards into capping grainstones with a subaerial exposure surface. Strata that onlap mounds and overlie them in outcrops are thin-bedded (cm's to 10s of cm) and may have dips greater than 20 degrees and laterally variable thicknesses due to early differential compaction (refer to Chapter 2). Therefore, these beds are restored to horizontal in the models based on the assumption that they were horizontal when deposited. For simplification, we do not account for lateral variation in bed thickness or compaction occurring prior to the deposition of all strata present within the model. For computational efficiency, the numerous thin onlapping strata were simplified into a few representative beds in the models. The model contains two grainstone layers (GS1 and GS2) overlying the mound to test the effect of increasing vertical distance from the mound on the required amount of differential subsidence to develop fractures.

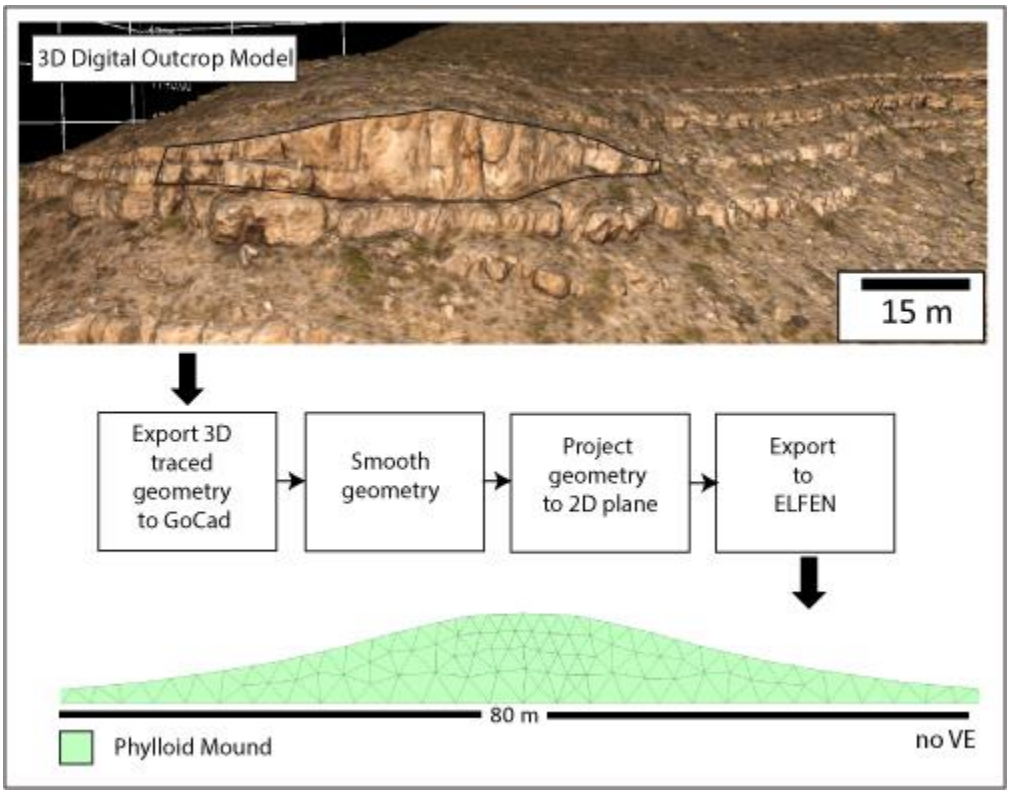

Figure 3.0.1: Workflow developed to create realistic initial geometries from 3D digital outcrop models.

2.2 Loading and Boundary Conditions

All models presented in this study are only subjected to gravitational loading. The gravitational loading is applied on the domain with a corresponding horizontal confining stress. The confining stress is assumed to be 80% of the vertical stress reflecting a slightly compressional settings known to be present during mound deposition (Pray, 1961; Wilson, 1967). However, sensitivity analysis is shown that lower confining stresses has little effect on the resulting stress state as it is more influenced by compaction. A linear load curve is used to apply gravity gradually on the domain. Along with gravity,

hydrostatic pore pressure is gradually introduced from the top of the domain. Drained conditions are assumed for the models with pore pressure remaining hydrostatic after the application of gravitational stresses. This is a valid assumption because modeled strata are near the surface (within 10s of meter), therefore overpressure is very unlikely to develop (Osborne and Swarbrick, 1997).

Two sets of boundary conditions are used in the models: permanent and temporary. The permanent boundary conditions prohibit vertical movement for the model base and lateral movement for the model sides. The temporary boundary conditions prohibit displacement (i.e. compaction/deformation) over the entire domain while initializing gravitational loading. Once gravity is completely applied, the temporary boundary conditions are relaxed using a linear function. Compaction and deformation initiate as the temporary boundary conditions relax. This step-wise gradual application of gravity and compaction is necessary for model stability by inhibiting velocities within the domain from exceeding quasi-static conditions (i.e., kinetic energy is less than 5% of elastic energy) (Rockfield, 2014).

Mesh size is balanced through trial and error to be able to capture fracturing behavior in grainstones while maintaining a reasonable processing time. Denser mesh regions are assigned to grainstones compared to the remainder of the domain to capture fracture locations with minimal mesh dependency. Remeshing is initiated if an element area is distorted more than 3%.

2.3 Rock Properties and Failure Criteria

Rock properties were assigned based on what is known about from lithologic, diagenetic, and mechanical characteristics of different facies present in mound complexes. Phylloid mounds and carbonate mounds in general are known to undergo extensive marine

cementation and organic binding that allows them to lithify and obtain relatively high strength prior to burial (Cross and Klosterman, 1981; Webb, 1996). Phylloid mounds can have upwards of 50% of their volume filled by cement and therefore are assumed to be resistant to compaction (Soreghan and Giles, 1999; Chapter 2). Based on this information we postulate that current (terminal) strength of Pennsylvanian mounds in outcrops is comparable to their strength soon after deposition. However, grainstones that underwent meteoric/marine cementation could have gained more strength with the addition of late burial cement. For that reason, we utilized a modern analogue from a cemented (~400 Ka) Pleistocene grainstone from the island of West Caicos, B.W.I. (Kerans et al., 2016) to approximate strength of cemented grainstones soon after deposition. Brazilian (indirect tensile strength) tests and uniaxial compression tests were performed to quantify tensile strength, compressive strength, and Young's modulus for both the modern grainstone samples and Pennsylvanian mound core samples (Table 1, refer to Appendix C). Mud-rich carbonates and shale that did not experience pervasive early cementation were assigned unconsolidated clay-rich material properties calibrated to experimental data (Nygard et al., 2004; Nygard et al., 2006) that allow them to compact in a ductile manner by porosity loss (Table 2). Initial porosity for mud-rich/shale layers are assumed to be 60% arbitrarily, but consistent with what is known of initial porosity of mud-rich carbonates (Goldhammer, 1997). Rock properties were distributed homogeneously in each bed.

The required differential subsidence for fracturing with different strengths was quantified in a series of models in which the tensile strength of cemented grainstones was increased progressively (T_o= 0.25-2.25 MPa). Tensile strength values greater than 2.25 MPa were not considered, because differential compaction associated with high strength values results in delamination of strata prior to initiating fractures.

Two failure criteria are utilized in our models: (1) Mohr-Coulomb with Rankine tension cutoff and (2) porous elastoplastic Modified CAM Clay model. The first criterion is assigned to strata that can undergo brittle failure (i.e., mound and early-cemented grainstones) while the second is assigned to strata that are prone to compaction (i.e., mud-rich carbonates/shale) by porosity loss and elastoplastic deformation. Strata using the first failure criterion experience development of tensile opening mode fractures at locations where the least principal stress is equal to the prescribed tensile strength of the strata. In contrast, mud-rich strata that are assigned the Modified CAM Clay model start compacting following a linear stress strain curve after pre-consolidation pressure is reached. For further information on the Modified Cam Clay model refer to Appendix A. Layer-parallel slip is incorporated in most of our models and prohibited in some to test its effect on fracture intensity and spatial distribution. In models where LPS is incorporated, boundaries between strata are assigned to be discrete contacts (i.e., inherent weaknesses with frictional properties). Coefficient of sliding friction (μ) and cohesion are assigned to these discrete contacts. The effect of variable coefficient of friction and cohesion on fracture development and behavior is tested. In models where LPS is not incorporated, contacts between strata are shared boundaries that cannot slip without initiating a layer-parallel fracture.

3. NUMERICAL MODELING RESULTS

Several suites of models are used to isolate variables and demonstrate their effect on early syndepositional fracturing. First, the evolution of stress under compaction is described for our base case model (LPS incorporated; Tables 1 and 2). A set of models is then utilized to quantify the amount of compaction required to initiate fractures in early cemented grainstones with variable tensile strength. A second set of models tests the effect of

variable mound geometry on the location of differential compaction fractures. The third set of models tests the effect of layer-parallel slip and interface frictional properties on fracture distribution and intensity. Refer to Appendix D for additional modeling results.

3.1 Stress Evolution and Differential Compaction Fracturing

Modeling results demonstrate evolution of the stress state leading to fracturing during differential compaction over carbonate mounds. All fractures present in our models initiate as effectively tensile opening-mode fractures. The minimum principal stress is the most relevant stress parameter to consider in our models, because the tensile failure criterion is met when the minimum principal stress reaches the prescribed tensile strength. Figure 2 illustrates the magnitudes and sense (i.e. compression or tension) of the minimum principal stress at key time steps in the model. The first time step shows the minimum principal stress at the time where gravitational stress state is fully applied prior to the relaxation of the temporary boundary conditions (i.e. prior to onset of compaction). The mound and the grainstone directly overlying it experience a compressive stress state (up to 0.2 MPa) while the second grainstone at the surface showing slightly tensile stress state (up to -0.1 MPa). The mud-rich strata exhibit a relatively low and approximately uniform compressive stress state consistent with their very weak mechanical properties. With continued progression of time and the onset of compaction, the model demonstrates the development of a tensile stress state in the grainstone overlying the mound crest (Fig. 2, Time Step 1.2). Additional compaction with increasing tension overlying the mound crest culminates with the development of the first fractures in time step 1.3. In the final time step of the model, six clusters of fractures have developed in both grainstone beds in regions overlying the mound crest and the mound flank-to-intermound regions.

All fracture clusters coincide with regions experiencing a heightened tensile stress state in response to warping caused by the compaction of the mud-rich strata. Figure 3 highlights areas where the minimum principal stress is effectively tensile in the grainstones prior to extensive development of differential compaction fractures within these areas. The vertical propagation and approximately horizontal opening of fractures are parallel to the orientation of the maximum and minimum principal stress directions respectively (Figure 3B). A notable difference between the tensile regions overlying the mound versus the ones that overlie the intermound areas is their location within the beds. In grainstone beds overlying the mound crest, tensile stress first emanates from the top of the beds and spread downwards through the bed. In contrast, grainstones in the intermound areas experience tensile stress development starting at the base of the beds and spreading upward. In both areas, the opposite side of the bed from the tensile stress state experiences heightened compression. This can be clearly seen in Figure 2 overlying the mound crest in areas shaded by dark blue in time step 1.3 and overlying the intermound fractures in time step 3. This is consistent with fracture nucleating at the top and propagating towards the bottom in strata overlying the mound crest and in the opposite direction (bottom to top) in strata overlying the intermound areas. Fractures overlying the mound crest break through the entire bed unlike in the intermound areas where they terminate prior to reaching the bedding plane because the amount and extent of tensile stress does not overcome the opposing compressive state. Few fractures in the intermound areas approach breaking through the bed but their vertical propagation path is deflected to horizontal (Figure 2, time step 3).

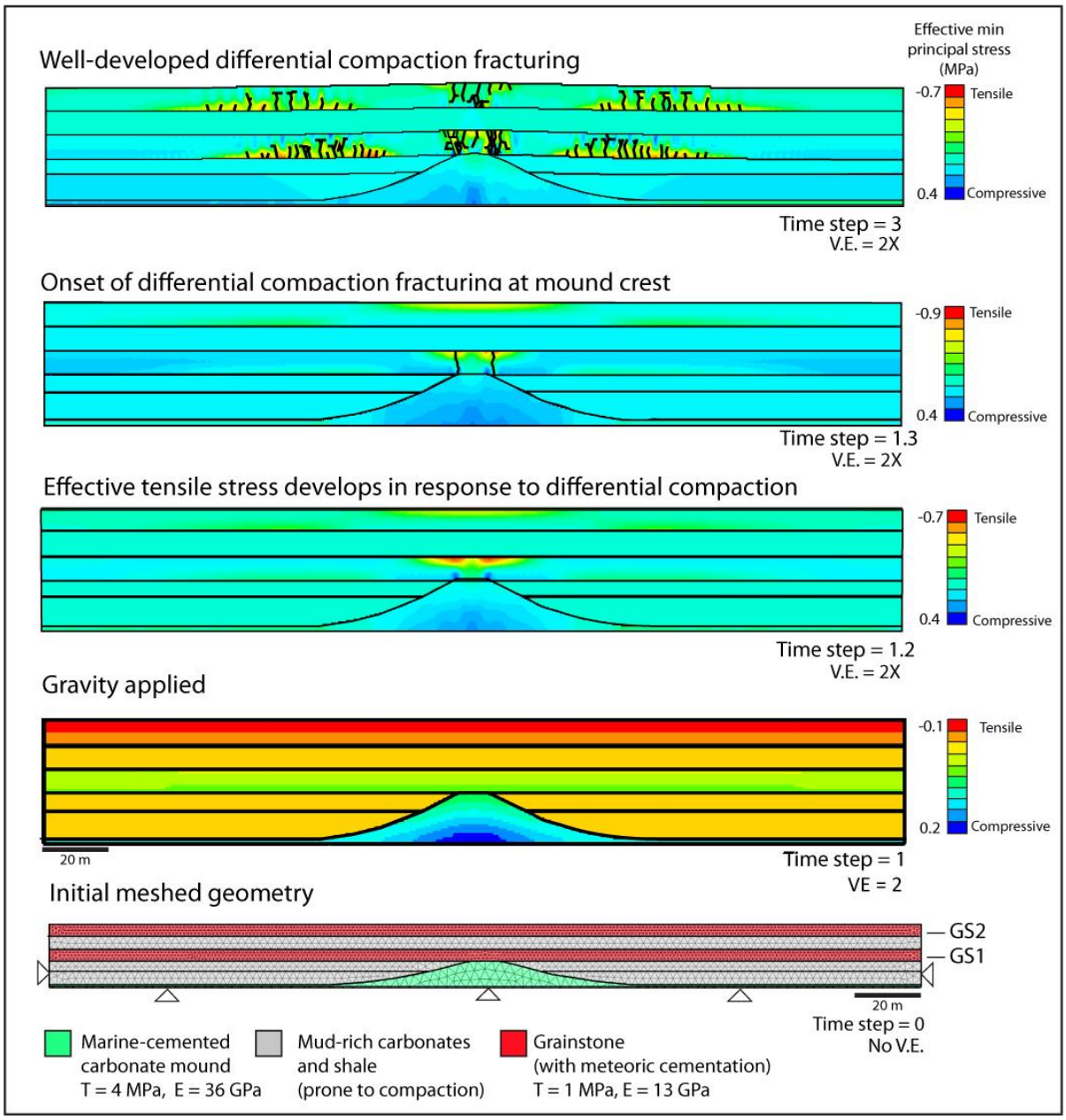

Figure 3.0.2: The evolution of stress state in a finite-discrete element model of a carbonate mound overlain by mud-rich strata and 2 early cemented grainstones during application of gravity, subsequent compaction, and differential compaction fracturing. Fractures initiates in area of heightened tensile stress overlying the mound crest. Additional compaction initiates more fractures overlying the mound crest and fractures overlying the intermound areas.

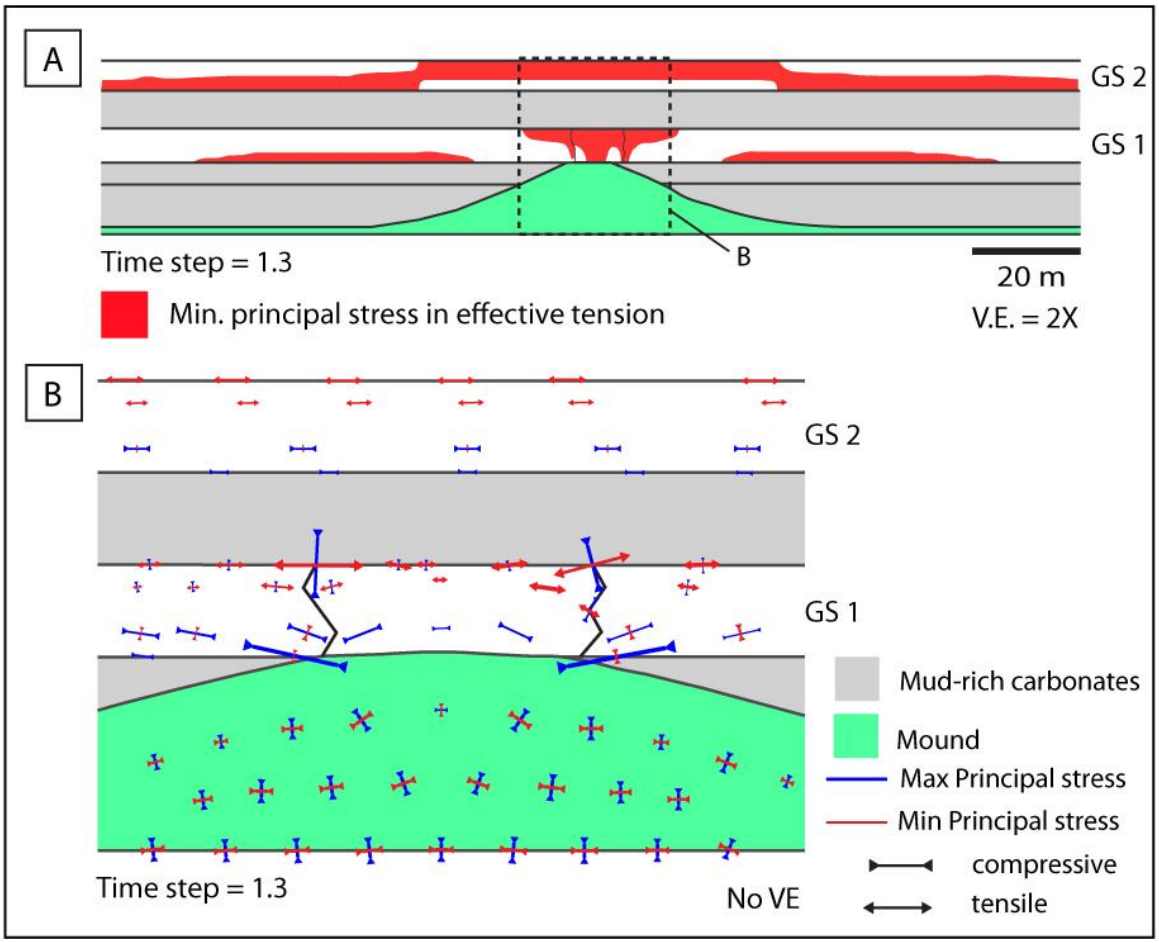

Figure 3.0.3: (A) Distribution of areas of effective tensile stress state in grainstones in response to differential compaction (red), unshaded areas are in compressive stress state. (B) Orientation of maximum and minimum principal stresses overlying the mound crest at the time of fracture initiation. Fractures propagate in the direction of the maximum principal stress and open in the direction of the minimum principal stress.

The development of tension is in response to differential subsidence of strata overlying the rigid mound. Figure 4 illustrates that the least subsidence occurs overlying the mound crest and that subsidence increases with increasing distance from the crest. Furthermore, the spatial distribution of subsidence mimics the geometry of the mound. The areas of

greatest subsidence overlie mud-rich strata with the greatest porosity loss by compaction (Figure 4b).

3.2 Quantification of required differential subsidence for fracturing

The amount of differential subsidence required to develop differential compaction fractures in our base case model is in the order of cm to tens of cm (Figure 4). Onset of fracture development in grainstones overlying the mound crest required 5 to 10 cm of maximum differential subsidence for the older (GS1) and younger (GS2) layers respectively. Fractures formed in the intermound areas required approximately 6 times the amount of differential subsidence compared to their crest counterparts (35 cm to 60 cm). This amount of subsidence corresponds to less than 1% maximum differential porosity loss due to compaction for crest fractures and less than 3% maximum porosity loss for intermound fractures. These values of differential subsidence that cause fracture development are 1-5% of the mound height.

Examining a series of models with variable grainstone tensile strength (T_0= 0.25 – 2.25 MPa) reveals a linear relationship between tensile strength and the amount of differential subsidence required to initiate fractures. This relationship is consistent regardless of fracture location (i.e. crest or intermound) (Figure 5). The difference between the amounts of required differential subsidence to initiate fractures at different locations increases with increasing tensile strength. For example, at tensile strength of 1 MPa the amount of differential subsidence required to initiate fractures in the youngest grainstone layer (GS2) is double that of the older one (GS1). In contrast, at tensile strength of 2 MPa the required amount of differential subsidence is increased by a factor of 3. The same relationships are observed with the amount of maximum differential porosity loss required to initiate fractures and the tensile strength of grainstones.

The amount of differential subsidence required for initiating fractures at all locations for the model with tensile strength of 2 MPa is still relatively low (10s of cm). Crest fractures in both grainstones require less than 0.5 m of differential subsidence to initiate and intermound fractures require less than 1 m. These values correspond to approximately 5% and 10% of the mound height.

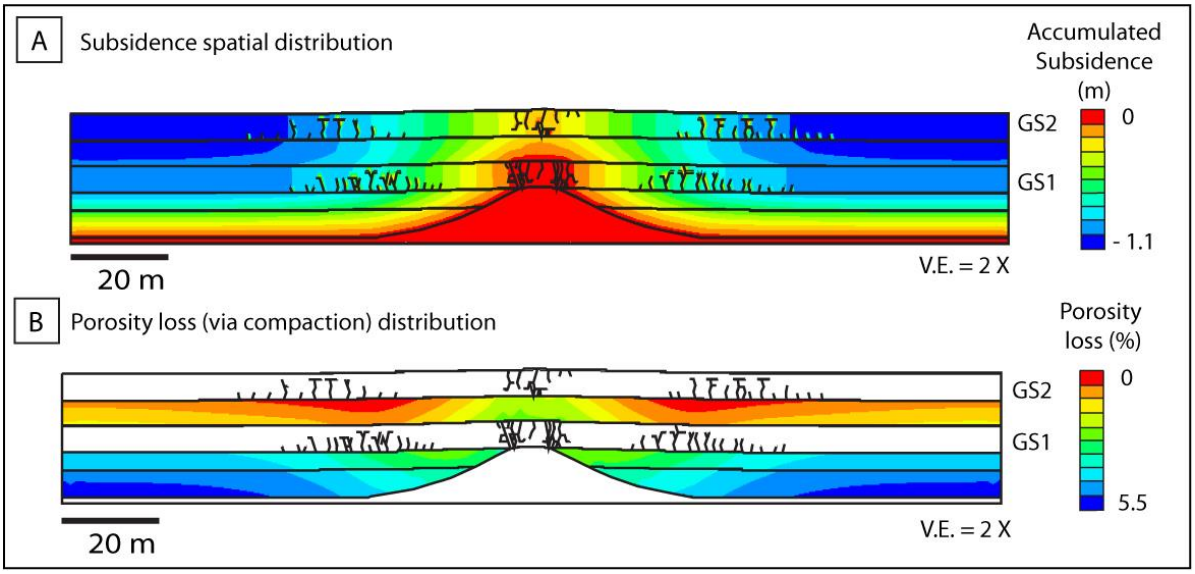

Figure 3.0.4: (A) Spatial distribution of subsidence at the time of model completion. The greatest subsidence occur at the edge of the model (i.e., furthest away from the mound) in response to compaction of the mud-rich strata. (B) Distribution of porosity loss from compaction of the mud-rich strata (negligible compaction occurs in the white areas). Areas of highest porosity loss correspond to areas of greatest subsidence.

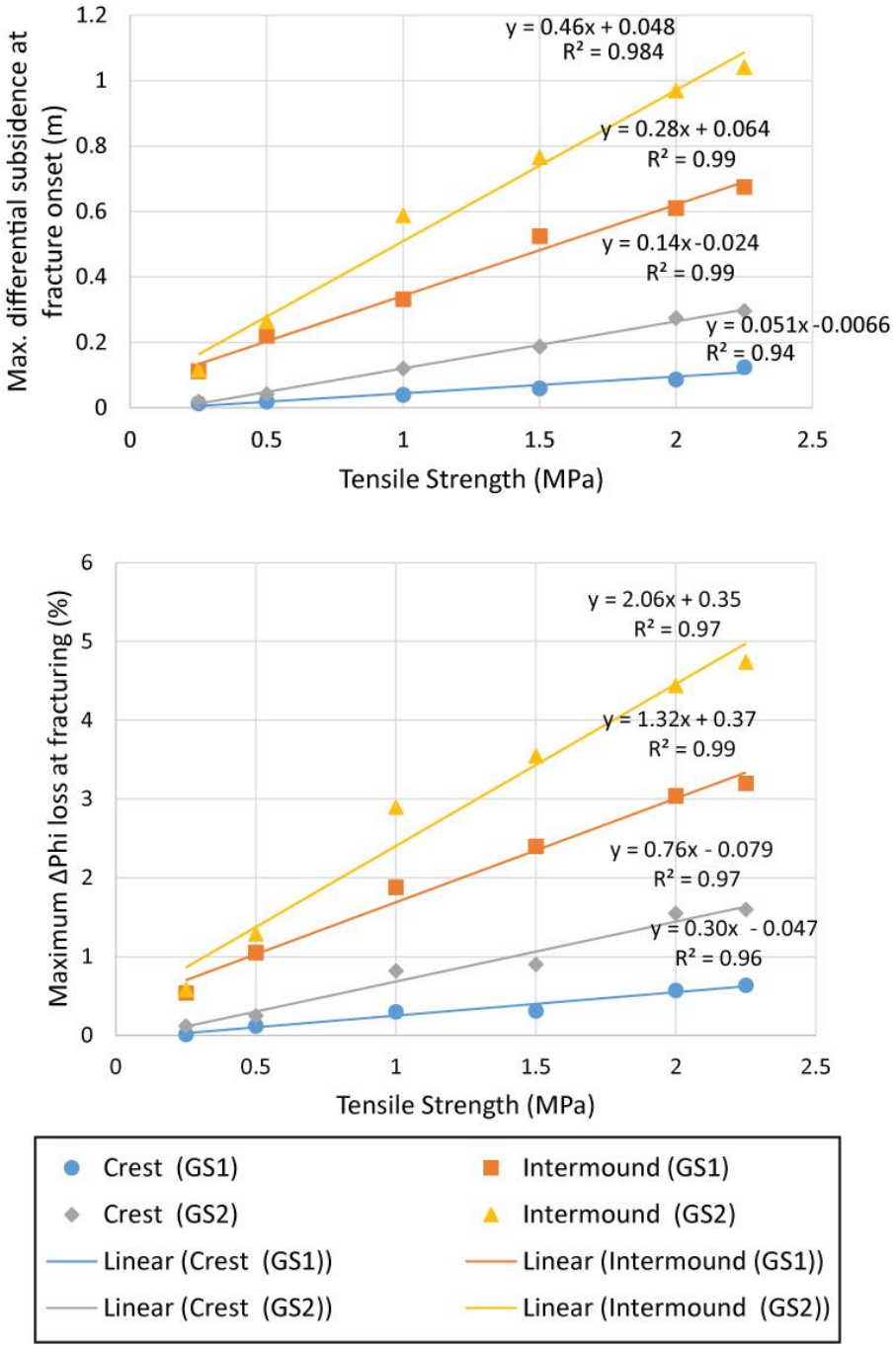

Figure 3.0.5: (A) Required differential subsidence to inititate fractures at the crest and the intermound areas for variable tensile strength of grainstones. (B) Maxmium porosity loss corresponding with fracture intiation at mound crest and intermound areas for grainstones of different tensile strength. In both graphs each coloumn of points represent a model run with the corresponding tensile strength of grainstones.

3.3 Fracture Location and Mound Geometry

Comparison between our base model of a convex-shaped mound and a tabular mound reveals how differential compaction fracture location changes with variation in mound geometry and stratal configuration (Figure 6). The tabular mound is 3 times taller and 5 times wider than the convex mound. Fracture development in the tabular mound model is similar to that of the convex mound model, with fractures developing in grainstones overlying the mound crest-to-flank transition and in the area overlying the flank-to-intermound areas. The crest of the convex mound is limited in area (few meters) compared to the extensive top of the tabular mound (100s m). Fracture development in grainstone overlying the convex mound crest starts with two distinct clusters corresponding to each mound crest-to-flank transitions. Further fracture development merges the two clusters into one owing to their initial proximity. In contrast, fracture clusters in grainstone overlying the tabular mound crest-to-flank transitions have hundreds of meters of initial separation and never merge. Furthermore, the width of fracture clusters overlying the tabular mound crest (~100 m) is significantly greater than its convex mound counterparts (~8 m).

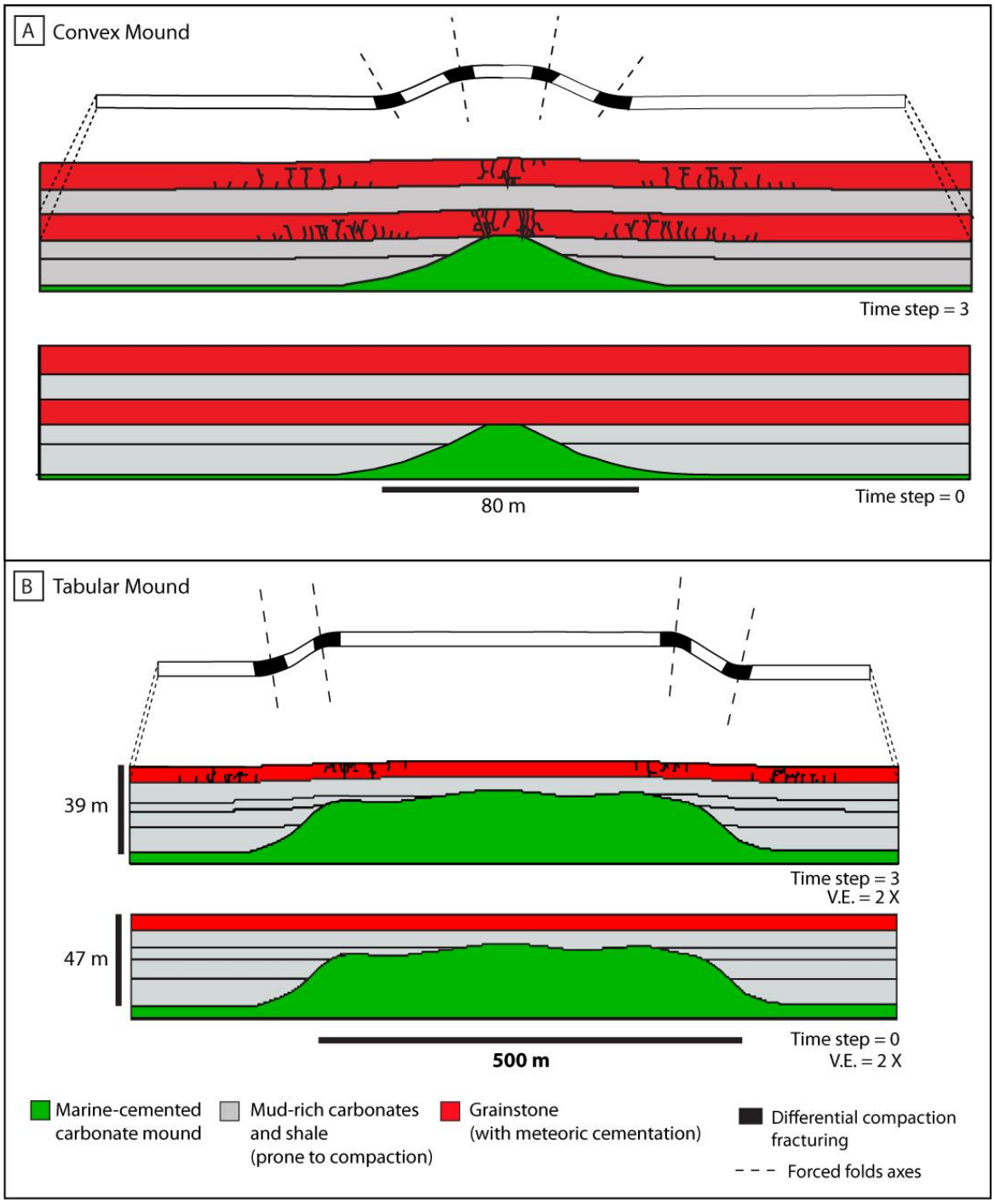

Figure 3.0.6: Comparison between locations of differential compaction fractures between numerical models of (A) Convex mound (B) Tabular mound. Note that schematics exaggerate the deformation that the grainstone layer experiences for illustration purposes.

3.4 Layer-Parallel Slip (LPS) and Differential Compaction Fracturing

The effect of LPS upon fracture intensity and style was illustrated by comparing two models with identical geometries and rock properties but different contact types (Figure 7). In the first model, the contact type was treated as a bonded interface that does not experience LPS; in the second, the contact was given a prescribed mechanical weakness that allowed LPS. Models with prescribed bedding weaknesses experience LPS coinciding with differential subsidence and fracturing. Mechanical interfaces between layers in our base case for LPS are cohesionless and specified a moderate 0.5 coefficient of friction (μ). The disparity in fracture development is immediately clear when visually inspecting the two models (Figure 7). While the location of fractures relative to the underlying mound is similar, the intensity is significantly higher when LPS is absent. The model without LPS exhibited more than double the number of fractures present in the LPS model. However, fractures present in the LPS model occurred with significantly wider apertures. Fracture aperture in LPS models is widest at the intersection with a slipping interface (i.e. at strata boundaries); in the non-LPS model, fracture aperture is widest at the center of the fracture.

The amount of slip along interfaces is minor (mm-cm scale) but it is widespread throughout the model (Figure 8). The area of greatest LPS is on bedding planes overlying the carbonate mound crest and flanks with decreased and diffused slip occurring away from them. A series of models with variable coefficient of friction and cohesion values were used to investigate their influence on fracture behavior and amount of slip. We found that the coefficient of friction and cohesion have minor influence over the overall spatial distribution and intensity of fractures. Models with bedding contacts prescribed high coefficient of friction (μ= 1) displayed the same fracture locations and only slightly increased intensity compared to the moderate and low coefficient of friction values (low:

μ = 0.2, moderate: μ=0.5). The amount of slip decreased with high coefficient of friction values but LPS still occurred. Decreased LPS was reflected in decreased fracture aperture size. Cohesion had no appreciable influence on fracture spatial distribution, intensity, or apertures.

A plot of the maximum principal strain values in all nodes of grainstone layers across the models show significantly different values between LPS model and the non-LPS model (Figure 9). The values of maximum principal strain in the non-LPS model are roughly double the values of strain for the LPS model. Differences in strain values at the crest location between the two models are more pronounced than in the intermound. In both models, heightened strain values corresponded with development of fractures clusters overlying the crest and the intermound areas. The maximum strain value over the crest in the non-LPS model is approximately 5 times the amount of maximum strain in the intermound areas for the same model. A similar relationship is observed for the LPS model but the factor of difference is 2.5.

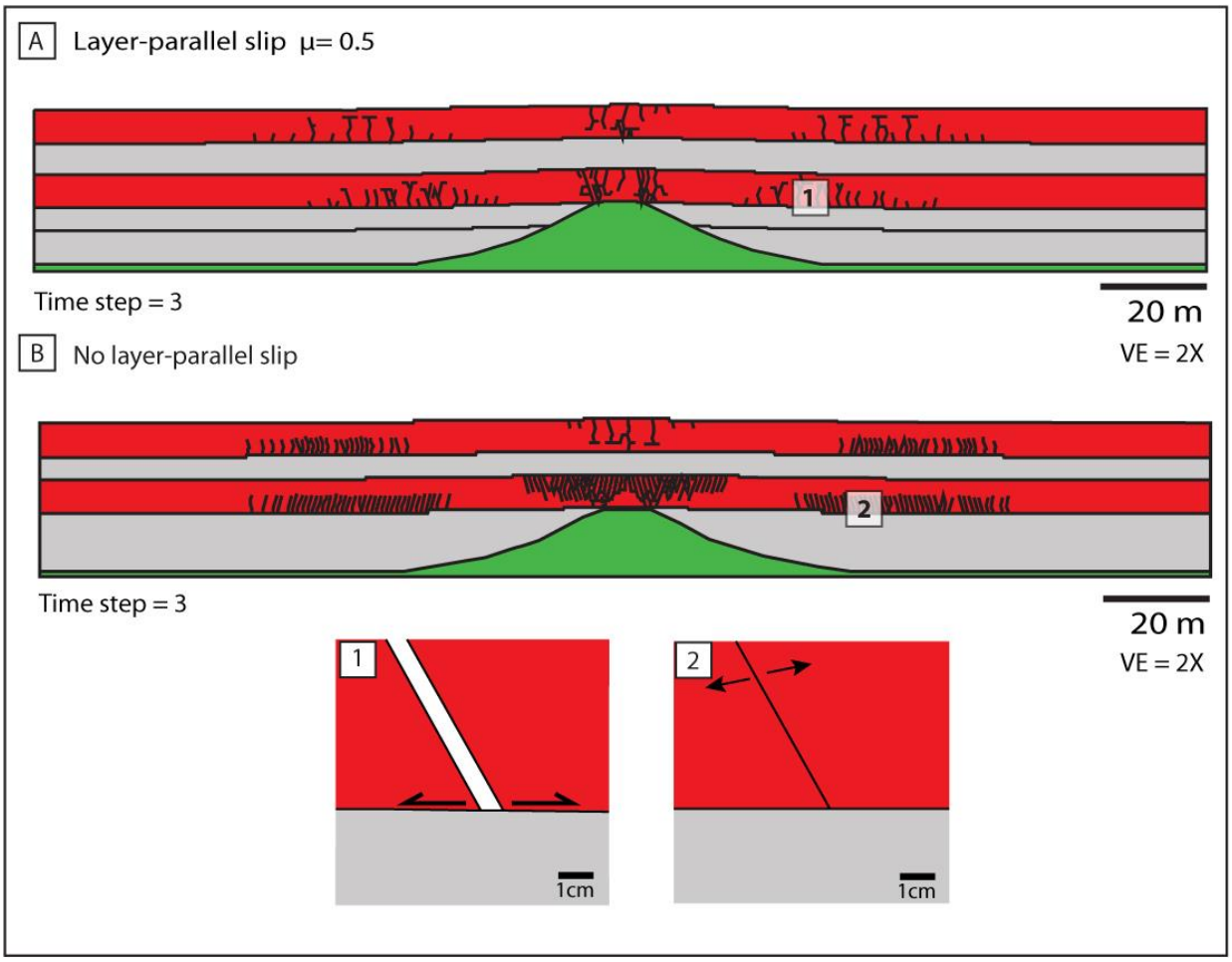

Figure 3.0.7: Comparison between differential compaction fracturing in (A) model with layer-parallel slip and (B) model without layer-parallel slip. The model without LPS has significantly more fractures relative to the model where LPS is incorporated. Fracture aperture is larger in A than B with fracture greatest width at slipping interfaces compared to the center of the fracture in B.

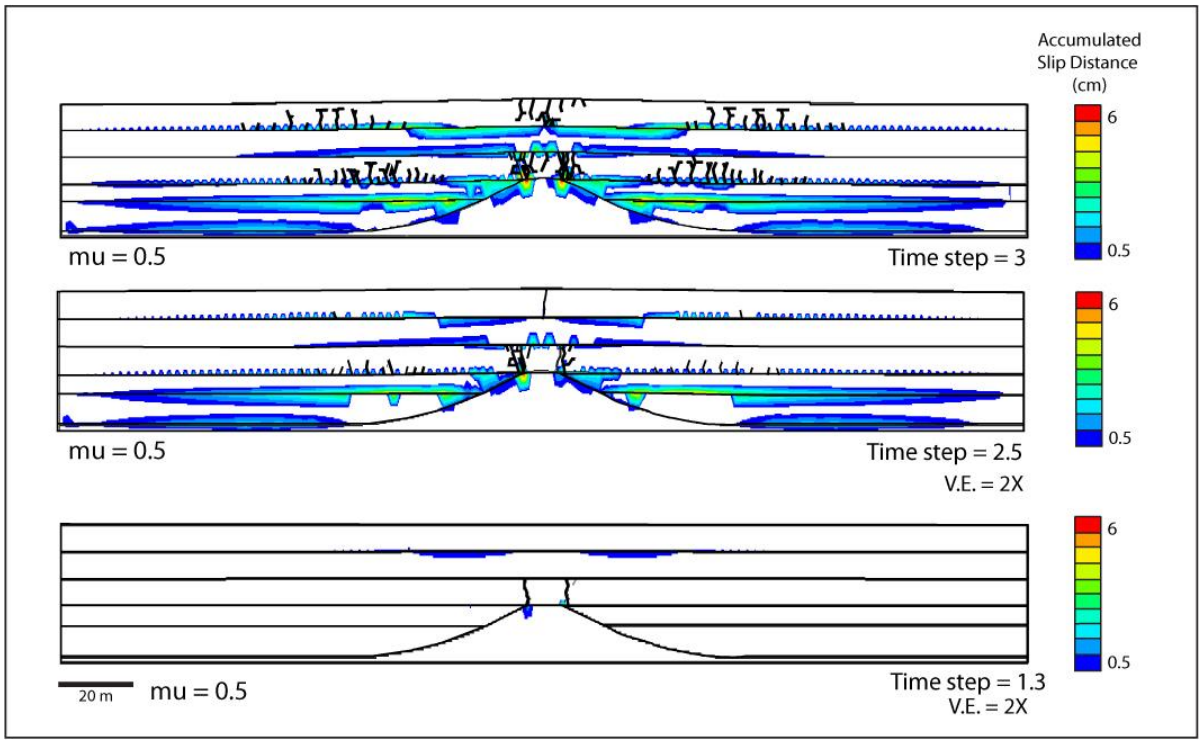

Figure 3.0.8: Accumulated slip along discrete contacts (bedding and fractures) at key time steps in our base case model. LPS is greatest overlying the mound and decreases away from it. At the onset of fractures at the mound crest LPS is minor and localized over the mound. Increase differential subsidence and fracture development is accompanied by increase in slip across the model with the greatest concentration of slip present overlying the mound crest.

4. DISCUSSION: CONTROLS ON DIFFERENTIAL COMPACTION FRACTURING

The modeling results presented here are the first to identify and test the factors controlling the development of fractures due to differential compaction in strata overlying carbonate mounds. Here, we demonstrate that mound geometry, amount of differential

subsidence, rock tensile strength, and bedding contact type are all controls on the development, location, intensity, and size of fractures.

4.1 Mound Geometry

Mound and stratal geometry dictates the location and size of the fractured region as a result of differential compaction. Comparison between fractures in strata overlying the convex and tabular mound models shows the control of mound geometry on fracture locations (Figure 6). The reason behind this control is that the differential compaction process over the rigid mounds results in the formation of several forced folds. The first one to develop is antiformal with two hinges corresponding to the mound crest-to-flank transitions and two synformal forced folds corresponding to the flank-to-intermound areas. Fractures develop in areas of increased tensile stress at the outer arc of these folds hinges (i.e., top of the layer for the antiformal fold and bottom of the layer in the synformal folds). The mound size and location of mound crest to flank transition controls the location of these forced folds and consequently the location of resulting fractures. Additionally, the slope of the transition from mound crest-to-flank influences the width of the fracture cluster. Wide fracture clusters are associated with gentle slopes as can be seen in the tabular mound model compared to the narrower clusters associated with the steeper transition in the convex mound model (Figure 6). The following relationship is inferred for the cluster width for the intermound fractures:

$$Intermound\ Fracture\ Cluster\ Width = \frac{mound\ height\ (relief\ from\ sea\ floor)}{tan\theta}, \theta > 0\ ,$$

where θ is the mound flank slope angle. A similar relationship is valid for the crest fractures cluster width with the substitution of height and slope angle for that of the

geometry of mound crest-to-flank transition. The aforementioned relationships are valid assuming the occurrence of LPS. In models without LPS the region of fracture development is initially similar to LPS models but with extensive fracturing the fractured region width extends further.

4.2 Amount of Differential Subsidence and Rock Tensile Strength

The amount of differential subsidence has direct relationship to the intensity and pervasiveness of differential compaction fracturing. Our modeling results suggest that differential compaction fractures in strata overlying mounds can be initiated by minor differential subsidence relative to the mound height (Figures 4 and 5). In all locations of fracture development, the intensity is directly proportional to amount of differential subsidence. However, fractures overlying the crest of the mound develop after less differential subsidence than their intermound counterparts. This behavior can be attributed to the proximity of the underlying rigid mound crest to the overlying grainstone, which promotes deformation; in grainstones overlying mud-rich strata, the mud provides a cushioning effect that delays deformation. Similarly, the younger grainstone (GS2) requires nearly double the amount of differential subsidence as the older grainstone (GS1) to develop fractures in both crest and intermound locations. This is inferred to be caused by underlying layers absorbing some of the deformation prior to differential subsidence affecting the younger grainstone. This suggests that differential compaction fracture development is likely to decrease in intensity and pervasiveness with increasing vertical distance from the antecedent mound.

The tensile strength of early cemented strata indirectly affects the intensity of fracture development. Increasing tensile strength requires increased differential subsidence for fracture development. Because fracture intensity is proportional to the amount of

differential subsidence, assuming all other variables held constant, increased tensile strength will decrease intensity. In other words, two strata that experienced the same amount of differential subsidence but have different tensile strength will result in higher fracture intensity in the one with the lower tensile strength.

4.3 Bedding type, LPS, and Stress Dissipation

Bedding type and the occurrence or absence of LPS exerts significant control on the style of fracture development. The two models presented simulating the occurrence and absence of LPS during differential compaction can be related to bed contact types observed in outcrops. Sharp bedding contacts represent an inherent bed-parallel weakness, which can have variable bonding strength and frictional properties. Fractures are known to terminate at weakly and moderately bonded bedding interfaces where layer-parallel slip can promote aperture widening (Cooke and Underwood, 2001; Smart et al., 2009). In our modeling work, fracture termination at interfaces between grainstones and mud-rich strata must occur because properties assigned to the mud-rich strata do not support brittle failure. The occurrence or absence of LPS primarily controls the behavior of the intersection between the fracture and the bedding contact. When LPS is incorporated in the model, fractures develop wide apertures at the intersection between the fracture and the bedding contact. In contrast, fractures exhibit single point termination at the same intersection in models where LPS is not permitted. The non-LPS models bedding contact can reflect gradational bedding contacts in which there is no clear sharp boundary between lithologies and thus no bedding-parallel weakness.

The bedding contact type and its implication for the occurrence or absence of LPS dramatically change fracture intensity. LPS dissipates some of the stress that the early cemented grainstones experience as a result of differential compaction over the carbonate

mound. After the generation of differential compaction fractures LPS increasingly widen their aperture. In non-LPS models, all the strain generated from differential compaction is accommodated by generating fractures. This explains why non-LPS models have significantly higher fracture intensity compared to models with LPS. While we cannot directly quantify the amount of strain accommodated by LPS in our models, we can infer that amount by comparison between strain magnitudes in grainstones in LPS vs non-LPS models (Figure 9). We estimate from that comparison that approximately 40% of the strain caused by differential compaction is accommodated by LPS. Because non-LPS models accommodate strain solely through fracturing, they develop roughly twice the number of fractures as the LPS model. These values highlight the importance of LPS as a stress dissipation mechanism and its profound impact on fracture intensity and style.

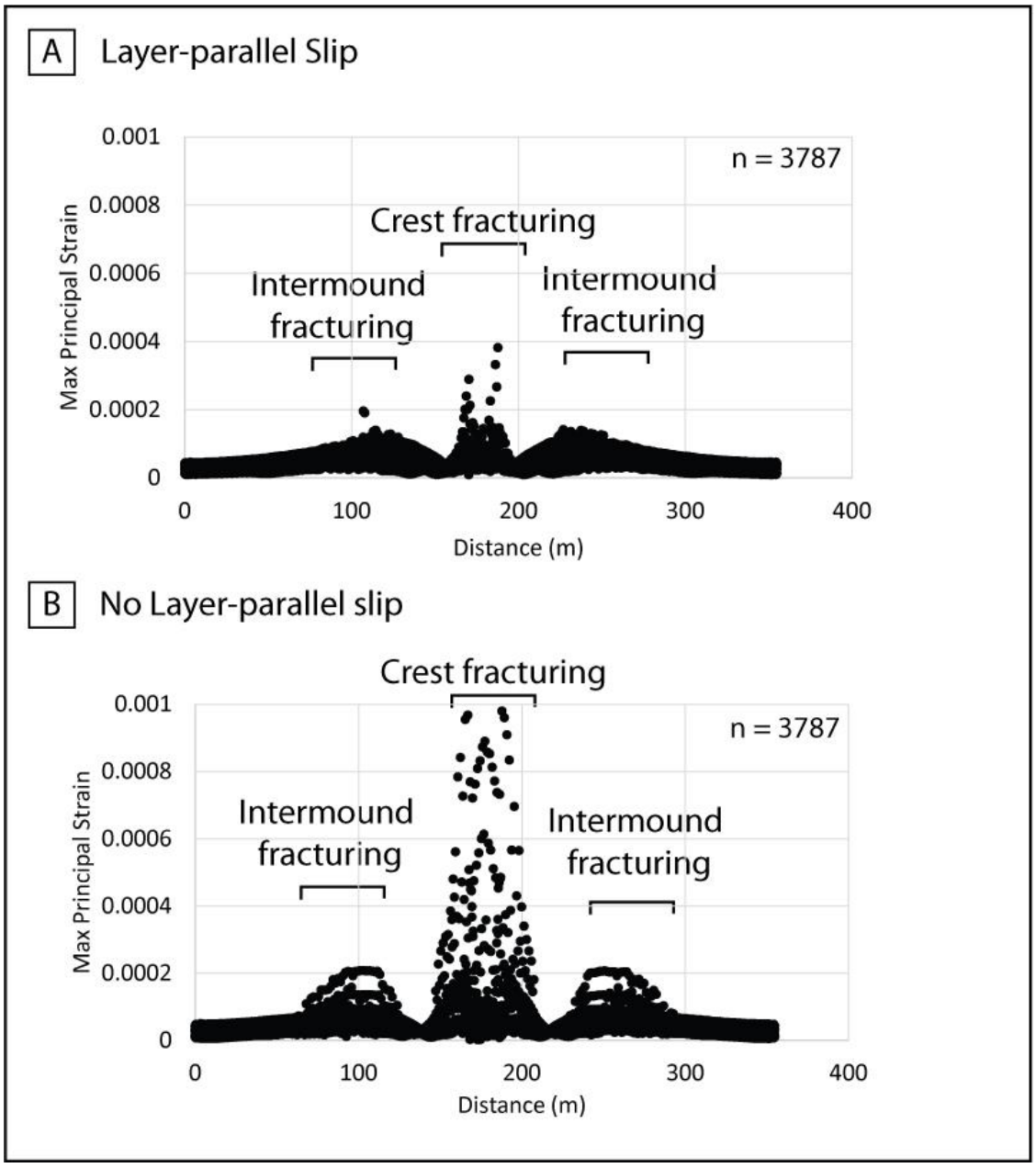

Figure 3.0.9: Plot of maximum principal strain at all nodes within the early cemented grainstones in (A) model with layer-parallel slip and (B) Model without layer-parallel slip. As expected highest strain values correspond to where fractures are present. Model without layer-parallel slip has more than double strain magnitudes of model with layer-parallel slip.

5. COMPARISON BETWEEN MODELING RESULTS AND FIELD OBSERVATIONS

Our modeling results are consistent with observations of early-formed fractures often attributed to differential compaction in outcrops of carbonate mounds and strata overlying them (Davies, 1977; Mazzullo and Cys, 1979; Shinn et al., 1983; Kirkby, 1994; Gutteridge, 1995; Frost and Kerans, 2009). Early sediment-filled and solution-widened fractures were documented in grainstones overlying phylloid mounds in the Late Pennsylvanian Holder Formation in Yucca Canyon of the Sacramento Mountains in New Mexico (Figure 10) (Chapter 2). While these particular outcrops guided the initial stratal geometries of the models presented in this study, the models are simplification of the observed geometries and do not take into account the 3D aspect of the outcrops. Therefore, an exact comparison to the outcrop observations is not appropriate. However, a comparison between modeling results and the general location of these fractures relative to the underlying mounds can provide validation. In outcrop, sediment-filled fractures were found to be located in grainstones overlying mound crest-to-flank transition and in grainstones overlying the inter-mound areas (Figure 10A) (refer to Chapter 2); the same relationships are observed in this work's modeling results. Observations of bed-parallel shear and soft sediment deformation in intermound strata (Figure 10B) suggest that models incorporating LPS are more realistic than ones without LPS. The number of observed fractures is small (10s of fracture across 800 m of outcrop), which could be a byproduct of LPS stress dissipation. However, this observation could also reflect the difficulty of distinguishing early fractures that are not solution widened in outcrops that have experienced significant diagenesis.

Other reasons behind the inexact match between outcrop observations and modeling results include the simplifying assumptions that the models were based on. This includes

the smoothing of stratal geometry and the assumption that they were originally horizontal. Additionally, the uniformity of rock properties distribution within each strata is a major simplifying assumption.

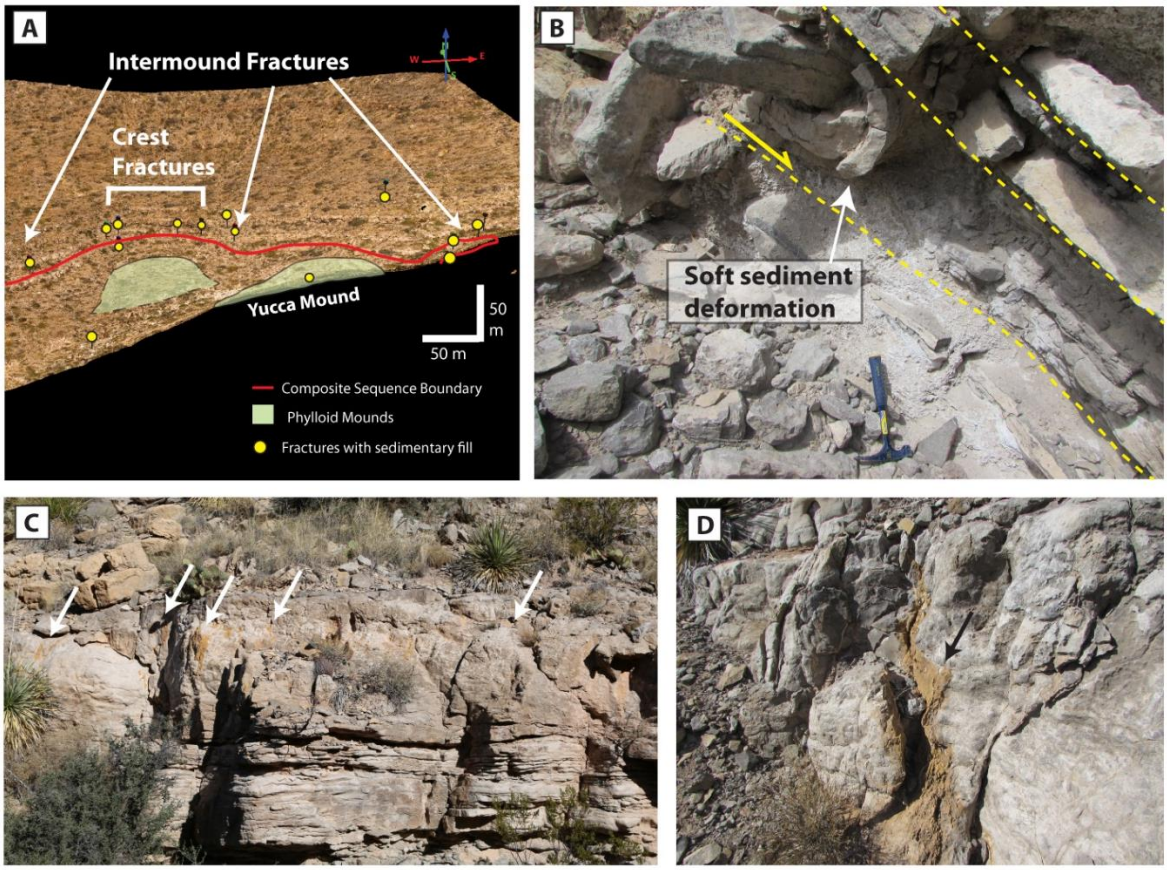

Figure 3.10: (A) GPS locations of solution-widened and sediment-filled fractures in grainstones overlying Pennsylvanian phylloid mounds in Yucca Canyon in the Sacramento Mountains, New Mexico. (B) Evidence of ductile behavior and layer-parallel shear (slip) in mud-rich carbonate and shale succession present in an intermound strata in Yucca Canyon. (C) and (D) Examples of solution-widened and sediment-filled fractures (arrows) in Yucca Canyon.

6. CONCLUSIONS

The novel numerical modeling approach presented here provides fundamental understanding of the primary controls on development of differential compaction fracturing in strata overlying carbonate mounds. The main control on the location and spatial extent of differential compaction fractures is the underlying rigid antecedent topography (mound) geometry. Fractures develop most extensively overlying the mound crest. In addition, wide fracture clusters can form in strata overlying the mound-flank to intermound transition. Therefore, characterizing the geometry of carbonate mounds/rigid antecedent topography is important for the prediction of differential compaction fracture locations. Relative to mound height, minor amounts of differential compaction (subsidence) are required to develop extensive differential compaction fracturing in strata overlying carbonate mounds. This suggests that differential compaction as a mechanism for early deformation may be underestimated in carbonate systems, especially in areas that experienced early differential diagenesis. Prior to this study, the effect of LPS on the spatial organization of fractures in a depositional setting has not been demonstrated. Our work shows the significant control that LPS exerts on the intensity of differential compaction fracturing. LPS is inferred to be able to accommodate up to 40% of the strain experienced by deformed strata, highlighting its importance as a major process for stress dissipation. The general consistency of outcrop observations with modeling results highlights the value of our modeling approach as a predictive tool for fracture development. This study demonstrates how a process-based approach to fracture characterization and prediction can overcome the shortcomings of diagenetically overprinted outcrop and core based observations of early fractures.

ACKNOWLEDGEMENTS

Kelly Hattori and Dr. Mehdi Haydri are thanked for discussions and review of this work. Rockfield is thanked for providing educational license for ELFEN. Melanie Armstrong is thanked for providing technical support of ELFEN. Virtual Reality Geological Studio (VRGS) is thanked for providing a research license.

Table 3.1 Brittle Material Properties with Mohr-Coulomb-Rankine Criteria

Property	Cemented Grainstone	Carbonate Mound
Tensile Strength (MPa)*	1	2.4
Fracture Energy (J/m^2) †	1.63	2.17
UCS (MPa)¥	4.65	72.1
Internal Friction Angle(°)	37	40
Internal Cohesion (MPa)	3	11
Young's Modulus (GPa)¥	13	35.5
Poisson's Ratio¥	0.30	0.24
Porosity	0.34	0.10
Bulk Density (kg/m^3)	2130	2540
Discrete Contact		
Coefficient of sliding Friction	0.5	
Discrete contact cohesion (MPa)	0	

* Based on Brazilian test data

¥ Based on uniaxial compressive test data

† Based on empirical relationship dependent on E and T_0 (Zhang, 2002)

Table 3.2 Material Properties for Mud-rich strata prone to compaction assigned a Modified CAM Clay model

Property	Mud-rich strata
Young's Modulus (GPa)	0.4
Poisson's Ratio	0.25
P_c (MPa)	0.05
P_t (MPa)	0.1
B	60
β_0	0.60
B_1	0.73
Φ	55
N	1.3
A	0.25
Porosity	0.60
Bulk Density (kg/m^3)	1670

Chapter 4: 3D Reservoir-Scale Numerical Modeling of Differential Compaction Fracturing in an Isolated Carbonate Platform: (SACROC Unit) Kelly-Snyder Field, Midland Basin, West Texas

ABSTRACT

Differential compaction is proposed to be a major mechanism for syndepositional fracture development in carbonate platforms. Outcrops and subsurface observations of syndepositional fractures are often insufficient to infer the 3D fracture variability. Quantification of stress evolution and amounts of differential subsidence required to develop fractures cannot be directly observed in outcrops. We address these limitations by developing the first 3D finite-element based geomechanical models that simulate differential compaction over an isolated carbonate platform. Models are based on the Late Pennsylvanian isolated carbonate platforms in the SACROC unit of the Kelly-Snyder Field located in the Midland Basin, West Texas. Results showing along strike variability in the stress state suggests that the antecedent topography controls locations of increased tensile stress regions in the Cisco Formation. Modeling results predict increased fracture intensity at the eastern margin of the Cisco platform, in the northern and southern part of SACROC. This coincides with the underlying increased windward-leeward asymmetry of the older Canyon platform. Toward the center of SACROC, increased fracture intensity is predicted at the center of the Cisco platform where the underlying Canyon platform display significantly less windward-leeward asymmetry. Fracture observations from image logs and indirectly from mud loss data within the Cisco Formation are consistent with our modeling results. While platform top fracture orientations in the Cisco Formation are consistent with the platform-scale models, fracture orientations in the eastern platform

margin are more consistent with local differential compaction associated with circular-shaped mounds. The modeling and prediction of fracturing due to differential compaction can be used to better characterize permeability anisotropy, which is critical to tertiary field development in SACROC.

1. INTRODUCTION

Syndepositional fracture and fault development in carbonate platforms produces early permeability anisotropy with implications to reservoir quality and fluid flow pathways (Kerans, 1988; Collins et al., 2006; Frost and Kerans, 2009). Early fracture systems are inherent weaknesses in carbonate platforms that are susceptible to repeated reactivation with subsequent stress regimes (Koša et al., 2003; Preto et al., 2011; Budd et al., 2013). Furthermore, they were shown to influence diagnetic and depositional patterns in carbonate systems (Frost et al., 2012; Budd et al., 2013). Several studies suggested that early brittle deformation in carbonate platforms is primarily driven by differential compaction between the grain-rich platform top carbonates and the mud-rich slope and basinal sediments (Hunt et al., 1996; Saller, 1996; Hunt and Fitchen, 1999; Rusciadelli and Di Simone, 2007; Frost and Kerans, 2010). Both experimental and subsurface data supports that mud-rich carbonates compact more rapidly with burial than their grain-rich counterparts (Schmoker and Halley, 1982; Goldhammer, 1997). While outcrop and subsurface studies documented the prevalence of syndepositional opening mode fractures and normal faults near shelf-margins of carbonate platforms (e.g., Playford et al., 1989; Cook et al., 2002; Koša et al., 2003; Narr et al., 2004; Frost and Kerans, 2009), these observations are not sufficient to predict the unobserved three-dimensional variability in deformation behavior. In addition, information regarding the evolution of the stress state and quantification of variables relevant to differential compaction fracturing cannot be

deduced from field observations. Here we address these limitations by constructing the first 3D geomechanical models of differential compaction-driven deformation on an isolated carbonate platform.

Conventional natural fracture modeling techniques utilizing observations from well data to infer fracture patterns in the interwell areas commonly fails to capture the complexity of natural fracture networks (Odling et al., 1999). The difficulty in predicting fractures away from wells stems from the inadequate sampling of the fracture population inherent to subsurface data. More recently, a process-based approach to modeling stress evolution in carbonate platforms using 2D mechanical models has been shown to facilitate testing and quantifying factors that controls fracture development in carbonate platforms with implication for enhanced fracture predictability (Resor and Flodin, 2010; Nolting et al., in review).

In this study, we investigate the influence of the 3D antecedent topography variability on differential compaction fractures spatial distribution on isolated carbonate platforms. Geomechanical models are based on the Late Pennsylvanian Canyon and Cisco formations that reflects isolated carbonate platform depositional settings located in Horseshoe Atoll in the Midland Basin, West Texas. These platforms are the major reservoirs for the Scurry Area Canyon Reef Operators Committee (SACROC) unit of the giant Kelly-Snyder Field. 3D finite-element based mechanical models are constructed to capture the evolution of the stress state during the compaction of mud-rich carbonate sediments located in basinal settings. Modeling results are compared to direct fracture observations from well data (image logs) and inferred fracture observations from drilling mud loss.

2. GEOLOGIC SETTING

The SACROC unit of the Kelly-Snyder field is located on the eastern edge of Horseshoe Atoll in the northern part of the Midland Basin (Figure 1). The field was discovered in 1948 and holds significant oil accumulation with an estimated original oil in place of 2.8 billion barrels (Allen and Thomas, 1959). More than 1.2 billion barrels of oil have already been produced since the time of discovery in 1948 through the early 1990s (Hawkins et al., 1996). One of the oldest CO_2 injection programs in the United States has been implemented in SACROC since 1972 to maximize recovery (Dicharry et al., 1973). Understanding the natural fracture spatial distribution within SACROC is critical, because they are known to greatly affect CO_2 injection flow paths (Larkin and Creel, 2008; Ghahfarokhi et al., 2016).

The Late Pennsylvanian (Missourian) Canyon and (Virgilian) Cisco Formations are the most prolific reservoirs on Horseshoe Atoll. At SACROC, the Canyon and Cisco platforms strike approximately northeast-southwest and are thickest toward the center of the platform (~250 m) with thinning toward the eastern (windward) and western (leeward) margins. The Canyon Formation reflects a predominantly aggrading isolated carbonate platform depositional system (Schatzinger, 1983; Alnazgha and Kerans, 2018). The Canyon can be divided into four high frequency sequences characterized by correlatable cyclic carbonates capped by oolitic or crinoidal and fusilinid-rich grainstones (Kerans, 2001; Alnazgha and Kerans, 2018) (Figure 2). The upper cycles of the Canyon Formation show evidence of frequent subaerial exposure, characteristic of the dramatic icehouse eustatic changes in sea levels present in the Late Pennsylvanian (Read, 1995; Kerans, 2001; Alnazgha and Kerans, 2018). The Cisco represents a mostly aggrading isolated carbonate platform with apparent westward progradation, however, an alternative

explanation would be the erosion of the platform top during times of low stand (Alnazgha and Kerans, 2018). The Cisco can be divided into 5 high frequency sequences that have complex stratigraphic architecture composed of phyloid and crinioidal mounds and their associated flank strata (Kerans, 2001). These mounds are analogous to classic phylloid mound outcrops of similar age in the Sacramento Mountains in New Mexico (Wilson, 1967; Rankey et al., 1999; Janson and Kerans, 2011).

The Canyon and Cisco platforms are expected to have undergone substantial early diagenesis via meteoric processes because of the frequent and significant (60-100 m) eustatic fluctuations of sea level (Heckel, 1983; Goldstein, 1988; Soreghan and Giles, 1999). Grain-rich facies present in the top of the Canyon platform and carbonate mounds in the Cisco Formation are subject to early (approximately instantaneous) marine and meteoric cementation (Cross and Klosterman, 1981; Grammer et al., 1993; Webb, 1996). The less permeable mud-rich and shale facies present deposited in basinal (off-platform) settings are likely to be susceptible to compaction (Figure 2).

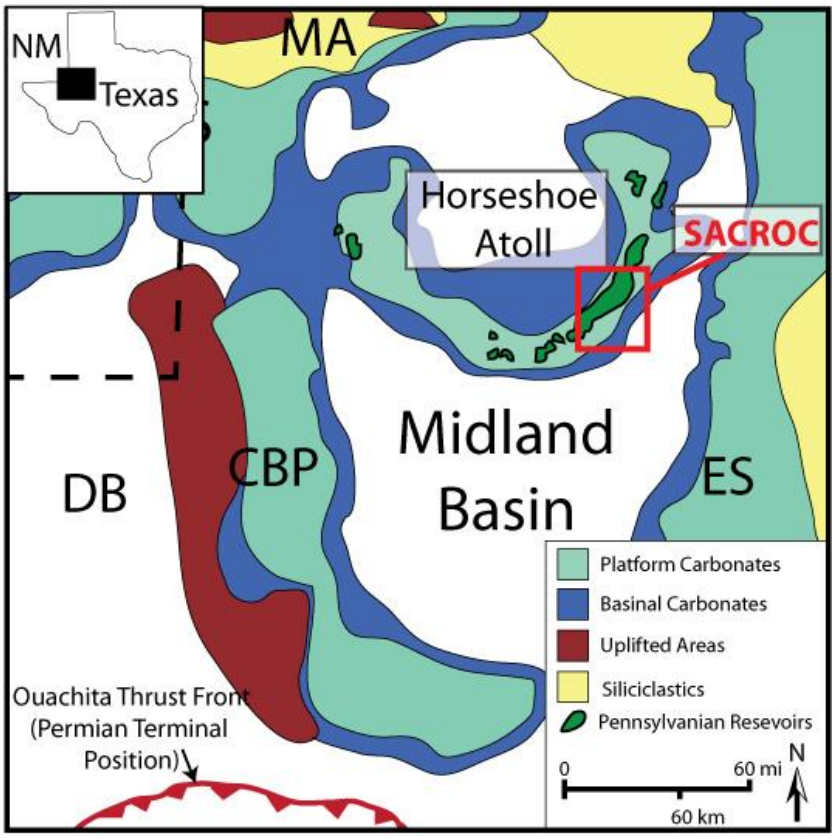

Figure 4.1: Paleogeographic map showing the location of the Kelly-Snyder Field relative to major carbonate platforms and uplifts in the Midland Basin region. DB = Delaware Basin, CBP = Central Basin Platform, ES = Eastern Shelf, MA = Matador Arch. After Wright (2011).

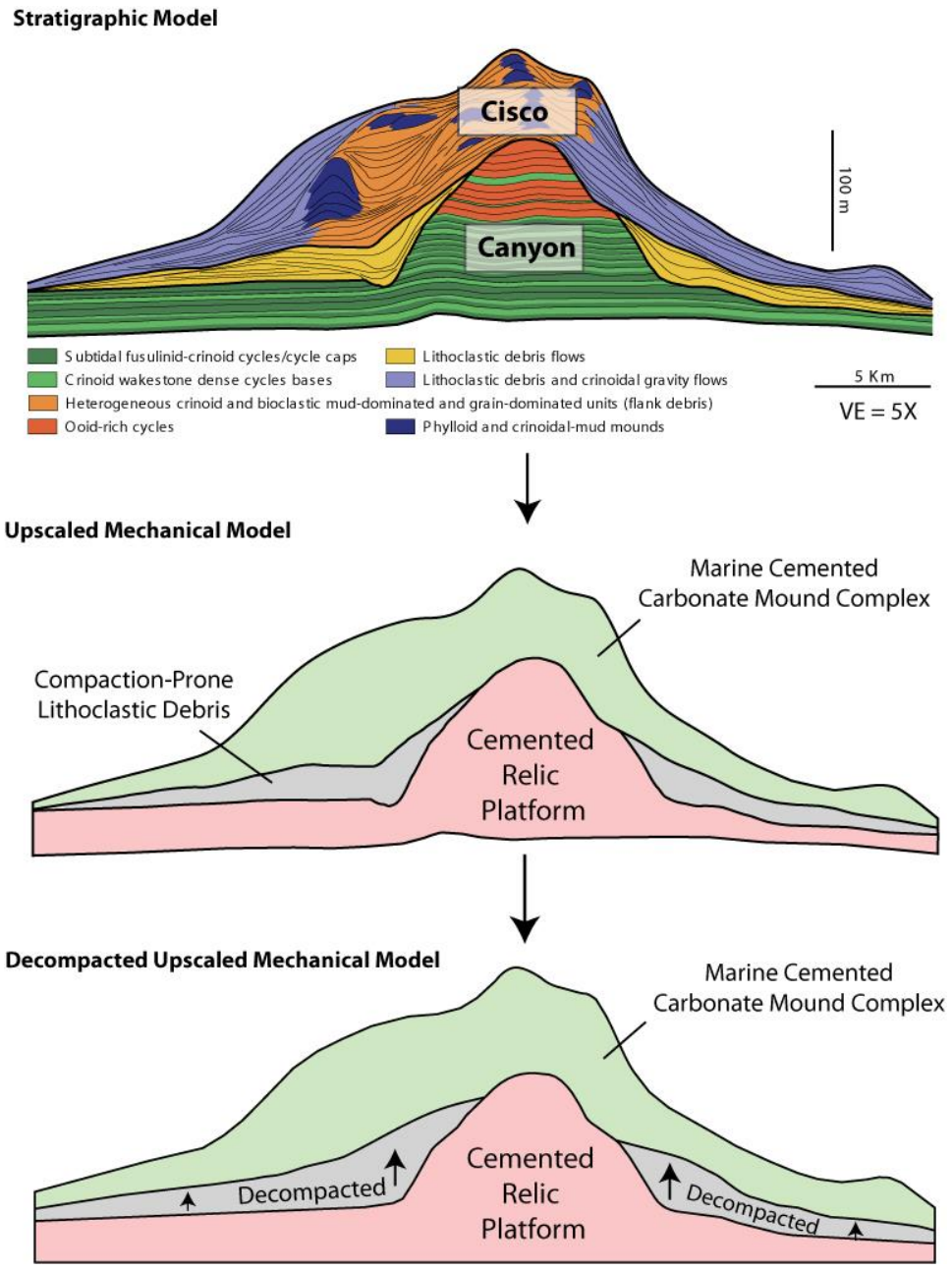

Figure 4.2: Schematic cross-section of SACROC showing the stratigraphic architecture of the Canyon and Cisco Formations. After Zahm et al. (2009). Mechanical models are constructed based on upscaling (simplification) of the stratigraphic architecture and restoration of compaction prone strata.

3. 3D NUMERICAL MODELING APPROACH

3D finite-element mechanical models are constructed using the hybrid finite-discrete element code ELFEN® to investigate differential compaction fracture development in isolated carbonate platforms. The initial 3D geometry is segmented using a tetrahedral mesh. At each time step of the model, values for stress, strain, and displacement are calculated at each node of the meshed geometry under the prescribed loading conditions. All models are subjected to gradual application of gravitational load with corresponding confining stress. We constructed models at two different scales: (1) field/platform-scale model, (2) individual mound/bank-scale models (i.e., sub-seismic scale). Here we explain each model inputs and setup including initial geometry, loading conditions, boundary conditions, and rock properties.

3.1 Platform-Scale Model Setup

An isolated carbonate platform-scale model is constructed based on the Canyon and Cisco formations in SACROC. The initial 3D geometry of the model is based on 3 surfaces created from seismic interpretation of key horizons on a 3D seismic survey of SACROC (Figure 3). The top surface of the model corresponds to the top of the Cisco Formation. The middle surface represents the off-platform basinal sediments (lithoclastic debris) that are prone to compaction. The last surface is of the top of the Canyon Formation. Based on present day depth and what is known about compaction of mud-rich and grain-rich carbonates (Goldhammer, 1997), a decompaction function was applied to the lithoclastic debris surface (Figure 3B). The off-platform (basinal) areas are expected to be mud-rich facies and thus were decompacted assuming 50% compaction has occurred. Platform-top areas are expected to be grain-rich facies and consequently they

were decompacted assuming 20% compaction has occurred. The top of Cisco was raised to accommodate the increased thickness of the decompacted layer.

Gravity is applied to the 3D model geometry gradually following a linear curve with a corresponding confining horizontal stress ($S_{horiztonal} = 0.8S_{vertical}$) and a hydrostatic pore pressure. Two types of boundary conditions are applied to the model to ensure numerical stability. The first set of boundary conditions is permanent (i.e., enforced throughout the model run). The permanent boundary conditions include constraining the vertical displacement of the base of the model (i.e. z-direction displacement = 0) and constraining the horizontal displacement of the model sides (i.e., x and y displacement = 0). The temporary boundary conditions prevent any compaction from occurring prior to the full application of the gravitational load. This is necessary to capture the effect of compaction in changing the local stress field as well as to ensure that the kinetic energy remains minimal to maintain quasi-static conditions (Rockfield, 2014). After completing the full application of the gravitational load, the temporary conditions are gradually relaxed and compaction occurs.

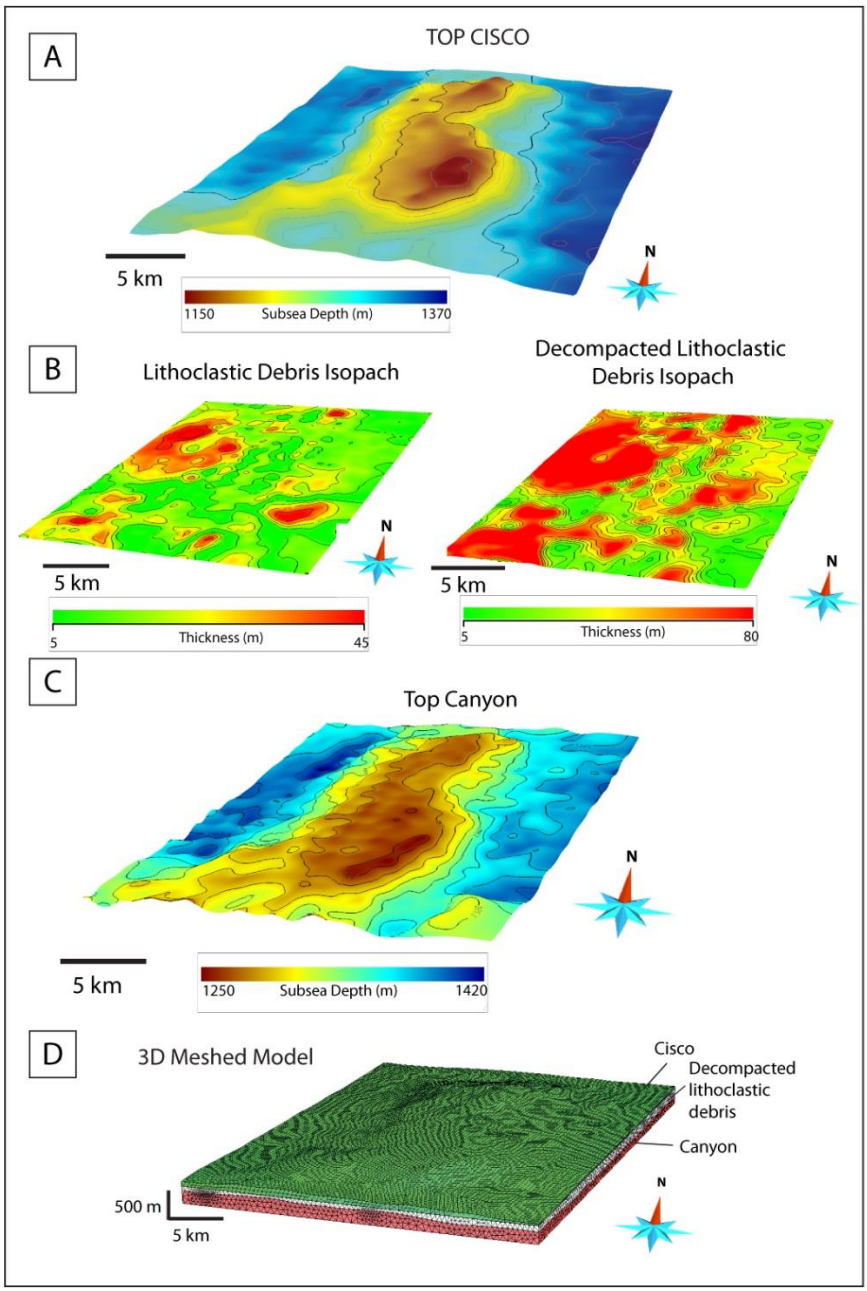

Figure 4.3: The initial geometry of the reservoir-scale 3D geomechanical model based on seismic data. (A) Structure contour map of the top of Cisco surface. (B) Isopach map of the compacted lithoclastic debris and its decompacted counterpart highlighting areas of thickening off the platform. (C) Structure contour map of the top of Canyon Formation. (D) The constructed 3D meshed model used as initial geometry of the geomechanical model.

Rock properties and constitutive laws governing deformation are assigned to each layer in the model based on the expected behavior soon after their deposition. Early cemented platform carbonates of the Canyon and Cisco formations are expected to be brittle and resistant to compaction. A Mohr-Coulomb with a Rankine tensile corner constitutive law is assigned to them. For simplification, properties are assigned homogenously within the Cisco and Canyon layers (Table 1). The most critical input for prediction of tensile fracture development is the prescribed tensile strength of the layer. The Canyon is assigned double the tensile strength of the Cisco given its older age and deeper location. Areas where the effective minimum principal stress (σ_3) reaches the prescribed tensile strength of the layer, fractures are predicted to form. The model is run in continuum only (i.e., no discrete fracture develop but areas of high fracture probability are predicted). The off-platform basinal sediments layer is assigned the elastoplastic Modified CAM Clay model that allows for compaction by ductile deformation and porosity loss (Table 2).

3.2 Mound-Scale 3D models

Sub-seismic scale 3D models are created to capture the influence of the local differential compaction fracture development within the Cisco mound complex (i.e., mound core, flank, and cover strata). Two 3D models are constructed to primarily investigate the difference in fracture development between strata overlying an approximately circular mound and an elongate bank (Figure 4). The 3D model consists of 3 layers: (1) mound/bank layer, (2) mud-rich carbonates layer filling the intermound area, (3) grainstone layer capping the cycle. The circular mound and elongate bank initial geometry are based on circular and elongate interpolation of a dip-oriented outcrop exposure of a phylloid mound similar in age in the Sacramento Mountains in New

Mexico. The geometry of the mound in outcrop was captured using a 3D digital outcrop model (Refer to Chapter 3). The mud-rich flank layer and the overlying grainstone were assumed to have been initially horizontal.

Boundary and loading conditions are similar to those applied to the platform-scale model described above. The marine-cemented mound and cemented grainstone are assigned brittle properties and Mohr-Coulomb-Rankine failure criteria. Properties of the mound are assigned based on uniaxial compressive strength and tensile stress laboratory tests on samples from mounds in the Sacramento Mountains (Table 3). The cemented grainstone properties are based on properties and laboratory tests on samples from a Pleistocene cemented grainstones (modern analogue). The model utilizes the discrete fracture modeling facility that creates discrete fracture planes in areas meeting the failure criteria. Because this type of modeling is computationally demanding the tensile strength of the grainstone is lowered to require less differential compaction and less computation time to develop fractures. The fracture location and orientation are not affected by the lowering of tensile strength (see Chapter 2). At each step of the model, the stress conditions are checked against the prescribed failure criteria. When the minimum principal stress reaches the prescribed tensile strength of a brittle layer a tensile fracture is created to dissipate the accumulated stress. The mud-rich layer is assigned the elastoplastic Modified CAM Clay criterion to allow for compaction (Table 2).

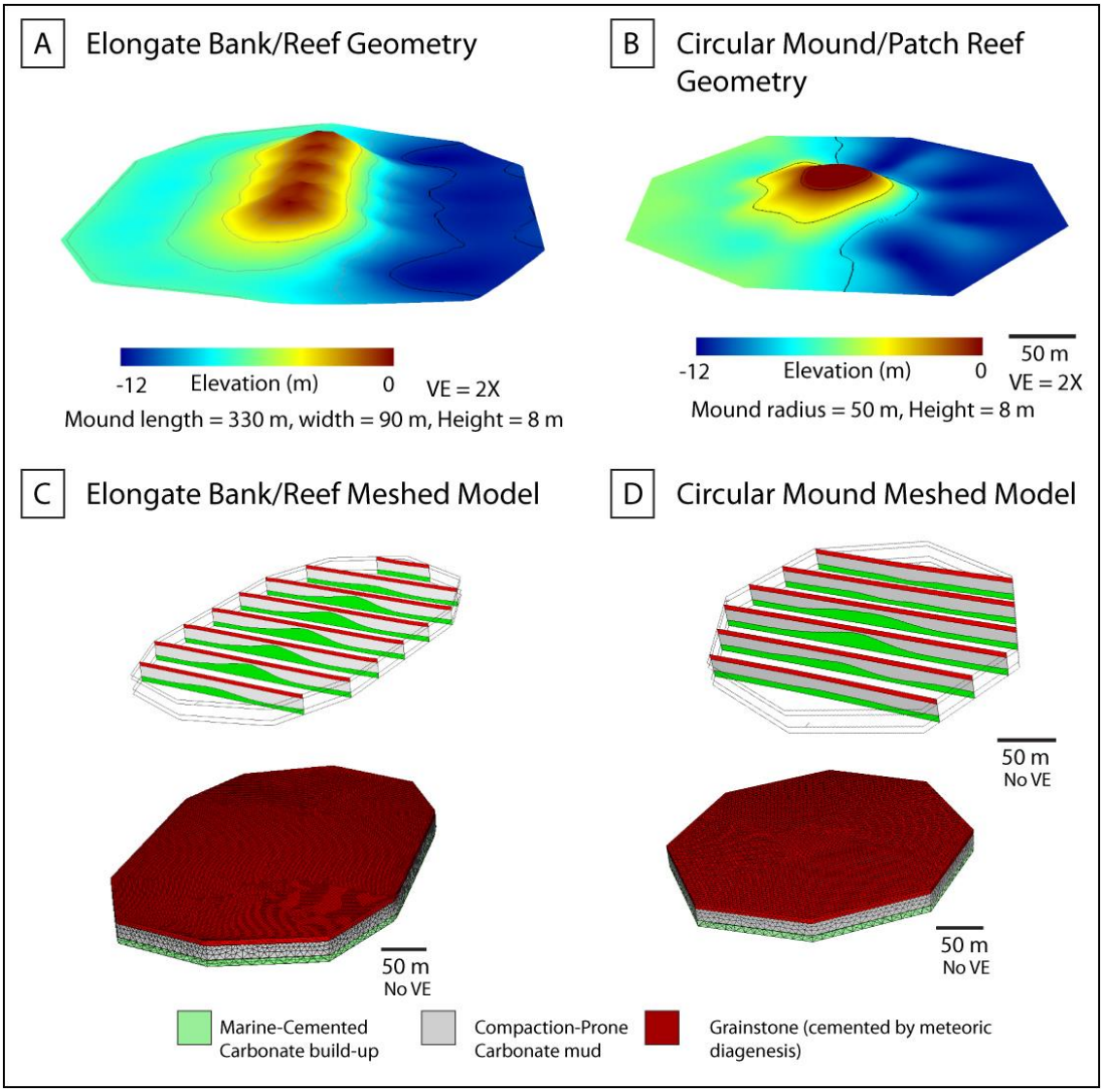

Figure 4.4: Initial 3D geometry of mound and bank-scale models based on circular and linear interpolation of 3D digital outcrop model of a mound. (A) 3D surface of elongate bank. (B) 3D surface of approximately circular mound. (C) Meshed initial 3D bank model geometry with several cross-sections to illustrate the internal geometry. (D) Meshed initial 3D circular mound model with corresponding cross-sections.

4. STRESS EVOLUTION DURING COMPACTION OVER THE CANYON ISOLATED CARBONATE PLATFORM

3D model of the isolated carbonate platforms in SACROC shows the evolution of the stress state during differential compaction and highlights areas of great propensity to tensile fracture development (i.e., areas of increased tensile stress) (Figure 5). After the full application of gravity and prior to any compaction all three principal stresses are initially compressive throughout the platform. The most relevant stress parameter to tensile fracture development is the effective minimum principal stress. Centimeter-scale differential subsidence (driven by compaction) of the Cisco mound complex over the antecedent Canyon platform is sufficient to initiate σ_3 tensile stress regions (≥1 MPa) over the eastern margin of the Cisco platform. Off-platform tensile regions (≥1 MPa) develop with minor amount of additional differential compaction (10s of cm). The areal extent and magnitude of tensile stress increases with increasing subsidence in the model. Meter-scale differential subsidence causes the entire Cisco platform top to experience tensile stress. The greatest magnitude of tensile stress in the Cisco platform is located in the southeastern and northeastern platform margins, which corresponds to primary windward thickening in both the Canyon and Cisco initial geometries (Figure 3). The greatest magnitudes of tensile stress off the platform are located in a (light blue) ring surrounding the platform margins and separated from the platform top tensile region by a region of compression (dark blue) (Figure 5, time step 1). The off-platform tensile region is more prominent in the windward side of the platform compared to the leeward side. The greatest areas of Cisco subsidence are located where the lithoclastic debris is thickest to the west and east of the Cisco and Canyon platforms (Figure 5).

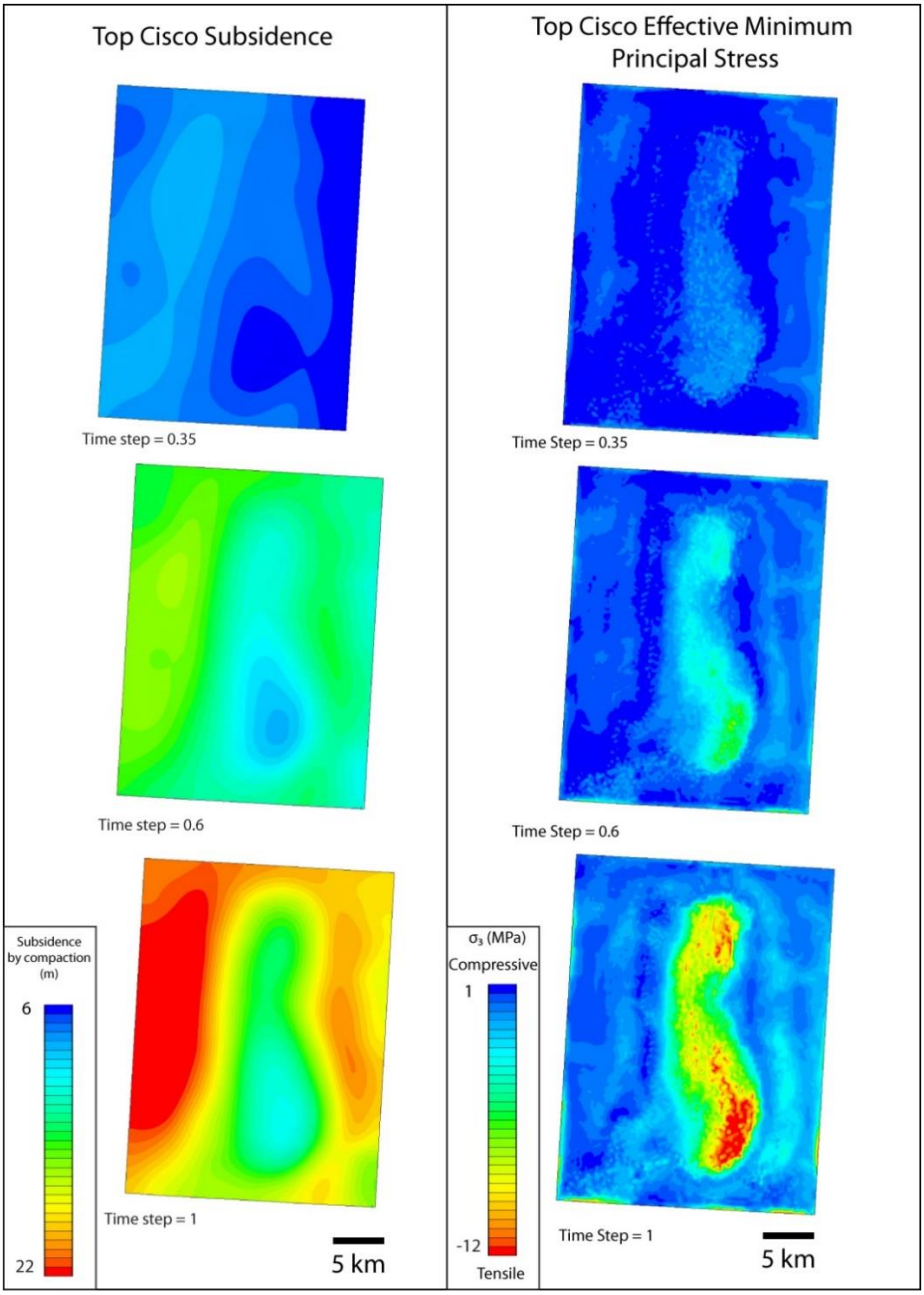

Figure 4.5: Evolution of subsidence and minimum principal stress on the top of the Cisco Formation during key time steps of the 3D model. Regions of increased tensile stress intensifies with increased subsidence. Tensile regions are areas susceptible to tensile (opening mode) fracture development. Probability of fracture development and its intensity is directly proportional to tensile stress.

5. FRACTURE DEVELOPMENT OVER CIRCULAR MOUND AND ELONGATE BANK

Results of 3D hybrid finite-discrete models of differential compaction over individual circular and elongate carbonate mound/bank show variability in stress, subsidence, and fracture distribution (Figure 6). Subsidence contours on the strata overlying buildups mimics the buildup shape. In the circular mound model, subsidence contours are circular. The least amount of subsidence is overlying the crest of the mound and subsidence increases outward. In the elongate bank model, subsidence contours are elliptical. The least amount of subsidence occurs overlying the bank crest and increases outward. In both models, a minor windward/leeward asymmetry in subsidence develops corresponding to the inherent slope (~1°) present in the initial buildup layer geometry (Figure 4 A, B). This asymmetry in subsidence can be best observed by the red contours distribution (i.e., areas of greatest subsidence) in time step 1.1 of the models (Figure 6). Similar to the platform-scale model, all principal stresses are compressive prior to compaction (Figure 6, step 0.1). After minor compaction, regions of elevated tensile stress, σ_3 develop in areas overlying mound and bank crests (Figure 6, time step 0.7). Eventually, the prescribed tensile strength of the layer is reached and fractures develop in the model (Figure 6, time step 0.8). Additional compaction corresponds to additional fracture development and growth over the mound and bank crests as well as minor fracturing in the off-buildup areas (Figure 6, time step 1.1).

A notable difference in fracture pattern can be observed between the circular mound and elongate bank models. In the circular mound model, fractures develop in a radial pattern initiating from the mound crest and growing outward in all directions (Figures 6, 8). In the elongate bank model, fractures grow in a linear fashion along the strike of the bank with some bifurcation toward the bank edges (Figures 6, 8). Length-weighted rose

diagrams and map view of the generated fractures illustrate the radial and linear fracture pattern (Figure 8). Off-buildup fracture distribution is also different between the two models. Circular mound model have off-buildup fractures form in a circular ring around the buildup (Figure 6, time step 1.1). In contrast, the off-buildup fractures in the elongate bank model are present in an elliptical pattern around the bank (Figure 6, time step 1.1).

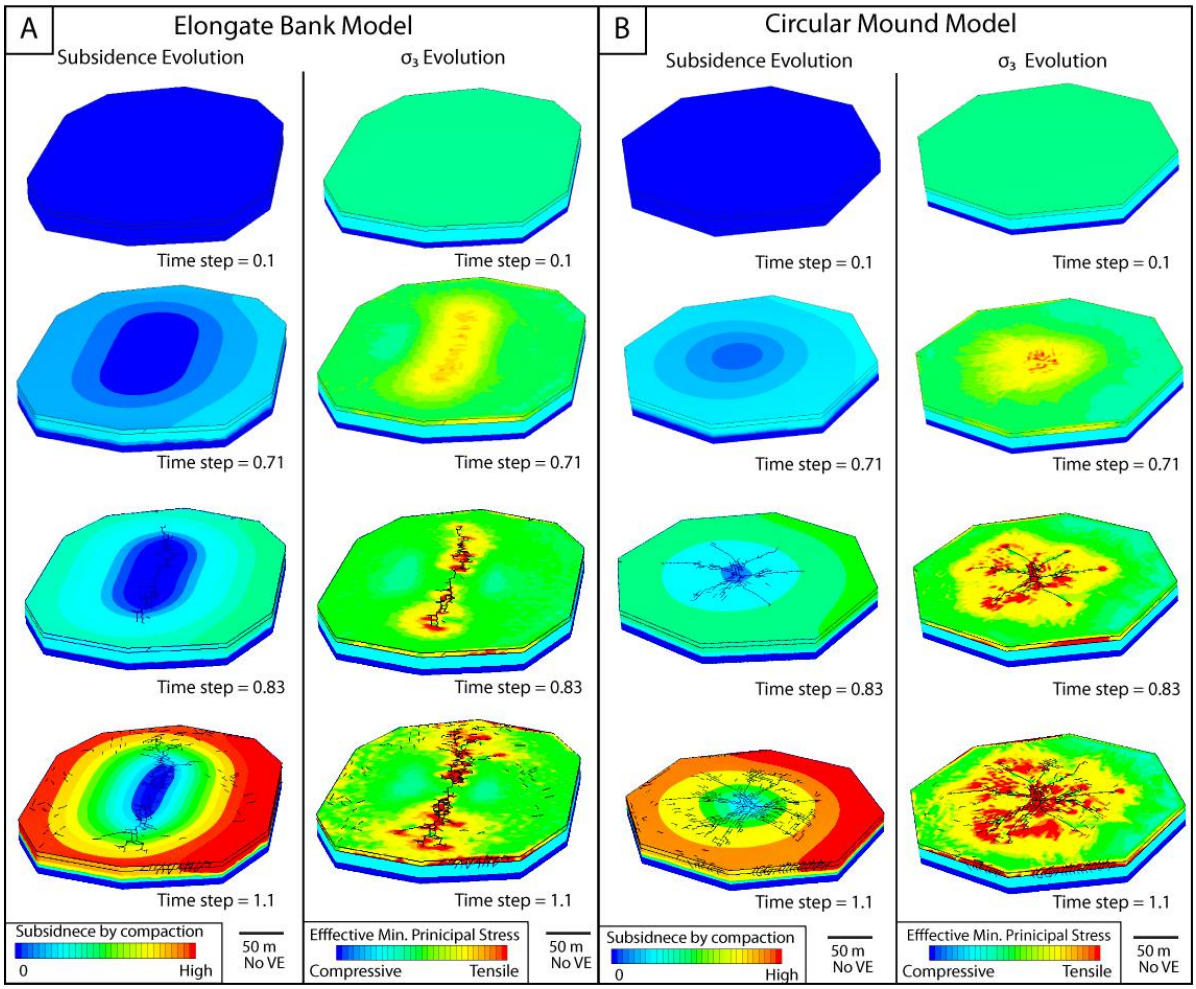

Figure 4.6: Comparison between the evolution of elongate and circular bank/mound models. (A) Subsidence and minimum principal stress evolution with progressive compaction ending with fracture development in the elongate bank model. (B) Subsidence and minimum principal stress evolution with progressive compaction ending with fracture development in the circular mound model.

6. NUMERICAL MODEL VALIDATION USING FIELD DATA

6.1 Dataset and Inherent Limitations

Image log data from 29 wells and mud loss data from 24 wells are used as a reference for comparison between our modeling results and field-based fracture observations in the Cisco Formation. Several limitations and biases are inherent to this dataset that should be kept in mind including geographic bias and interpreter's bias. The location of wells with image logs is biased to more recent wells in the southeastern part of SACROC. Fractures in image logs were interpreted by multiple interpreters introducing interpreter bias to the data. 1D average (vertical) fracture intensity (P10) is calculated from interpreted fractures within the Cisco Formation. Fracture fill and relative time of fracture development (i.e., early versus late) cannot be determined from image logs. Therefore, fracture intensity may include both syndepositional fractures (i.e. from differential compaction) and later burial and/or tectonic related fractures. However, areas of syndepositional fracture development are known to be susceptible to repeated reactivation (Cozzi, 2000; Di Naccio et al., 2005; Koša and Hunt, 2005; Budd et al., 2013; see Chapter 2). Syndepositional deformation fabric is even more important in areas that has not been modified by major tectonism like SACROC.

Data of drilling mud losses within the Cisco Formation can be used to infer the presence of natural fractures. During the drilling operations, if the wellbore trajectory intersects a fractured zone, the drilling mud within the wellbore can be drained by the highly permeable fractured rocks and mud losses occur. Mud loss probability increases with increased fracture intensity. However, there are alternative causes for mud loss other than the presence of natural fractures. Mud loss could occur when encountering rocks with highly permeable (connected) vuggy or cavernous porosity. Less likely to cause mud loss is using

excessively heavy mud weight that overcomes the minimum principal stress and hydraulically fractures the formation, causing mud to drain out of the borehole.

6.2 Well data and Numerical Model Predictions

Cisco average fracture intensity and mud loss data from SACROC wells are plotted on the last time step of our 3D model for comparison between model prediction and fracture observations (Figure 7 B). Wells with greatest fracture intensities (0.8-1.3 frac/m) are located on the southeastern part of the Cisco platform overlying areas of greatest tensile stress shaded in red (i.e. areas of highest propensity to differential compaction fracturing). The majority (75%) of wells with Cisco mud losses are located in areas of increased tensile stress. This includes mud losses in a well located in the tensile region off the western platform margin that also has high fracture intensity (0.7 frac/m). Some of the low fracture intensity values are located in areas of increased tensile stress in the model. This could be reflecting poor fracture sampling inherent to vertical wells as well as interpreter bias. Overall, our 3D modeling results and predictions are consistent with observed fracture intensity and mud loss data.

Cisco fracture orientations measured from image logs are compared to predicted orientation of platform-scale and mound-scale differential compaction fractures. Orientation of principal stresses in the platform-scale model can be used to infer predicted orientation of differential compaction induced fractures. Fractures develop parallel to the maximum (σ_1 = vertical) and intermediate principal stress (σ_2 = Shmax) orientations and open in the direction of the minimum principal stress (σ_3 = shmin). Given that the maximum principal stress direction is vertical, differential compaction fractures are expected to be vertical and parallel to the Shmax orientation (Figure 7A). Shmax orientation is approximately parallel to the Cisco platform margin. Orientation of fractures observed in

the Cisco Formation on the platform top shows N-S trend (Figure 9), which is consistent with our platform-scale model prediction. However, orientation of Cisco fractures on the eastern platform margin shows significant azimuthal variation with no clear directional trend (i.e. radial pattern) (Figure 9). The radial fracture pattern on the eastern shelf margin is more consistent with the small-scale circular mound model than the large-scale platform model (Figure 8). This suggests that the local differential compaction around mounds and mounds geometry is likely to be the controlling factor on fracture orientations at the shelf margin. Therefore, characterizing the distribution and geometry of carbonate buildups in subsurface reservoirs is critical to differential compaction fracture characterization.

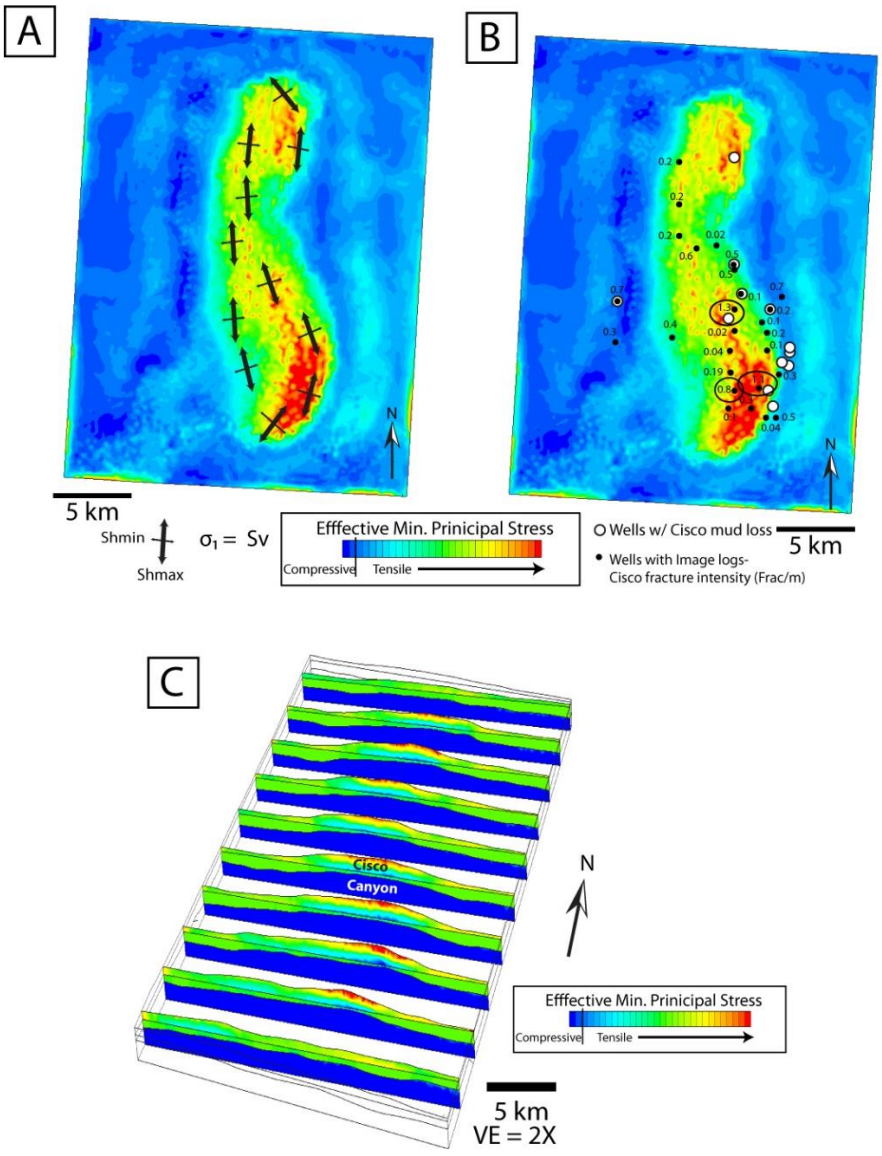

Figure 4.7: (A) The principal stress orientations on top of the Cisco surface at the end of the model run. Direction of maximum horizontal stress (Shmax) can be used as a proxy for differential compaction fractures orientations. (B) Mud loss and fracture intensity within the Cisco Formation from image log data superimposed on the 3D model prediction of areas of predicted fracture development from differential compaction (areas of tensile minimum principal stress). The highest values for fracture intensity (circled) correspond to areas of predicted differential compaction (tensile) fractures. (C) Series of cross-sections through the 3D model showing along-strike variability of tensile stress distribution in the Cisco Formation.

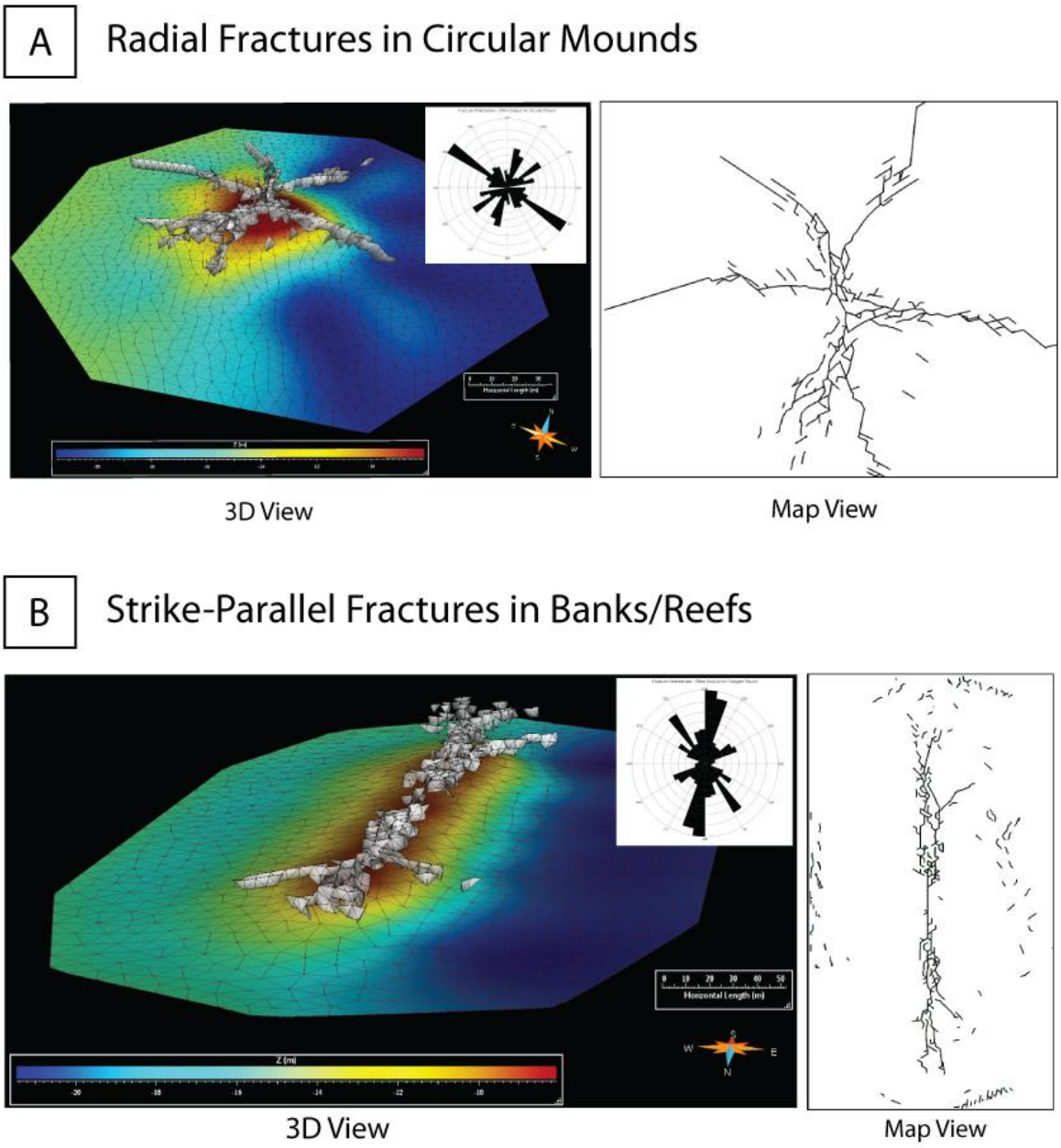

Figure 4.8: Fracture geometry associated with circular mound and an elongate bank. (A) 3D fracture planes generated by differential compaction over a circular mound. Length weighted rose diagram and the observed geometry reflects a radial fracture pattern. (B) 3D fracture planes generated by differential compaction over an elongate bank. Length weighted rose diagram and the observed fracture geometry reflects fracture pattern that is parallel to the bank strike.

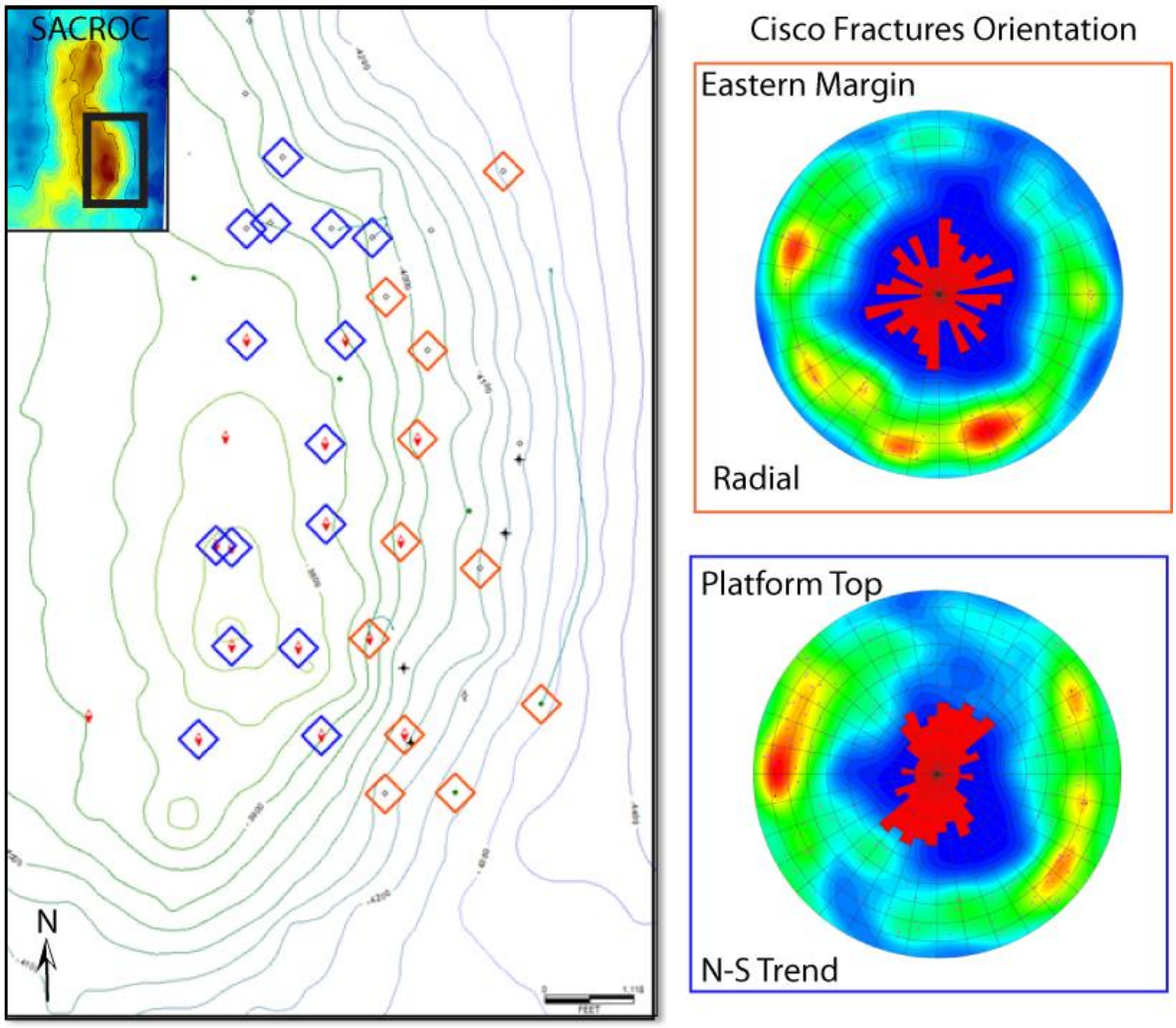

Figure 4.9: Rose diagram of fractures interpreted from image logs obtained from wells located at the eastern margin and platform top of the Cisco platform. Fractures in the eastern margin (n = 127) reflects a radial fracture pattern. Platform top (n = 161) exhibit preferential N-S trend in fracture orientation.

7. CONTROLS ON DIFFERENTIAL COMPACTION FRACTURES IN ISOLATED CARBONATE PLATFORMS

The 3D antecedent topography of the Canyon isolated carbonate platform is the primary control on the locations of elevated tensile stress regions in the overlying Cisco platform. A series of E-W cross-sections through our platform-scale 3D model illustrate the relationship between antecedent topography and tensile regions in the Cisco platform (Figure 7 C). Similar to previous 2D numerical modeling work of differential compaction deformation (see Chapter 3), regions of elevated tensile stress develop (i.e. where tensile fractures likely to occur) in outer hinges of forced folds driven by the underlying differential compaction. The greatest effective tensile stress values occur in the Cisco where it overlies the antecedent Canyon platform top (crest). Another region of elevated tensile stress in the Cisco is located where it overlies the Canyon platform lower slope-to-toe of slope transition in both the leeward and windward margins. The location of Canyon platform top and lower slope-to-toe of slope transition varies across the platform strike from south to north as well as the inherent windward-leeward asymmetry (Figure 7 C). Toward the southern and northern parts of the Canyon platform, the windward side (eastern margin) shows significant thickening and relief compared to the leeward side (western margin) (Figure 3). This pronounced asymmetry corresponds with the greatest effective tensile stress being concentrated in the windward side of the Cisco in the north and south of SACROC (Figure 7 C). In contrast, toward the center of SACROC, the Canyon platform top is flatter with less windward-leeward asymmetry. As a result, the region of greatest effective tensile stress is located at the center of the Cisco platform. The windward side of the Canyon platform naturally has a steeper slope than the leeward side. This causes the

off-platform tensile region that corresponds to slope-to-toe of slope transition to be closer to the platform margin in the windward side compared to the leeward side.

The more subtle (i.e., ~1˚ slope) leeward-windward asymmetry present in the mound/bank-scale models does not appear to influence the location of tensile stress regions or the resulting fractures (Figure 4, 6). This suggests that only substantial asymmetry in the antecedent topography influence location of tensile stress developed by differential compaction.

The magnitudes of differential subsidence required to initiate tensile stress regions within the Cisco are minor (cm-10's cm scale). These values are similar to values required for fracture development over the approximately 10 times smaller mounds (see Chapter 3). This observation, in combination with the relatively similar location of tensile regions over the mound-scale and the platform-scale models suggests that differential compaction deformation process is scale independent.

8. CONCLUSIONS

Differential compaction driven deformation is simulated in 3D geomechanical models of isolated carbonate platforms and the smaller scale mounds in the SACROC unit of the Kelly-Snyder Field in West Texas. We show for the first time how the 3D antecedent topography of an isolated carbonate platform can control locations of syndepositonal fracture development in the overlying younger carbonate platform. Minor amounts of differential subsidence over an isolated carbonate platform were required for the development of tensile stress regions suggestive of opening mode fracture development. This is consistent with previous modeling work of differential compaction driven deformation at a smaller scale, indicating that the process is scale independent. This illustrates that differential compaction driven fracturing may be underestimated in carbonate platforms. Our 3D model predictions of areas of increased fracture development were supported by observations of increased fracture intensity in image logs as well as mud loss data from SACROC. At platform top locations observations of fracture orientations were consistent with the platform scale model. However, fracture orientations at the platform margins appear to be influenced by local differential compaction associated with individual mounds. This suggests that characterizing the carbonate buildup shapes and spatial distribution in the subsurface is critical for characterization of syndepositional fractures.

ACKNOWLEDGEMENTS

Mahmoud Alnazgha is thanked for collaborating on this study by engaging in discussions about the SACROC and providing interpreted seismic surfaces. FMI fracture data and mud loss data was provided by Dr. Chris Zahm. Rockfield is thanked for providing educational license for ELFEN.

Table 4.1 Brittle Material Properties with Mohr-Coulomb-Rankine Criteria for the platform-scale model

Property	Canyon	Cisco
Tensile Strength (MPa)*	2.4	1
Fracture Energy (J/m^2) †	2.2	1.63
Internal Friction Angle(°)	40	37
Internal Cohesion (MPa)	15	3
Young's Modulus (GPa)¥	36	13
Poisson's Ratio¥	0.24	0.30
Porosity	0.10	0.34
Bulk Density (kg/m^3)	2500	2130
Discrete Contact		
Coefficient of sliding Friction	0.5	
Discrete contact cohesion (MPa)	0	

* Based on Brazilian test data

¥ Based on uniaxial compressive test data

† Based on empirical relationship dependent on E and T_0 (Zhang, 2002)

Table 4.2 Material Properties for Mud-rich strata (lithoclastic debris and basinal sediments) prone to compaction assigned a Modified CAM Clay model

Property	Mud-rich strata
Young's Modulus (GPa)	0.4
Poisson's Ratio	0.25
P_c (MPa)	0.05
P_t (MPa)	0.1
B	60
β_0	0.60
B_1	0.73
Φ	55
N	1.3
A	0.25
Porosity	0.60
Bulk Density (kg/m^3)	1670

Table 4.3 Brittle Material Properties with Mohr-Coulomb-Rankine Criteria for the mounds and banks in the small-scale models

Property	Canyon
Tensile Strength (MPa)*	4
Fracture Energy (J/m^2)†	3
Internal Friction Angle(°)	40
Internal Cohesion (MPa)	15
Young's Modulus (GPa)¥	36
Poisson's Ratio¥	0.24
Porosity	0.05
Bulk Density (kg/m^3)	2600

* Based on Brazilian test data

¥ Based on uniaxial compressive test data

† Based on empirical relationship dependent on E and T_0 (Zhang, 2002)

Chapter 5: Conclusions

Syndepositional fracture development driven by differential compaction in carbonate mound complexes is investigated through a field-based study and a multi-scale 2D and 3D numerical modeling investigation. The main findings of this research are summarized below.

Characterizing syndepositional and late tectonic fractures at a classic Late Pennsylvanian carbonate mound complex locality in the Sacramento Mountains of New Mexico yielded important insight into the evolution of mechanical stratigraphy with respect to fracture development. Syndepositional fractures are limited to the early-cemented mound core and grainstone facies, suggesting that mechanical differentiation was initially high. Syndepositional fractures are preferentially located in early-cemented strata overlying the flanks of mound core and are not consistently oriented with respect to the syndepositional La Luz anticline, which indicates that their origination is more consistent with differential compaction. This supports earlier work postulating that differential compaction can be a major process driving early deformation in carbonate mound complexes and in carbonate systems in general.

Highest intensities of late tectonic fractures are coincident with locations of early fractures, highlighting early fractures potential for reactivation and the significance of constraining their spatial distribution. Field measurements of rock strength –reflecting rock terminal strength– suggest that burial diagenesis obscured the early mechanical contrast and homogenized rock strength across grain-rich and mud-rich lithologies. Late tectonic fractures have consistent orientation with both Laramide and Rio Grande rift stresses and are commonly throughgoing (i.e., not bed-bound) indicating that they post-dated strength homogenization. However, bedding style and primary depositional fabric

still imposed a control on maximum fracture height. The results of the field-based investigation showed that fracture development in carbonate mounds is affected by an evolving mechanical stratigraphy reflective of early and late diagenetic processes.

The novel numerical modeling approach adopted in this work provides fundamental understanding of the primary controls on development of differential compaction fracturing in strata overlying carbonate mounds. 2D finite-discrete element models based on mound outcrops of the Holder Formation in the Sacramento Mountain of New Mexico were used to identify the main controls on differential compaction fracturing. The main control on the location and spatial extent of differential compaction fractures is the underlying rigid antecedent topography (mound) geometry. Fractures develop most extensively overlying the mound crest. In addition, wide fracture clusters can form in strata overlying the mound-flank to intermound transition. Therefore, characterizing the geometry of carbonate mounds/rigid antecedent topography is important for the prediction of differential compaction fracture locations. Relative to mound height, minor amounts of differential compaction (subsidence) are required to develop extensive differential compaction fracturing in strata overlying carbonate mounds. This suggests that differential compaction as a mechanism for early deformation may be underestimated in carbonate systems, especially in areas that experienced early differential diagenesis. Prior to this work, the effect of layer-parallel slip (LPS) on the spatial organization of fractures in a depositional setting has not been demonstrated. Modeling results show the significant control that LPS exerts on the intensity of differential compaction fracturing. LPS is inferred to be able to accommodate up to 40% of the strain experienced by deformed strata, highlighting its importance as a major process for stress dissipation.

Differential compaction driven deformation is simulated in 3D geomechanical models of isolated carbonate platforms and the smaller scale mounds in the SACROC unit of the Kelly-Snyder Field in West Texas. This work shows for the first time how the 3D antecedent topography of an isolated carbonate platform can control locations of syndepositonal fracture development in the overlying younger carbonate platform. Minor amounts of differential subsidence over an isolated carbonate platform were required for the development of tensile stress regions suggestive of opening mode fracture development. This is similar to 2D modeling results of differential compaction driven deformation at a smaller scale, indicating that the process is scale independent. Another implication is that differential compaction driven fracturing may be generally underestimated in carbonate platforms. Our 3D model predictions of areas of increased fracture development were supported by observations of increased fracture intensity in image logs as well as mud loss data from the SACROC. Observations of fracture orientations were consistent with platform scale model in platform top locations. However, fracture orientations at the platform margins appear to be more consistent with local differential compaction associated with individual mounds. This suggests that characterizing the carbonate buildup shapes and spatial distribution in the subsurface is critical for characterization of syndepositional fractures. This work demonstrates how a process-based approach to fracture characterization and prediction can overcome the shortcomings of outcrop and core based observations of early fractures.

Appendix A: Failure Criteria

MOHR-COULOMB-RANKINE FAILURE MODEL

The Mohr-Coulomb failure criteria describes the response of brittle materials (e.g., rocks) to applied normal and shear stresses. The failure envelope is approximated by a linear relationship between normal stresses and shear stresses described by the following equation:

$$\tau = c + \sigma_n . \tan(\phi) \quad (1)$$

Where τ is the shear stress, ϕ is the angle of internal friction, σ_n is the normal stress, and c is the cohesion.

The failure envelope varies depending on the type of material/rock and is typically derived from laboratory triaxial experiments carried out at variable confining stress. The envelope is constrained by the best fit tangent line to the Mohr circles representing the stress state at failure under different confining stresses (Figure A1). In principal stress space, the Mohr-Coulomb failure envelope is represented by hexagonal conical yield surface (Figure A2).

The Mohr-Coulomb linear formulation detailed above does not incorporate the tensile strength of the tested material. Therefore, a tensile cut-off (Rankine criterion) needs to be included to better capture the brittle material behavior in tension (Figure A1). The Rankine tensile cut-off is defined by the following equation:

$$\sigma_i - T = 0\ ,\ \ i = 1, 2, 3 \quad (2)$$

Where σ_i refers to each principal stress and T is the prescribed tensile strength.

The Mohr-Coulomb-Rankine failure criterion is governed by the Mohr-Coulomb envelope in compression (shear failure) and the Rankine criterion in tension (tensile

failure). Tensile strength is the most relevant parameter for tensile failure (see eq. 2) and is commonly measured by the indirect uniaxial tensile strength test (Brazilian test) (ASTM D3967-08). There are direct tensile strength measurement tests (e.g., direct pull/pull-off test), however, they are less commonly used because they are relatively difficult and expensive to preform (ASTM D2936-08). No softening law is included explicitly in ELFEN, however, indirect softening occurs from degradation of cohesion according to the following equation:

$$T \leq \frac{c\,(1-sin\phi)}{cos\phi} \tag{3}$$

Where T is tensile strength, c is cohesion, and ϕ is angle of internal friction. Refer to Rockfield (2014) and Klerck (2004) for further information of how the Mohr-Coulomb-Rankine Criterion is implemented in ELFEN.

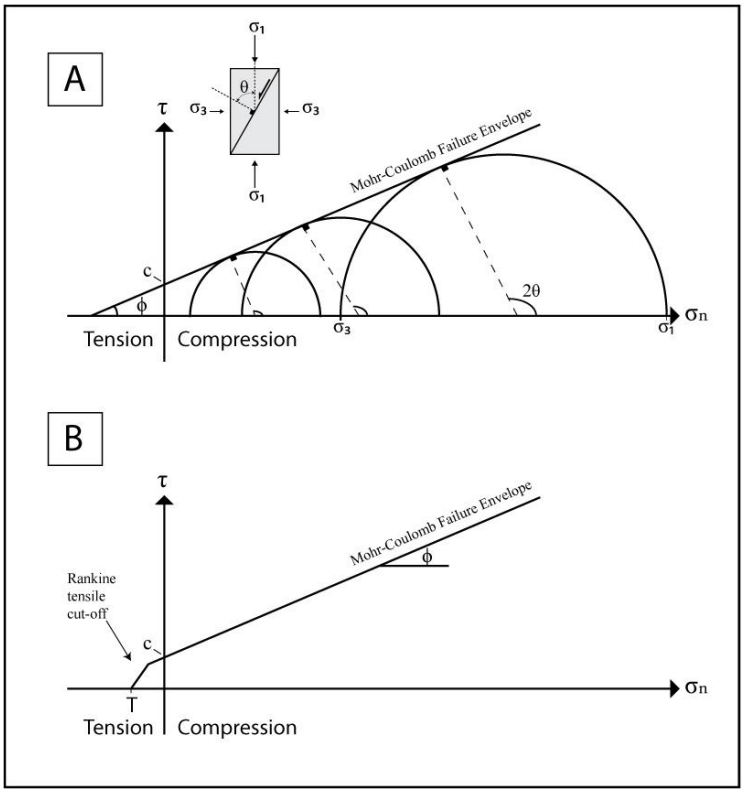

Figure A.1: (A) Mohr-Coulomb Failure Criteria with illustration of its derivation from triaxial tests. (B) Modified Mohr-Coulomb Failure with Rankine tensile cut-off.

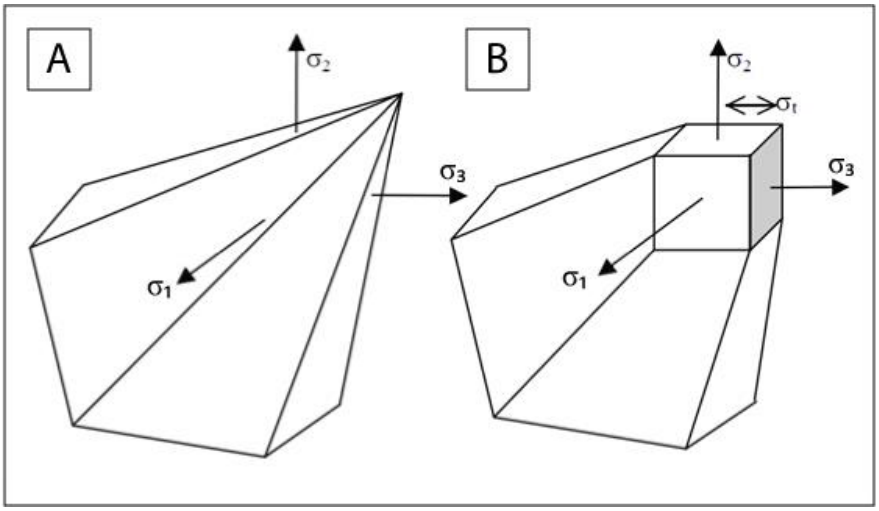

Figure A.2: A) Mohr-Coulomb failure envelope in principal stress space. B) Mohr-Coulomb with Rankine tensile corner (modified from Rockfield (2014)).

MODIFIED CAM-CLAY (SR3) FAILURE MODEL

The SR3 failure model in ELFEN is a modified CAM-Clay model based on critical state soil mechanics (Roscoe et al., 1958; Muir Wood, 1990). The model is a single surface, porous elasto-plastic, rate-independent, and non-associated constitutive law (Crook et al., 2006; Rockfield, 2014). The yield surface (Figure A.3) is a smooth surface that intersects the hydrostatic axis in both tension and compression and is defined by the following equation:

$$\phi\,(\sigma, \varepsilon_v^P) = g(\theta, p)q + (p - p_t)tan\beta\,(\frac{p-p_c}{p_t-p_c})^{1/n} \qquad (4)$$

Where p is the effective stress, q is the deviatoric stress, θ is the lode angle, p_t is the yield surface tensile intercept with the hydrostatic axis, p_c is the pre-consolidation pressure (compressive intercept of the yield surface with the hydrostatic axis), β and n are material constants that controls the shape of the yield surface in the p-q plane and g(θ, p) is a function that controls the shape of the yield surface in the deviatoric plane.

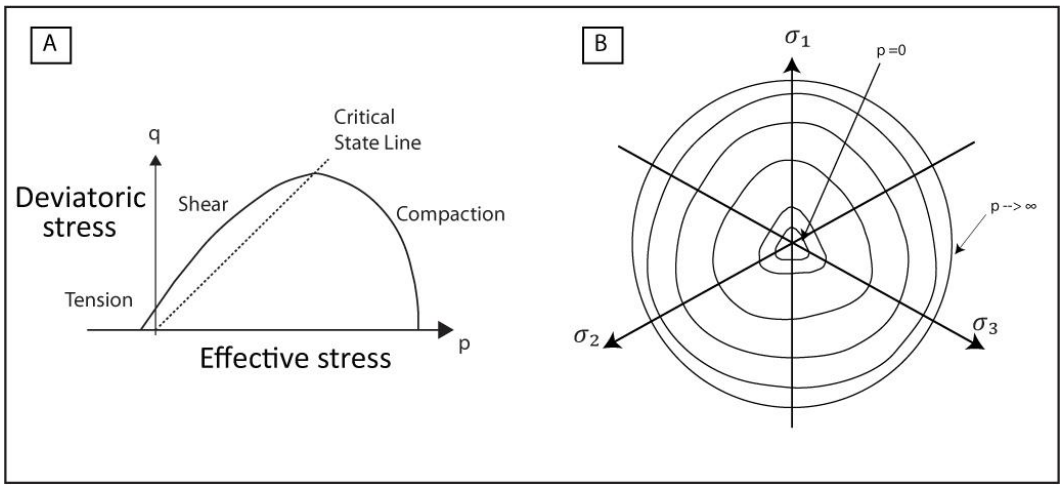

Figure A.3: (A) Modified CAM-Clay yield surface in p-q plane. (B) Modified CAM-Clay yield surface geometry with variable effective stress in principal stress plane. (After Rockfield, 2014).

The evolution of the yield surface of the Modified CAM-Clay model is controlled by the void ratio and the plastic volumetric strain through a piecewise linear hardening or softening law. Initialization of the yield surface can be either defined by the initial pre-consolidation pressure or in terms of initial porosity. Parameters controlling the evolution of the yield surface can be calibrated to laboratory test results (e.g., Nygård et al., 2004; Nygård et al., 2006; Mondol et al., 2007; Graham et al.,). Four types of failure is possible in the Modified CAM-Clay model depending on the stress state (effective and deviatoric stresses) including: compressive plastic yielding (i.e., compaction), shear/dilation, critical-state, and tensile failure (Figure A.3). For more information about the SR3 Modified CAM-Clay model refer to Rockfield (2014).

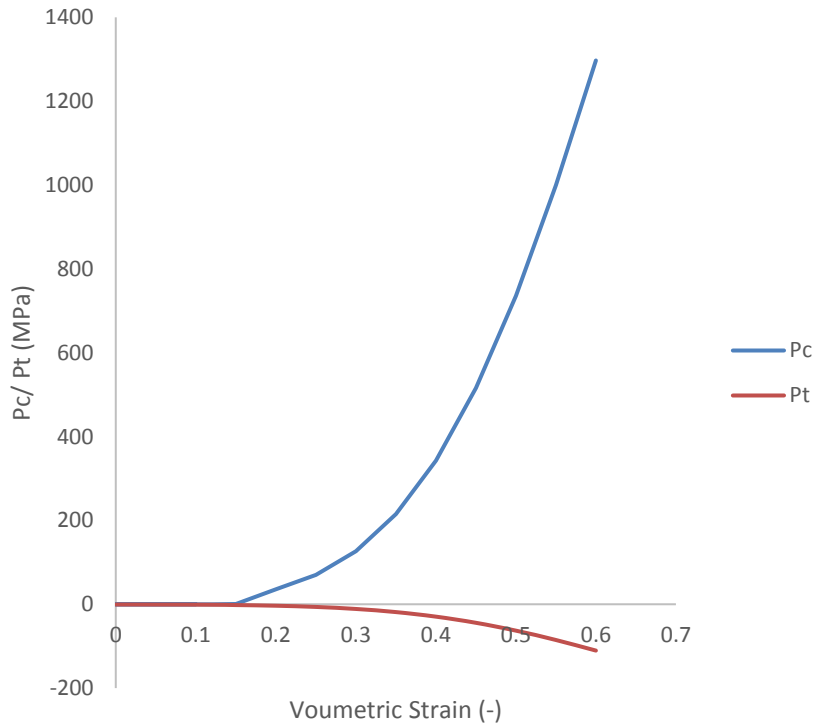

Figure A.4: Hardening curve used for the SR3-cam clay model modified from (Rockfield, 2014). Pc = Pre-consolidation pressure, Pt = tensile intercept.

Appendix B: Additional Fracture Interpretation from Yucca and Dry Canyons

High-resolution Photopanoramas Fracture Interpretation

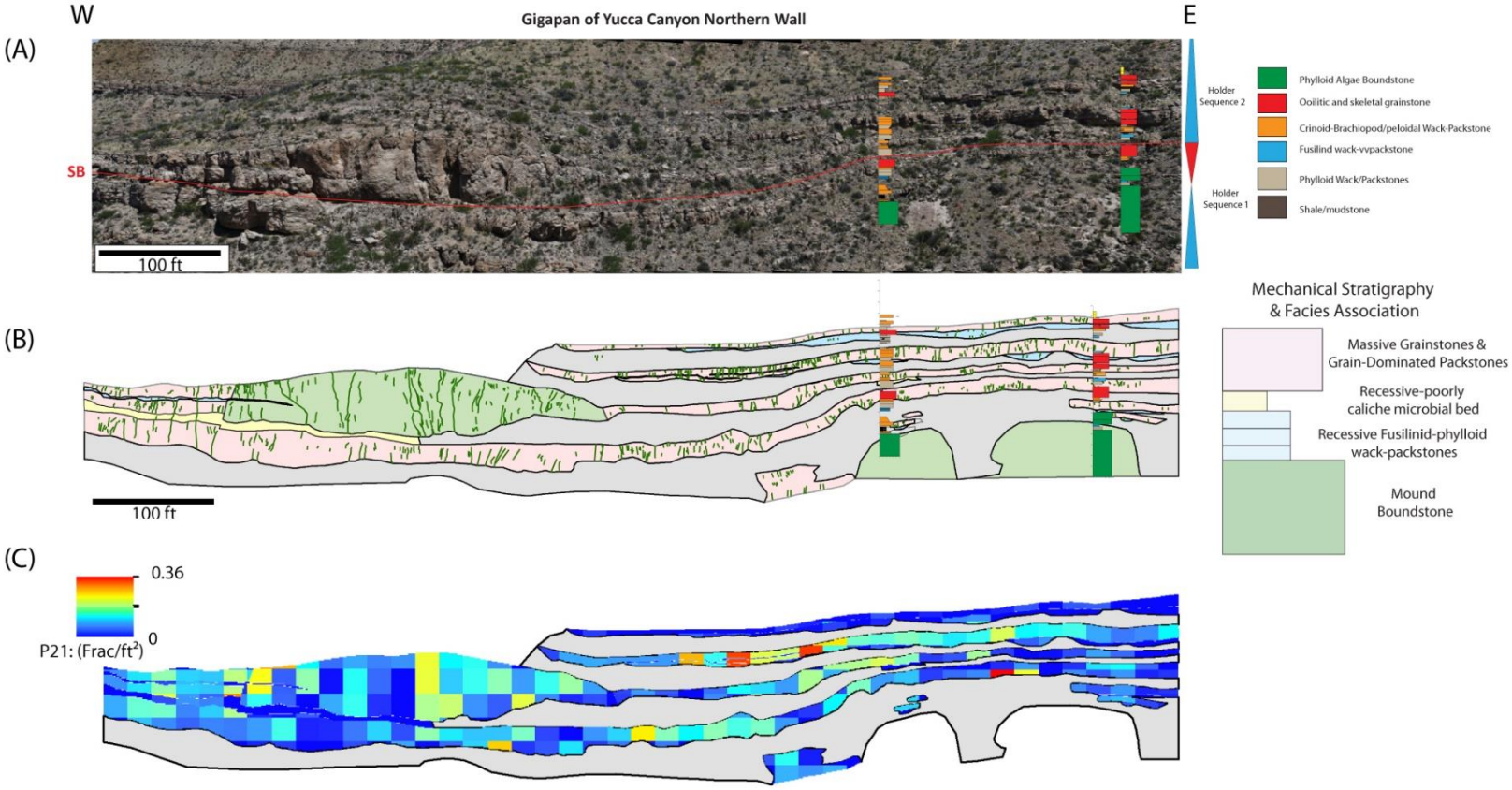

Yucca Canyon Southern Wall

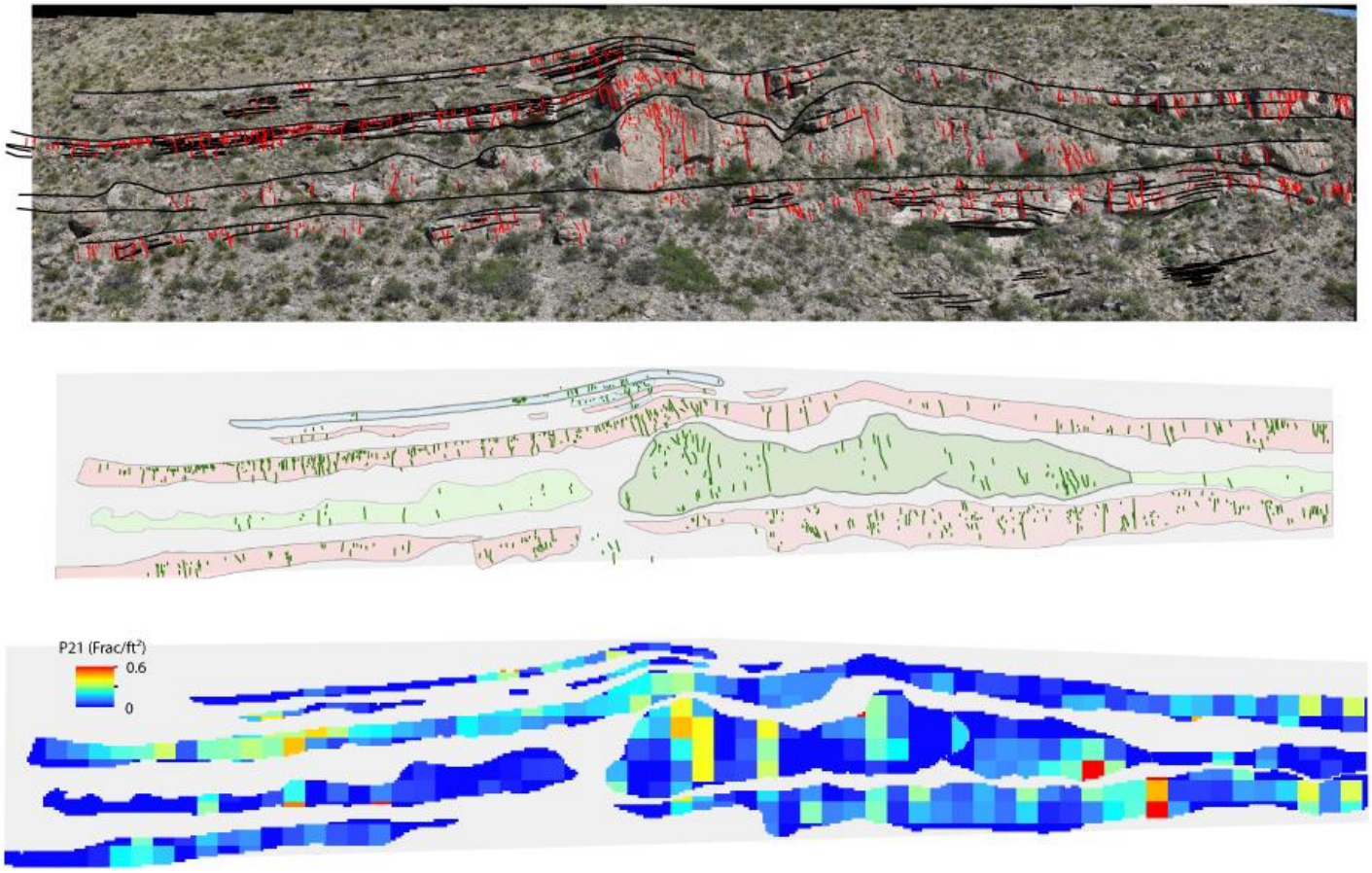

Dry Canyon

#	Frac azimuth	unit	fill	Aperture (mm)	n	lithology	bed bound	Notes
1	358	Y1	silt/sand	50	1	massive phylloid packstone	y	
2	005	Y1	caliche filled calcite lined	3	4	massive phylloid packstone	y	
3	310	Y1	calcite	2	2	massive phylloid packstone	y	
4	050	Y1	calcite	1	1	massive phylloid packstone	y	
5	010	Y1	Calcite + caliche	10	2	massive phylloid packstone	y	
6	315	Y1	caliche +some calcite	1	1	massive phylloid packstone	y	
7	015	Y1	caliche +some calcite	1	1	massive phylloid packstone	y	
8	315	Y1	calcite	10	1	massive phylloid packstone	y	
9	315	Y1	calcite lined	1	1	massive phylloid packstone	y	
10	020	Y1	caliche lined	3-5	5	massive phylloid packstone	y	
11	030	Y1	caliche lined	3-5	5	massive phylloid packstone	y	
12	010	Y1	calcite +caliche	3-5	7	massive phylloid packstone	y	
13	030	Y3	calcite	3	1	nodular to debris wackestone-packstone	n	under LR2
14	330	Y3	calcite	30	1	nodular to debris wackestone-packstone	n	under LR2
15	020	LR1	calcite	1-3	4	Leopard rock 1	?	
16	040	LR1	calcite	1-2	3	Leopard rock 1	?	
17	340	LR1	calcite?	3	1	Leopard rock 1	?	irregular strike
18	010	LR1	calcite	1-3	7	Leopard rock 1	?	
19	350	Y8	?	1-2	2	fusilinid brachiopod packstone	y	3 beds overlying LR3
20	030	Y8	?	1	2	fusilinid brachiopod packstone	y	3 beds overlying LR3/ irregular stike

#	Frac azimuth	unit	fill	Aperture (mm)	n	lithology	bed bound	Notes
21	290	Y8	?	1	2	fusilinid brachiopod packstone	y	3 beds overlying LR3/ irregular stike
22	340	Y8	calcite	3	1	fusilinid brachiopod packstone	n	3 beds overlying LR3
23	030	Y8	calcite	1	1	fusilinid brachiopod packstone	n	3 beds overlying LR3
24	055	UYM	calcite	1-3	3	phylloid wackestone (boundstone)	?	
25	050	UYM	calcite/ caliche?	1-2	3	phylloid wackestone (boundstone)	?	
26	005	UYM	calcite	5	2	phylloid wackestone (boundstone)	?	
27	105	UYM	calciche?	3	2	phylloid wackestone (boundstone)	?	
28	130	UYM	caliche?	3	1	phylloid wackestone (boundstone)	?	
29	010	UYM	calcite potentially lined with caliche?		1	phylloid wackestone (boundstone)	?	
30	045	UYM	calcite lined caliche filled?	5	5	phylloid wackestone (boundstone)	?	
31	065	UYM	caliche filled	1-5	5	phylloid wackestone (boundstone)	?	pic (6:08 pm)
32	350	GS1?	silt/sand	50	1	grainstone	Y	pic 4:20 pm - grainstone directly above UYM flank

#	Frac azimuth	unit	fill	Aperture (mm)	n	lithology	bed bound	Notes
33	075	LR4	clay?	1-3	1	microbial boundstone	Y	irregular strike
34	010	LR4	calcite	1-2	5	microbial boundstone	?	
35	015	LR4	calcite	1-3	8	microbial boundstone	?	cross-cuts 075 (frac 34)
36	055	LR4	calcite	1	2	microbial boundstone	?	
37	030	LR4F1	calcite	1-20	7	fusilinid brachiopod packstone-wackestone	Y	bounded by shale layer
38	030	LR4F2	calcite	1-10	8	fusilinid brachiopod packstone-wackestone	?	
39	030	LR4-syrng	calcite	1-3	4	syrngoporids boundstone	?	
40	015	LR4-syrng	calcite	1-3	2	syrngoporids boundstone	?	
41	060	LYM	calcite	3-20	2	phylloid dasycladan algae boundstone	?	lower yucca mound
42	020	LYM	calcite? (weathered)	1-3	6	phylloid dasycladan algae boundstone	?	lower yucca mound
43	018	LYM	calcite?	1-5	7	phylloid dasycladan algae boundstone	?	lower yucca mound
44	295	LYM	calcite	1-3	3	phylloid dasycladan algae boundstone	?	lower yucca mound
45	350	LYM	caliche or iron stained calcite	1	1	phylloid dasycladan algae boundstone	y	lower yucca mound
46	000	LYM	silt/sand	10-20	1	phylloid dasycladan algae boundstone	y	lower yucca mound

#	Frac azimuth	unit	fill	Aperture (mm)	n	lithology	bed bound	Notes
47	005	LYM	calcite reddish fill	3-10	2	phylloid dasycladan algae boundstone	?	lower yucca mound
48	010	LYM	silt/sand	2-7	1	phylloid dasycladan algae boundstone	?	irregular strike
49	275	LYM	calcite	1	2	phylloid dasycladan algae boundstone	?	lower yucca mound
50	030	LYM	calcite	1-7	3	phylloid dasycladan algae boundstone	?	lower yucca mound
51	035	UYM-fl	calcite	3-8	5	phylloid algae wakestone	N	upper yucca mound back flank
52	010	UYM-fl	calcite	2-4	8	phylloid algae wakestone	?	top of upper yucca eastern flank
53	290	UYM-fl	calcite	1-2	3	phylloid algae wakestone	?	top of upper yucca eastern flank
54	030	Frac-YD	calcite	2-5	2	nodular wackestone-GDP-GS on top	N	yucca drainage throughgoing fracs
55	050	Frac-YD	calcite	2-5	4	nodular wackestone-GDP-GS on top	N	yucca drainage throughgoing fracs
56	305	Frac-YD	calcite	2-5	1	nodular wackestone-GDP-GS on top	N	yucca drainage throughgoing fracs
57	010	FRC-YD3	silt	1-5	3	grainstone	Y	yucca drainage gs below sb1
58	025	FRC-YD3	calcite	2	3	grainstone	Y	yucca drainage gs below sb1
59	275	FRC-YD3	silt	1-4	4	grainstone	Y	yucca drainage gs below sb1

#	Frac azimuth	unit	fill	Aperture (mm)	n	lithology	bed bound	Notes
60	255	FRC-YD3	silt	2	1	grainstone	Y	yucca drainage gs below sb1
61	030	FRC-YD3	calcite	1	1	grainstone	Y	yucca drainage gs below sb1
63	035	FRC-YD4	calcite	1-2	3	GDP	?	in gdp below sb2
64	025	SD9	calcite	2-8	2	foram skeletal brack wackestone	?	
65	030	FRC-NY1	calcite	1-2	1		Y	
66	030	FRC-NY2	calcite	10	4		?	
67	345	FRC-NY2	caliche?	3	3		?	large scale
68	020	FRC-NY3	calcite	1-10	4	MDP-GDP-GS	N	throughgoing
69	025	FRC-NY4	silt	10-50	1	GS	Y	directly below sb1
70	030	SD16	calcite	1-4	5	phylloid boundstone	Y	lowest twin mound flank
71	310	SD16	calcite	1	2	phylloid boundstone	Y	lowest twin mound flank
72	040	SD16	calcite	1-10	7	phylloid boundstone-underlying wackestone	N	lowest twin mound
73	335	FRC-NY5	some silt? (not clear)	300-900	1	phylloid boundstone	Y	large fissure in mound (mound bound)

#	Frac azimuth	unit	fill	Aperture (mm)	n	lithology	bed bound	Notes
74	290	FRC-NY5	some silt? (not clear)	300-900	1	phylloid boundstone	Y	large fissure in mound (mound bound)
75	070	FRC-NY5	?	50	1	phylloid boundstone	Y	large fissure in mound (mound bound)
76	350	FRC-NY5	?	50	1	phylloid boundstone	Y	large fissure in mound (mound bound)
77	030	FRC-NY6	calcite	1-3	12	massive skeletal grainstone	?	
78	010	FRC-NY7	?	30-150	1	phylloid boundstone	Y	mound bound
79	325	FRC-NY8	calcite	30-60	1	phylloid boundstone	Y	large fracture in upper twin mound
80	290	FRC-NY9	silt	10	1	grainstone	Y	below SB1 grainstone
81	010	FRC-NY10	calcite	1	2	grainstone	?	cross cuts silt patch overlying grainstone below sb1

#	Frac azimuth	unit	fill	Aperture (mm)	n	lithology	bed bound	Notes
82	015	SD21	calcite	1-5	8	wack-pack	?	wack-pack overlying middle mound
83	015	FRC-NY11	reddish fill with occasional white calcite in the middle	1-5	13	phylloid boundstone	?	middle mound western exposure
84	280	FRC-NY11	calcite	1-4	7	phylloid boundstone	?	cross cuts 10-20 subhorizontal
85	035	FRC-NY11	?	3-5	2	phylloid boundstone	?	cross cut by 005-010
86	045	FRC-NY11	?	3-5	2	phylloid boundstone	?	cross cut by 005-010
87	295	FRC-NY12	dark colored silt fill	2-20	3	grainstone	?	3 pm @04/16/2016 pic
88	045	FRC-NY13	calcite	1-5	6	grainstone	Y	
89	350	FRC-NY14	silt	10-50	1	grainstone	Y	cross cut by the below frac i.e. 030

#	Frac azimuth	unit	fill	Aperture (mm)	n	lithology	bed bound	Notes
90	030	FRC-NY14	calcite	1-2	6	grainstone		
91	065	FRC-NY15	brown to yellow silt	10-30	1	grainstone	Y	cross cut by the below frac i.e. 025
92	025	FRC-NY15	calcite	1-10	30	grainstone	N	
93	035	FRC-NY16	calcite	30-50	1	massive phylloid packstone	?	equivellent to the upper twin mound filled with large calcite crystals
94	280	FRC-NY17	silt	10	1	GDP bellow Sb1	Y	cross cut by below frac 015
95	015	FRC-NY17	calcite	1-2	2	GDP bellow Sb1	?	
96	030	ML-FRC1	silt and breccia	10-30	1	phylloid mound	Y?	strike changes from 30-350
97	020	ML-FRC1	calcite	1-3	7	phylloid mound	?	

#	Frac azimuth	unit	fill	Aperture (mm)	n	lithology	bed bound	Notes
98	040	ML-FRC1	calcite	1-3	7	phylloid mound	?	
99	330	MR-sch	calcite	1	5	fissile shale	N	throughgoing potentially in the beeman

Table B.1: Summary of fracture data collected in the field in Yucca Canyon, Sacramento Mountains, New Mexico. n = number of fractures measured.

INTERPRETED FRACTURES SPATIAL ANALYSIS

Increase in 5-meter binned fracture intensity of fractures interpreted on photopanormas was confirmed using the normalized fracture intensity method using Marrett et al. (2018) code. The code was also used to examine trends in fracture spatial distribution using the normalized correlation count method. Refer to Marrett et al. (2018) for further explanation on these methods and graphs interpretation.

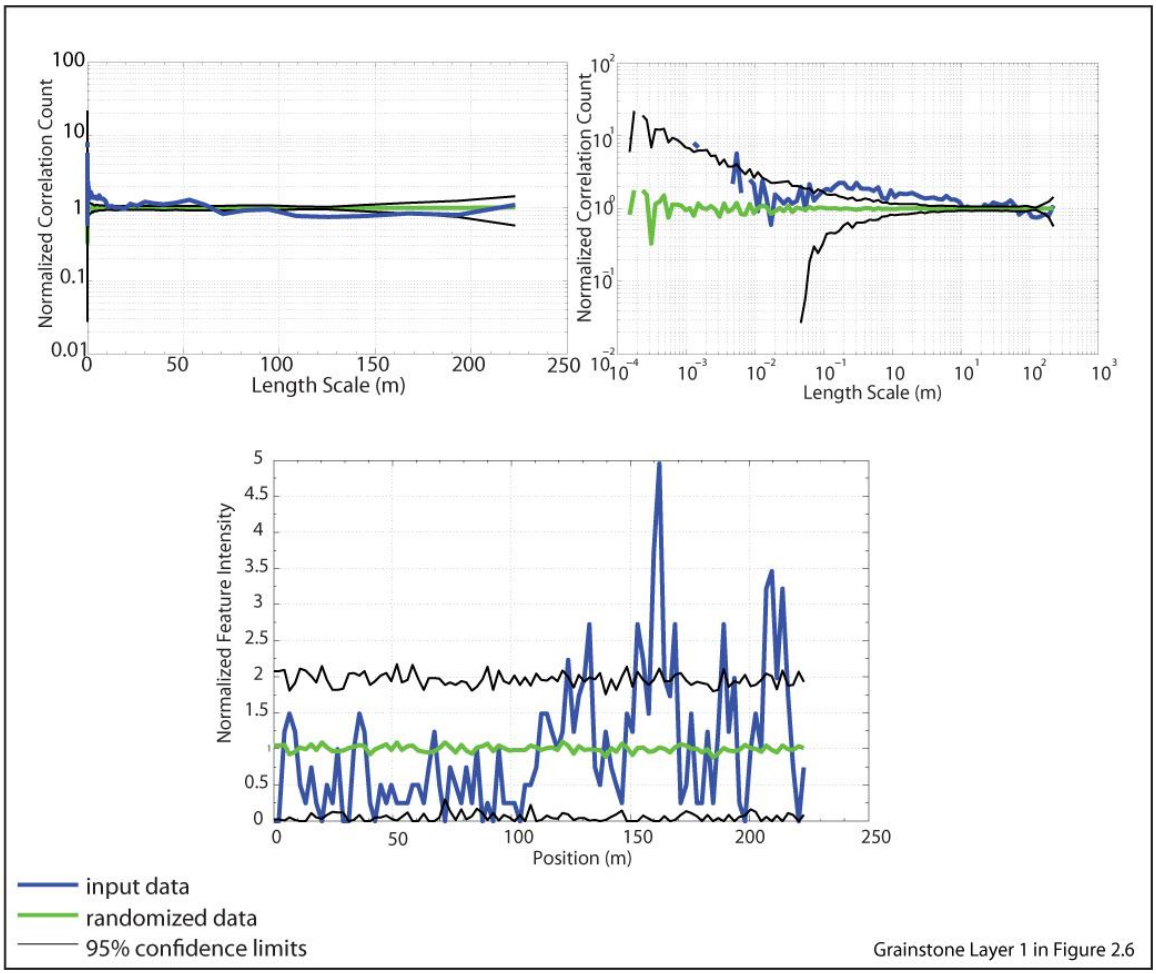

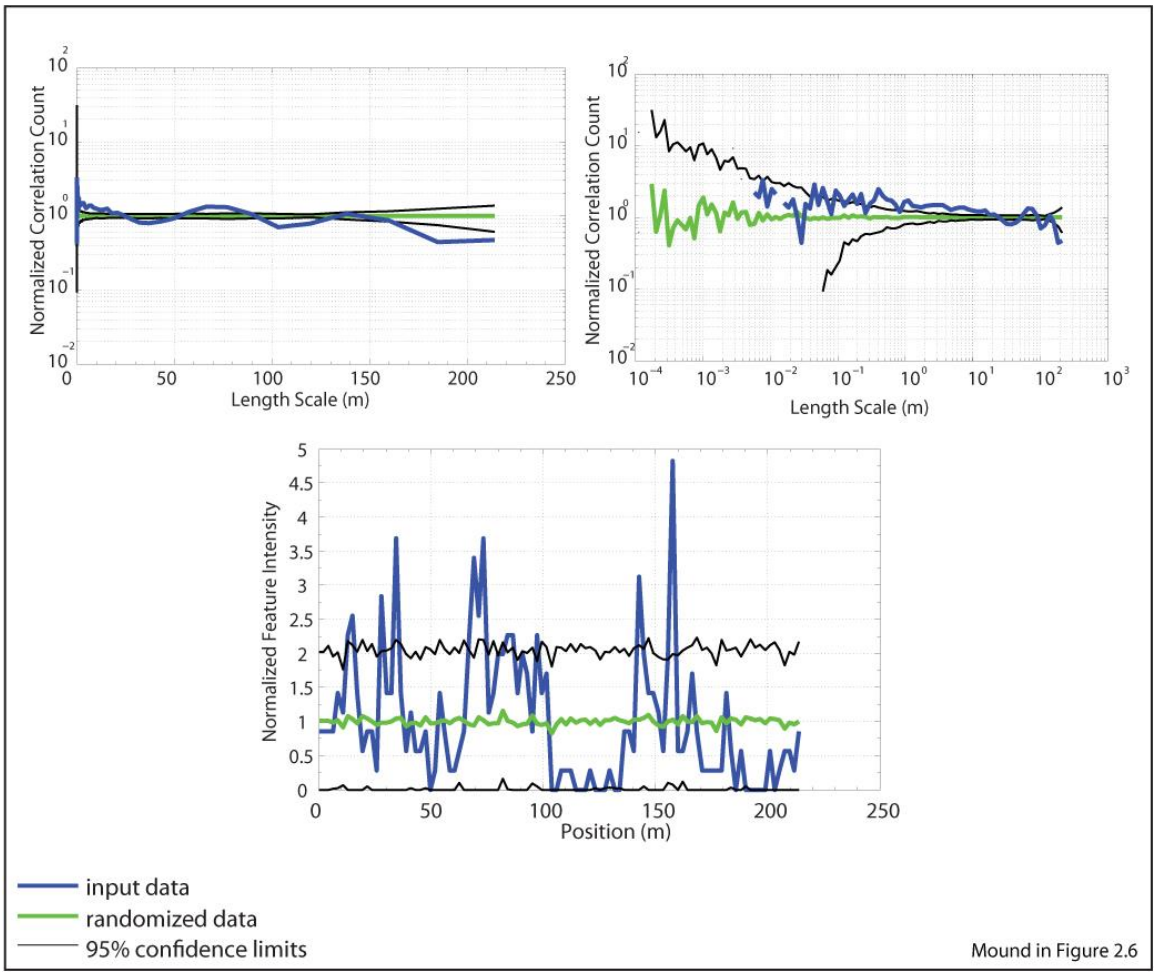
Normalized Correlation Count
Length Scale (m)
Normalized Correlation Count
Length Scale (m)
Normalized Feature Intensity
Position (m)
input data
randomized data
95% confidence limits
Mound in Figure 2.6

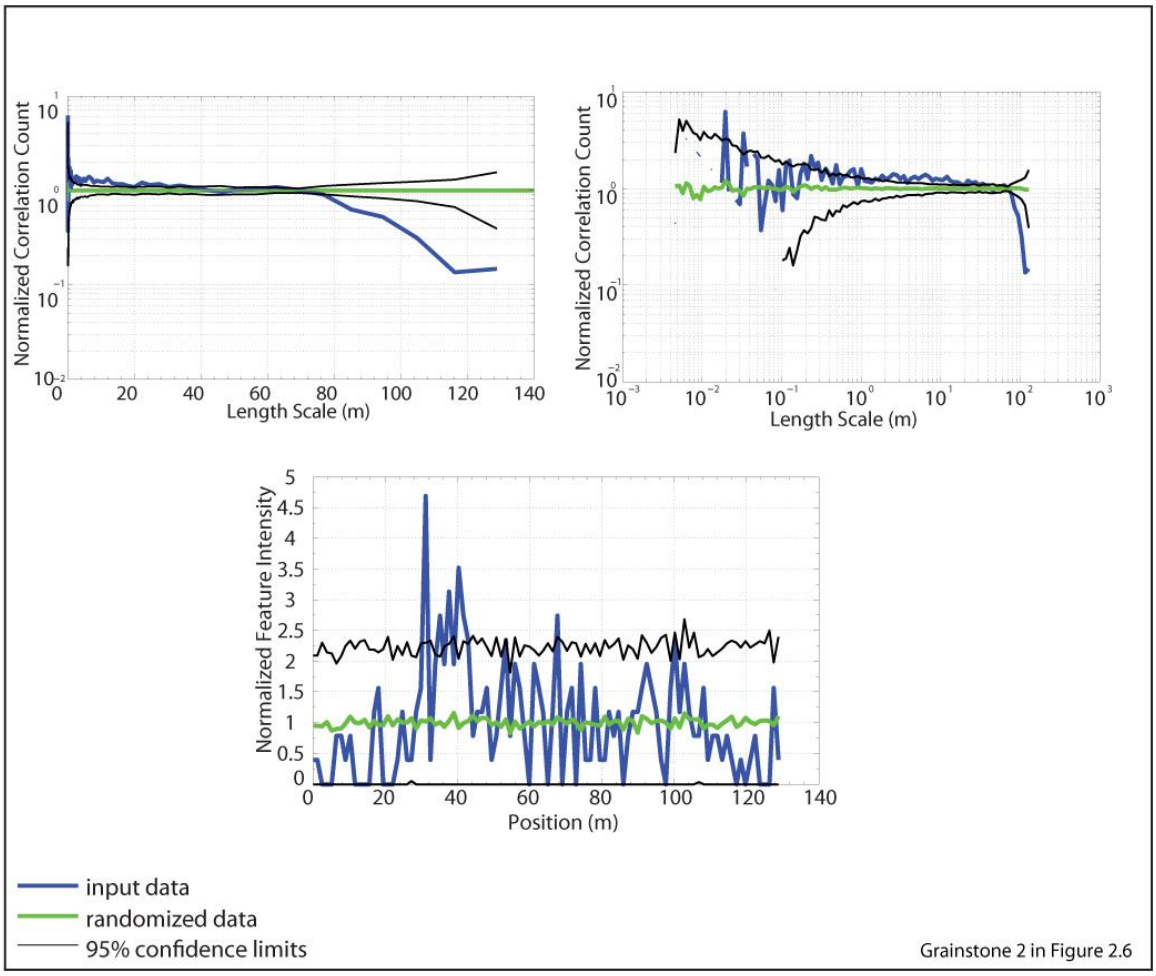
Normalized Correlation Count
Length Scale (m)
Normalized Correlation Count
Length Scale (m)
Normalized Feature Intensity
Position (m)
input data
randomized data
95% confidence limits
Grainstone 2 in Figure 2.6

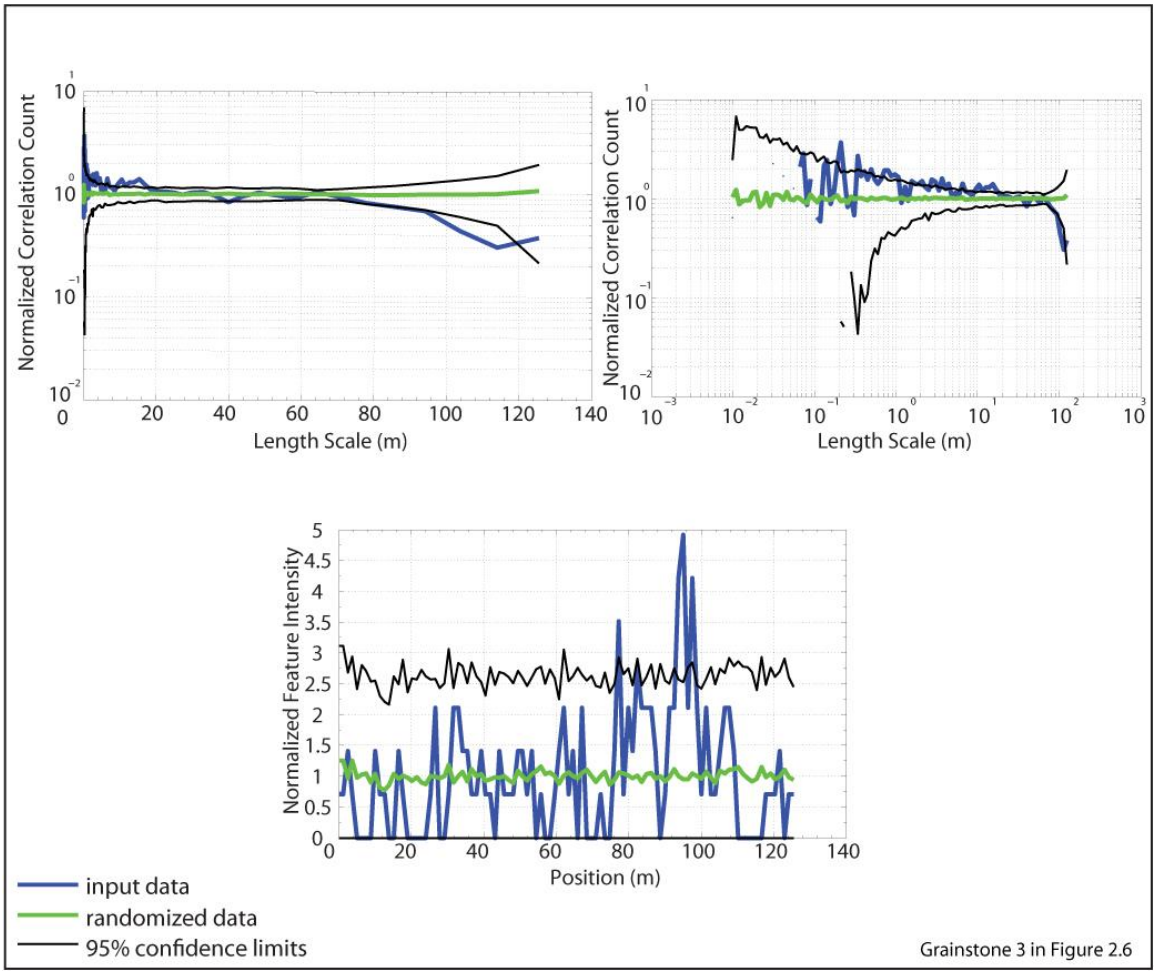
Normalized Correlation Count
Length Scale (m)
Normalized Correlation Count
Length Scale (m)
Normalized Feature Intensity
Position (m)
input data
randomized data
95% confidence limits
Grainstone 3 in Figure 2.6

Appendix C: Mechanical Properties Measurements

MECHANICAL PROPERTIES CALCULATIONS

Uniaxial unconfined compressive test

Uniaxial unconfined compressive tests were conducted on Pennsylvanian carbonate samples from the Holder formation (Sacramento Mountains, New Mexico) to quantify mechanical properties of different carbonate facies. The testing procedures followed ASTM-D7012. The test yields several parameters including the unconfined compressive strength, Young's modulus, and several other properties can be calculated including Poisson's ratio, bulk modulus, and shear modulus. In the following a brief summary of how each parameter was recorded/calculated.

UCS: peak stress

Young's modulus (E): Linear elastic slope of the stress-axial strain curve

Poisson's ratio: $\upsilon = -\frac{Lateral\ (transverse) strain}{Axial\ Strain}$

Bulk modulus: $K = \frac{E}{3(1-2\upsilon)}$

Shear modulus: $G = \frac{E}{2(1+\upsilon)}$

Brazilian (indirect tensile strength) Test

Brazilian tests were conducted on Pennsylvanian carbonate samples from the Holder Formation (Sacramento Mountains, New Mexico) to quantify tensile strength of different facies. In addition, three grainstone samples from Pleistocene outcrops (~400 ka) in West Caicos Island, British West Indies were used to quantify tensile strength of a modern example. The Brazilian tests were conducted following ASTM D3967-08. Tensile strength (T_0) is calculated using the following equation:

$T_0 = \frac{2\times Force}{\pi\times Length\times Diameter}$

Figure C.1: Upper left: uniaxial unconfined test. Upper right: Brazilian test. Bottom: Autolab 1000 equipment used for testing.

DATA SUMMARY

The following table summarizes all mechanical properties collected using the aforementioned testing methods. High-resolution full slide photomicrographs were used for petrographic analysis. Samples are sorted by Dunham's Classification.

Sample	UCS (MPa)	E (GPa)	ν	K (GPa)	G (GPa)	Avg Tensile Strength (MPa)	Facies	Dunham	Strain data quality
YS_11_LYM	72.11	56.10	0.28	43.29	21.84	2.39	Lower Yucca Phylloid Boundstone	Boundstone	good
YS_LR3	74.49	67.19	0.29	52.57	26.10	3.25	Microbial Boundstone	Boundstone	good
YS_36	114.39	69.32	0.27	49.86	27.33	4.00	Upper Yucca Phylloid Boundstone	Boundstone	good
YS_11_LYM_B	91.68	67.54	0.35	77.23	24.94			boundstone	good
YS_27	22.35						Microbial peloidal GDP	GDP	
YS_25	54.92	41.95	0.35	46.08	15.56	3.55	skeletal GDP	GDP	good
YS_25B	92.39	43.19	0.17	22.01	18.41		skeletal GDP	GDP	good
YS_32	80.72	36.51	~~1.27~~	~~-7.92~~	~~8.05~~	1.91	phylloid algae GDP	GDP	Invalid lateral strain data
YS_14	51.88		~~8.10~~	~~-9.99~~	~~25.04~~	3.15	Peloidal Phylloid Grainstone	grainstone	invalid

YS_26B	80.47	63.71	0.17	31.82	27.31	1.04	Ooilitic grainstone	grainstone	good
YS_34	134.67	45.80	0.31	40.71	17.45	4.82	Skeletal grainstone	grainstone	good
Y_cor_s2	147.01	59.75	0.27	43.71	23.48	6.29	skeletal grainstone	grainstone	good
M1						4.26	Phylloid skeletal grainstone	grainstone	
SW_s1_w_caicos	4	13.30				1.08	Ooilitic grainstone (400 ka)	grainstone	
YS_14B	58.18	29.57	0.28	22.38	11.55			grainstone	good
YS_6	85.33	77.68	0.29	60.77	30.18	5.24	skeletal (brach) MDP	MDP	good
YS_23	87.96	31.51	0.24	20.59	12.66		skeletal (brach) MDP	MDP	good
YS_12	98.66	~~33.76~~	~~0.33~~	~~32.51~~	~~12.72~~	4.27	phylloid mdp	mdp	invalid
YS_38	162.60	75.27	0.31	64.70	28.81	4.28	Oncoid fusilinid phylloid MDP - GDP	mdp	good
YS_5						4.38	fusilinid mdp	MDP	
YS_8	37.30		~~1.60~~	~~-62.47~~	~~79.48~~	~~5.82~~	laminated skeletal Brachiopod MDP	MDP	invalid
YS_fl_s1	92.80	57.48	0.27	41.35	22.66	5.03	Phylloid skeletal laminated phylloid wackestone	MDP	good
YS_7	128.73	37.89	0.25	25.19	15.17	3.40	laminated limemudstone	mudstone	good

YS_13	77.67	44.89	0.20	25.15	18.67		reworked skeletal mudstone	mudstone	good
YS_37	162.6	70.43	0.27	50.20	27.81	7.40	skeletal wackestone	wackestone	good
YS_9	162.6	61.61	0.32	58.46	23.26		skeletal wackestone	wackestone	good
YS_2						4.3	Intraclast wackestone	Wackestone	

Table C.1: Mechanical properties summary

MDP/GDP: mud-/grain-dominated packstone
UCS: unconfined compressive strength
E: Young's modulus
K: Bulk modulus
G: Shear modulus
ν: Poisson's ratio

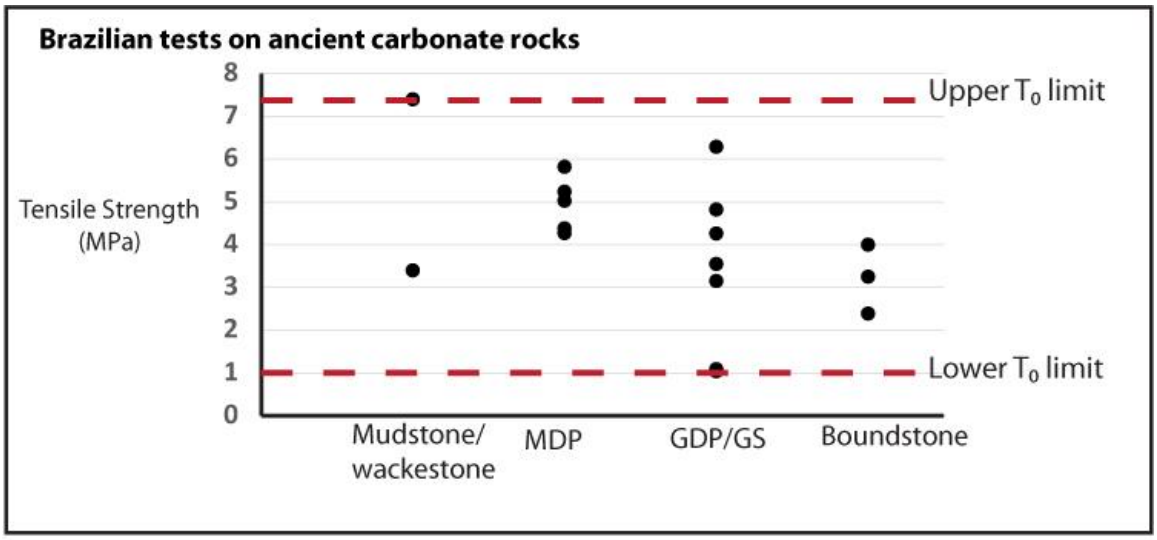
Brazilian tests on ancient carbonate rocks
Tensile Strength (MPa)
8
7
6
5
4
3
2
1
0
Upper T_0 limit
Lower T_0 limit
Mudstone/ wackestone
MDP
GDP/GS
Boundstone

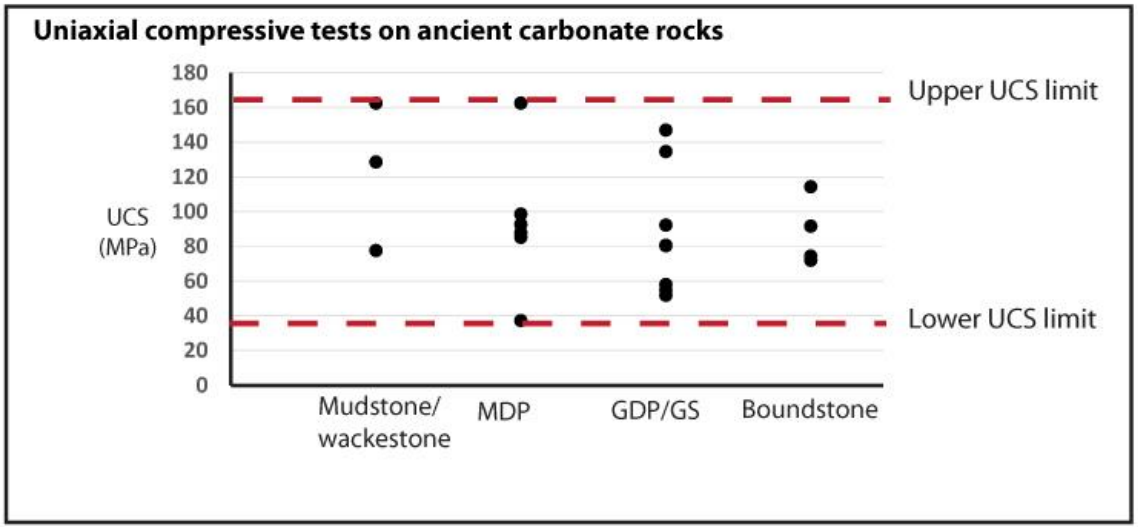
Uniaxial compressive tests on ancient carbonate rocks
UCS (MPa)
180
160
140
120
100
80
60
40
20
0
Upper UCS limit
Lower UCS limit
Mudstone/ wackestone
MDP
GDP/GS
Boundstone

POROSITY TENSILE STRENGTH RELATIONSHIP

Tensile strength tests on grainstones (from the Holder Formation) with different porosities reveal a logerthmic decrease in tensile strength with increasing porosity, however, more sampling is required to verify the validity of this relationship. The presence of partially cemented natural fractures appear to have stronger influence on tensile strength than porosity. Tensile strength of a naturally fractured Pennsylvanian grainstone with <4% porosity (sample YS_26) is equal to the tensile strength of a Pleistocene grainstone with 15% porosity (sample SW_s1_w_caicos).

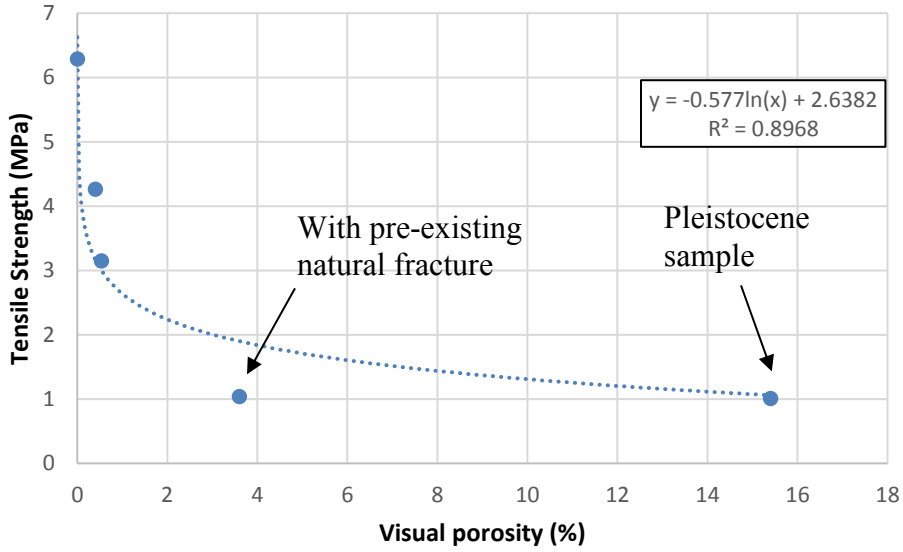

Figure C.2: Grainstone porosity versus tensile strength plot.

YS_11_LYM

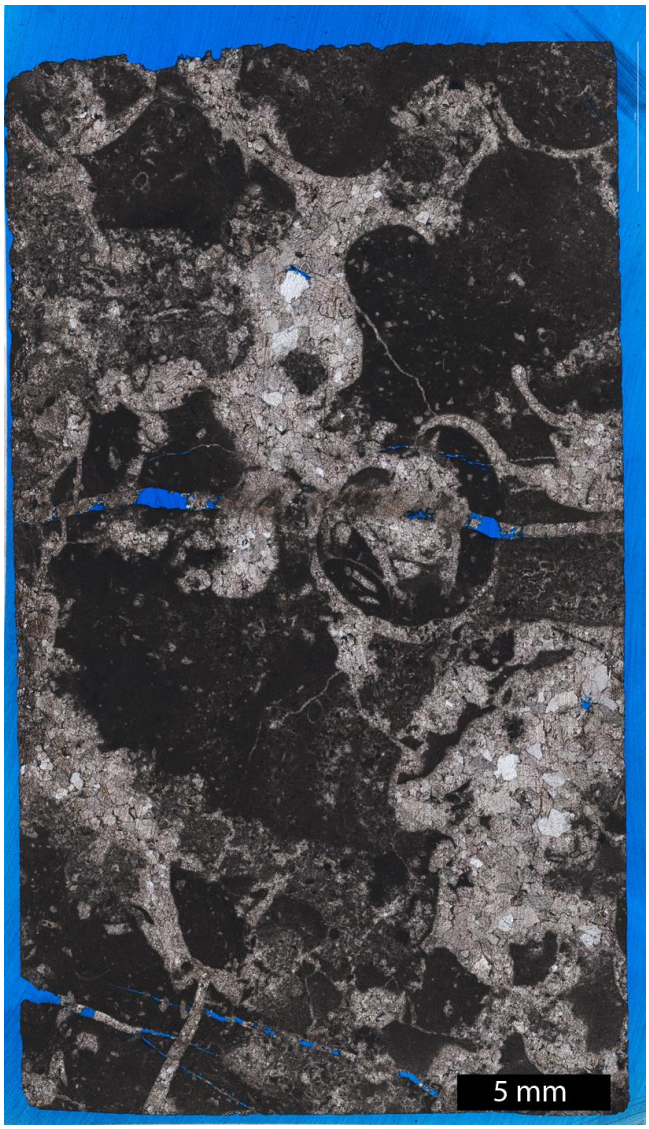

Point Counting Data

n =250 points

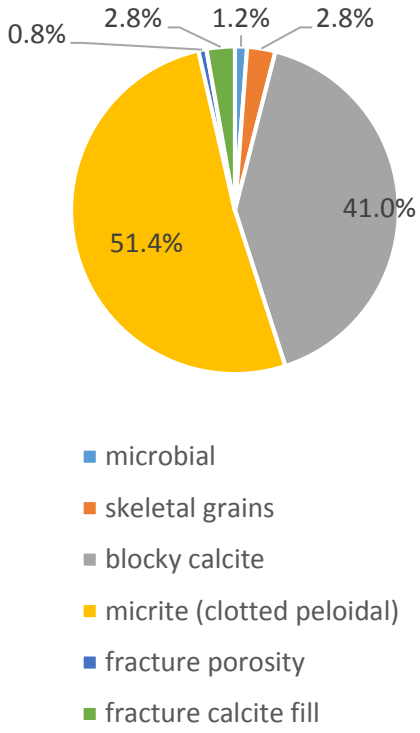

Uniaxial Unconfined Compressive Strength Test Data

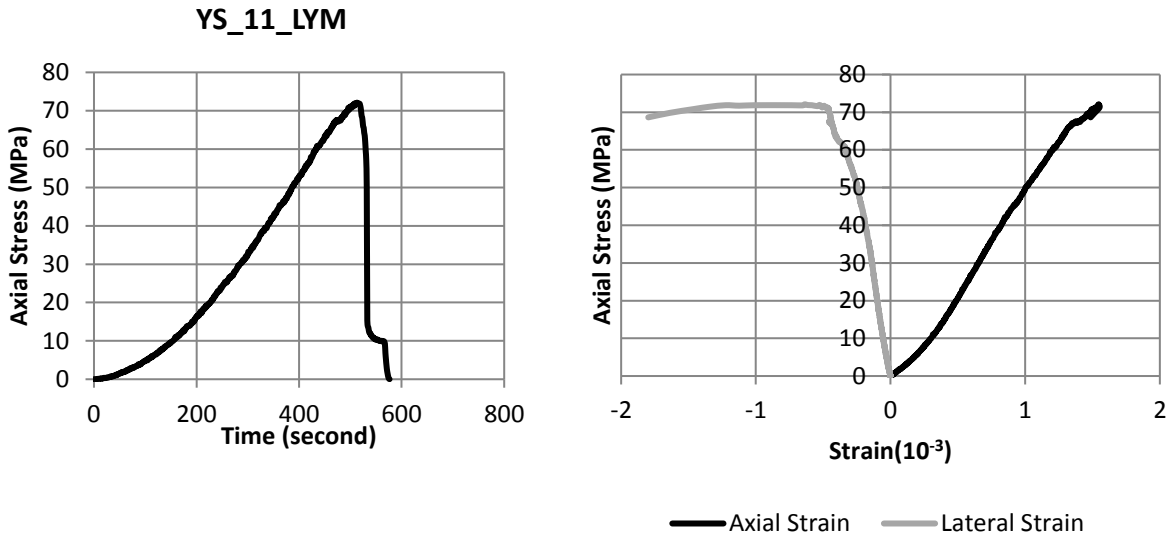

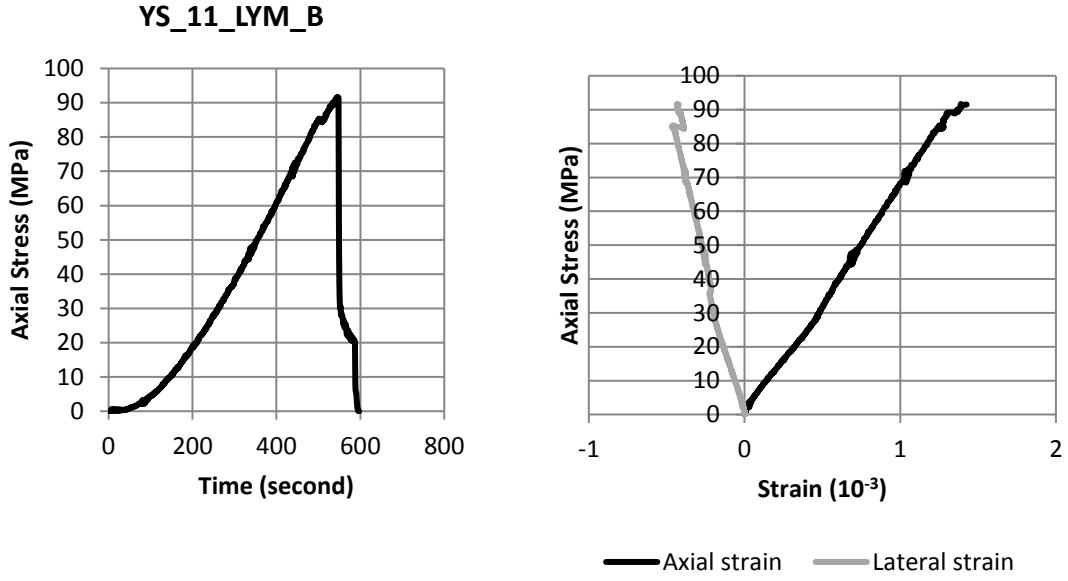

Mechanical Properties	YS_11_LYM	YS_11_LYM_B
UCS (MPa)	72.11	91.68
~75% Tangent E (GPa)	56.10	67.54
Poisson Ratio	0.28	0.35
Bulk Modulus (GPa)	43.29	77.23
Shear Modulus (GPa)	21.84	24.94

Brazilian Test Data

Sample	Diameter (mm)	Length (mm)	Peak Stress (MPa)	Force (N)	Tensile Strength (MPa)
YS_11_LYM	25.43	14.05	2.65	1344.03	**2.39**

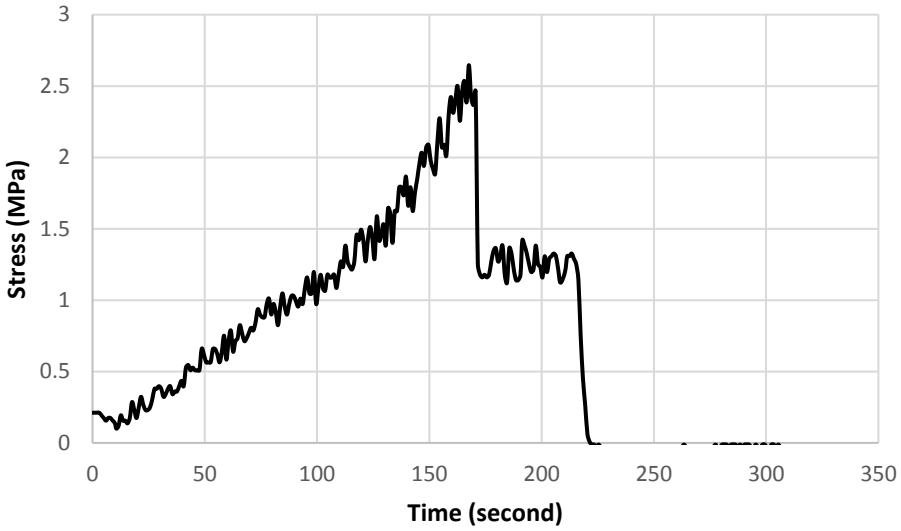

YS_LR3

Point Counting Data

n = 250 points

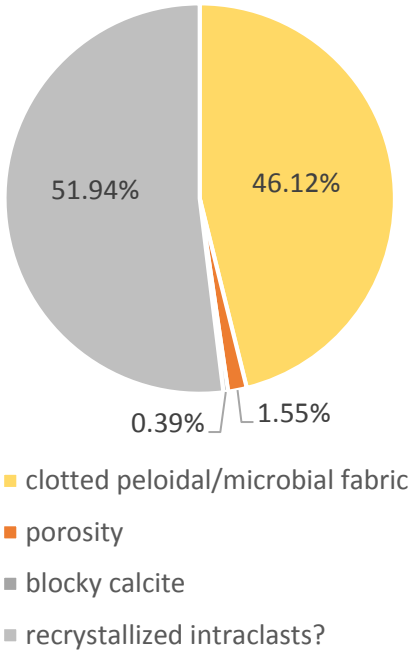

Uniaxial Unconfined Compressive Strength Test Data

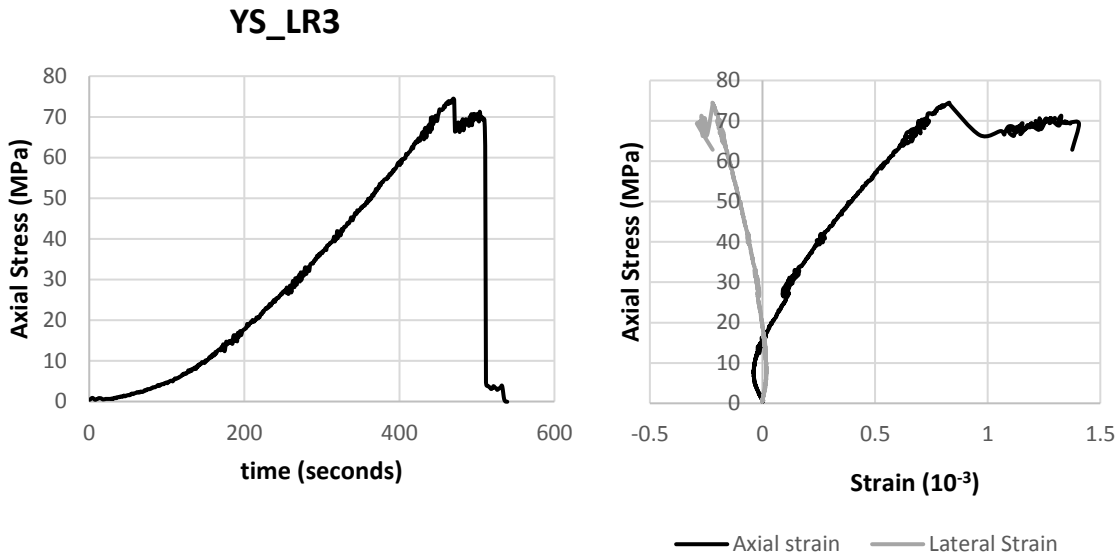

Mechanical Properties	YS_LR3
Ultimate UCS (MPa)	74.49
~75% Tangent E (GPa)	67.19
Poisson Ratio	0.29
Bulk Modulus (GPa)	52.57
Shear Modulus (GPa)	26.10

Brazilian Test Data

Sample	Diameter (mm)	Length (mm)	Peak Stress (MPa)	Force (N)	Tensile Strength (MPa)
YS_LR3	25.44	13.49	3.45	1751.32	3.25

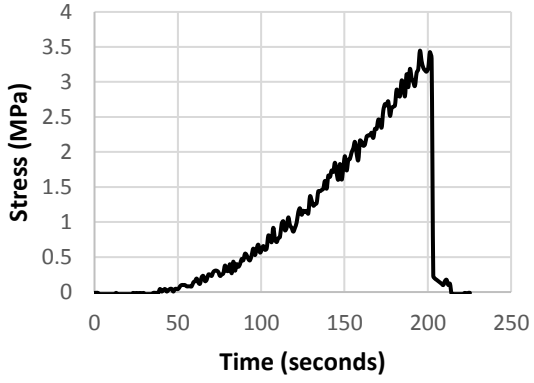

YS_36

Point Counting Data

n=250

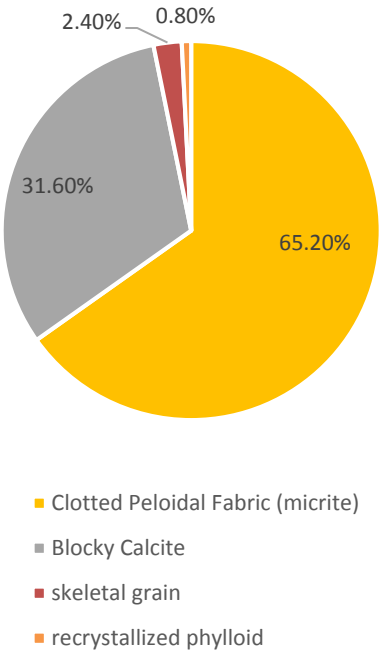

Uniaxial Unconfined Compressive Strength Test Data

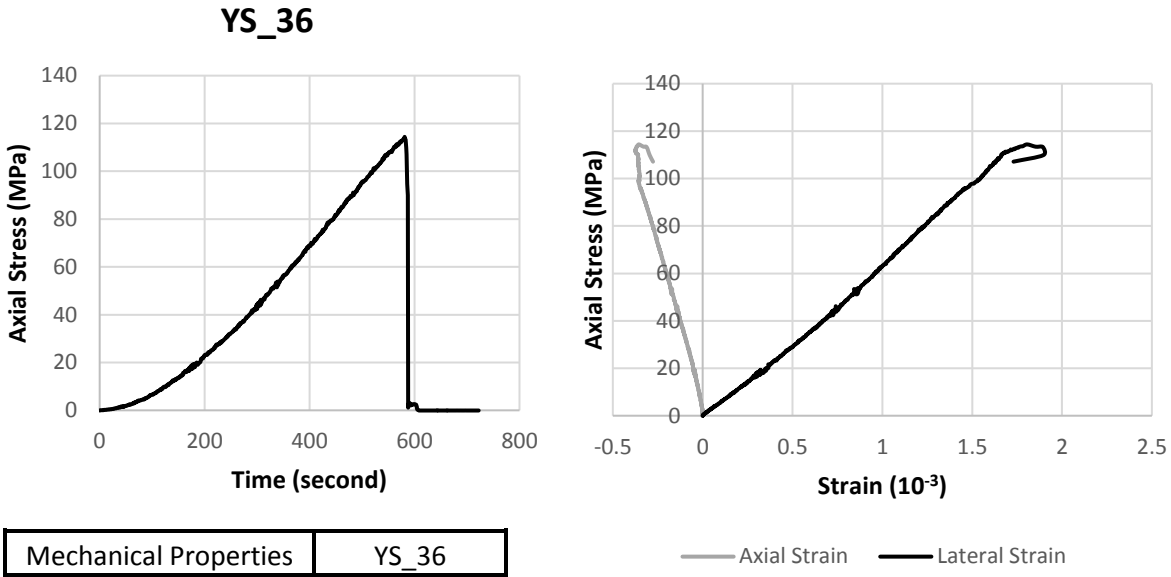

Mechanical Properties	YS_36
Ultimate UCS (MPa)	114.39
~75% Tangent E (GPa)	69.32
Poisson Ratio	0.27
Bulk Modulus (GPa)	49.86
Shear Modulus (GPa)	27.33

Brazilian Test Data

Sample	Diameter (mm)	Length (mm)	Peak Stress (MPa)	Force (N)	Tensile Strength (MPa)
YS_36	25.42	14.08	4.43	2248.47	4.00

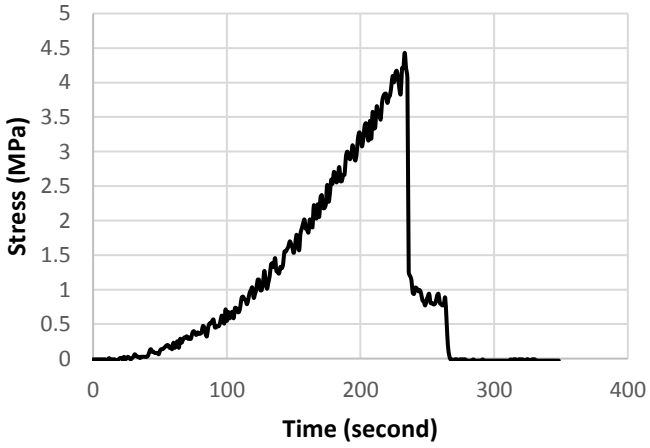

YS_27*

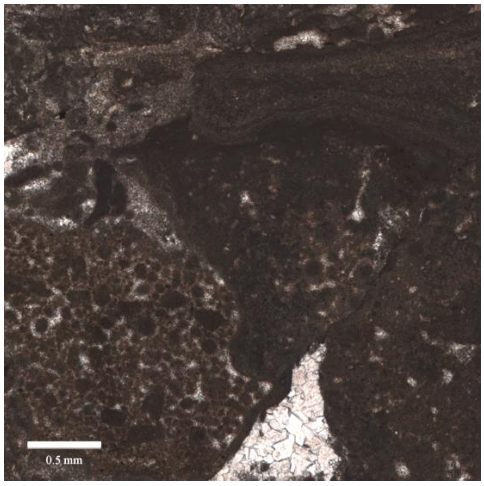

*no point counting data – peloidal microbial grain-dominated packstone

Uniaxial Unconfined Compressive Strength Test Data[φ]

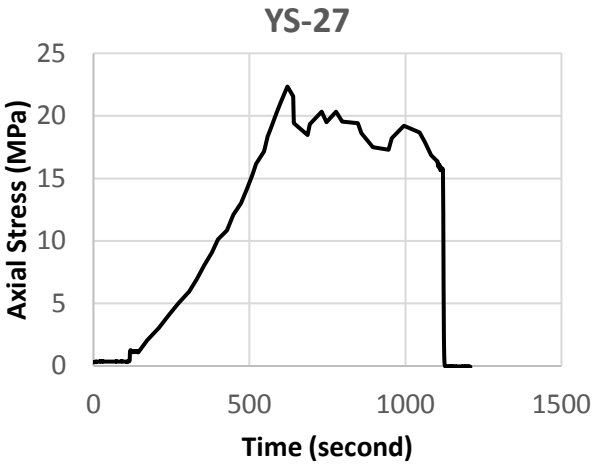

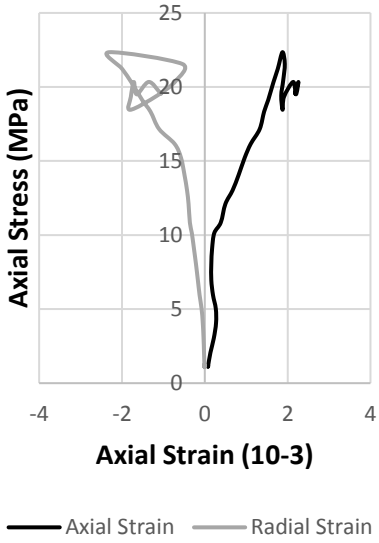

[φ] invalid strian data due to strain gauge failure

Mechanical Properties	YS_27
Ultimate UCS (MPa)	22.3465

YS-25

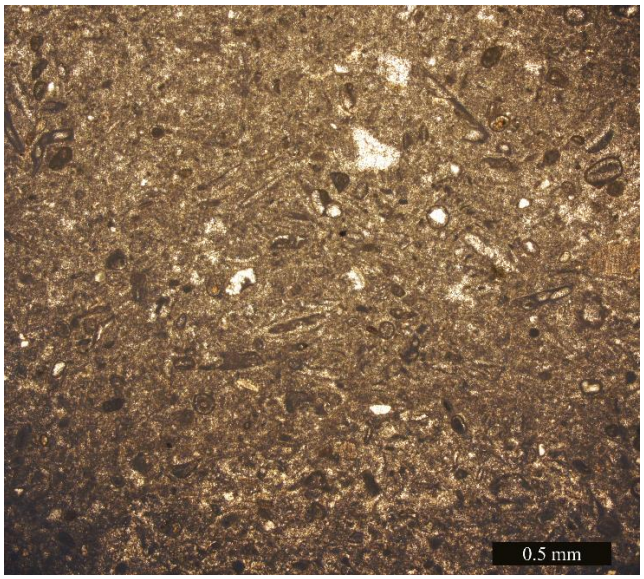

* No point counting data- phylloid skeletal grain-dominated packstone

Uniaxial Unconfined Compressive Strength Test Data

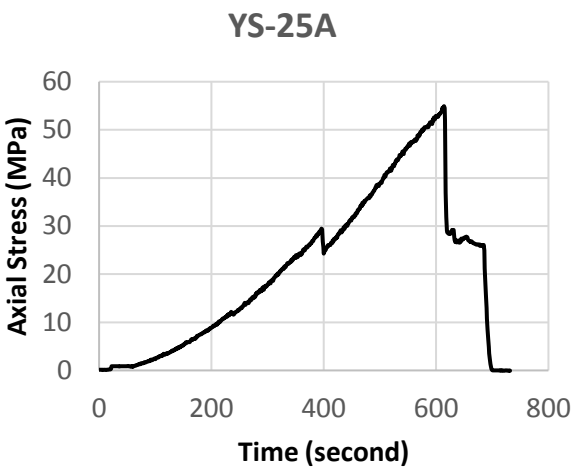

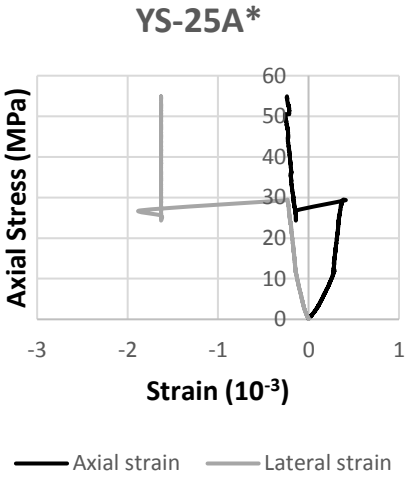

*invalid strain data due to strain gauge failure

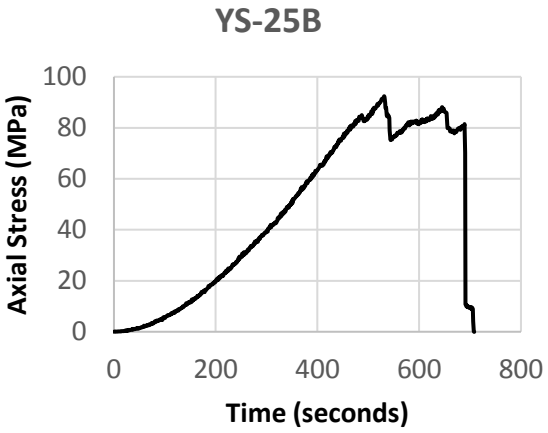

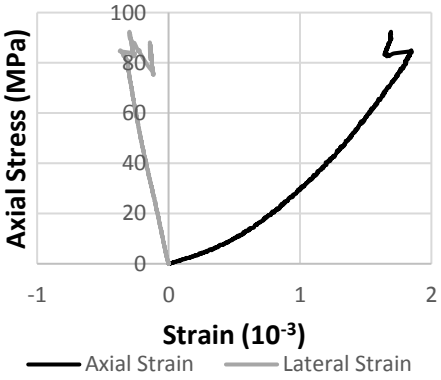

Mechanical Properties	YS_25A	YS_25B
Ultimate UCS (MPa)	54.9224	92.39
~75% Tangent E (GPa)		43.19
Poisson Ratio		0.17
Bulk Modulus (GPa)		22.01
Shear Modulus (GPa)		18.41

Brazilian Test Data

Sample	Diameter (mm)	Length (mm)	Peak Stress (MPa)	Force (N)	Tensile Strength (MPa)
25A	25.43	13.20	3.63	1844.34	3.50
25B	25.43	12.99	3.69	1872.66	3.61

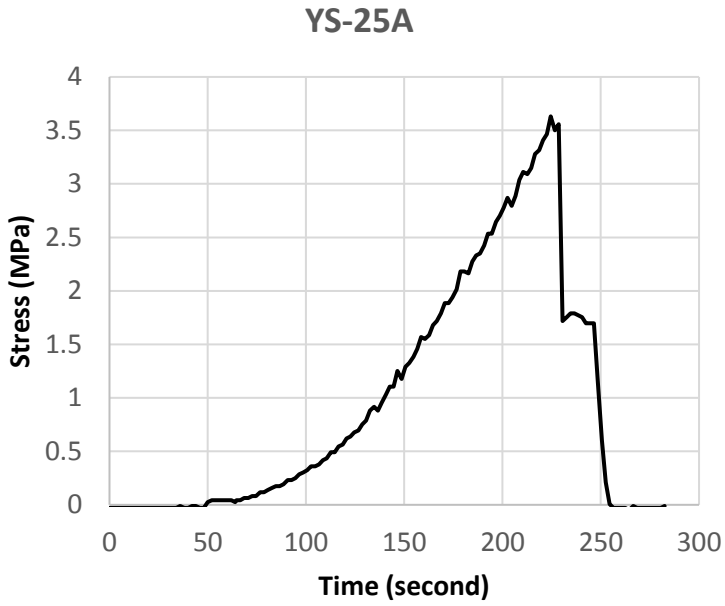

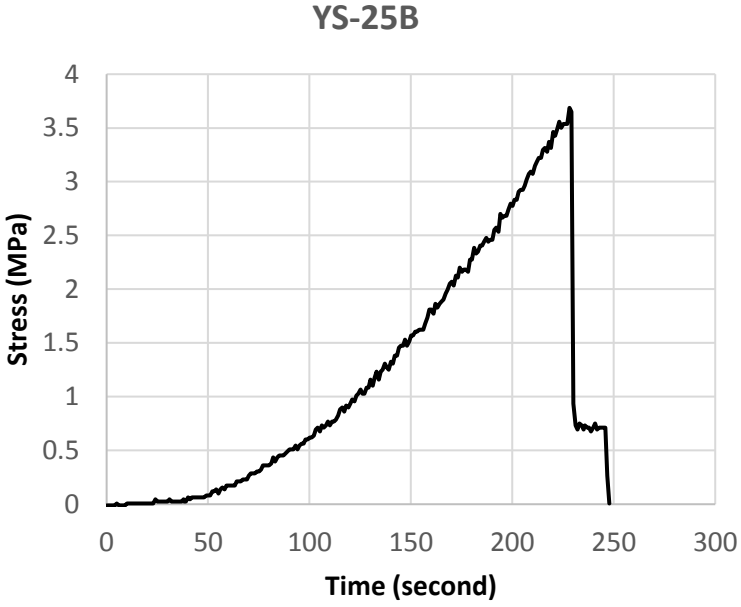

YS_32

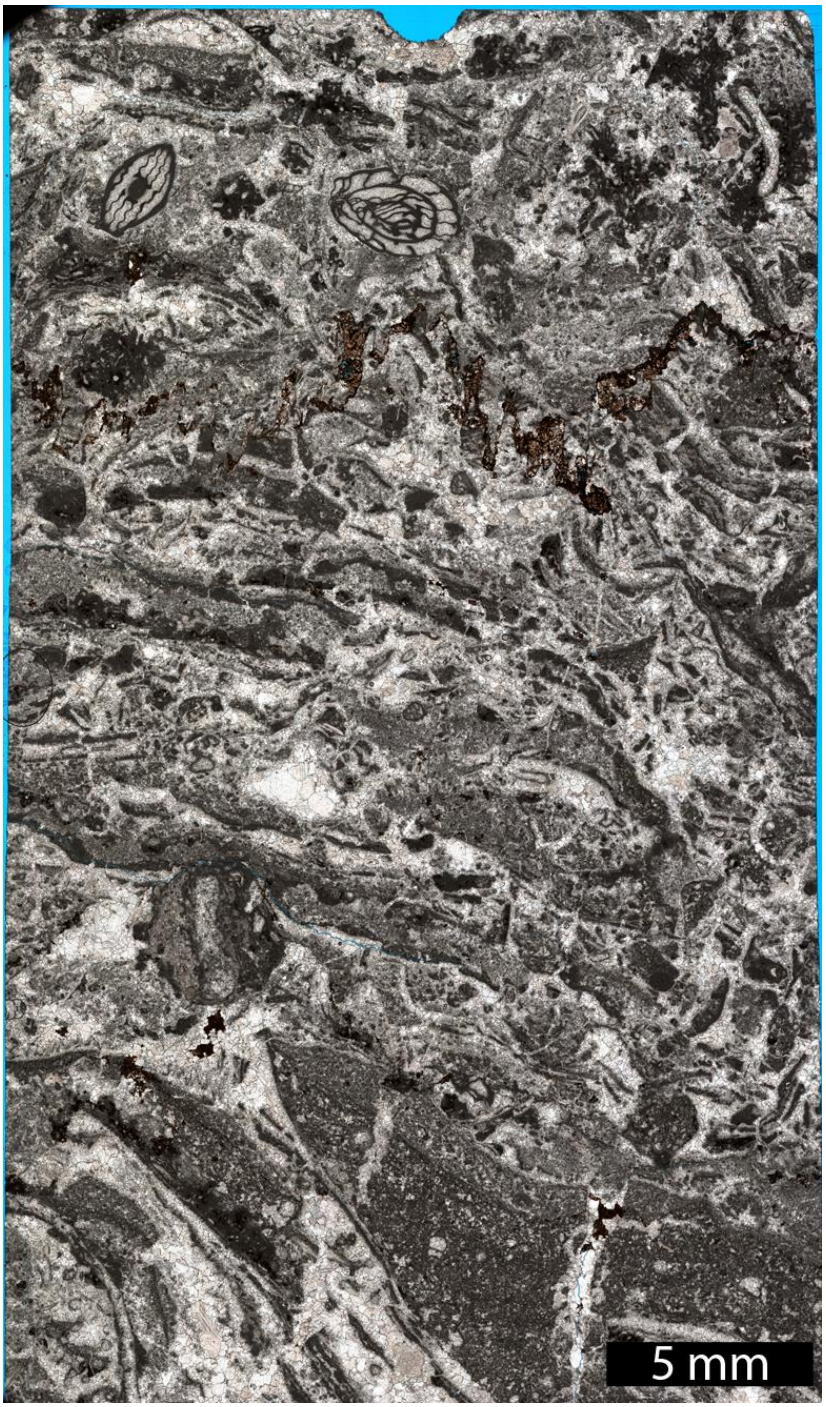

*No point counting data- Phylloid peloidal grain-dominated packstone

Uniaxial Unconfined Compressive Strength Test Data

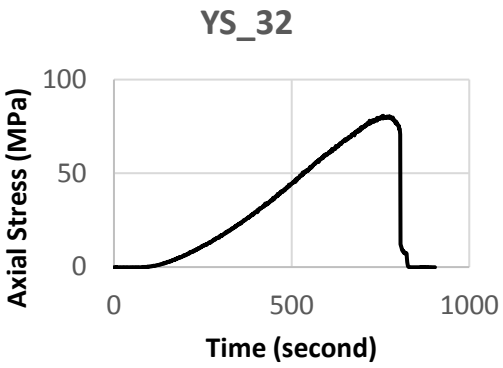

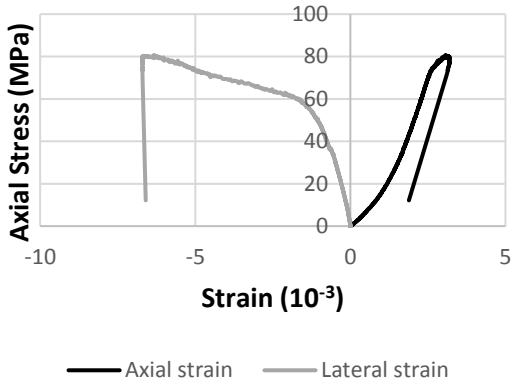

*Lateral strain invalid due to lateral strain gauge failure

Mechanical Properties	YS_32
Ultimate UCS (MPa)	80.72
~75% Tangent E (GPa)	36.51
Poisson Ratio	
Bulk Modulus (GPa)	
Shear Modulus (GPa)	

Brazilian Test Data

Sample	Diameter (mm)	Length (mm)	Peak Stress (MPa)	Force (N)	Tensile Strength (MPa)
32	25.40	13.17	1.98	1001.84	1.91
32B	25.41	12.86	2.59	1313.64	2.56

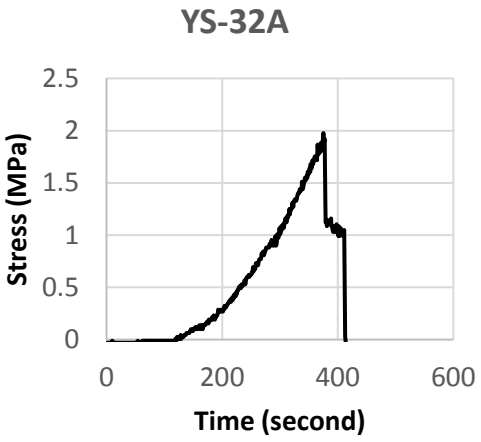

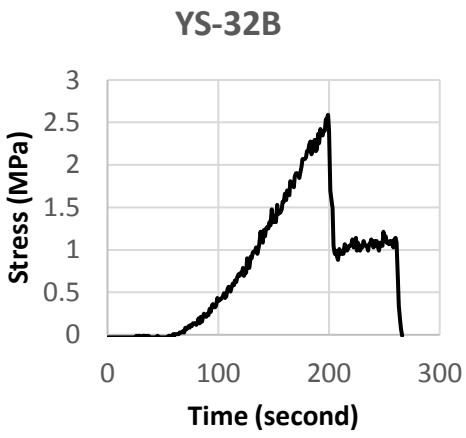

YS_14

Point Counting Data
n = 373
Grains in order of abundance: Peloids, phylloid algae, skeletal fragments, syrngoporid, bryazoan, daisyclad algae.

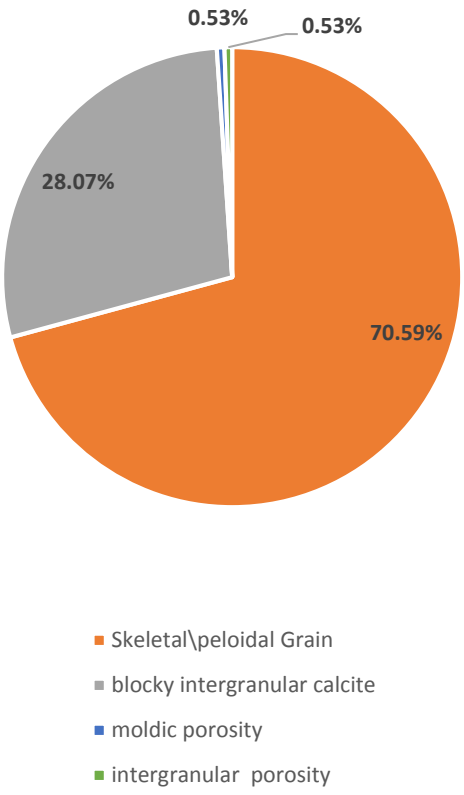

Uniaxial Unconfined Compressive Strength Test Data

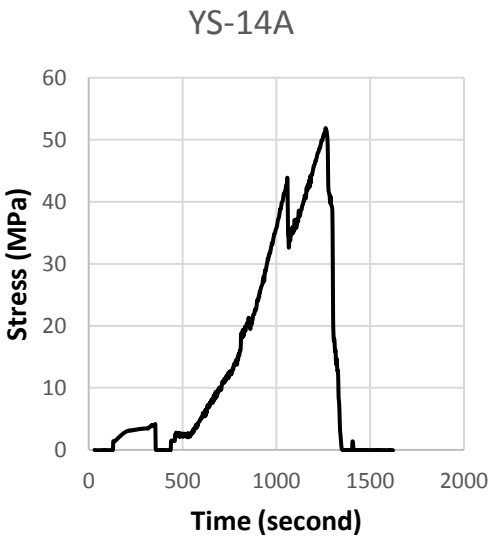

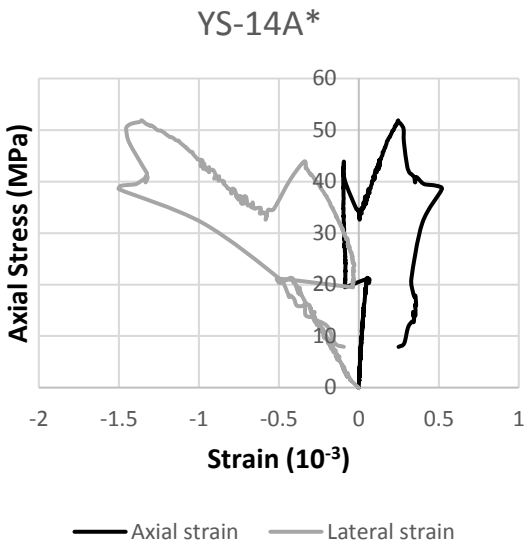

*invalid strain data due to strain gauge failure

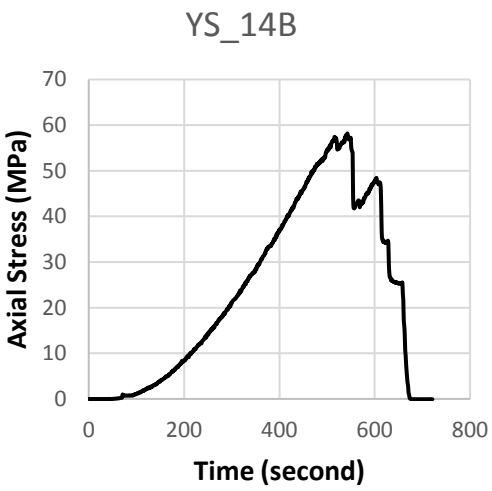

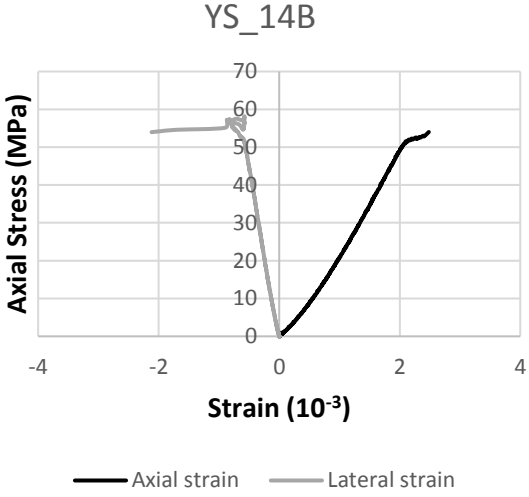

Mechanical Properties	YS_14A	YS_14B
Ultimate UCS (MPa)	51.87	58.18
~75% Tangent E (GPa)		29.57
Poisson Ratio		0.28
Bulk Modulus (GPa)		22.38
Shear Modulus (GPa)		11.55

Brazilian Test Data

Sample	Diameter (mm)	Length (mm)	Peak Stress (MPa)	Force (N)	Tensile Strength (MPa)
YS_14A	25.40	14.06	2.09	1058.34	1.89
YS_14B	25.40	13.26	4.62	2339.11	4.42

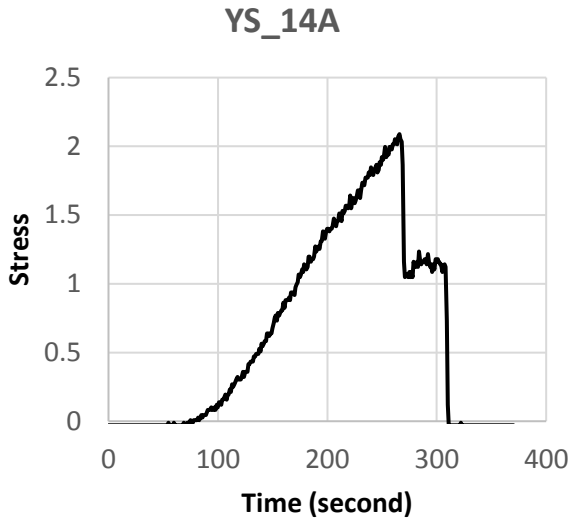

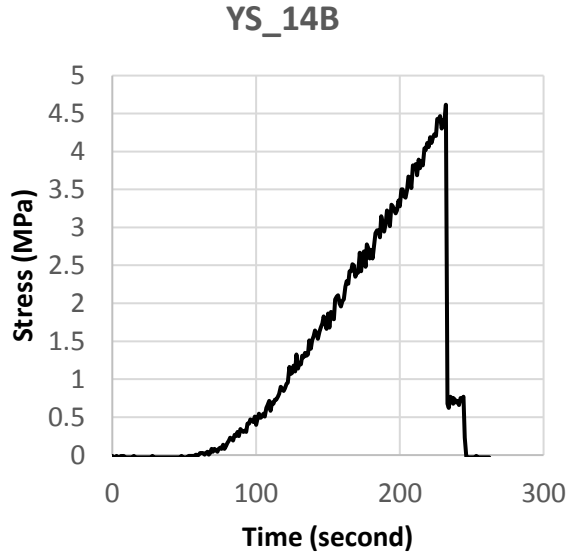

YS_26

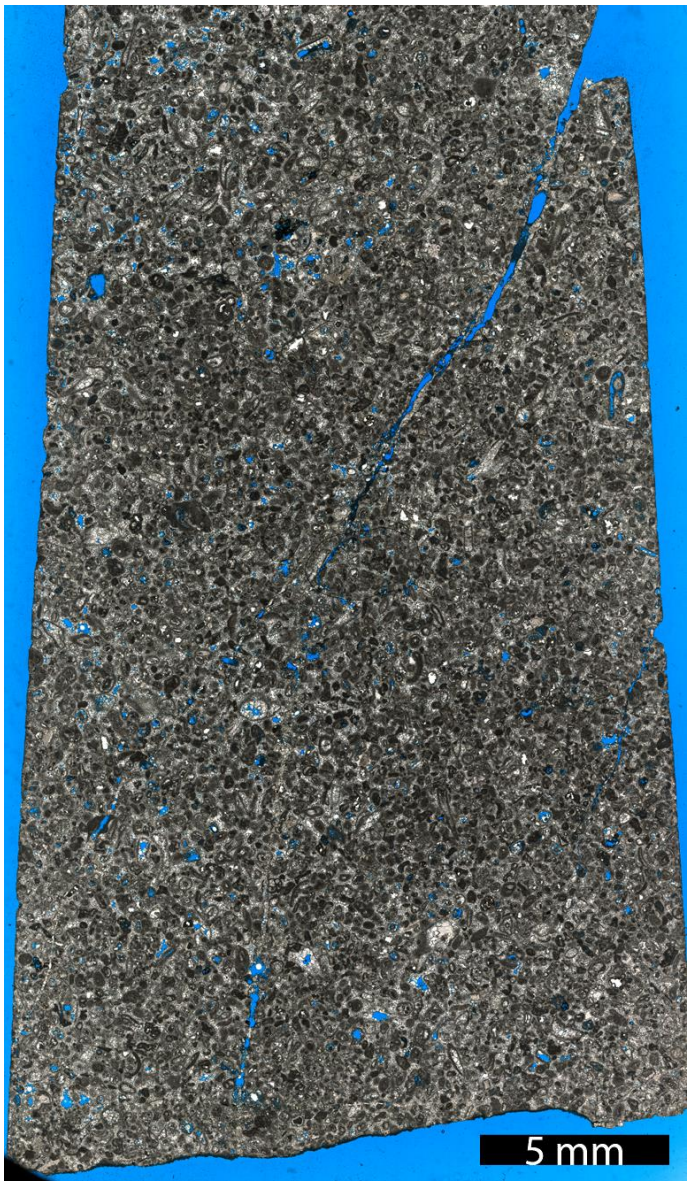

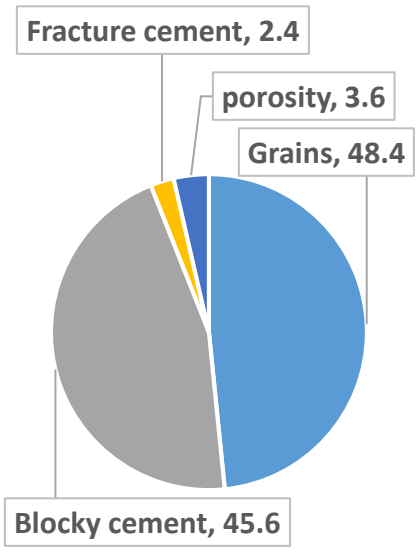

Point Counting Data:

n = 250

Uniaxial Unconfined Compressive Strength Test Data

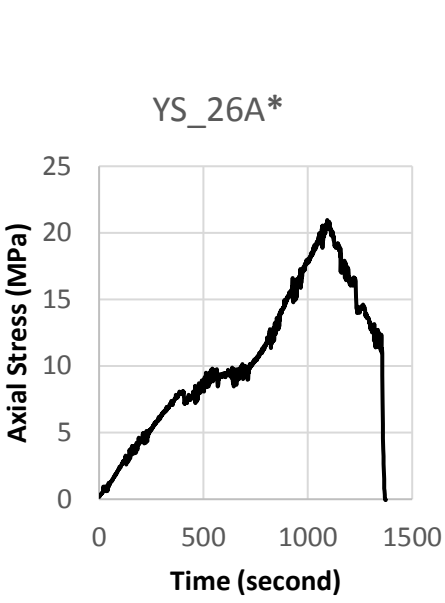

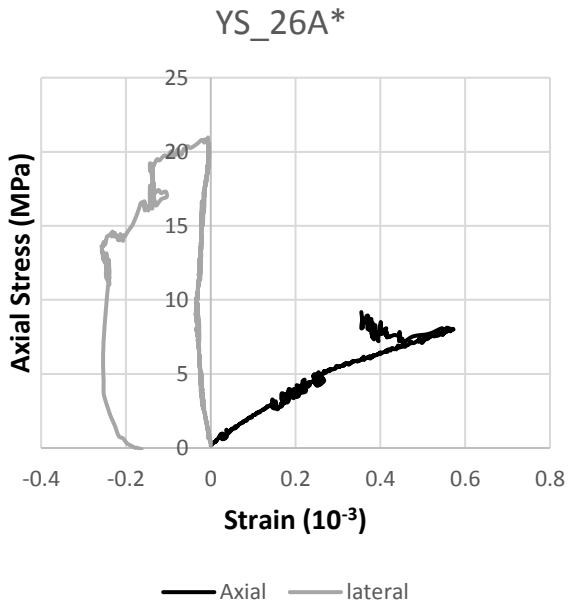

*invalid test due to strain gauge failure/natural fracture reactivation?

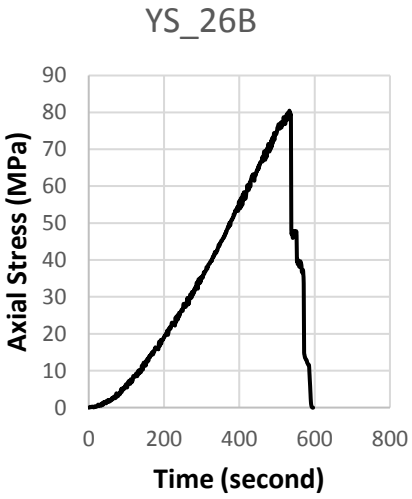

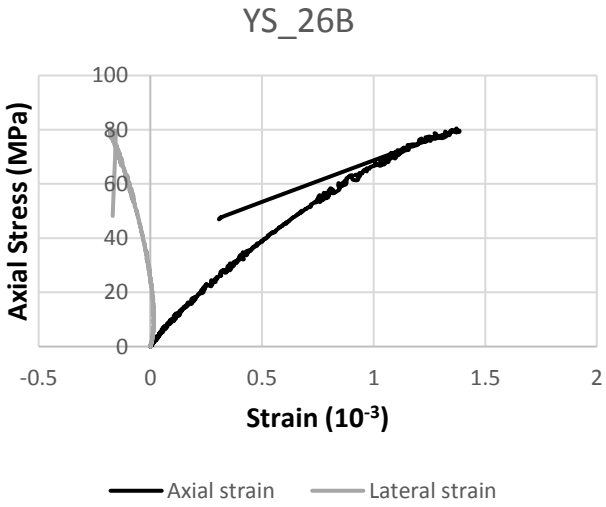

Mechanical Properties	YS_26B	YS_26A
Ultimate UCS (MPa)	80.47	20.9665
~75% Tangent E (GPa)	63.71	
Poisson Ratio	0.17	
Bulk Modulus (GPa)	31.82	
Shear Modulus (GPa)	27.31	

Brazilian Test Data

Sample	Diameter (mm)	Length (mm)	Peak Stress (MPa)	Force (N)	Tensile Strength (MPa)
26	25.42	13.29	1.09	550.66	1.04

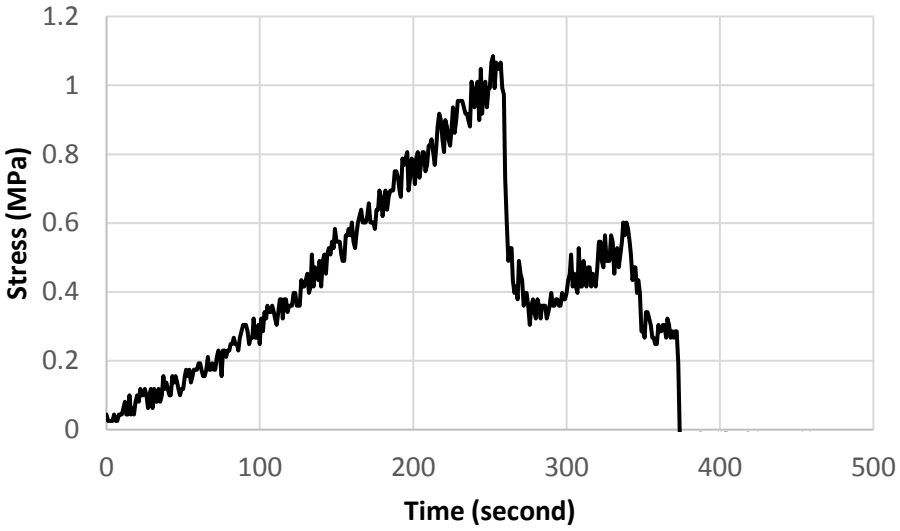

YUCCA-COR-S2

Point Counting Data

n = 256

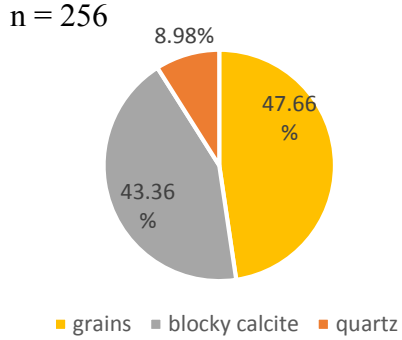

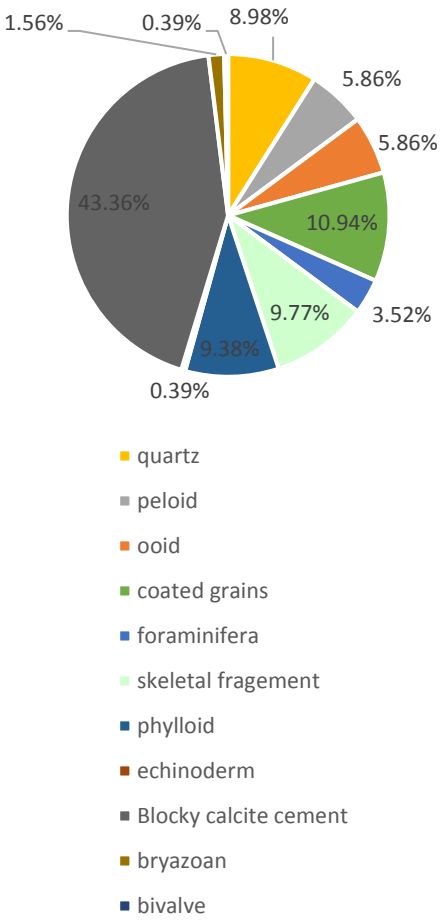

Uniaxial Unconfined Compressive Strength Test Data

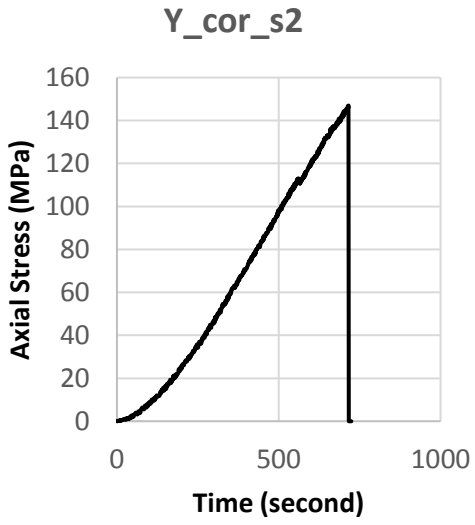

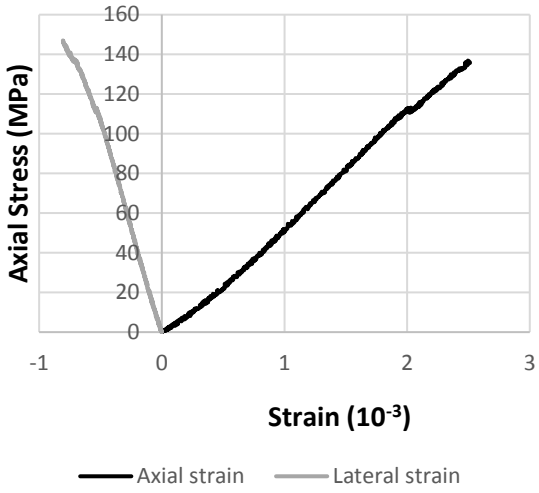

Mechanical Properties	Y_cor_s2
Ultimate UCS (MPa)	147.01
~75% Tangent E (GPa)	59.754
Poisson Ratio	0.272
Bulk Modulus (GPa)	43.713
Shear Modulus (GPa)	23.485

Brazilian Test Data

Sample	Diameter (mm)	Length (mm)	Peak Stress (MPa)	Force (N)	Tensile Strength (MPa)
Y_Cor_S2	25.41	13.12	6.49	3292.87	6.29

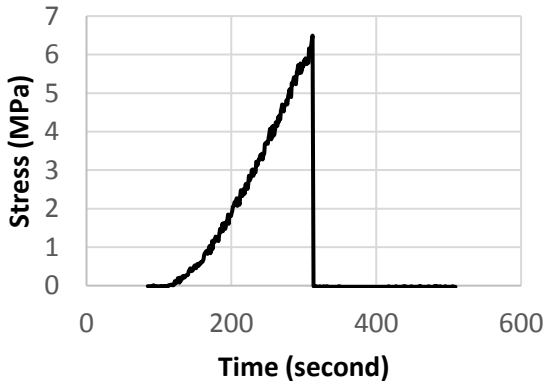

M1

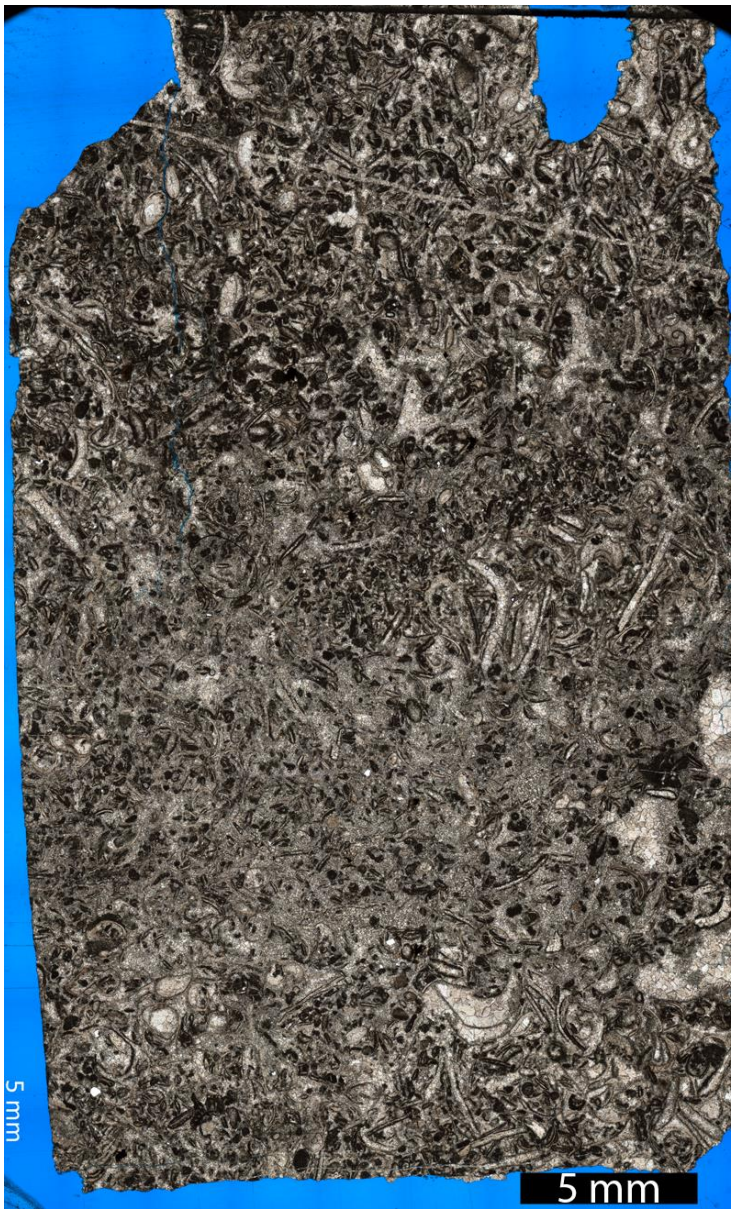

Point Counting Data

N =250

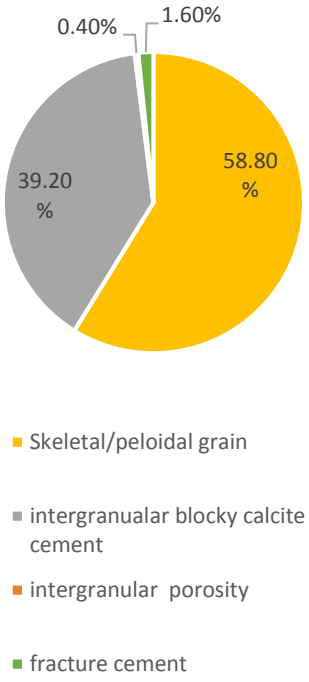

Brazilian Test Data

Sample	Diameter (mm)	Length (mm)	Peak Stress (MPa)	Force (N)	Tensile Strength (MPa)
M1_A	25.42	12.61	4.84	2455.99	4.88
M1_B	25.41	10.35	3.43	1737.76	4.21
M1_C	25.4	12.63	3.67	1858.82	3.69

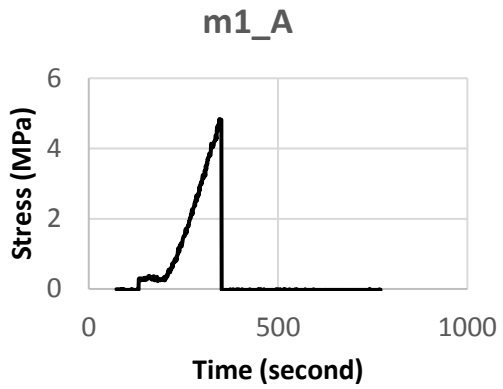

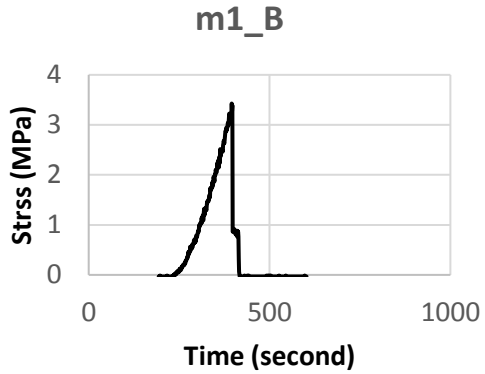

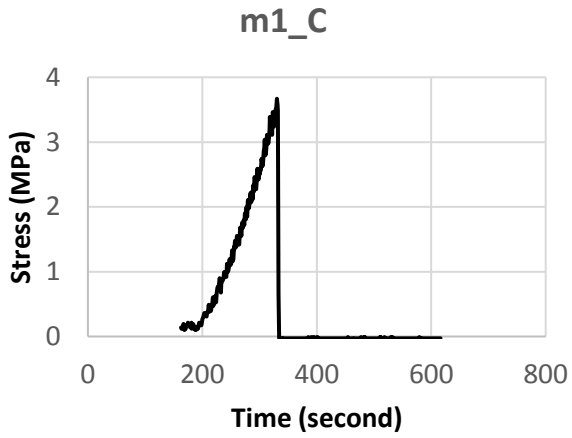

SW_S1_W_CAICOS

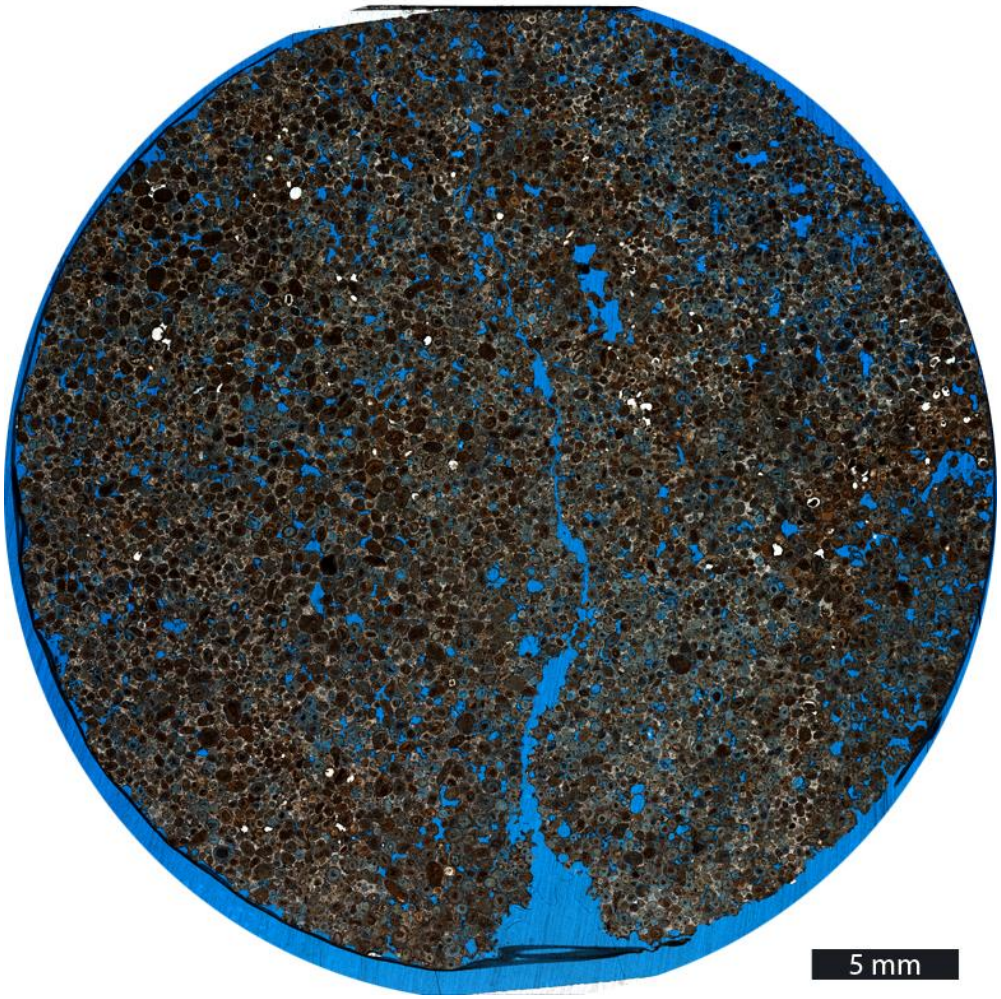

Point Counting Data

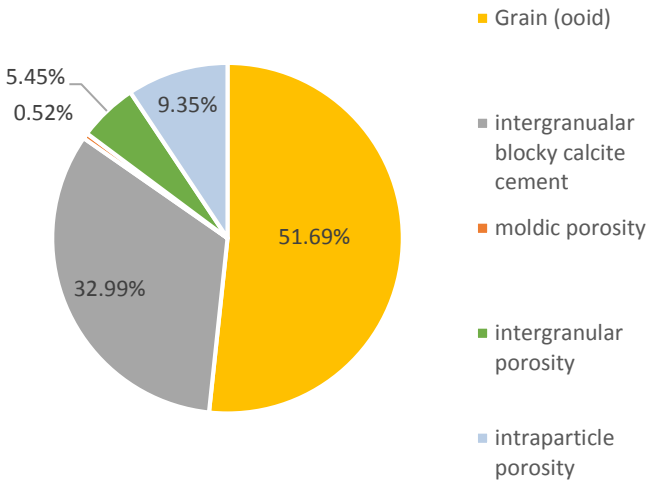

Brazilian Test Data

Sample	Diameter (mm)	Length (mm)	Peak Stress (MPa)	Force (N)	Tensile Strength (MPa)
SW_s1_w_caicos_A	25.46	13.79	1.16	590.25	1.07
SW_s1_w_caicos_B	25.49	12.53	1.16	591.64	1.18
SW_s1_w_caicos_C	25.47	12.42	0.97	496.02	1.00

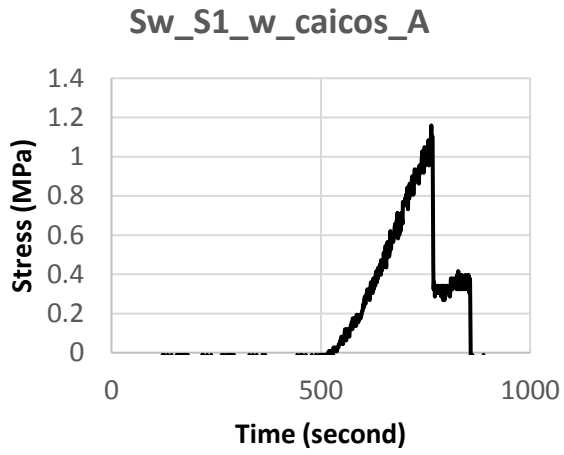

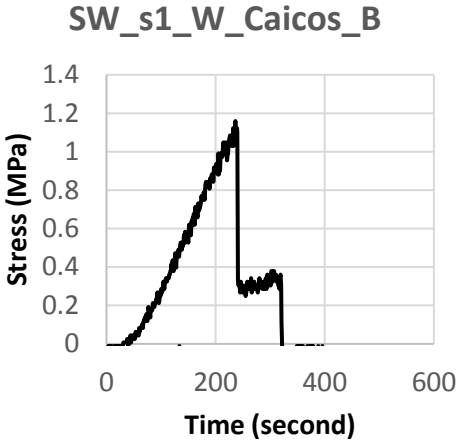

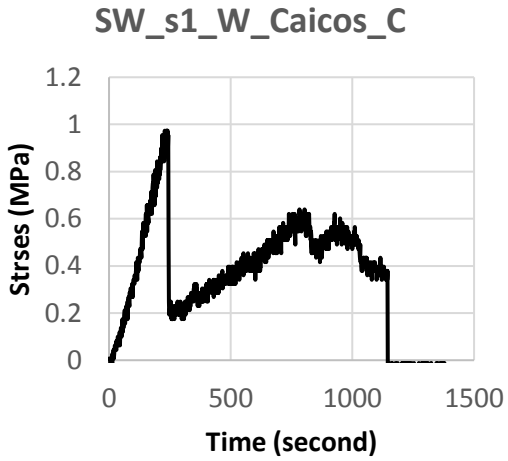

YS_6

Point Counting Data

N = 250

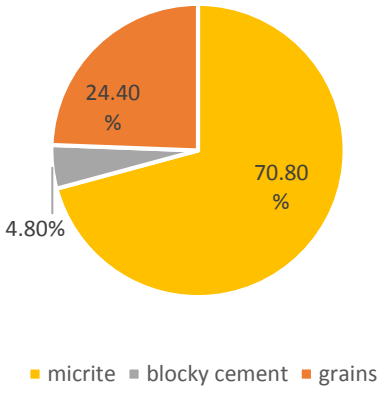

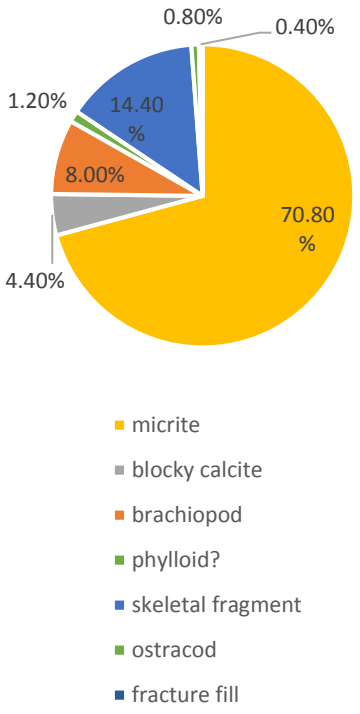

Uniaxial Unconfined Compressive Strength Test Data

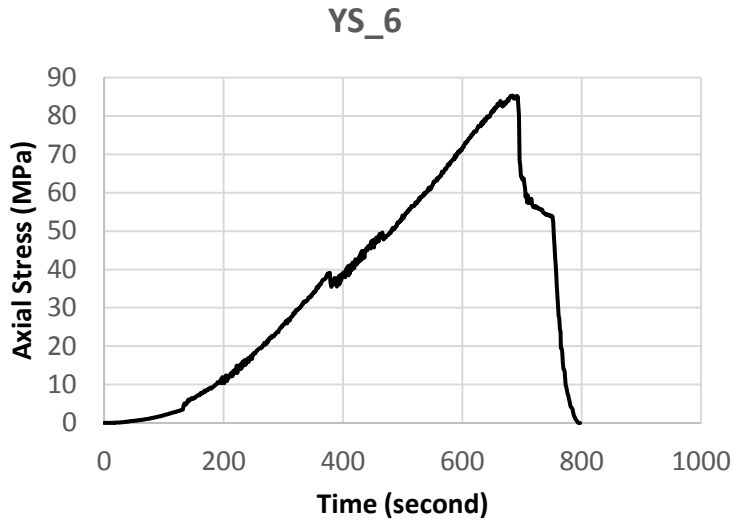

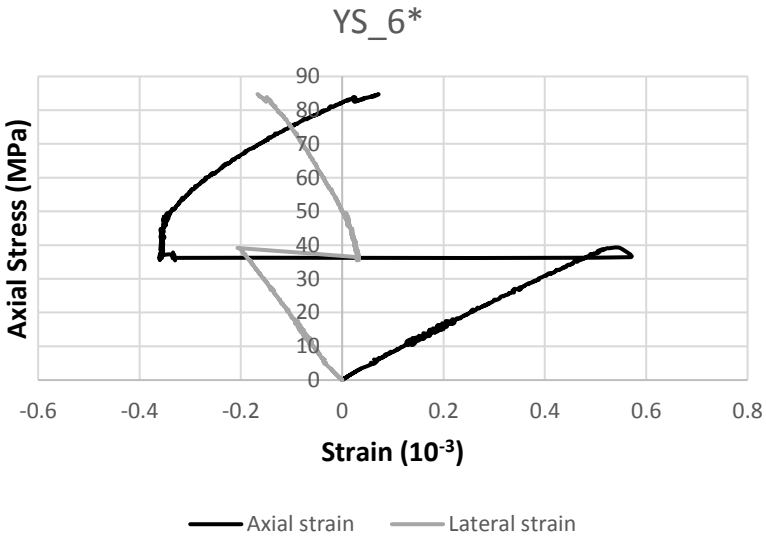

*Strain data valid up to 40 MPa axial stress (natural fracture reactivation at ~40 MPa?)

Mechanical Properties	YS_6
Ultimate UCS (MPa)	85.33
Tangent E (GPa)	77.678
Poisson Ratio	0.287
Bulk Modulus (GPa)	60.770
Shear Modulus (GPa)	30.179

Brazilian Test Data

Sample	Diameter (mm)	Length (mm)	Peak Stress (MPa)	Force (N)	Tensile Strength (MPa)
6A	25.36	15.75	6.55	3308.08	5.27
6B	25.41	15.27	6.25	3170.34	5.20

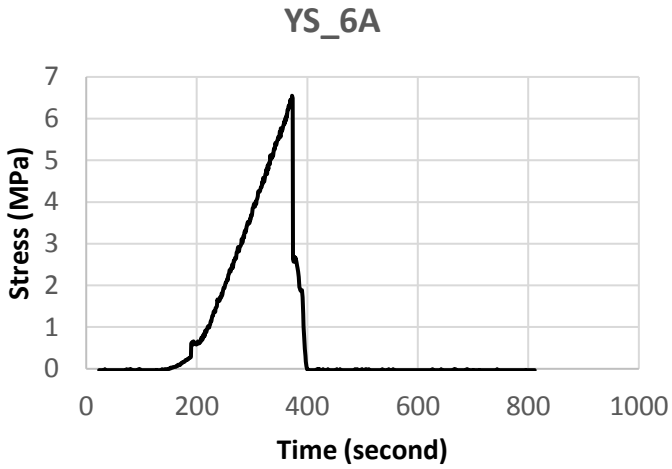

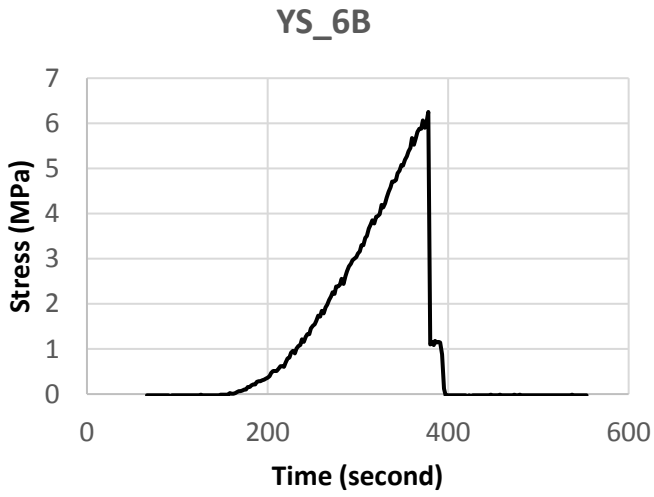

YS-12

Point Counting Data

N = 255

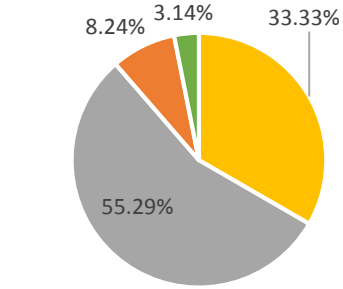

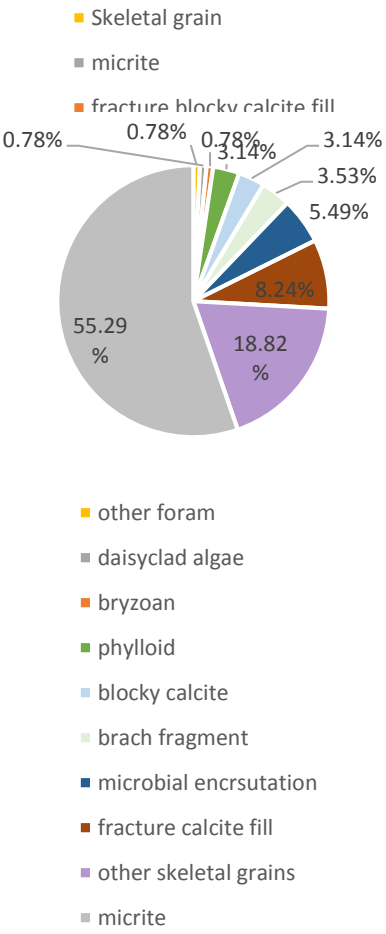

Uniaxial Unconfined Compressive Strength Test Data

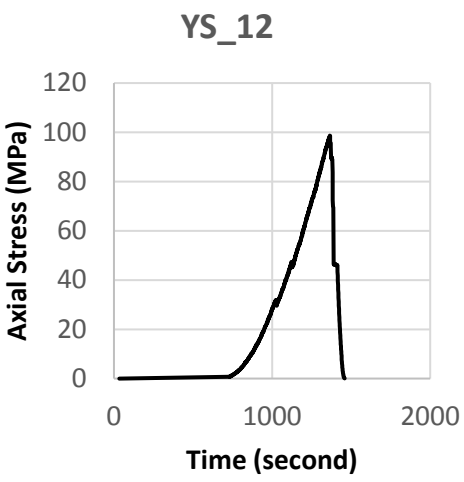

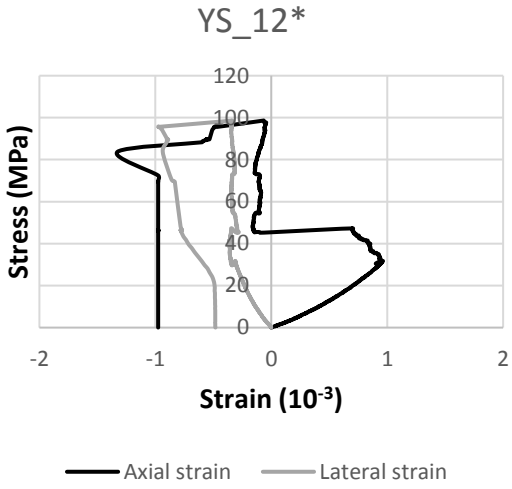

*Invalid strain data due to strain gauge failure

Mechanical Properties	YS_12
Ultimate UCS (MPa)	98.6635

Brazilian Test Data

Sample	Diameter (mm)	Length (mm)	Peak Stress (MPa)	Force (N)	Tensile Strength (MPa)
12	25.43	13.42	4.50	2288.01	4.27

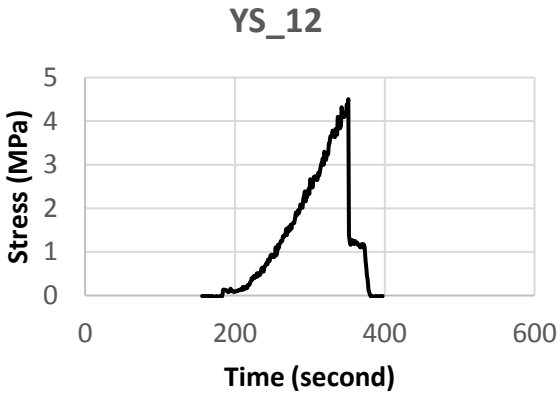

YS-38

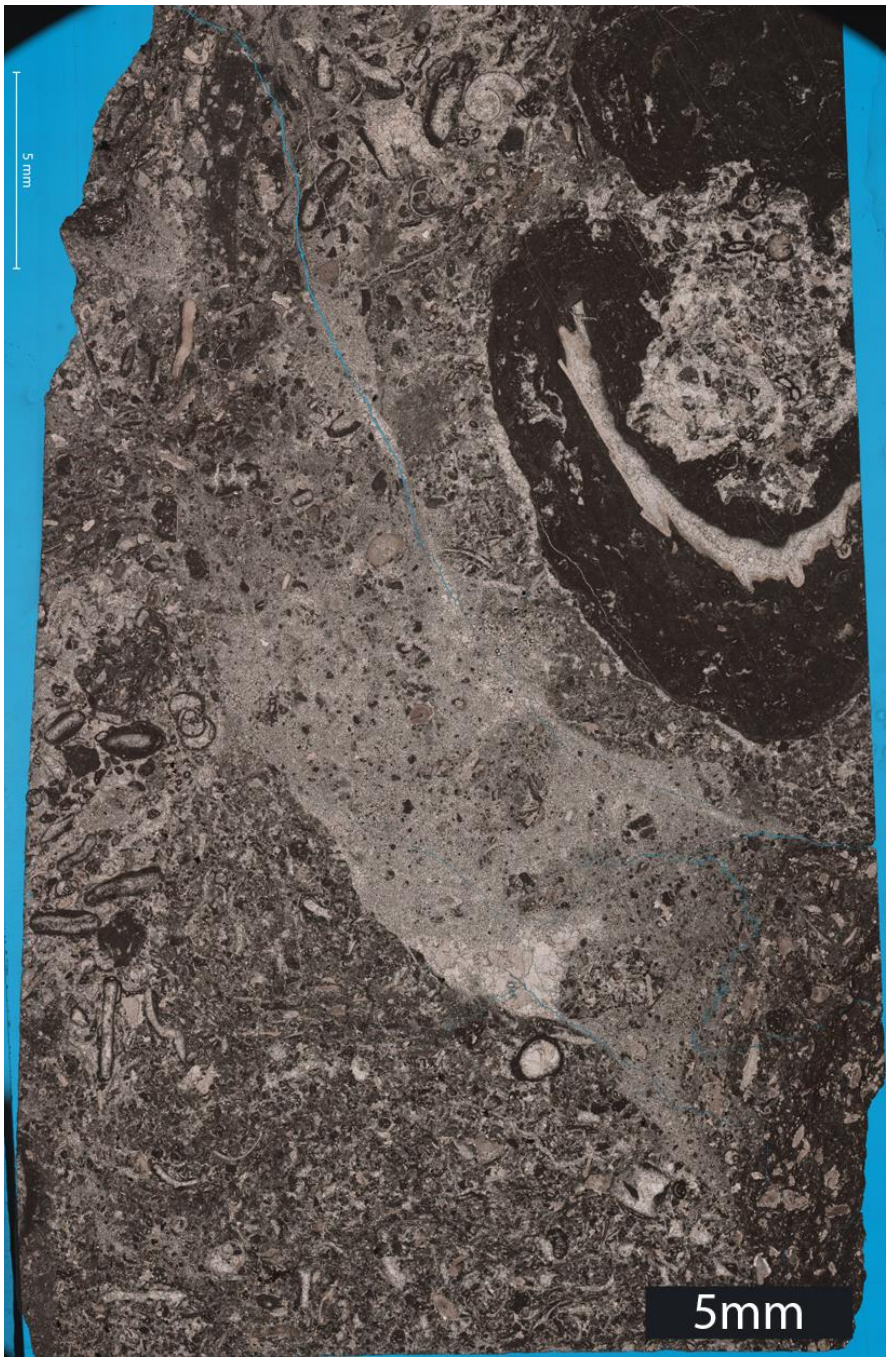

*No point counting data- oncoid fusilinid phylloid mud-dominated packstone

Uniaxial Unconfined Compressive Strength Test Data

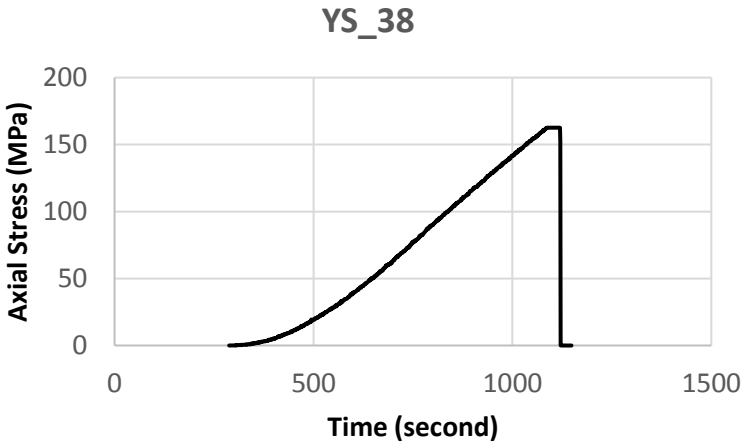

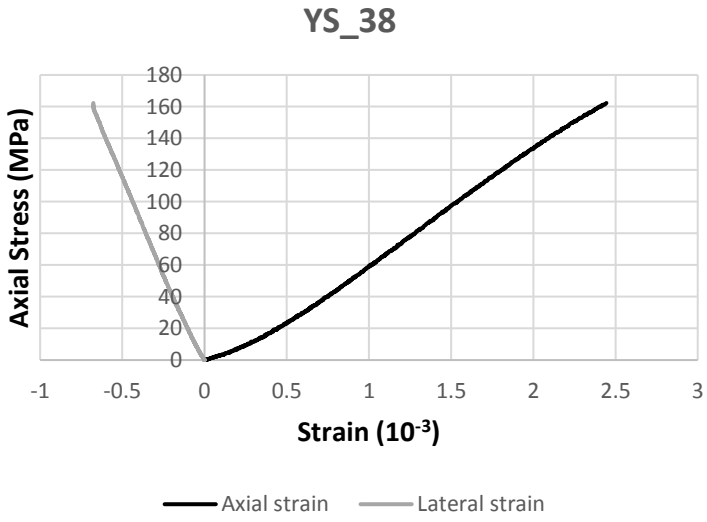

Mechanical Properties	YS_38
Ultimate UCS (MPa)	162.60
~75% Tangent E (GPa)	75.27
Poisson Ratio	0.31
Bulk Modulus (GPa)	64.70
Shear Modulus (GPa)	28.81

YS-5

Point Counting Data

N =250

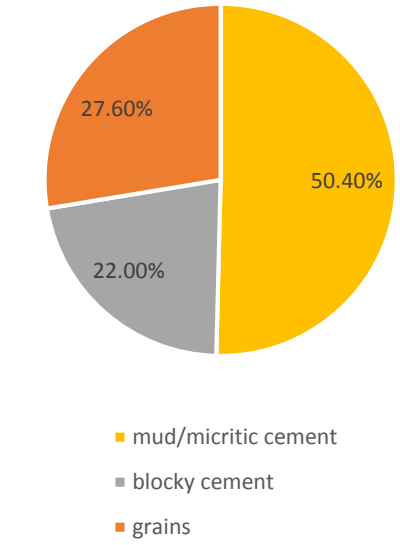

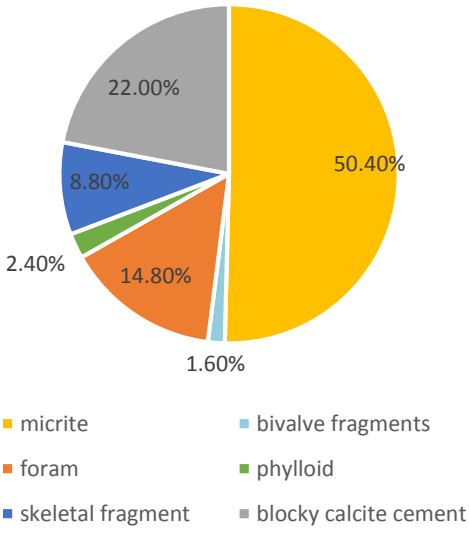

Uniaxial Unconfined Compressive Strength Test Data

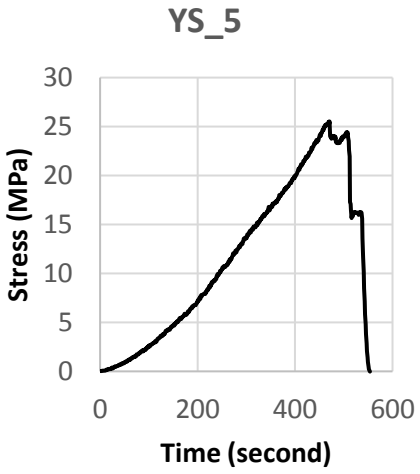

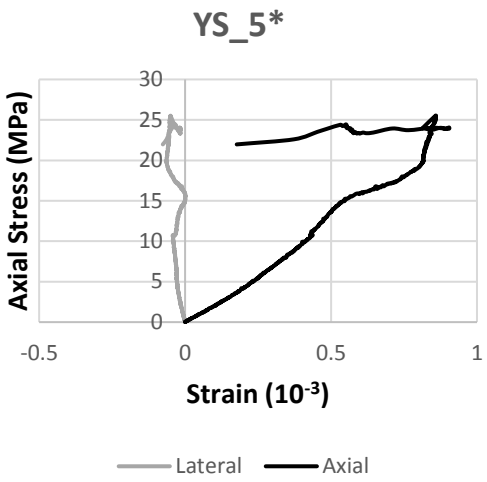

* invalid strain data

Mechanical Properties	YS_5
Ultimate UCS (MPa)	25.52

Brazilian Test Data

Sample	Diameter (mm)	Length (mm)	Peak Stress (MPa)	Force (N)	Tensile Strength (MPa)
5	25.40	13.67	4.86	2461.54	4.51

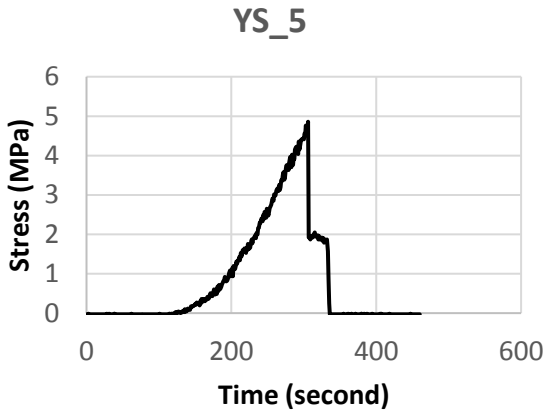

YS-8

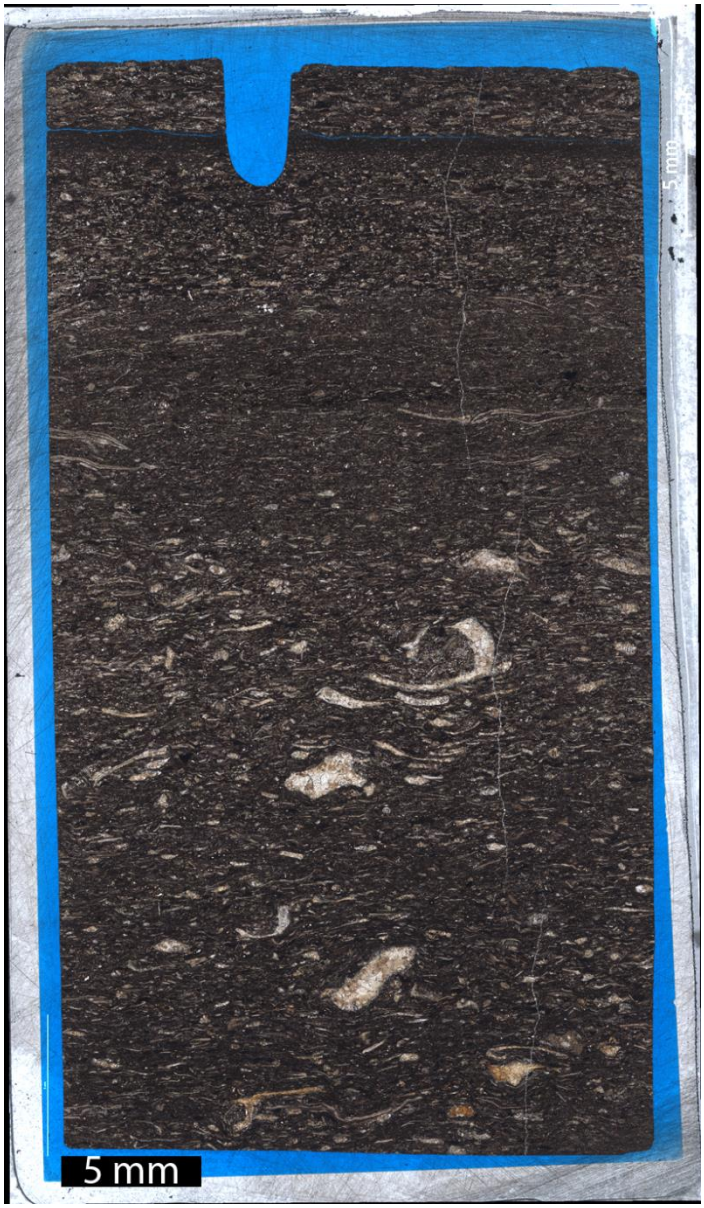

Point Counting Data

N = 250

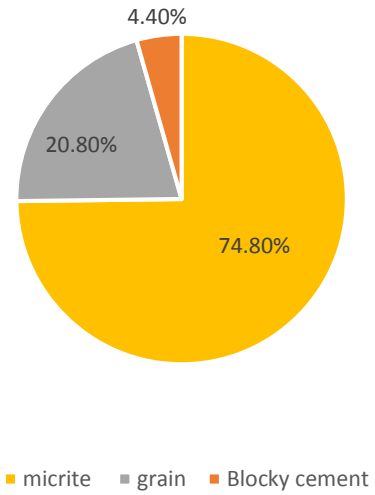

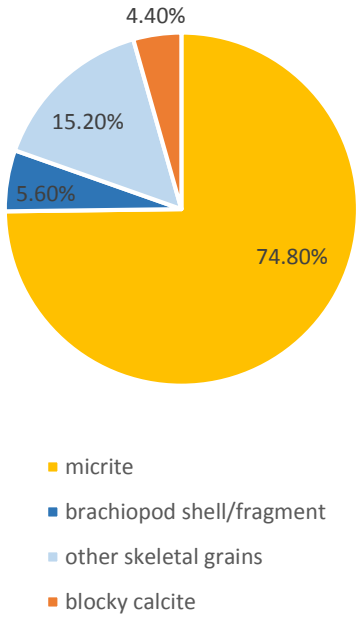

Uniaxial Unconfined Compressive Strength Test Data

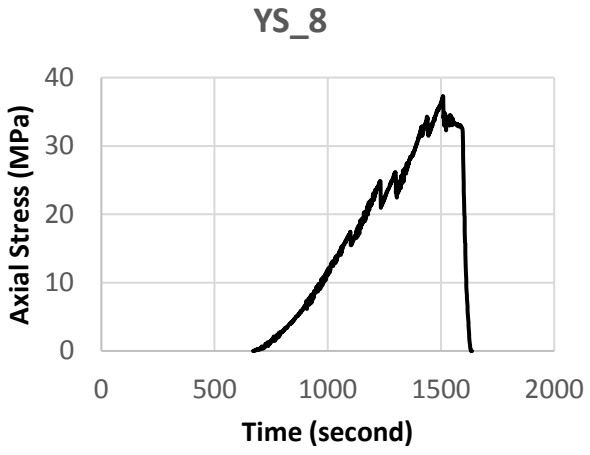

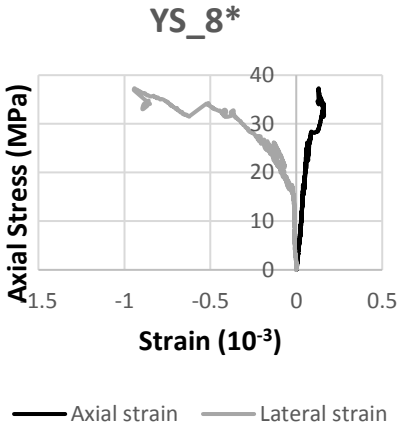

*invalid strain data due to strain guage failure

Mechanical Properties	YS_8
Ultimate UCS (MPa)	37.3035

Brazilian Test Data

Sample	Diameter (mm)	Length (mm)	Peak Stress (MPa)	Force (N)	Tensile Strength (MPa)
8A	25.43	13.17	5.92	3005.42	5.71
8B	25.39	12.15	5.68	2873.65	5.93

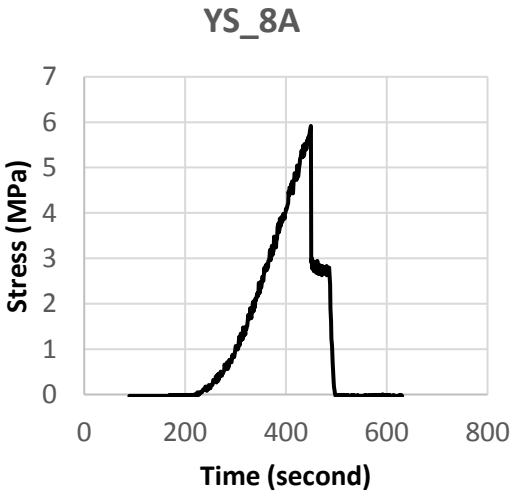

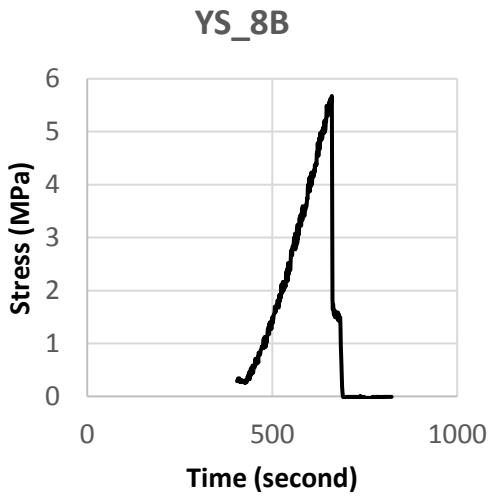

YUCCA-FL-S1

*No point counting data- Skeletal phylloid mud-dominated packstone

Uniaxial Unconfined Compressive Strength Test Data

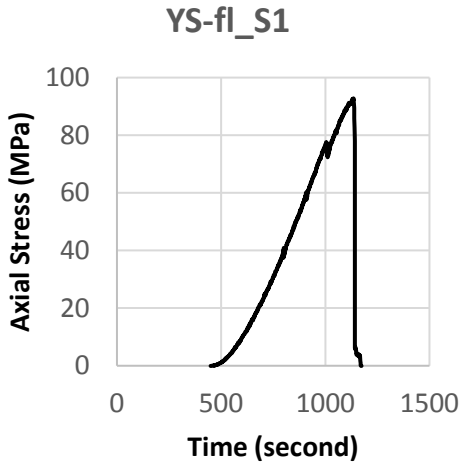

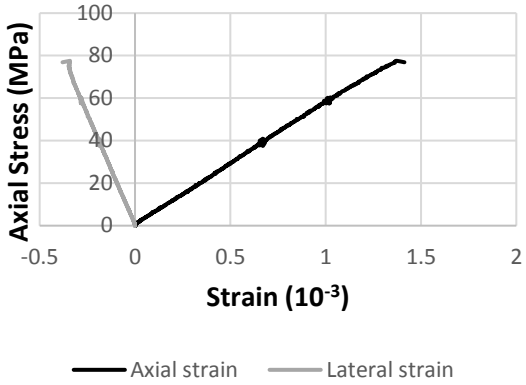

Mechanical Properties	YS_fl_s1
Ultimate UCS (MPa)	92.8
~75% Tangent E (GPa)	57.48
Poisson Ratio	0.268
Bulk Modulus (GPa)	41.351
Shear Modulus (GPa)	22.660

Brazilian Test Data

Sample	Diameter (mm)	Length (mm)	Peak Stress (MPa)	Force (N)	Tensile Strength (MPa)
YS_fl_S1	25.31	14.27	5.68	2855.57	5.03

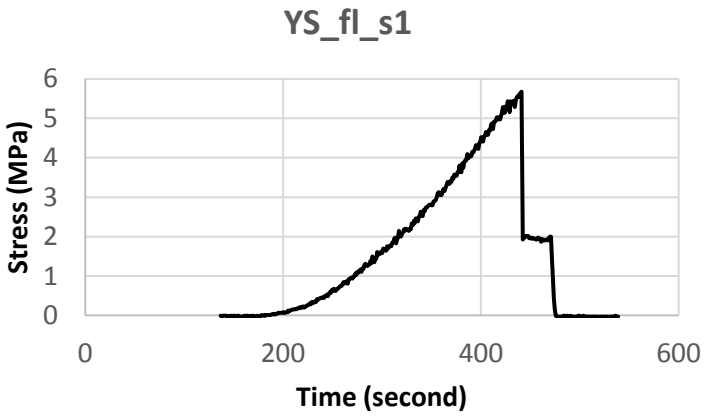

YS-7

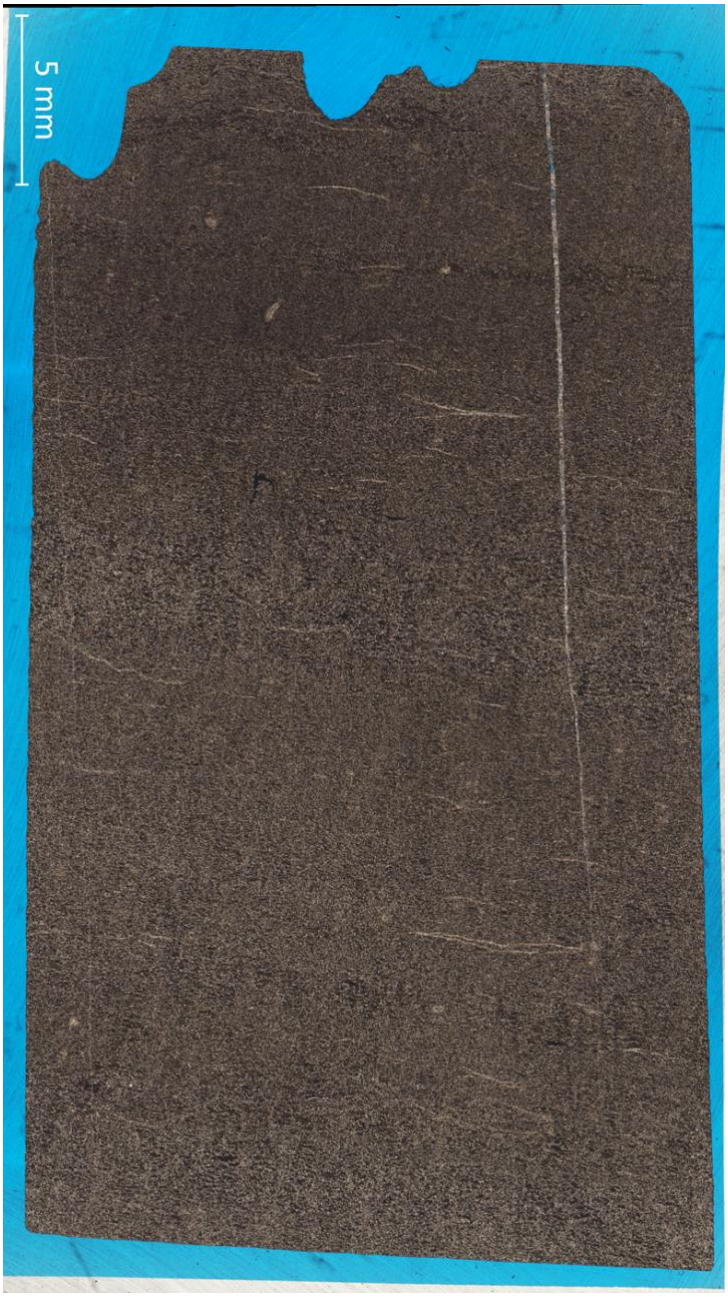

Point Counting Data

N = 500

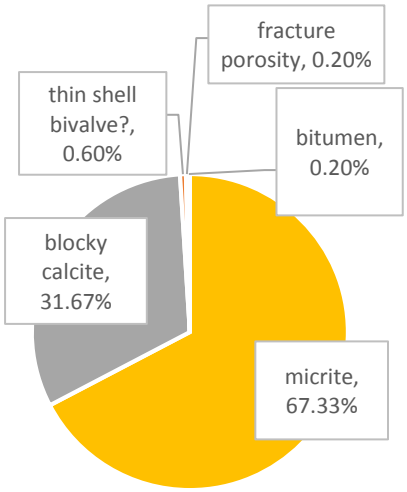

Uniaxial Unconfined Compressive Strength Test Data

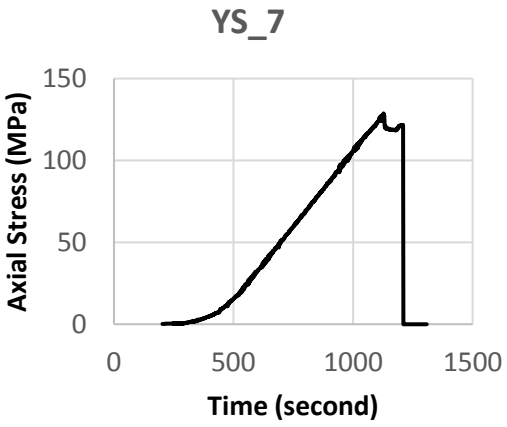

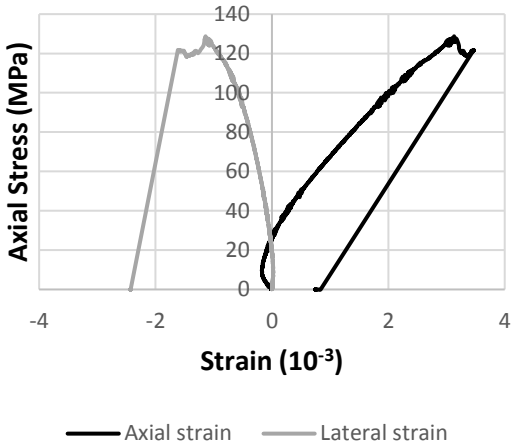

Mechanical Properties	YS_7
Ultimate UCS (MPa)	128.73
Tangent E (GPa)	37.89
Poisson Ratio	0.25
Bulk Modulus (GPa)	25.19
Shear Modulus (GPa)	15.17

Brazilian Test Data

Sample	Diameter (mm)	Length (mm)	Peak Stress (MPa)	Force (N)	Tensile Strength (MPa)
7A	25.39	10.78	2.89	1462.14	3.40
7B	25.32	12.93	1.98	995.54	1.94

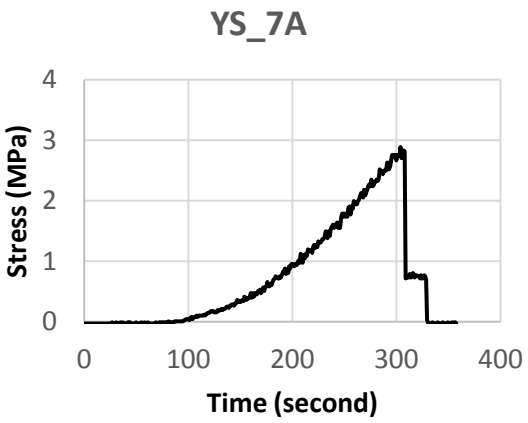

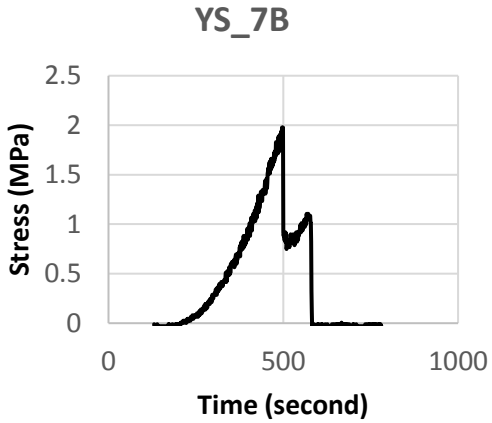

YS-13

Point Counting Data

N = 250

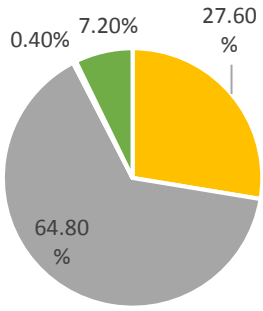

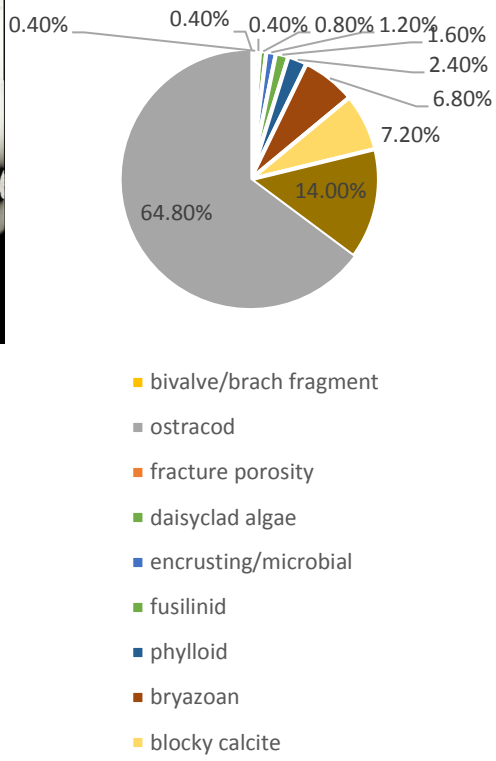

Uniaxial Unconfined Compressive Strength Test Data

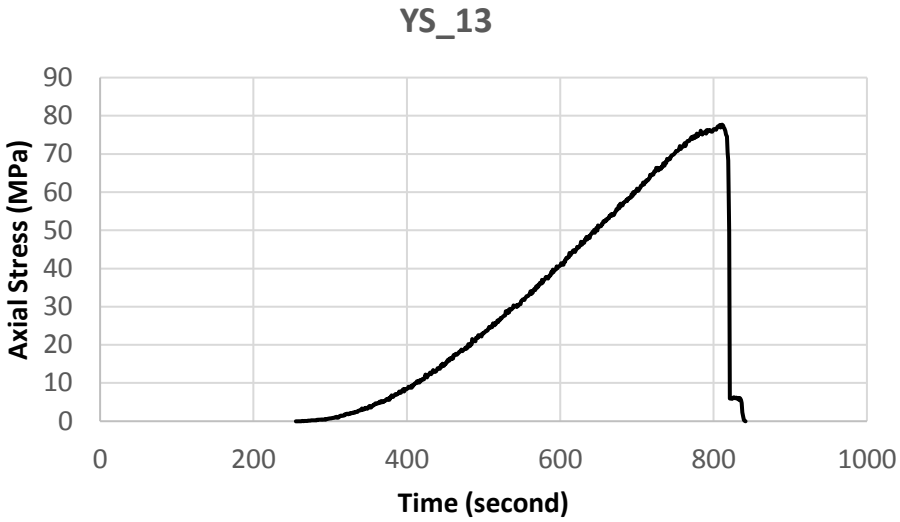

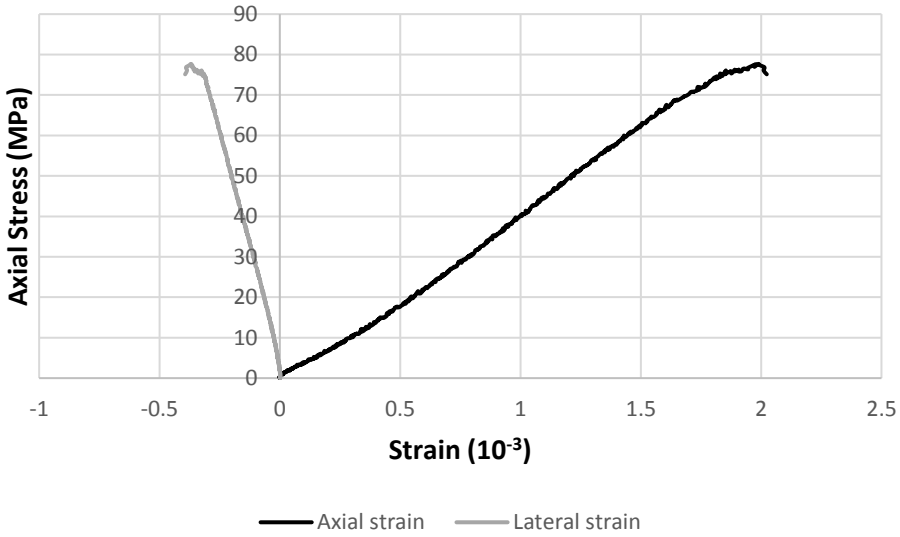

Mechanical Properties	YS_13
Ultimate UCS (MPa)	77.67
~75% Tangent E (GPa)	44.89
Poisson Ratio	0.20
Bulk Modulus (GPa)	25.15
Shear Modulus (GPa)	18.67

YS-37

* No point counting data - Skeletal wackestone

Uniaxial Unconfined Compressive Strength Test Data

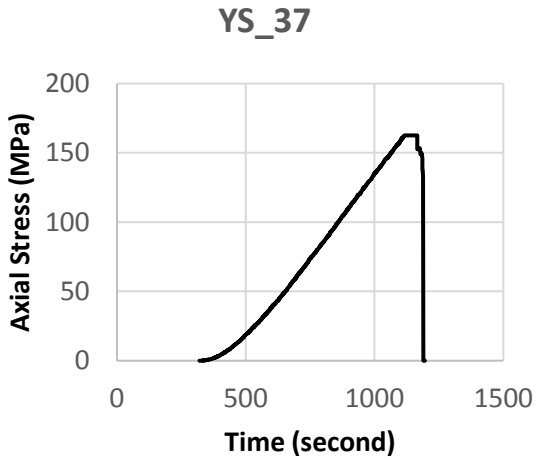

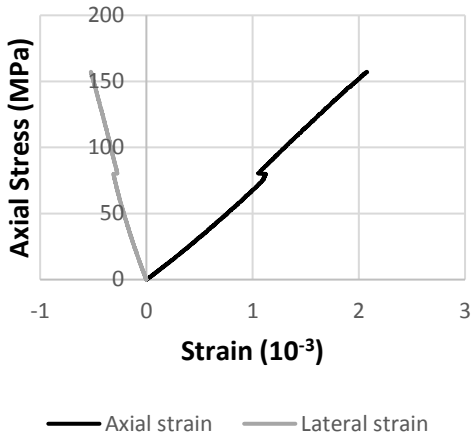

Mechanical Properties	YS_37
Ultimate UCS (MPa)	162.60
Reactivation UCS (MPa)	
~75% Tangent E (GPa)	70.43
Poisson Ratio	0.27
Bulk Modulus (GPa)	50.20
Shear Modulus (GPa)	27.81

Brazilian Test Data

Sample	Diameter (mm)	Length (mm)	Peak Stress (MPa)	Force (N)	Tensile Strength (MPa)
37A	25.39	14.70	8.80	4454.53	7.60
37B	25.40	12.06	6.85	3469.21	7.21

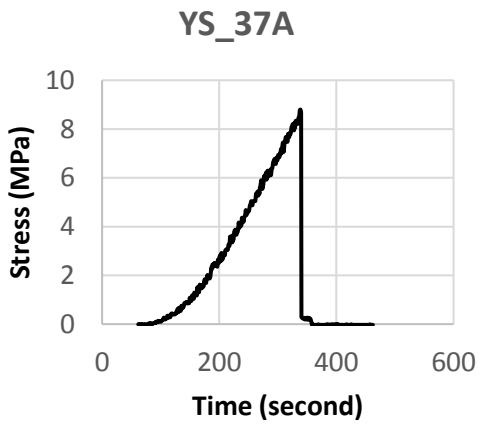

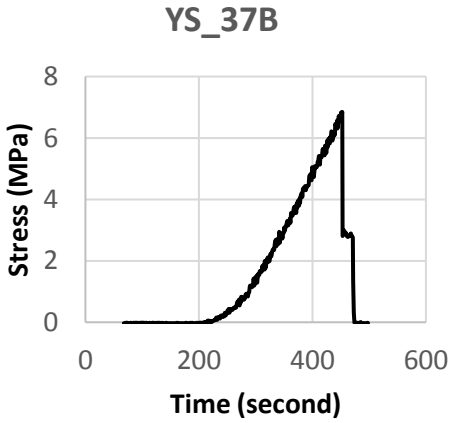

YS-9

Point Counting Data

N= 433

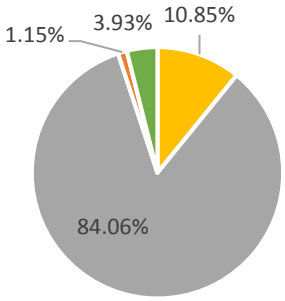

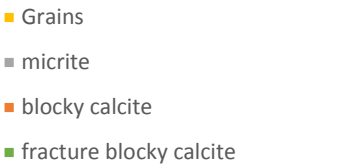

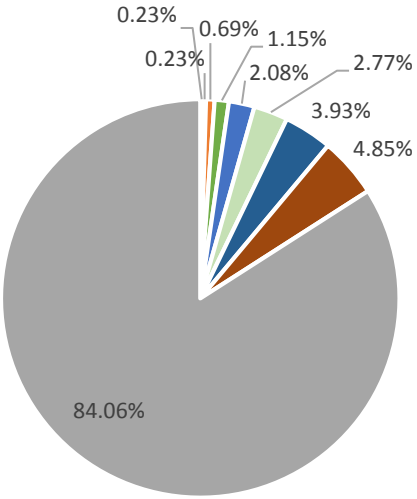

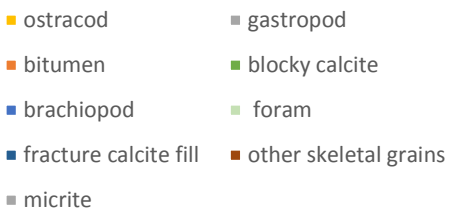

Uniaxial Unconfined Compressive Strength Test Data

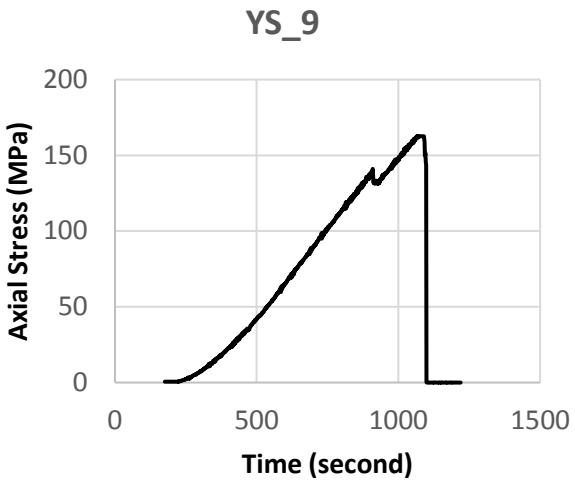

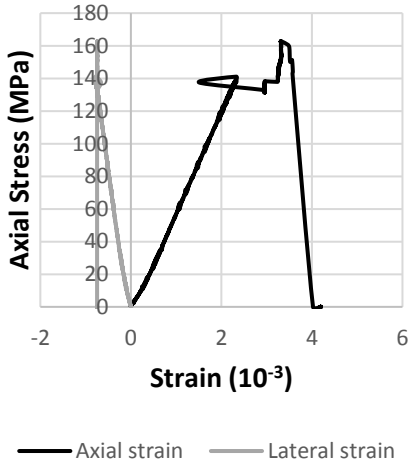

Mechanical Properties	YS_9
Ultimate UCS (GPa)	162.60
Tangent E (MPa)	61.61
Poisson Ratio	0.32
Bulk Modulus (GPa)	58.46
Shear Modulus (GPa)	23.26

YS-2

Point Counting Data

N = 212

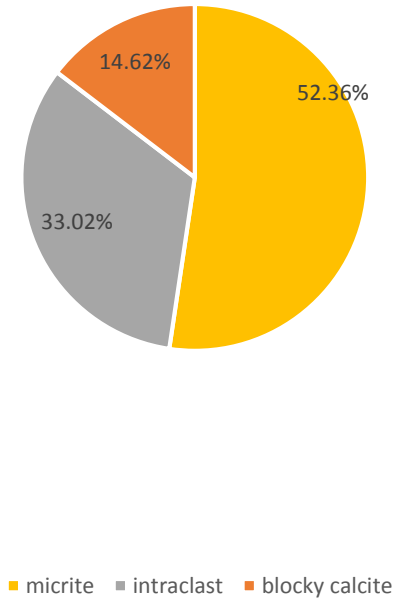

Brazilian Test Data

Sample	Diameter (mm)	Length (mm)	Peak Stress (MPa)	Force (N)	Tensile Strength (MPa)
YS_2	25.41	12.86	4.43	2246.71	4.38

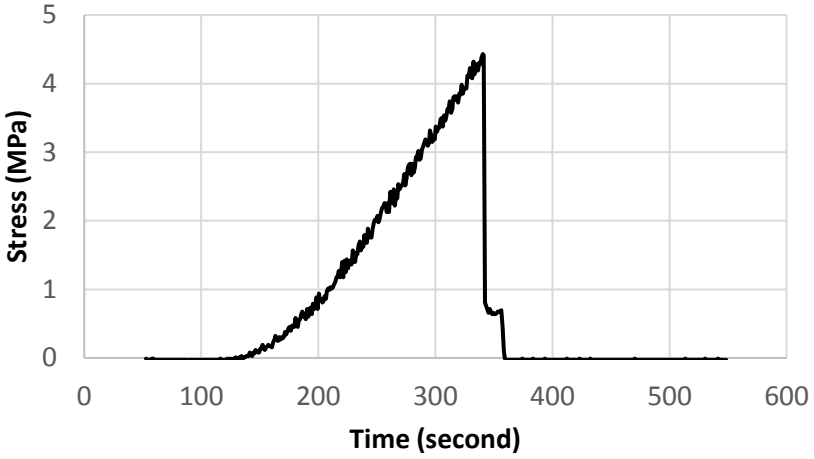

Schmidt Hammer Measurements

#	R	UCS (MPa)	Lithology	#	R	UCS (MPa)	Lithology
1	67.8	72	BS	37	65.9	79.9	BS
2	67.8	72	BS	38	65.9	80	BS
3	69.4	77.5	BS	39	64.8	75.5	BS
4	70.3	81	BS	40	61.3	63	BS
5	67.9	72	BS	41	59.1	56.5	BS
6	72.1	88	BS	42	62.5	67	BS
7	65.8	65	BS	43	67.0	84.5	BS
8	66.5	61	BS	44	56.5	49.5	BS
9	55.8	40.5	BS	45	59.6	58	BS
10	58.6	46	BS	46	58.2	54	BS
11	64.3	60.5	BS	47	60.5	78	BS
12	65.8	65	BS	48	61.9	69.5	BS
13	66.5	67.5	BS	49	62.6	91.5	BS
14	72.6	90.5	BS	50	68.4	80	BS
15	72.6	90.5	BS	51	68.4	75.5	BS
16	71.9	81.5	BS	52	66.3	63	BS
17	68.5	74	BS	53	64.4	67	BS
18	68.5	74	BS	54	64.4	84.5	BS
19	66.5	67.5	BS	55	62.6	46.5	BS
20	68.7	75	BS	56	64.7	58	BS
21	68.9	75.5	BS	57	64.8	55	BS
22	68.9	75.5	BS	58	64.8	50	BS
23	68.8	75	BS	59	64.7	58	BS
24	64.5	61	BS	60	60.6	54	BS
25	65.9	65	BS	61	61.9	47	BS
26	54.8	38.5	BS	62	51.6	44.5	BS
27	65.6	64.5	BS	63	61.7	81	BS
28	56.5	62.9	BS	64	61.2	54	BS
29	68.9	75.5	BS	65	64.8	71	BS
30	68	72.5	BS	66	64.0	67.5	Cong matrix
31	58.9	47	BS	67	55.5	55.5	Cong peb
32	58.9	47	BS	68	55.5	68.5	Cong peb
33	63.9	56.5	BS	69	59.5	48	GDP
34	60.2	50	BS	70	57.4	43.5	GDP
35	57.6	44	BS	71	58.7	46.5	GDP
36	54.4	44.5	BS	72	58.3	45.3	GDP

#	R	UCS (MPa)	Lithology	#	R	UCS (MPa)	Lithology
73	65.8	65	GDP	109	49.7	35	GDP
74	56.9	42.5	GDP	110	58.8	55.5	GDP
75	61.4	53	GDP	111	55.1	46	GDP
76	53.8	36.5	GDP	112	50.6	35	GDP
77	49.8	30	GDP	113	56.8	42	GS
78	57.6	44	GDP	114	59.4	48	GS
79	54.4	41.5	GDP	115	59.5	48	GS
80	56.4	37.5	GDP	116	56.1	41	GS
81	60.9	51.5	GDP	117	58.9	48	GS
82	60.9	51.5	GDP	118	63.6	58.5	GS
83	51.9	33.5	GDP	119	53.6	42	GS
84	58.9	47	GDP	120	62.8	56.5	GS
85	54.4	37.5	GDP	121	59.2	47.5	GS
86	59.8	49	GDP	122	59.4	48	GS
87	59.5	48	GDP	123	61.5	52	GS
88	54.7	38.5	GDP	124	59.8	49	GS
89	54.5	38	GDP	125	55	39	GS
90	59.2	47.5	GDP	126	58.7	46.5	GS
91	59.3	47.5	GDP	127	57.8	44.5	GS
92	61.6	53.5	GDP	128	58.1	45	GS
93	64.3	60.5	GDP	129	42.3	21	GS
94	63.1	57.5	GDP	130	56.8	42.5	GS
95	57	42.5	GDP	131	59.8	49	GS
96	45.3	24.5	GDP	132	60	49.5	GS
97	60.3	50	GDP	133	64	60	GS
98	59.7	48.5	GDP	134	56.7	42	GS
99	62.9	56.5	GDP	135	52.9	35	GS
100	63.1	57.5	GDP	136	56.4	41.5	GS
101	62.9	56.5	GDP	137	59.8	49	GS
102	58.4	45.5	GDP	138	58.9	47	GS
103	66.2	60.5	GDP	139	57.1	43	GS
104	64	60	GDP	140	53.3	36	GS
105	68.9	75.5	GDP	141	52.1	34	GS
106	61.3	52.5	GDP	142	56.3	41.5	GS
107	49.7	35	GDP	143	58.5	45	GS
108	49.7	35	GDP	144	59.9	49	GS

#	R	UCS (MPa)	Lithology	#	R	UCS (MPa)	Lithology
145	59.7	48.5	GS	181	54.9	50	MDP
146	59.1	47.5	GS	182	65	62.5	MDP
147	64.6	61.5	GS	183	63.6	58.5	MDP
148	59.3	47.5	GS	184	60.4	50.5	MDP
149	58	45.5	GS	185	60.2	50	MDP
150	57.5	44	GS	186	54.8	38.5	MDP
151	57.5	44	GS	187	51	32	MDP
152	59.1	47.7	GS	188	47.5	62	MDP
153	66.5	67.5	GS	189	65	62	MDP
154	65.7	65	GS	190	64.5	61	MDP
155	61.1	52	GS	191	51.7	32.5	MDP
156	63.7	59	GS	192	53.5	36	MDP
157	62.3	55	GS	193	53.4	36	MDP
158	66.3	67	GS	194	58.3	45.5	MDP
159	59.5	48	GS	195	65.6	64.5	MDP
160	61.3	52.5	GS	196	58	45	MDP
161	44.6	23.5	GS	197	61.6	53.5	MDP
162	50.1	30.5	GS	198	57.1	43	MDP
163	59.9	49	GS	199	59.2	47.5	MDP
164	58.2	54	GS	200	64.4	61	MDP
165	48.9	33.5	GS	201	49.7	30	MDP
166	59.1	56.5	GS	202	58	45	MDP
167	48.9	33.5	GS	203	48.8	29	MDP
168	59.6	58	GS	204	64.4	61	MDP
169	58.2	54	GS	205	65.4	64	MDP
170	56.7	50	GS	206	60.5	50.5	MDP
171	52.4	40	GS	207	55.5	40	MDP
172	59.1	56.5	GS	208	60.3	50	MDP
173	59.6	58	GS	209	55.5	47	MDP
174	55.1	46	GS	210	54.4	44.5	MDP
175	61.3	52	MDP	211	56.7	50	MDP
176	56.9	40	MDP	212	63.0	69	MDP
177	70.3	81	MDP	213	55.7	47.5	MDP
178	65.4	64	MDP	214	60.9	62	MDP
179	63.3	58	MDP	215	66.8	83.5	MDP
180	59.8	49	MDP	216	59.1	56.5	MDP

#	R	UCS (MPa)	Lithology	#	R	UCS (MPa)	Lithology
217	54.4	44.5	MDP	253	27.5	10.5	wacke
218	56.7	50	MDP	254	59.8	49	wacke
219	59.0	56	MDP	255	62	54.5	wacke
220	52.4	40	MDP	256	57.6	44	wacke
221	41.9	23.5	MDP	257	61.6	53.5	wacke
222	65.6	78.5	MDP	258	54.7	38.5	wacke
223	60.9	62	MDP	259	69.8	79	wacke
224	59.1	56.5	MDP	260	54.9	38.5	wacke
225	55.5	47	MDP	261	47	26.5	wacke
226	45.0	27.5	MDP	262	65	62.5	wacke
227	59.6	58	MDP	263	51.4	32.5	wacke
228	59.0	56	MDP	264	49.9	30.5	wacke
229	58.8	55.5	MDP	265	39.5	18.5	wacke
230	59.8	49	mud	266	60.3	50	wacke
231	63.3	58	mud	267	57.5	44	wacke
232	68.1	73	mud	268	61.8	54	wacke
233	62.3	55	mud	269	62.2	55	wacke
234	59.9	49	mud	270	59.9	49	wacke
235	61.8	54	mud	271	45.3	24.5	wacke
236	61.8	54	mud	272	66.3	67	wacke
237	66.8	68.5	mud	273	61	52	wacke
238	65.6	64.5	mud	274	61	52	wacke
239	56.8	42.5	mud	275	56.7	42	wacke
240	56.8	42.5	mud	276	64.2	60.5	wacke
241	58.3	45.5	mud	277	65.1	63	wacke
242	63.1	57.5	mud	278	59.2	47.5	wacke
243	66.1	66	sh	279	63	57	wacke
244	45.0	27.5	sh	280	54.7	45	wacke
245	22.0	22	sh	281	67.6	87	wacke
246	17.2	17.2	sh	282	51.3	38	wacke
247	45.0	27.5	Sh	283	54.7	45	wacke
248	43.1	25	Sh	284	68.6	91.5	wacke
249	28.7	12	Sh	285	55.5	47	wacke
250	69.7	97	SS	286	59.6	58	wacke
251	56.1	48.5	SS	287	52.4	40	wacke
252	48.8	29	wacke	288	49.7	35	wacke

#	R	UCS (MPa)	Lithology
289	47.7	31.5	wacke
290	43.5	25.5	wacke
291	55.7	47.5	wacke
292	54.4	44.5	wacke
293	49.7	35	wacke
294	52.4	40	wacke
295	47.7	31.5	wacke
296	51.3	38	wacke

Table C.2: Schmidt hammer measurements summary

Table Key:
Summary of all Schmidt hammer field measurements from the Holder Formation at Yucca and Dry canyons, Sacramento Mountains, New Mexico.

R: rebound hardness measurement
UCS: Calculated unconfined compressive strength
Sh: shale
SS: sandstone
Cong. matrix: conglomerate matrix
Cong. peb: conglomerate pebble
Mud: mudstone
Wacke: wackestone
MDP: mud-dominated packstone
GDP: grain-dominated packstone
GS: grainstone
BS: boundstone

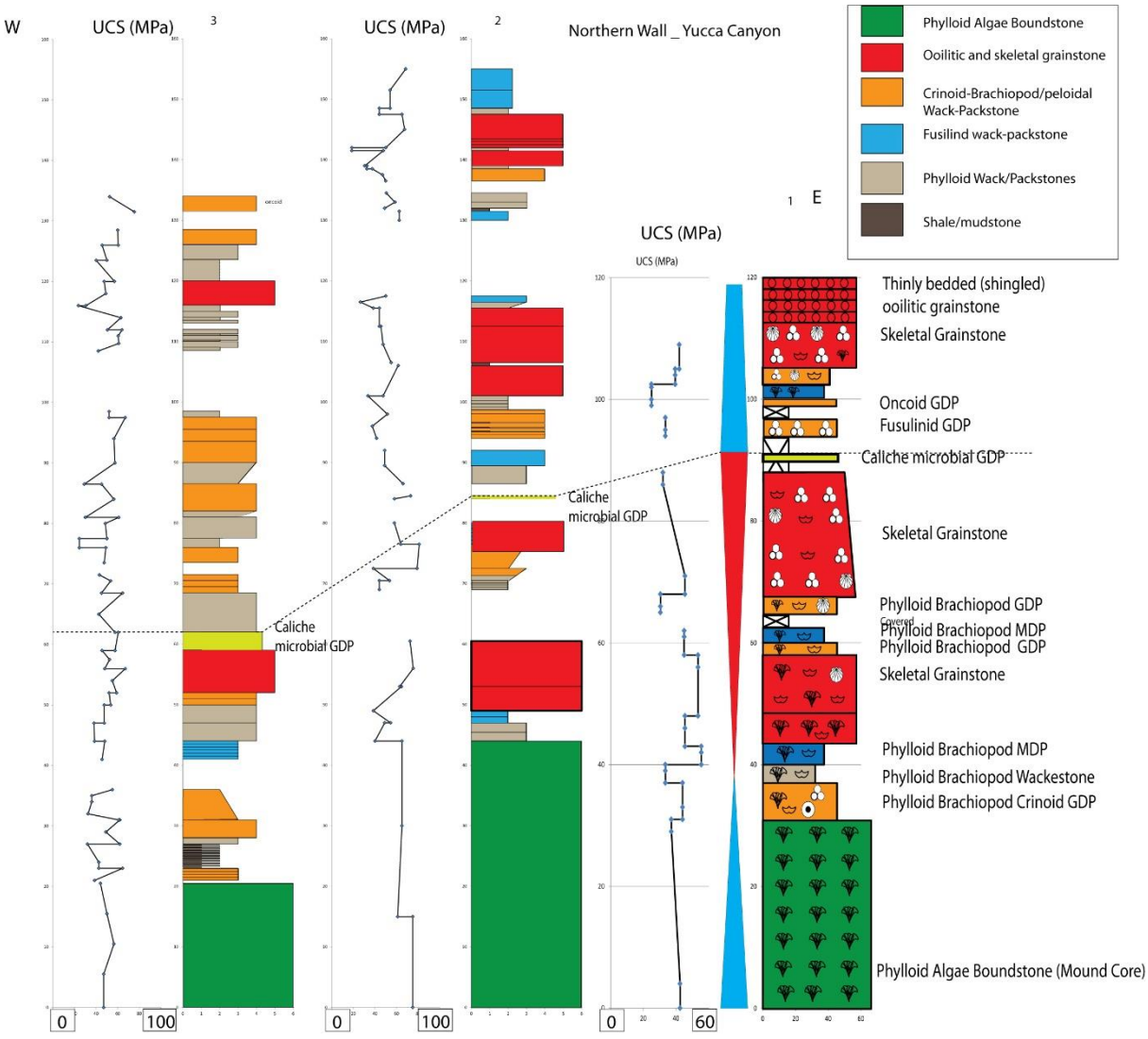

Figure C.3: Schmidt hammer measurements in stratigraphic sections context in from northern wall of Yucca Canyon, Saramento Mountains, New Mexico. Section 1 located on western flank of Yucca mound. Section 2 located on the eastern flank of middle mound. Section 3 located western flank of middle mound.

Appendix D: Additional Numerical Modeling Results

FORWARD NUMERICAL MODEL WITH DEPOSITION (CONTINUUM)

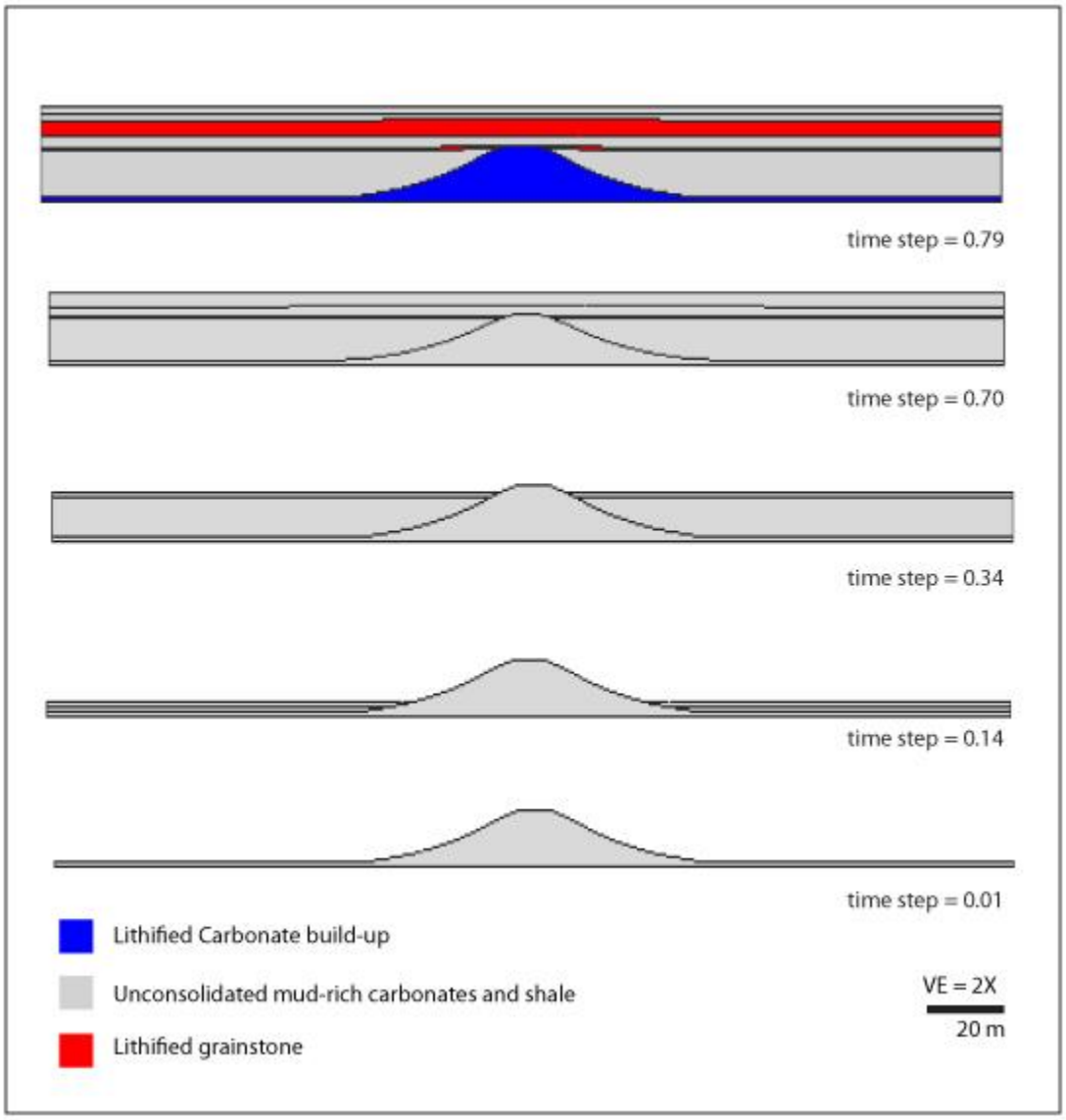

Note: 1- legend only applicable to time step 0.79

2- material properties and failure criteria used for this model similar to the base case in chapter 3.

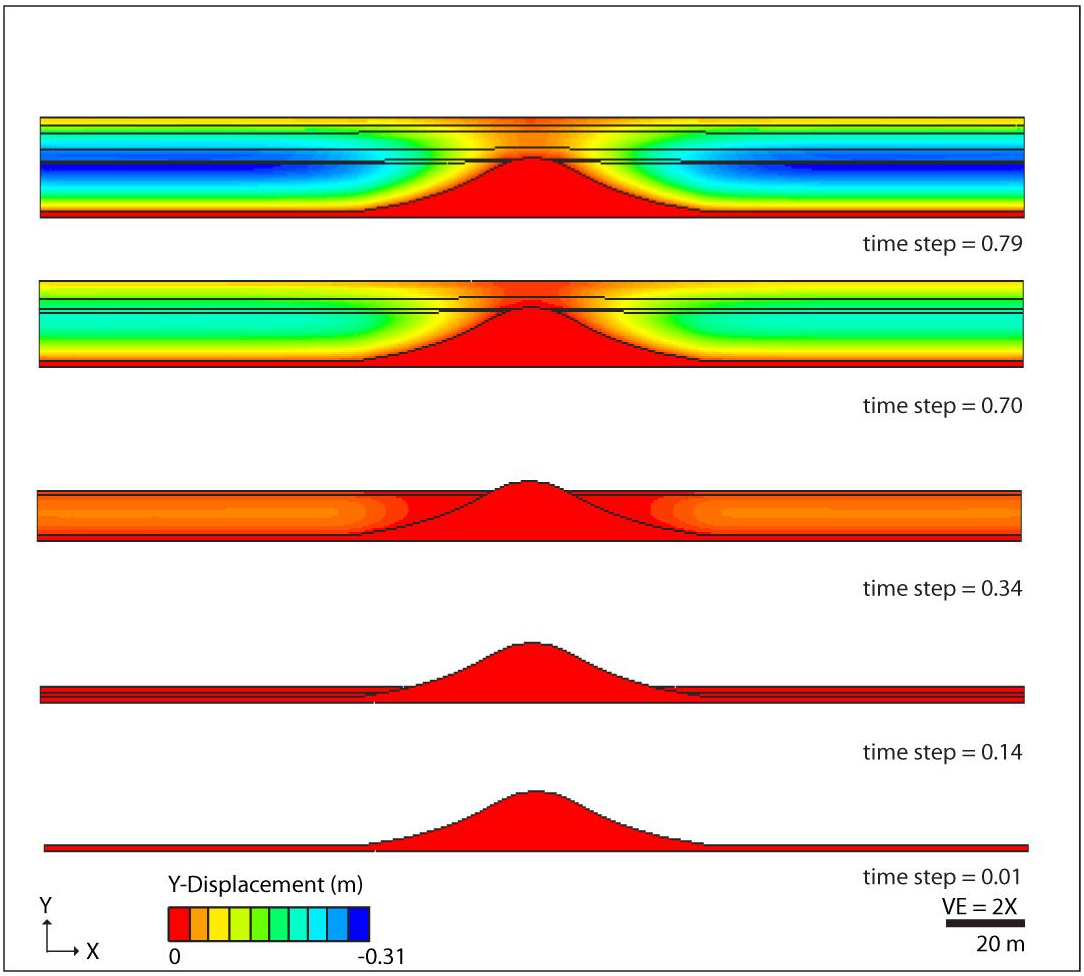
time step = 0.79
time step = 0.70
time step = 0.34
time step = 0.14
time step = 0.01
Y-Displacement (m)
0
-0.31
Y
X
VE = 2X
20 m

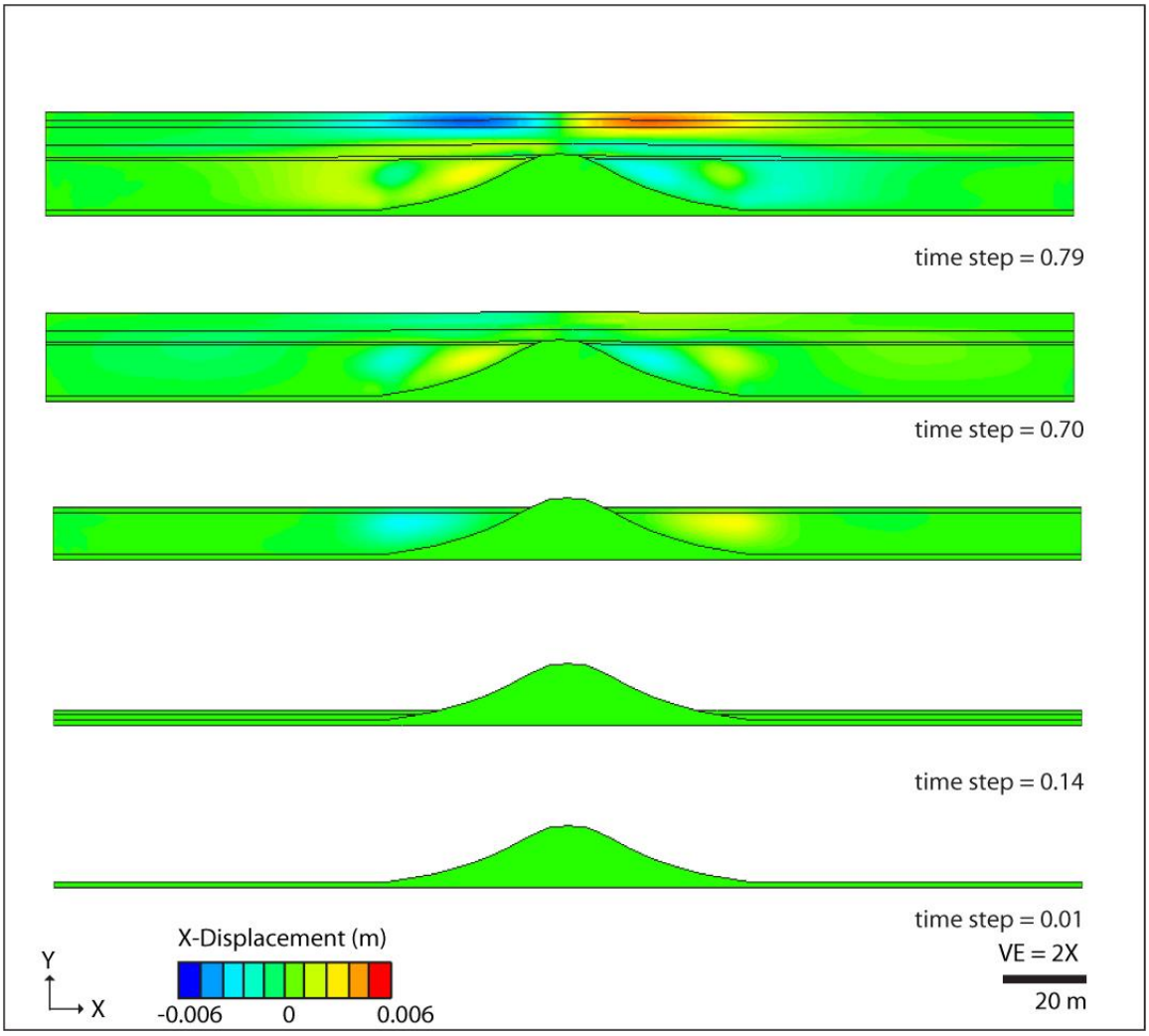
time step = 0.79
time step = 0.70
time step = 0.14
time step = 0.01
VE = 2X
20 m
X-Displacement (m)
-0.006
0
0.006
Y
X

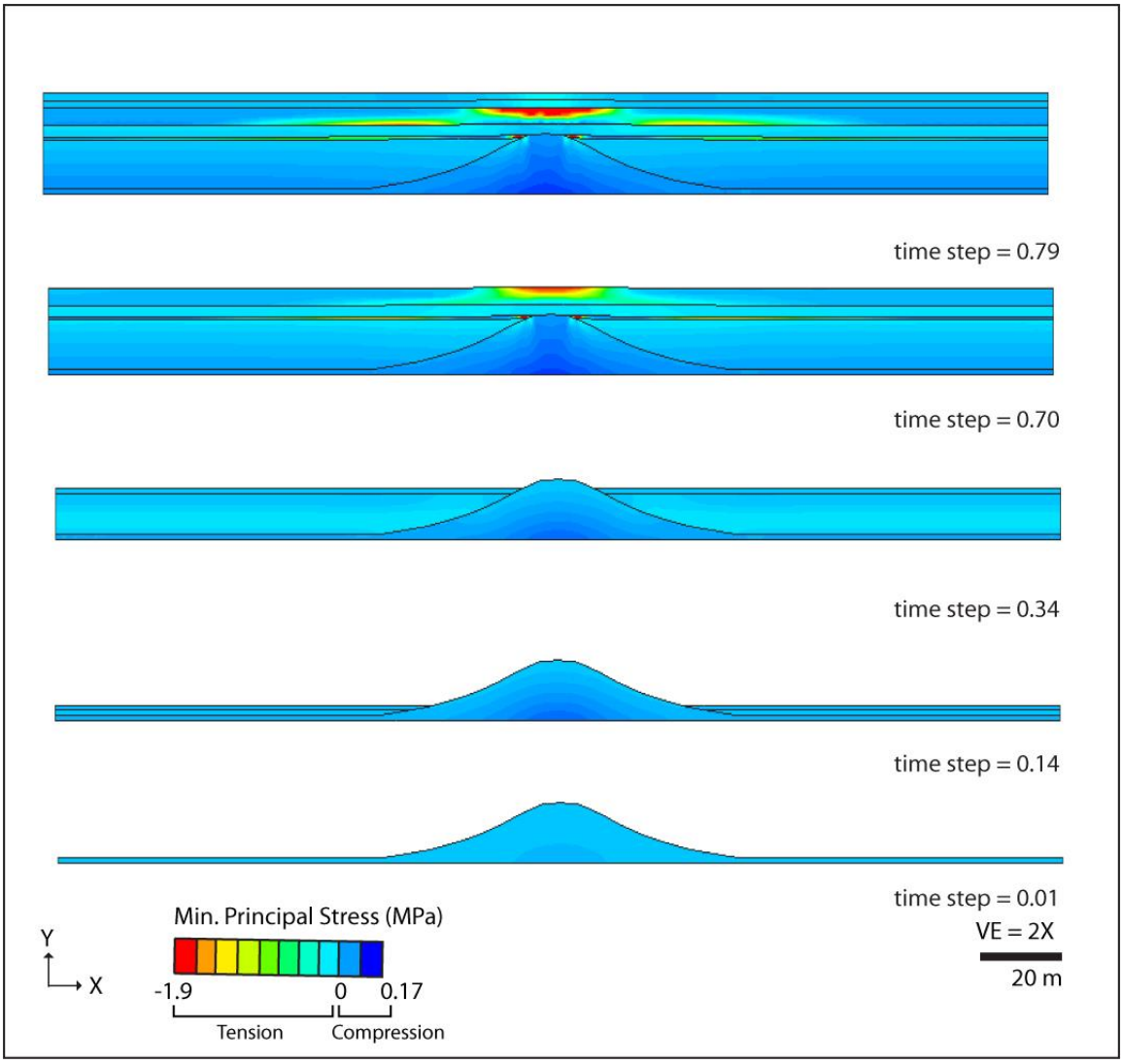
time step = 0.79
time step = 0.70
time step = 0.34
time step = 0.14
time step = 0.01
VE = 2X
20 m
Min. Principal Stress (MPa)
-1.9
0
0.17
Tension
Compression
Y
X

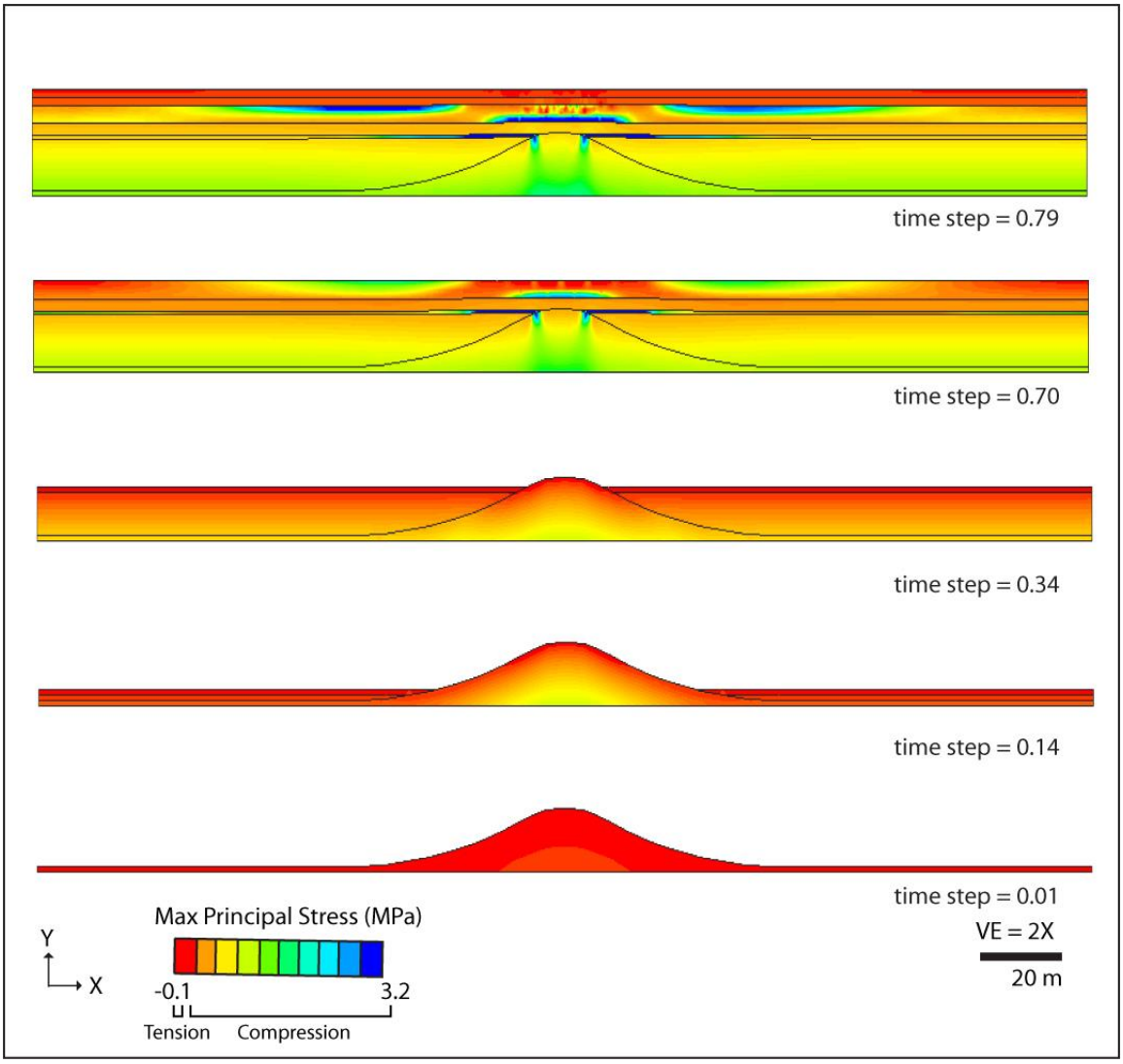
time step = 0.79
time step = 0.70
time step = 0.34
time step = 0.14
time step = 0.01
VE = 2X
20 m
Max Principal Stress (MPa)
-0.1
3.2
Tension
Compression
Y
X

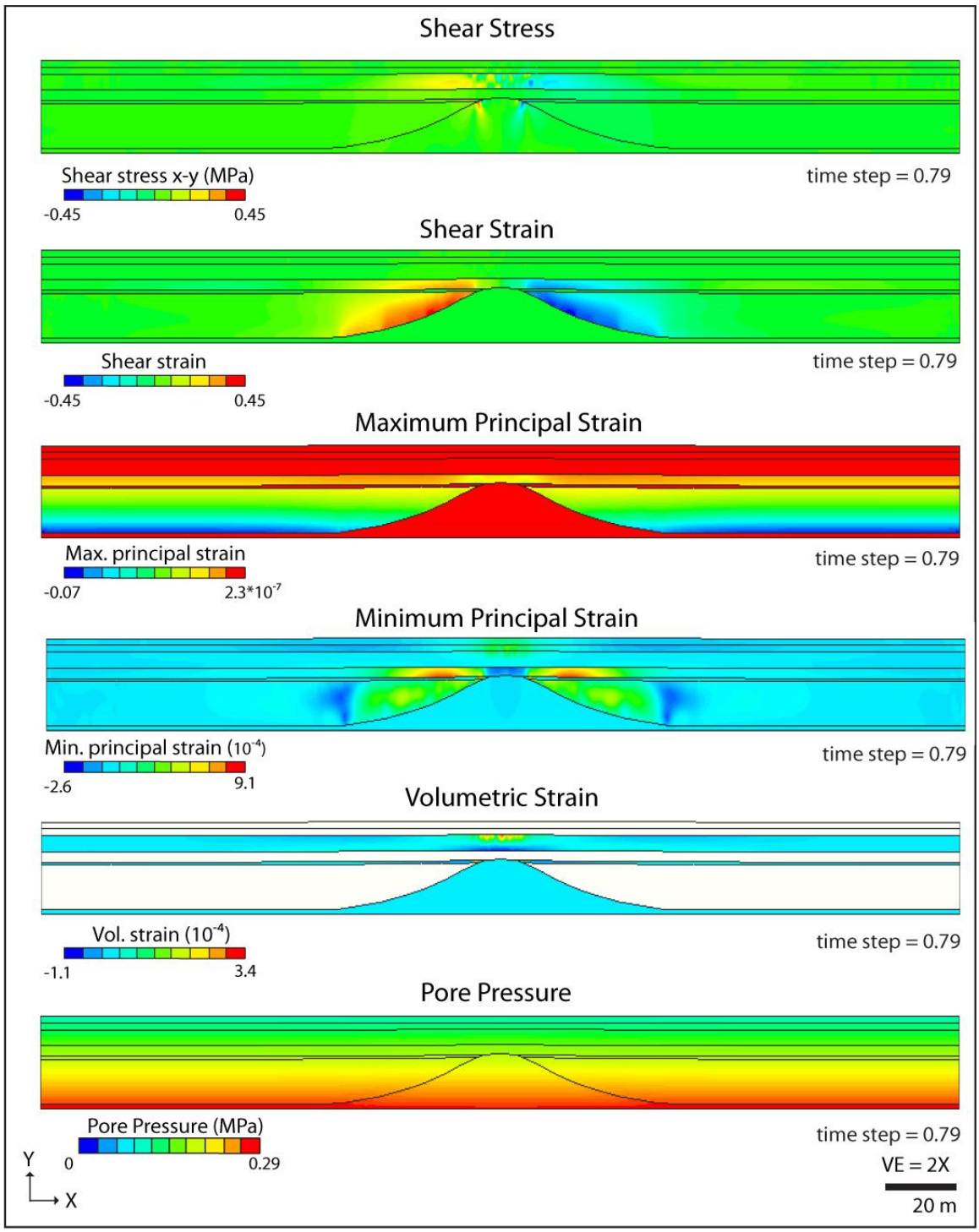
Shear Stress
Shear stress x-y (MPa)
-0.45
0.45
time step = 0.79
Shear Strain
Shear strain
-0.45
0.45
time step = 0.79
Maximum Principal Strain
Max. principal strain
-0.07
2.3*10-7
time step = 0.79
Minimum Principal Strain
Min. principal strain (10-4)
-2.6
9.1
time step = 0.79
Volumetric Strain
Vol. strain (10-4)
-1.1
3.4
time step = 0.79
Pore Pressure
Pore Pressure (MPa)
0
0.29
time step = 0.79
VE = 2X
20 m
Y
X

FORWARD NUMERICAL MODEL WITH DISCRETE FRACTURING (DISCONTINUUM)

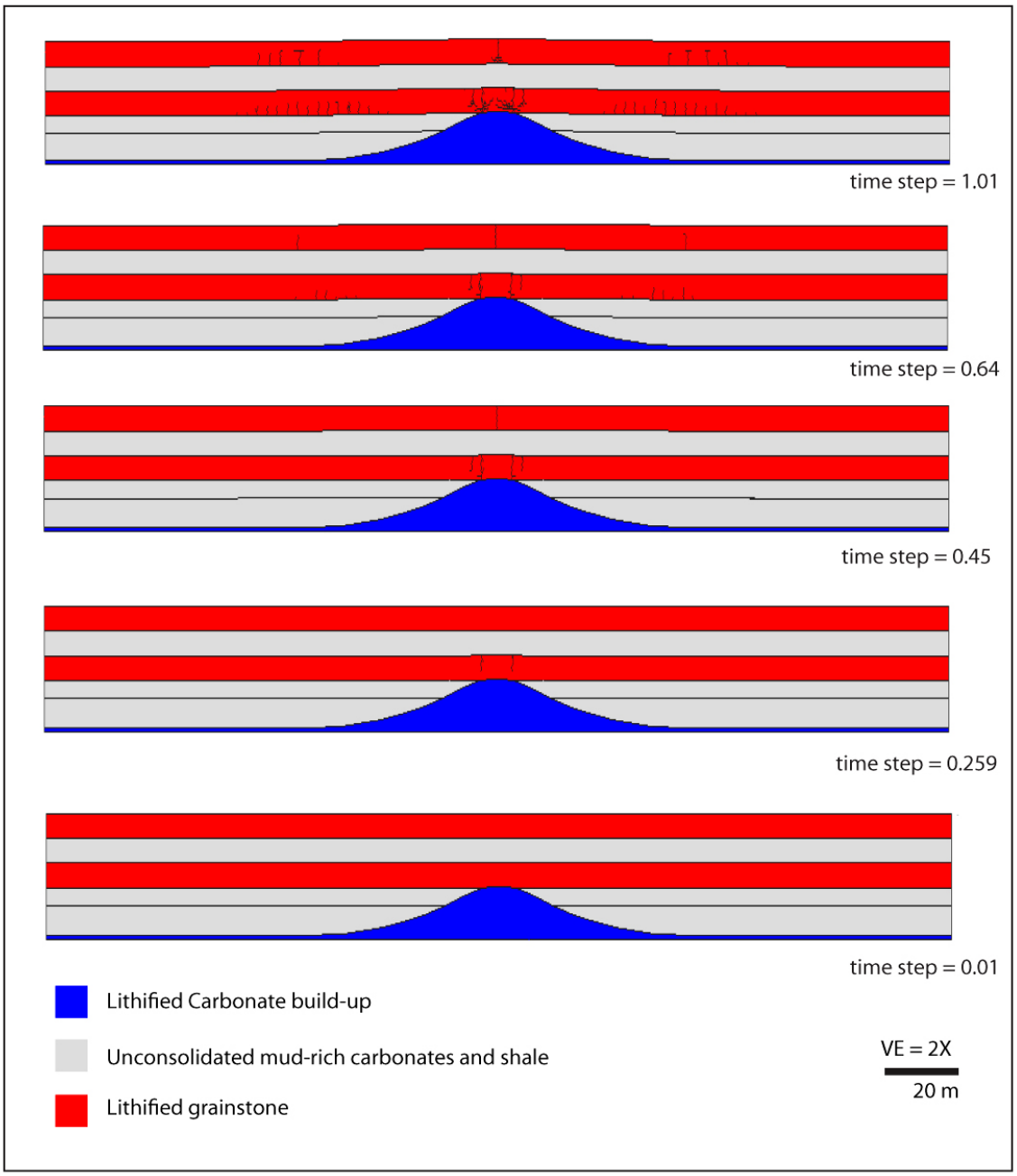

Note: Gravity load is fully applied at time step 0.01 after which displacement constraints are relaxed gradually over 1.0 time step to allow for compaction. Material properties and failure criteria used for this model similar to the base case in chapter 3.

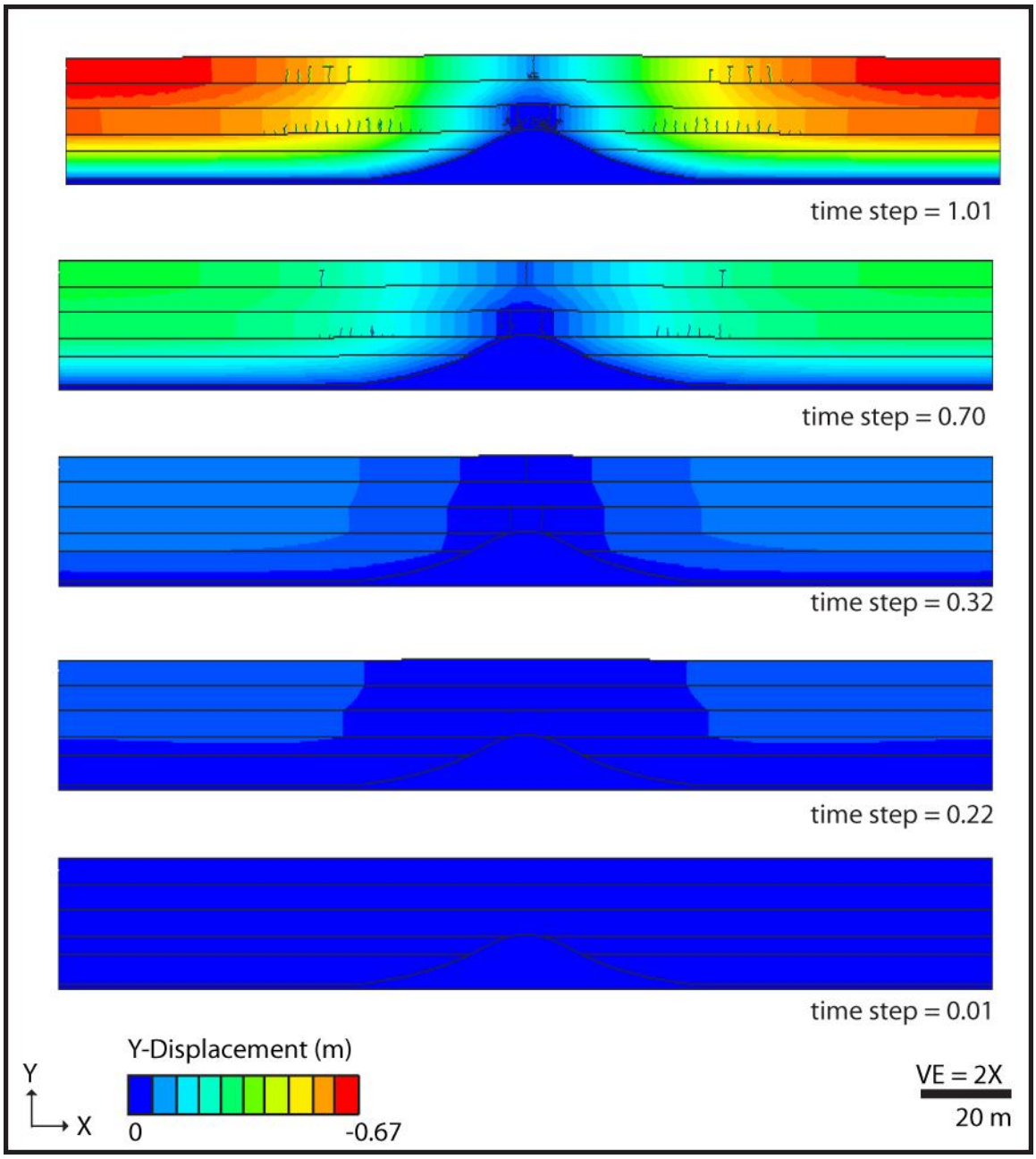
time step = 1.01
time step = 0.70
time step = 0.32
time step = 0.22
time step = 0.01
Y-Displacement (m)
0
-0.67
Y
X
VE = 2X
20 m

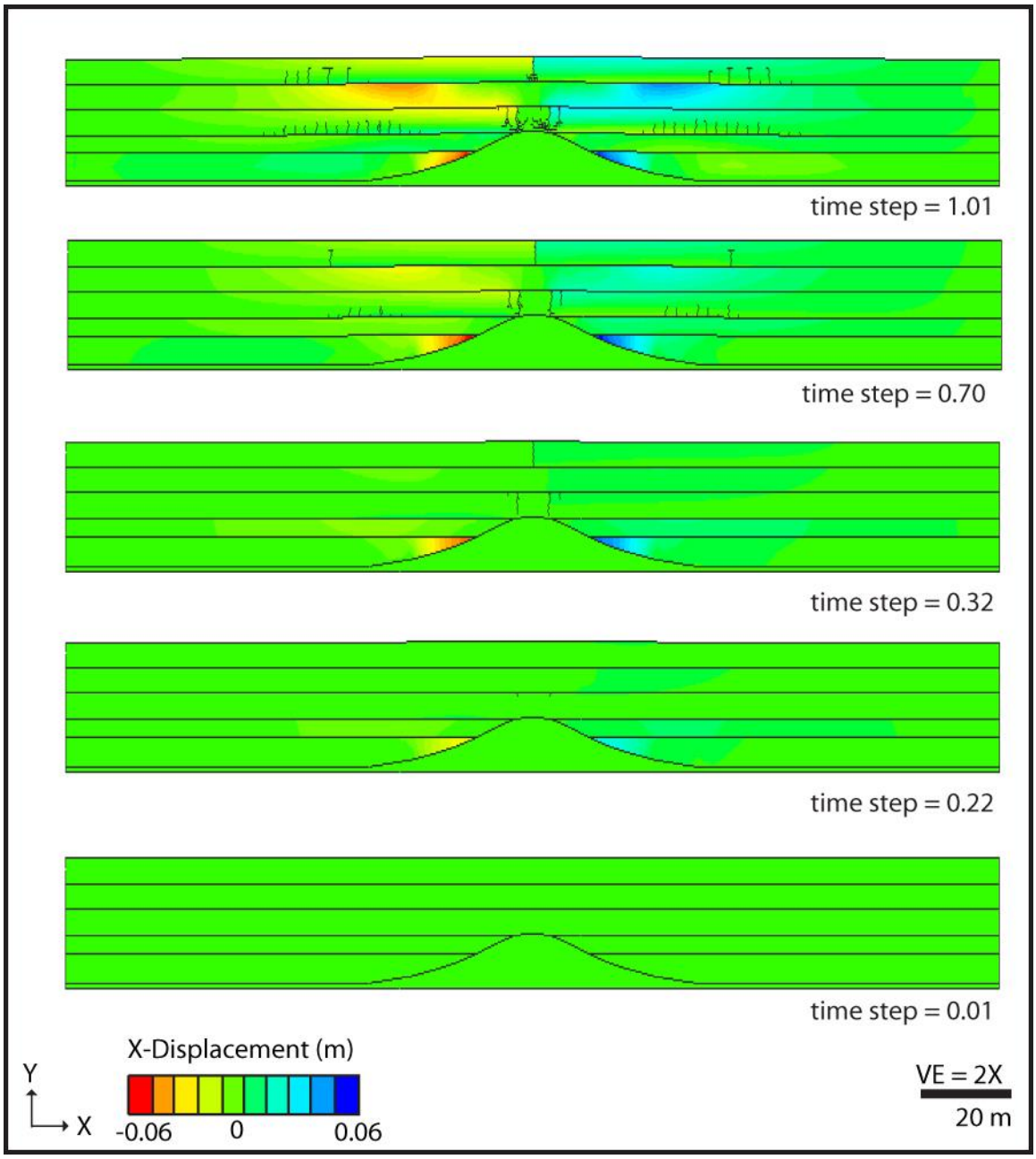
time step = 1.01
time step = 0.70
time step = 0.32
time step = 0.22
time step = 0.01
X-Displacement (m)
-0.06
0
0.06
Y
X
VE = 2X
20 m

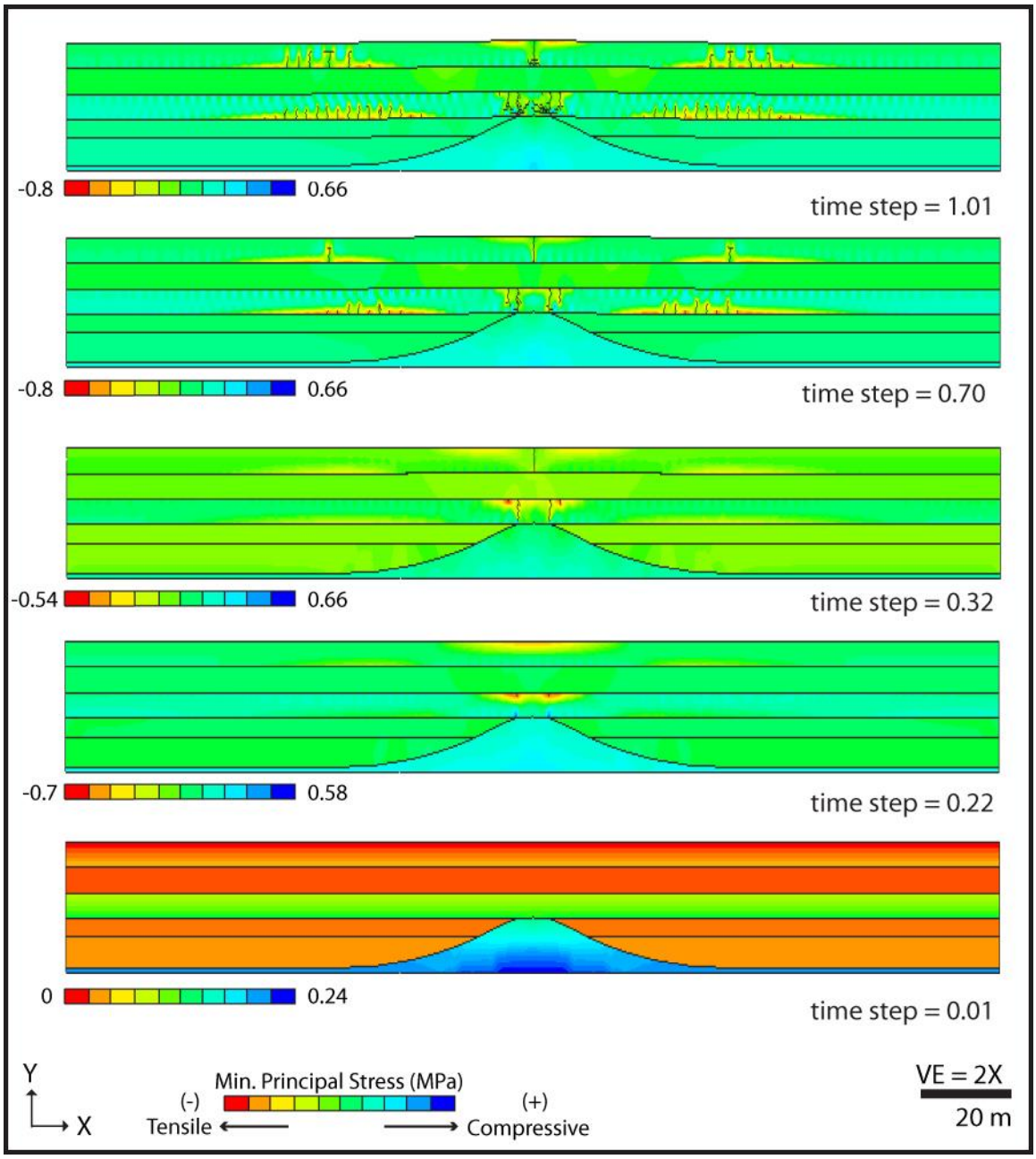
-0.8
0.66
time step = 1.01
-0.8
0.66
time step = 0.70
-0.54
0.66
time step = 0.32
-0.7
0.58
time step = 0.22
0
0.24
time step = 0.01
Y
X
Min. Principal Stress (MPa)
(-)
Tensile
(+)
Compressive
VE = 2X
20 m

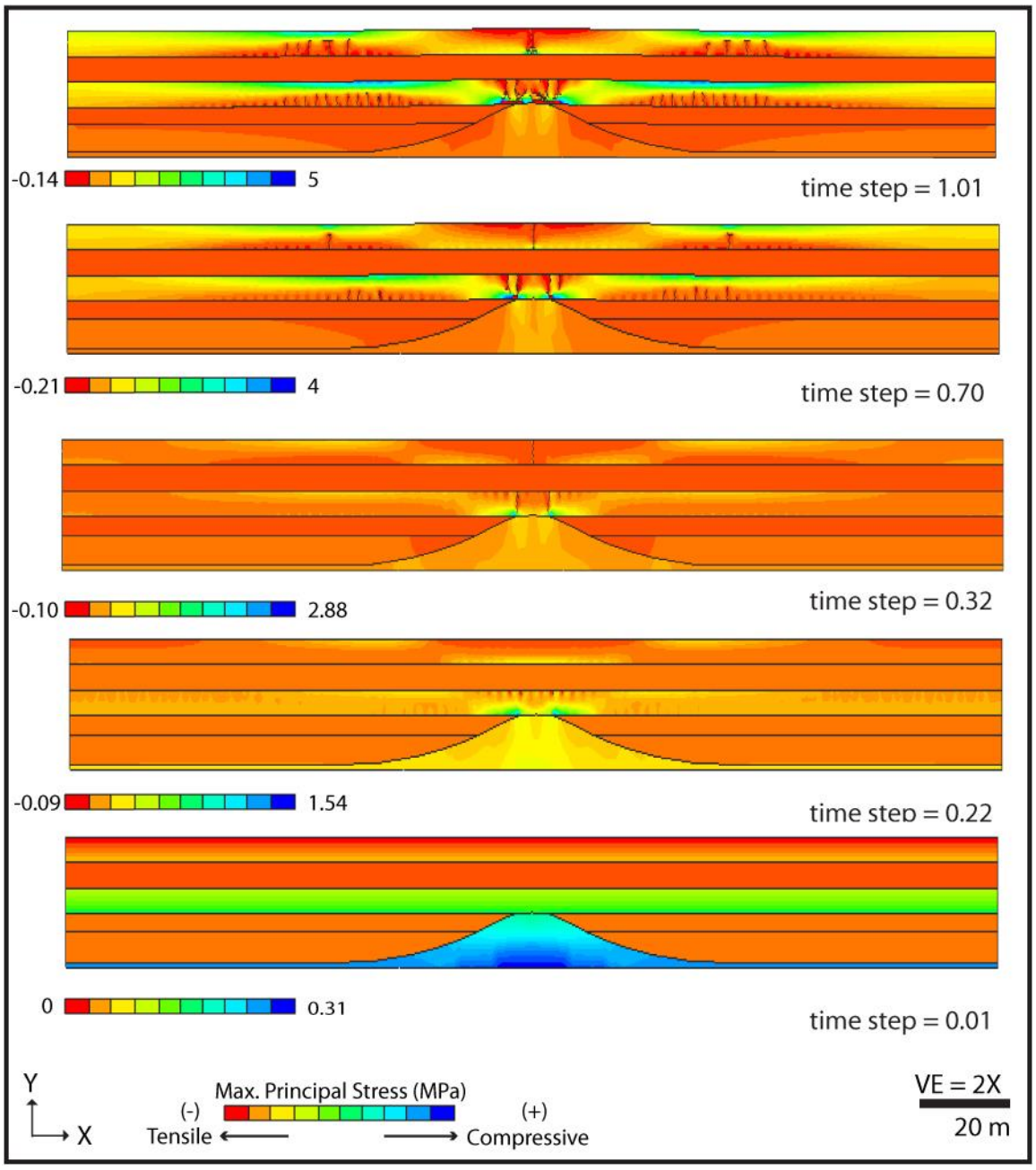
-0.14
5
time step = 1.01
-0.21
4
time step = 0.70
-0.10
2.88
time step = 0.32
-0.09
1.54
time step = 0.22
0
0.31
time step = 0.01
Y
X
Max. Principal Stress (MPa)
(-)
Tensile
(+)
Compressive
VE = 2X
20 m

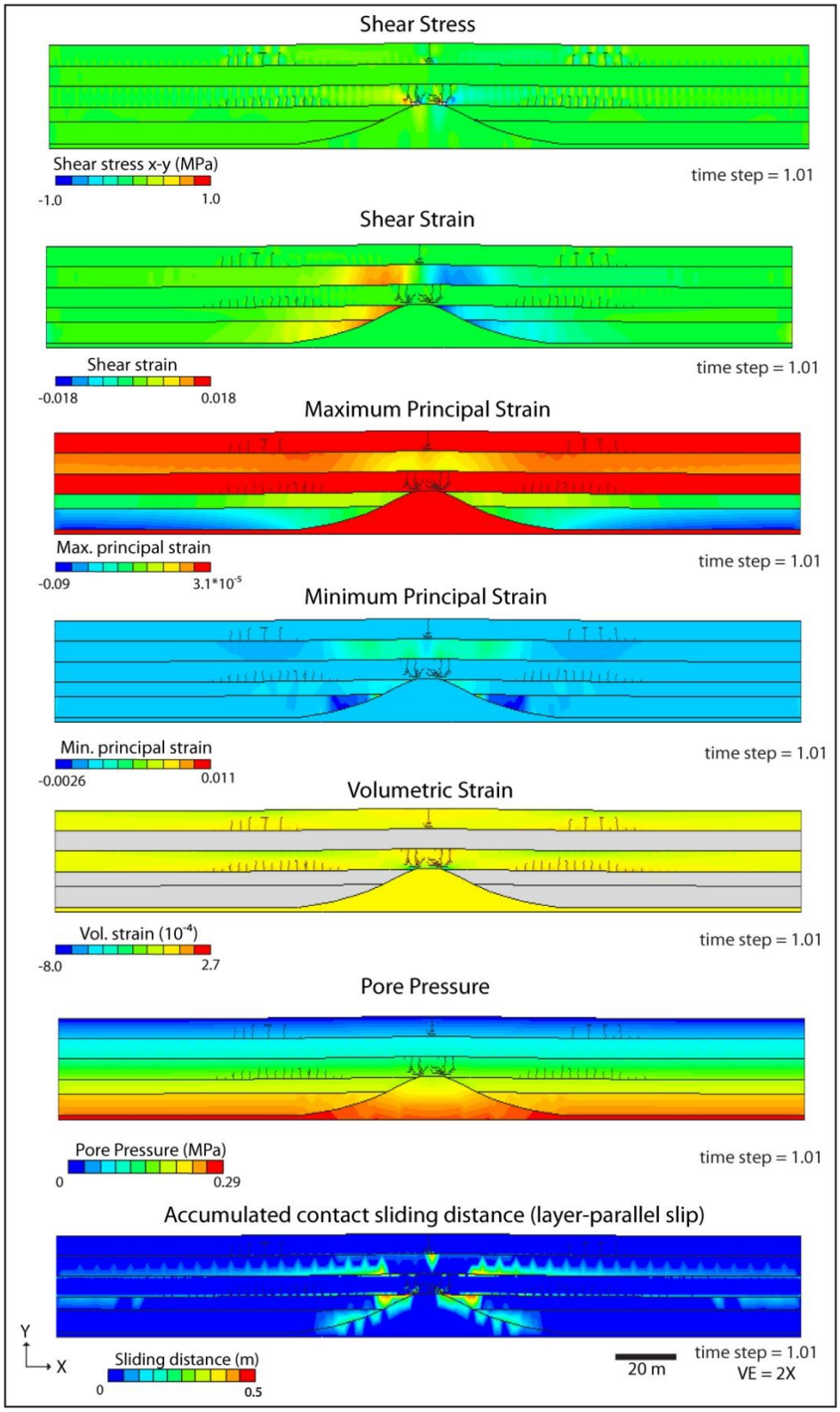
Shear Stress
Shear stress x-y (MPa)
-1.0
1.0
time step = 1.01
Shear Strain
Shear strain
-0.018
0.018
time step = 1.01
Maximum Principal Strain
Max. principal strain
-0.09
3.1*10-5
time step = 1.01
Minimum Principal Strain
Min. principal strain
-0.0026
0.011
time step = 1.01
Volumetric Strain
Vol. strain (10-4)
-8.0
2.7
time step = 1.01
Pore Pressure
Pore Pressure (MPa)
0
0.29
time step = 1.01
Accumulated contact sliding distance (layer-parallel slip)
Y
X
Sliding distance (m)
0
0.5
20 m
time step = 1.01
VE = 2X

Stress, Strain, and Displacment Evolution

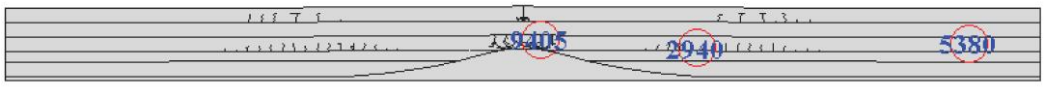

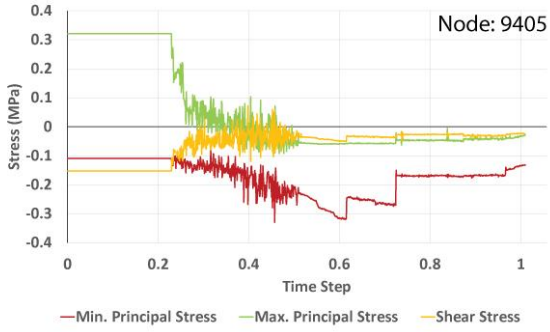

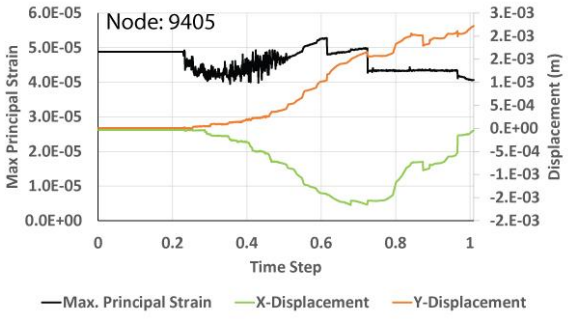

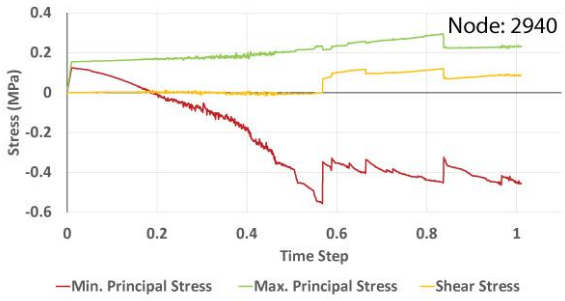

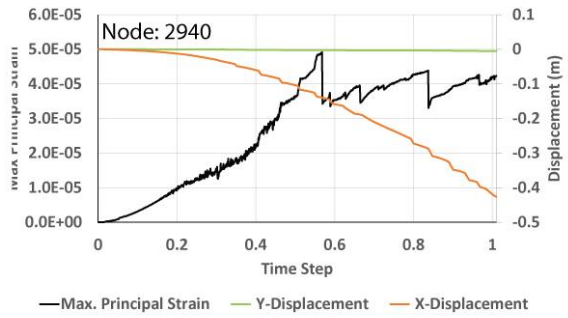

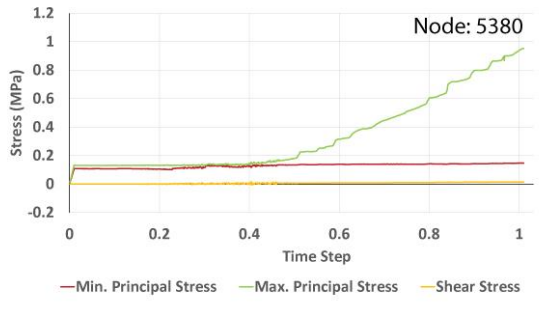

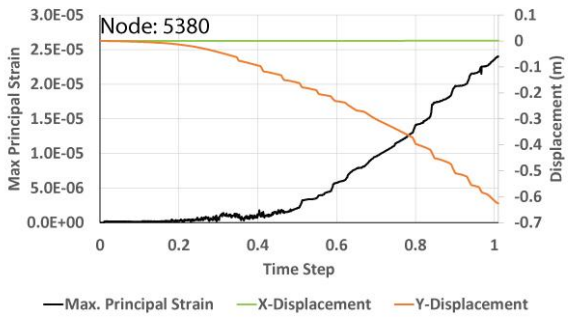

+ stress = compressive, -stress = tensile

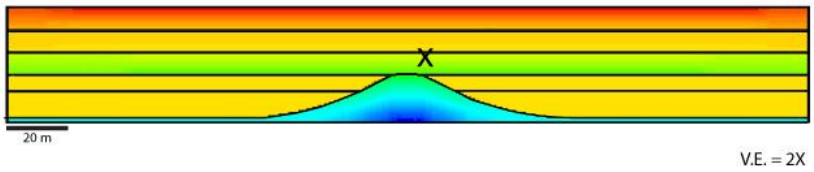

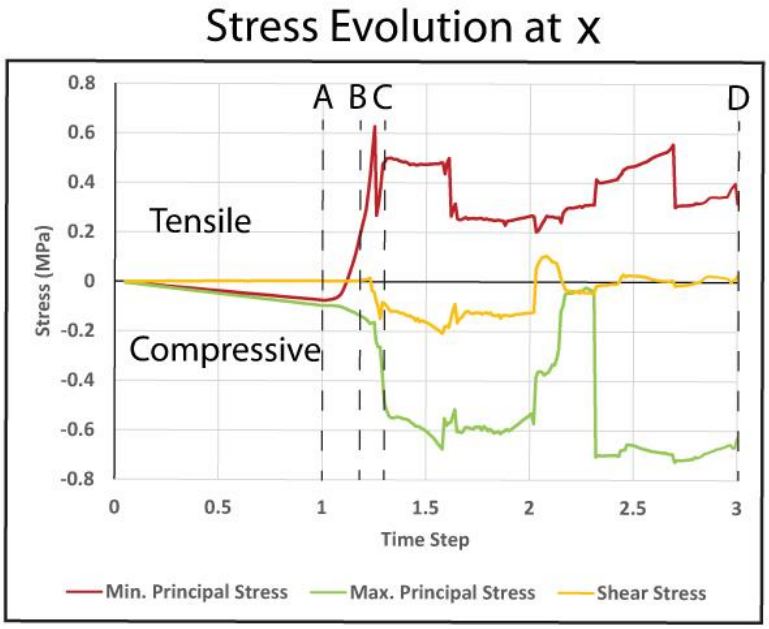

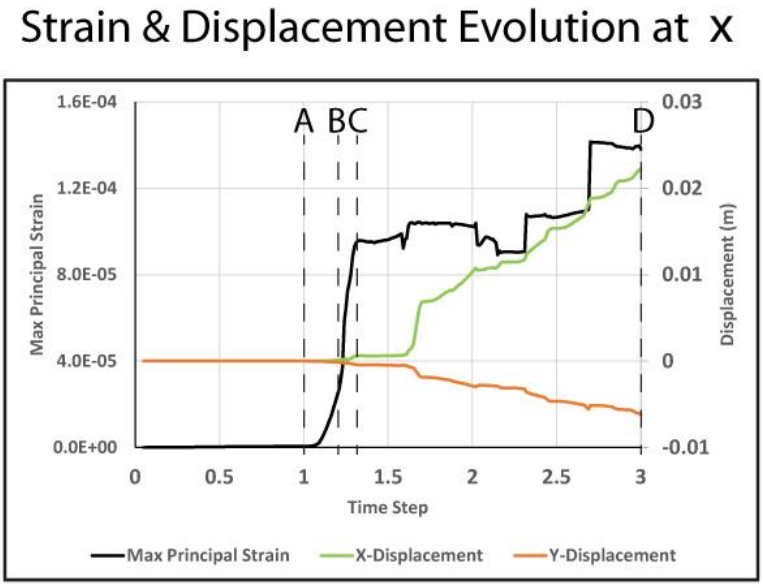

Stress, strain and displacement evolution for base model in chapter 3

Appendix E: Additional SACROC Data

SEISMIC VOLUME ATTRIBUTES

3D Dip illumination Attribute (delineates mounds)

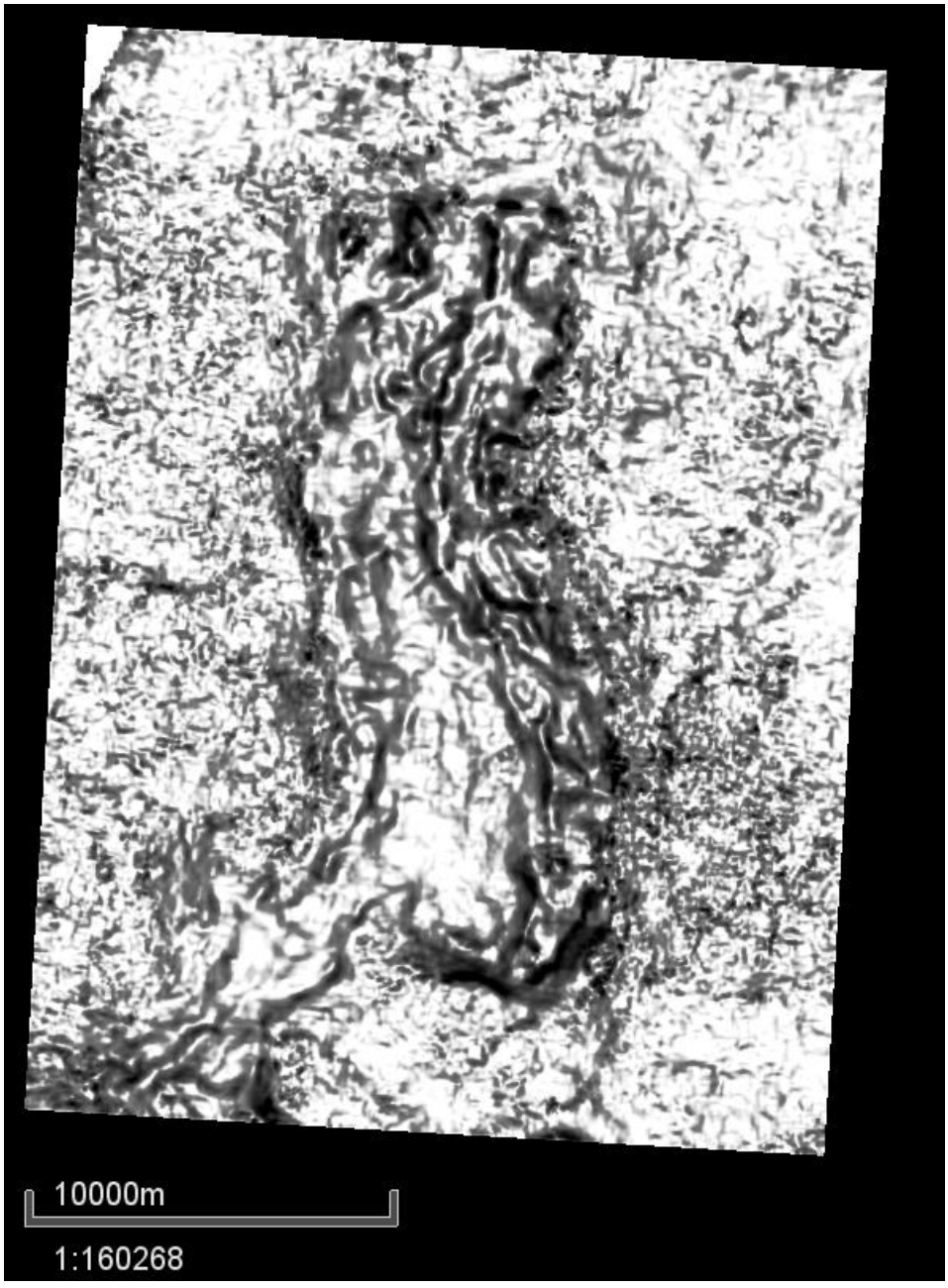

Top Cisco (platform) time slice

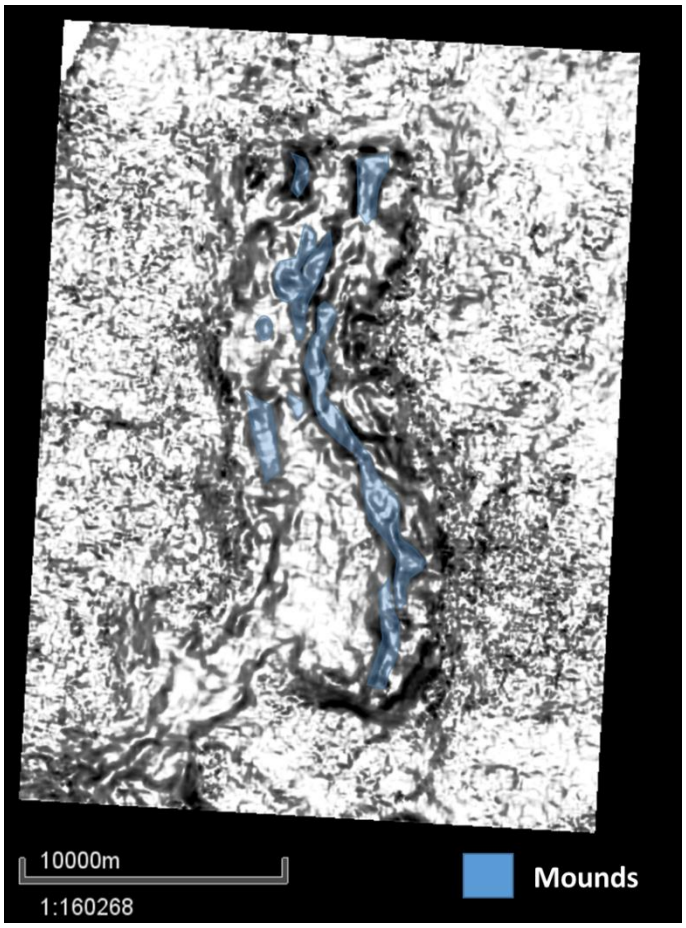

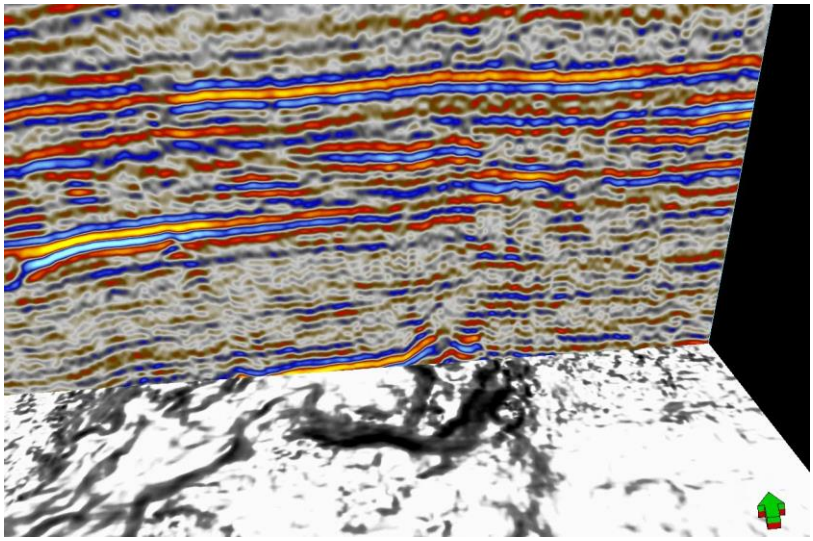

Interpreted N-S trending phylloid mounds/banks with seismic cross-section (50X) showing mounded seismic morphology corresponding to the interpreted mound features

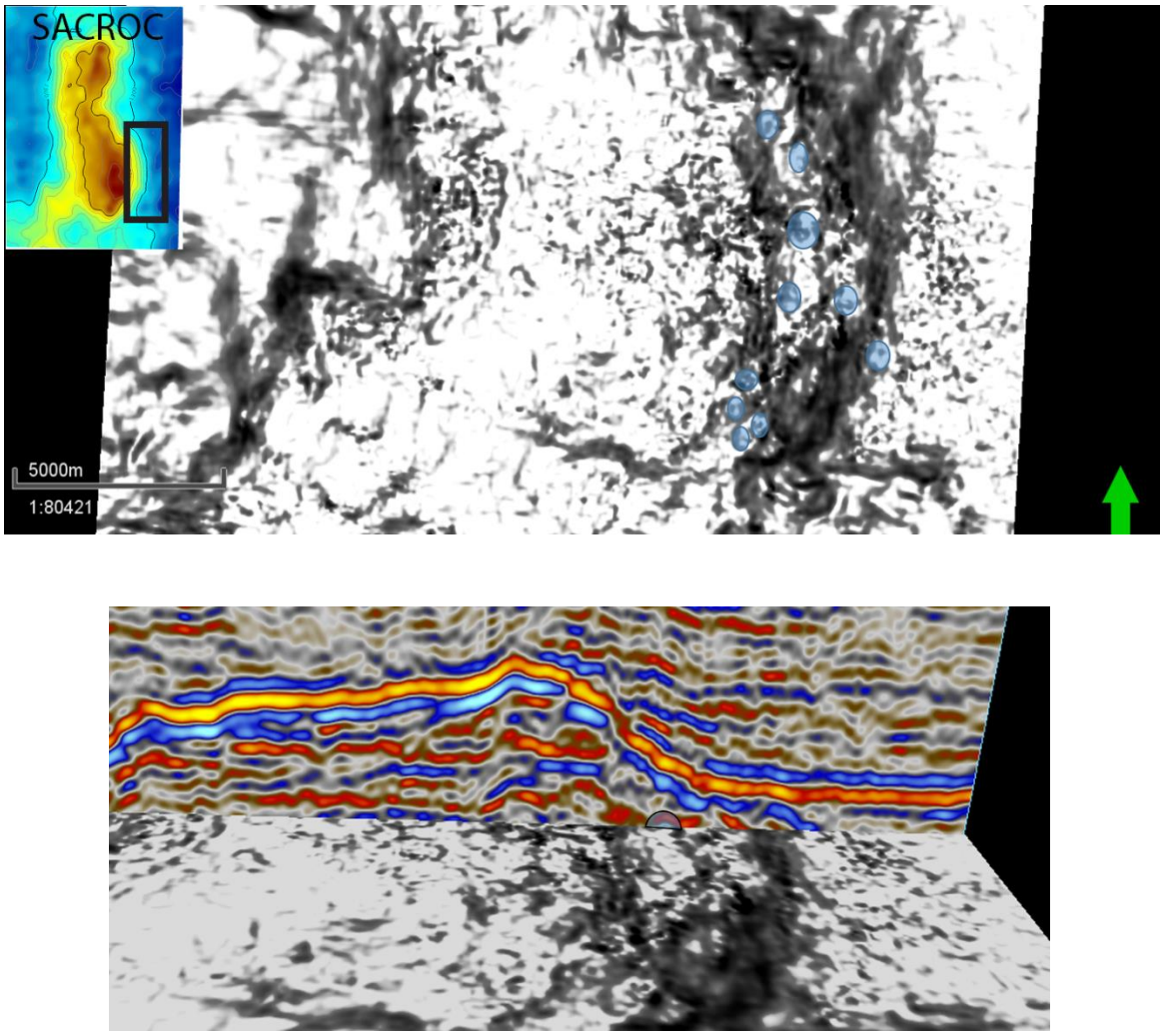

Cisco platform slope time slice with interpreted circular mounds

Maximum Curvature

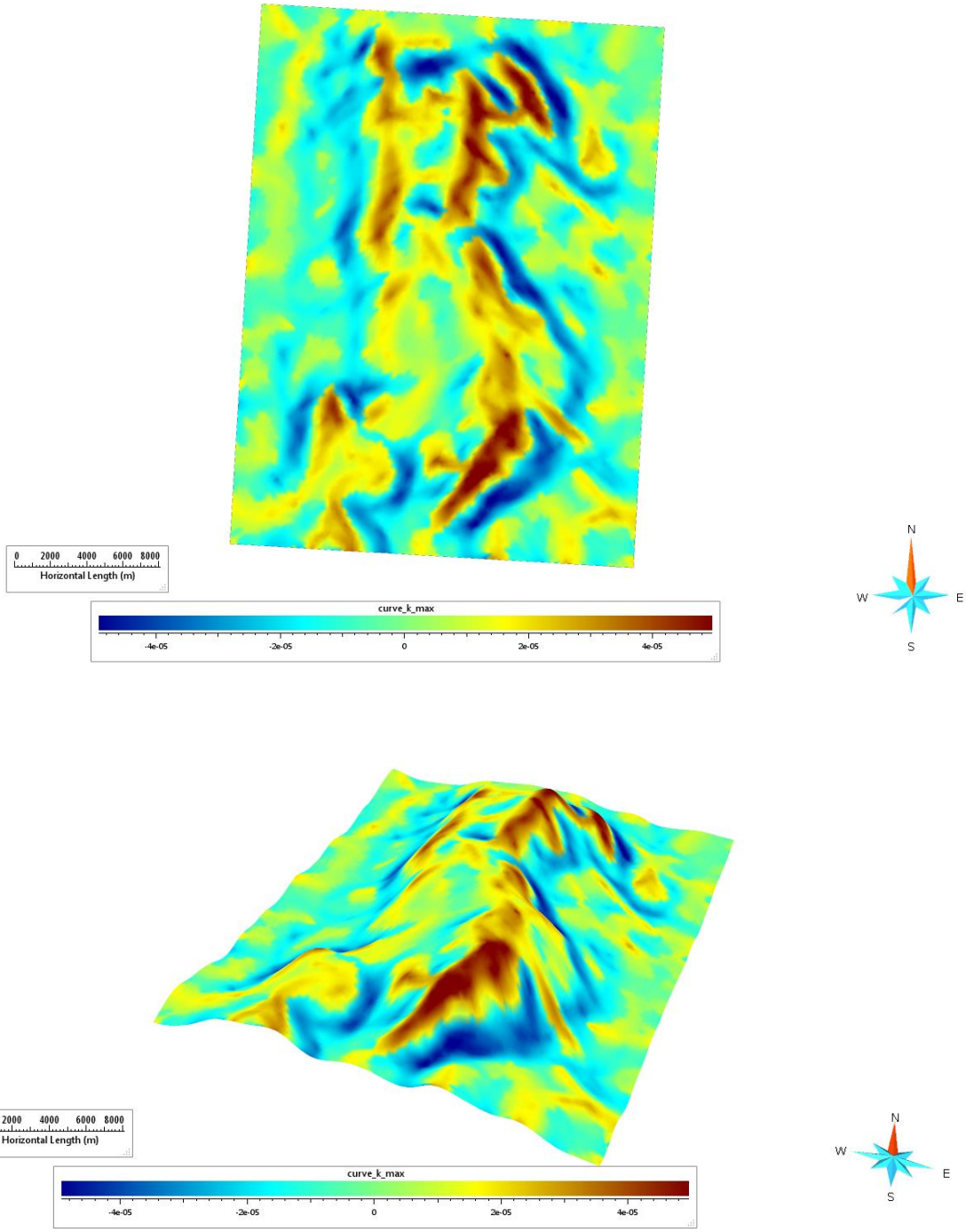

Map view and side view of top Cisco maximum curvature. Note: vertical exaggeration = 25X.

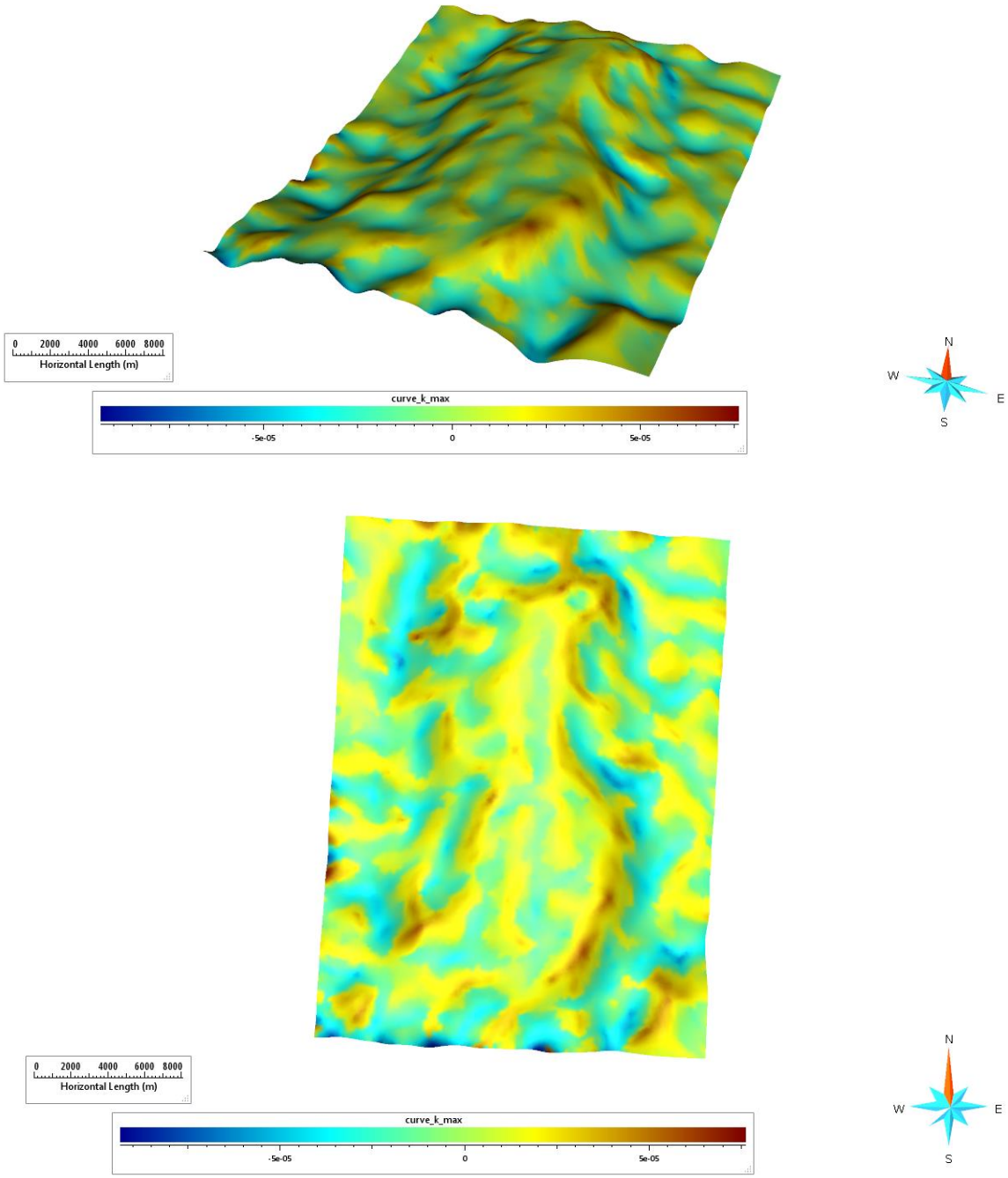

Map view and side view of top Canyon maximum curvature. Note: vertical exaggeration = 25X.

FRACTURE DATA

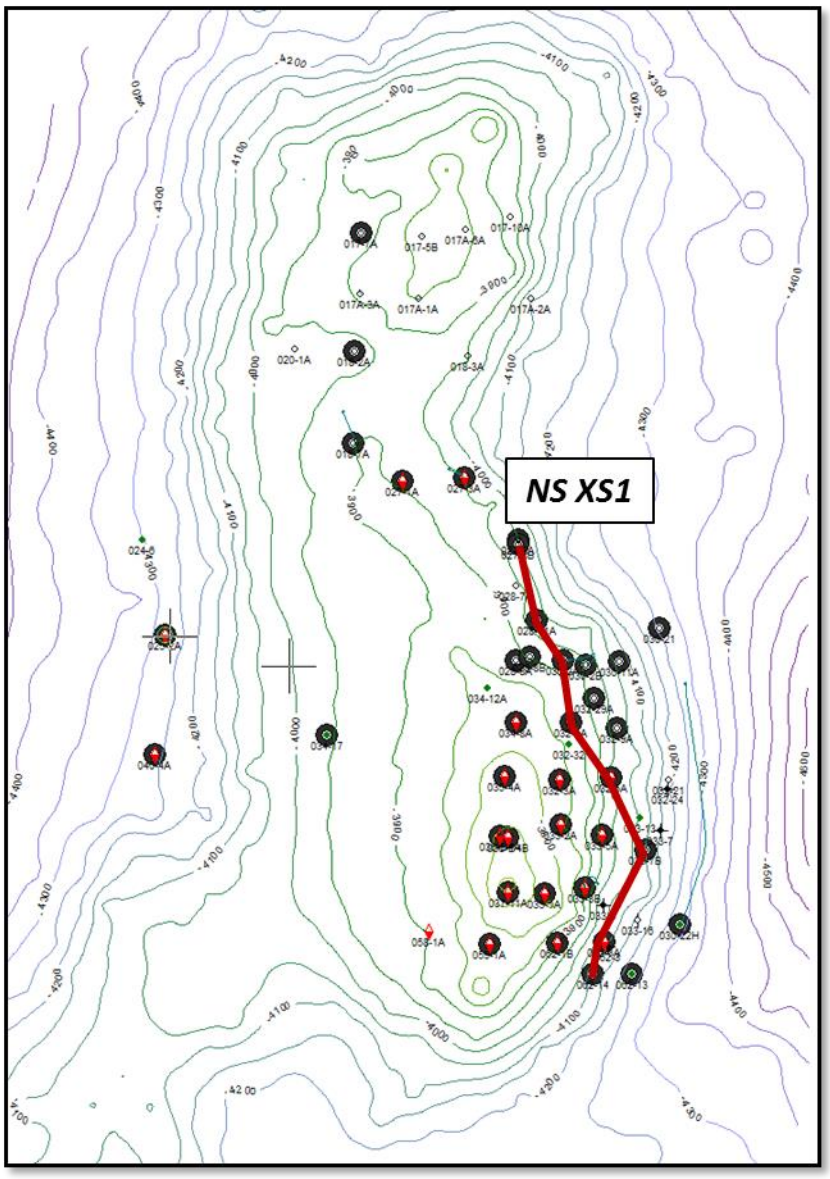

Note: Fracture data presented here is courtesy of Chris Zahm

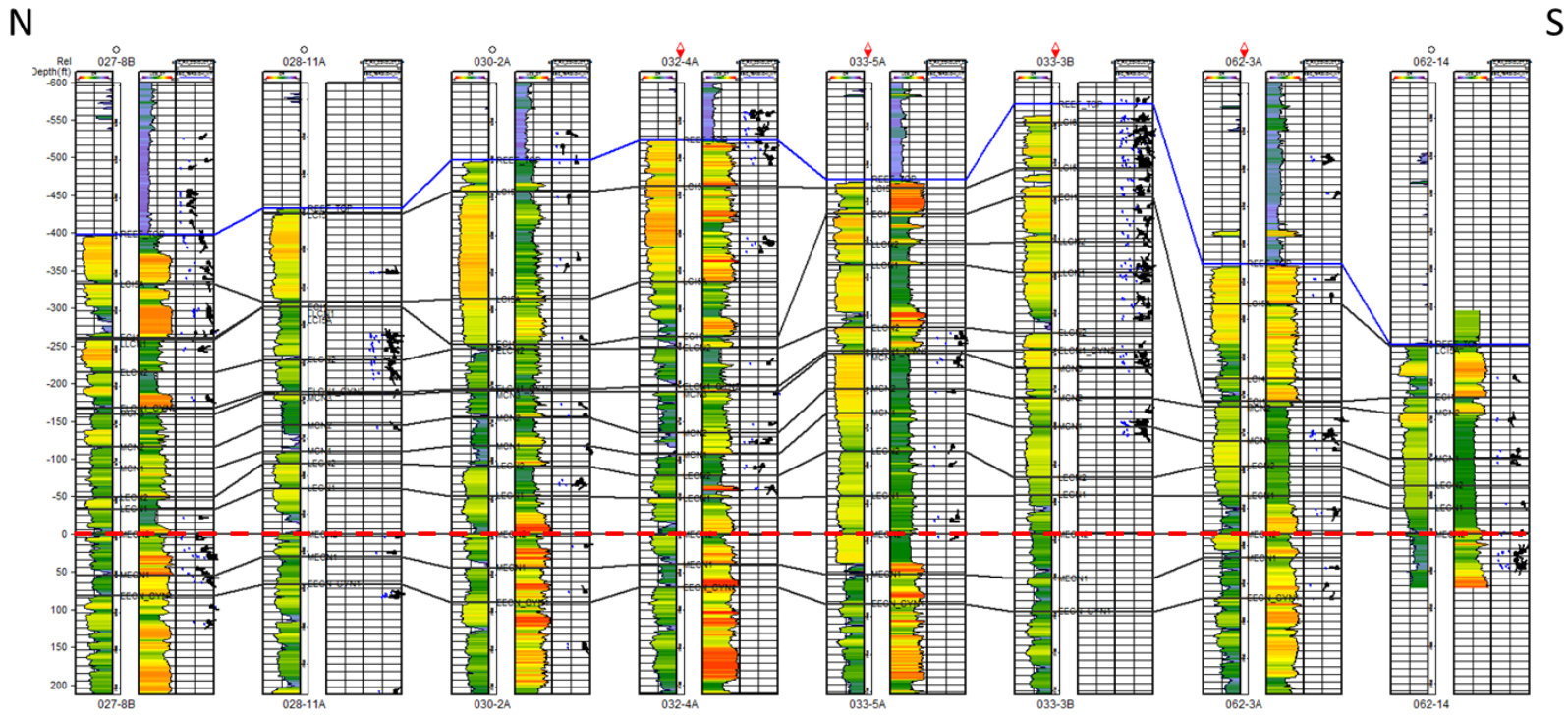

Track 1 = Gamma ray
Track 2 = UCS from DT (sonic)
Track 3 = dip, dip azimuth tadpole and Terzaghi fracture intensity

Top Cisco- blue line

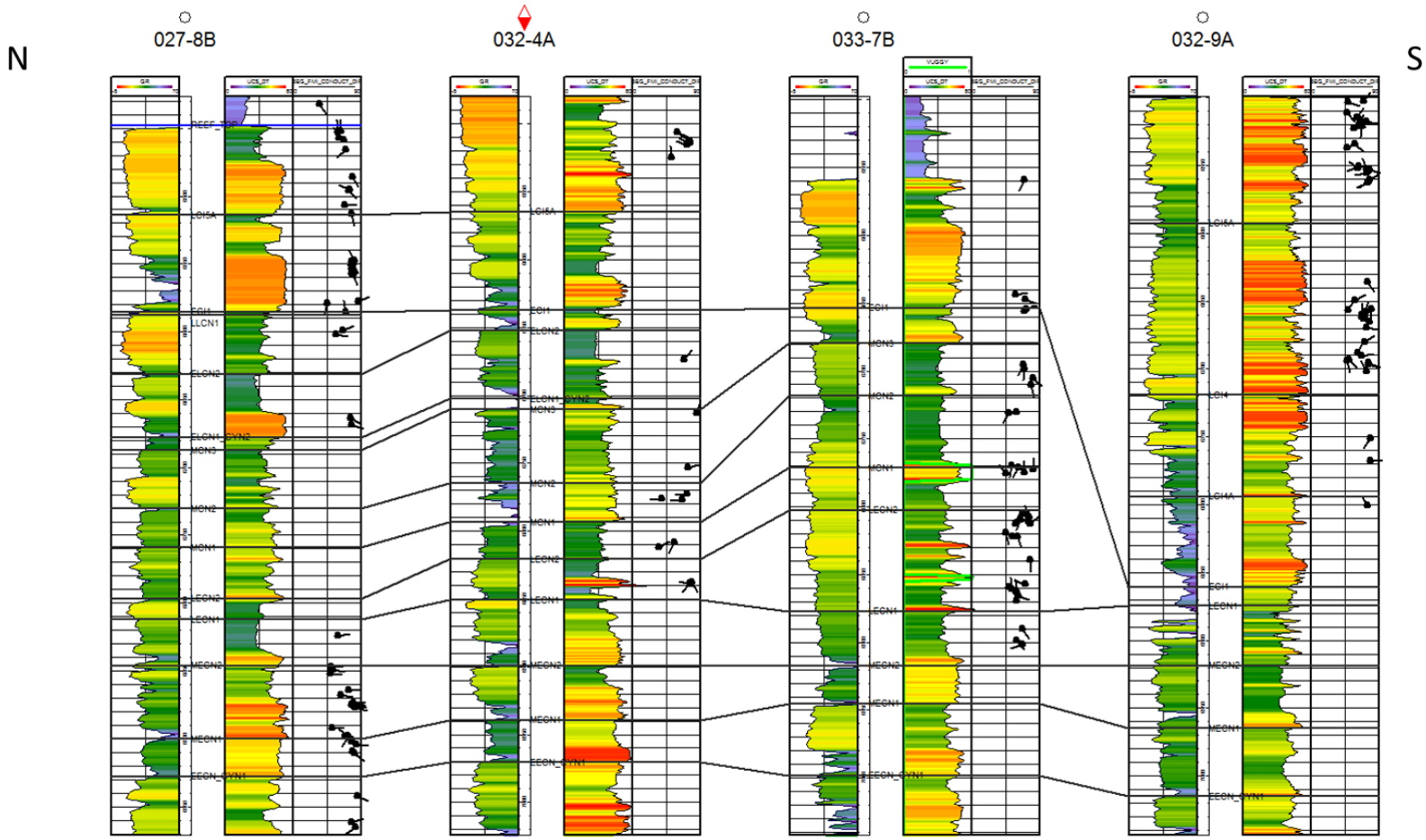

Track 1 = Gamma ray
Track 2 = UCS from DT (sonic log)
Track 3 = dip, dip azimuth tadpole

References

Albertz, M., and P. F. Sanz, 2012, Critical state finite element models of contractional fault-related folding: Part 2. Mechanical analysis: Tectonophysics, v. 576-577, p. 150-170.

Aldrich, M., C. Chapin, and A. Laughlin, 1986, Stress history and tectonic development of the Rio Grande rift, New Mexico: Journal of Geophysical Research: Solid Earth (1978–2012), v. 91, p. 6199-6211.

Allen, H. H., and J. B. Thomas, 1959, Pressure Maintenance in SACROC Unit Operations January 1, 1959.

Alnazgha, M., and C. Kerans, 2018, Stratigraphic Architecture and Platform Geometry of Isolated Platform: SACROC Field, Horseshoe Atoll, Texas

ASTM, 2014, Standard Test Method for Determination of Rock Hardness by Rebound Hammer Method, ASTM D5873-14, West Conshohocken, Pa, International.

Aydin, A., 2008, ISRM suggested method for determination of the Schmidt hammer rebound hardness: revised version, The ISRM Suggested Methods for Rock Characterization, Testing and Monitoring: 2007-2014, Springer, p. 25-33.

Aydin, A., and A. Basu, 2005, The Schmidt hammer in rock material characterization: Engineering Geology, v. 81, p. 1-14.

Bathurst, R. G. C., 1982, Genesis of stromatactis cavities between submarine crusts in Palaeozoic carbonate mud buildups: Journal of the Geological Society, v. 139, p. 165-181.

Berglund, H. T., A. F. Sheehan, M. H. Murray, M. Roy, A. R. Lowry, R. S. Nerem, and F. Blume, 2012, Distributed deformation across the Rio Grande rift, Great Plains, and Colorado plateau: Geology, v. 40, p. 23-26.

Bourrouilh, R., P.-A. Bourque, P. Dansereau, F. Bourrouilh-Le Jan, and P. Weyant, 1998, Synsedimentary tectonics, mud-mounds and sea-level changes on a Palaeozoic carbonate platform margin: a Devonian Montagne Noire example (France): Sedimentary geology, v. 118, p. 95-118.

Brown, C. D., and R. J. Phillips, 1999, Flexural rift flank uplift at the Rio Grande rift, New Mexico: Tectonics, v. 18, p. 1275-1291.

Budd, D. A., E. L. Frost, K. W. Huntington, and P. F. Allwardt, 2013, Syndepositional Deformation Features In High-Relief Carbonate Platforms: Long-Lived Conduits for Diagenetic Fluids: Journal of Sedimentary Research, v. 83, p. 12-36.

Chapin, C. E., 1979, Evolution of the Rio Grande rift–A summary: Rio Grande rift: tectonics and magmatism, v. 14, p. 1-6.

Collins, J. F., J. A. Kenter, P. M. Harris, G. Kuanysheva, and D. F. K. Steffen, 2006, Facies and reservoir-quality variations in the late Visean to Bashkirian outer platform, rim, and flank of the Tengiz buildup, Precaspian Basin, Kazakhstan.

Cook, H. E., V. G. Zhemchuzhnikov, W. G. Zempolich, V. Y. Zhaimina, V. M. Buvtyshkin, E. A. Kotova, L. Y. Golub, A. Y. Zorin, P. J. Lehmann, and D. V. Alexeiev, 2002, Devonian and Carboniferous carbonate platform facies in the Bolshoi Karatau, Southern Kazakhstan: outcrop analogs for coeval carbonate oil and gas fields in the North Caspian Basin, Western Kazakhstan.

Cooke, M. L., P. N. Mollema, D. D. Pollard, and A. Aydin, 1999, Interlayer slip and joint localization in the East Kaibab Monocline, Utah: field evidence and results from numerical modelling: Geological Society, London, Special Publications, v. 169, p. 23-49.

Cooke, M. L., J. A. Simo, C. A. Underwood, and P. Rijken, 2006, Mechanical stratigraphic controls on fracture patterns within carbonates and implications for groundwater flow: Sedimentary Geology, v. 184, p. 225-239.

Cooke, M. L., and C. A. Underwood, 2001, Fracture termination and step-over at bedding interfaces due to frictional slip and interface opening: Journal of Structural Geology, v. 23, p. 223-238.

Corbett, K., M. Friedman, and J. Spang, 1987, Fracture development and mechanical stratigraphy of Austin Chalk, Texas: AAPG Bulletin, v. 71, p. 17-28.

Cozzi, A., 2000, Synsedimentary tensional features in Upper Triassic shallow-water platform carbonates of the Carnian Prealps (northern Italy) and their importance as palaeostress indicators: Basin Research, v. 12, p. 133-146.

Crook, A. J. L., S. M. Willson, J. G. Yu, and D. R. J. Owen, 2006, Predictive modelling of structure evolution in sandbox experiments: Journal of Structural Geology, v. 28, p. 729-744.

Cross, T. A., and M. J. Klosterman, 1981, Primary Submarine Cements and Neomorphic Spar in a Stromatolitic-Bound Phylloid Algal Bioherm, Laborcita Formation (Wolfcampian), Sacramento Mountains, New Mexico, U.S.A, p. 60-73.

Davies, G. R., 1977, Former magnesian calcite and aragonite submarine cements in upper Paleozoic reefs of the Canadian Arctic: a summary: Geology, v. 5, p. 11-15.

Di Naccio, D., P. Boncio, S. Cirilli, F. Casaglia, E. Morettini, G. Lavecchia, and F. Brozzetti, 2005, Role of mechanical stratigraphy on fracture development in carbonate reservoirs: Insights from outcropping shallow water carbonates in the Umbria–Marche Apennines, Italy: Journal of volcanology and geothermal research, v. 148, p. 98-115.

Dicharry, R. M., T. Perryman, and J. Ronquille, 1973, Evaluation and design of a CO2 miscible flood project-SACROC unit, Kelly-Snyder field: Journal of Petroleum Technology, v. 25, p. 1,309-1,318.

Dickinson, W. R., W. S. Snyder, and V. Matthews, 1978, Plate tectonics of the Laramide orogeny, v. 3, Matthews.

Dravis, J. J., 1996, Rapidity of freshwater calcite cementation—implications for carbonate diagenesis and sequence stratigraphy: Sedimentary Geology, v. 107, p. 1-10.

Eberhardt, E., D. Stead, and J. S. Coggan, 2004, Numerical analysis of initiation and progressive failure in natural rock slopes—the 1991 Randa rockslide: International Journal of Rock Mechanics and Mining Sciences, v. 41, p. 69-87.
Elmo, D., A. Vyazmensky, D. Stead, and J. R. Rance, 2007, A Hybrid FEM/DEM Approach to Model the Interaction Between Open-pit And Underground Block-caving Mining, 1st Canada - U.S. Rock Mechanics Symposium, Vancouver, Canada, American Rock Mechanics Association.
Enos, P., and L. H. Sawatsky, 1981, Pore networks in Holocene carbonate sediments: Journal of Sedimentary Research, v. 51, p. 961-985.
Frost, E. L., D. A. Budd, and C. Kerans, 2012, Syndepositional deformation in a high-relief carbonate platform and its effect on early fluid flow as revealed by dolomite patterns: Journal of Sedimentary Research, v. 82, p. 913-932.
Frost, E. L., and C. Kerans, 2009, Platform-Margin Trajectory as a Control on Syndepositional Fracture Patterns, Canning Basin, Western Australia: Journal of Sedimentary Research, v. 79, p. 44-55.
Frost, E. L., and C. Kerans, 2010, Controls on syndepositional fracture patterns, Devonian reef complexes, Canning Basin, Western Australia: Journal of Structural Geology, v. 32, p. 1231-1249.
Ghahfarokhi, R. B., S. Pennell, M. Matson, and M. Linroth, 2016, Overview of CO2 Injection and WAG Sensitivity in SACROC: SPE Improved Oil Recovery Conference.
Goldhammer, R., 1997, Compaction and decompaction algorithms for sedimentary carbonates: Journal of Sedimentary Research, v. 67.
Goldstein, R., 1988a, Paleosols of Late Pennsylvanian cyclic strata, New Mexico*: Sedimentology, v. 35, p. 777-803.
Goldstein, R. H., 1988b, Cement stratigraphy of Pennsylvanian Holder Formation, Sacramento Mountains, New Mexico: AAPG bulletin, v. 72, p. 425-438.
Graham, J., M. Noonan, and K. Lew, 1983, Yield states and stress–strain relationships in a natural plastic clay: Canadian geotechnical journal, v. 20, p. 502-516.
Grammer, G. M., R. N. Ginsburg, and P. M. Harris, 1993, Timing of Deposition, Diagenesis, and Failure of Steep Carbonate Slopes in Response to a High-Amplitude/High-Frequency Fluctuation in Sea Level, Tongue of the Ocean, Bahamas: Chapter 4.
Guidry, S. A., M. Grasmueck, D. G. Carpenter, A. M. Gombos, S. L. Bachtel, and D. A. Viggiano, 2007, Karst and Early Fracture Networks in Carbonates, Turks and Caicos Islands, British West Indies: Journal of Sedimentary Research, v. 77, p. 508-524.
Gutteridge, P., 1995, Late Dinantian (Brigantian) Carbonate Mud-Mounds of the Derbyshire Carbonate Platform, *in* C. L. V. Monty, D. W. J. Bosence, P. H. Bridges, and B. R. Pratt, eds., Carbonate Mud-Mounds: Oxford, UK. , Blackwell Publishing Ltd., p. 289-307.
Haramy, K. Y., and M. J. DeMarco, 1985, Use Of The Schmidt Hammer For Rock And Coal Testing, American Rock Mechanics Association.

Hawkins, J. T., A. J. Benvegnu, T. P. Wingate, J. D. McKamie, C. D. Pickard, and J. T. Altum, 1996, SACROC Unit CO2 Flood: Multidisciplinary Team Improves Reservoir Management and Decreases Operating Costs.

Hayes, M., and C. L. Hanks, 2008, Evolving mechanical stratigraphy during detachment folding: Journal of Structural Geology, v. 30, p. 548-564.

Heckel, P. H., 1983, Diagenetic model for carbonate rocks in Midcontinent Pennsylvanian eustatic cyclothems: Journal of Sedimentary Research, v. 53.

Heidari, M., M. A. Nikolinakou, M. R. Hudec, and P. B. Flemings, 2016, Geomechanical analysis of a welding salt layer and its effects on adjacent sediments: Tectonophysics, v. 683, p. 172-181.

Hunt, D., T. Allsop, and R. E. Swarbrick, 1996, Compaction as a primary control on the architecture and development of depositional sequences: conceptual framework, applications and implications: Geological Society, London, Special Publications, v. 104, p. 321-345.

Hunt, D., and W. M. Fitchen, 1999, Compaction and the dynamics of carbonate-platform development: insights from the Permian Delaware and Midland basins, Southeast New Mexico and West Texas, USA.

Janson, X., and C. Kerans, 2011, Paleozoic mounds stratigraphic architecture in the Sacramento Mountains: implication for reservoir characterization, SEPM Field Trip Guidbook, SEPM Permian Basin Section.

Janson, X., and D. D. Madriz, 2012, Geomodelling of carbonate mounds using two-point and multipoint statistics: Geological Society, London, Special Publications, v. 370, p. 229-246.

Kelley, S. A., and C. E. Chapin, 1997, Cooling histories of mountain ranges in the southern Rio Grande Rift based on apatite fission-track analysis; a reconnaissance survey: New Mexico Geology, v. 19, p. 1-14.

Kerans, C., 1988, Karst-controlled reservoir heterogeneity in Ellenburger Group carbonates of west Texas: AAPG bulletin, v. 72, p. 1160-1183.

Kerans, C., 1995, Milankovitch sea level changes, cycles and reservoirs on carbonate platforms in greenhouse and ice-house worlds.

Kerans, C., 2001, Stratigraphic and Diagenetic Controls on Reservoir Architecture of a Non-Reefal Icehouse Isolated Platform—Sacroc Unit, Horseshoe Atoll, Texas: AAPG Southwest Section Meeting.

Kerans, C., C. Zahm, S. L. Bachtel, J. Lambert, N. Danger, and A. Nolting, 2016, Stratigraphic Evolution of an Icehouse Stranplain System — West Caicos, BWI, American Association of Petroleum Geologist Conference and Exhibition, Calgary, Canada.

Kirkby, K. C., 1994, Growth and reservoir development in Waulsortian mounds: Pekisko formation, west central Alberta and Lake Valley formation, New Mexico, The University of Wisconsin - Madison, Madison, Wisconsin.

Klerck, P. A., E. J. Sellers, and D. R. J. Owen, 2004, Discrete fracture in quasi-brittle materials under compressive and tensile stress states: Computer Methods in Applied Mechanics and Engineering, v. 193, p. 3035-3056.

Kluth, C. F., and P. J. Coney, 1981, Plate tectonics of the ancestral Rocky Mountains: Geology, v. 9, p. 10-15.
Koša, E., D. Hunt, W. M. Fitchen, M.-O. Bockel-Rebelle, and G. Roberts, 2003, The heterogeneity of paleocavern systems developed along syndepositional fault zones: the Upper Permian Capitan Platform, Guadalupe Mountains, USA.
Kosa, E., and D. W. Hunt, 2006, Heterogeneity in fill and properties of karst-modified syndepositional faults and fractures: Upper Permian Capitan platform, New Mexico, USA: Journal of Sedimentary Research, v. 76, p. 131-151.
Koša, E., and D. W. Hunt, 2005, Growth of syndepositional faults in carbonate strata: Upper Permian Capitan platform, New Mexico, USA: Journal of Structural Geology, v. 27, p. 1069-1094.
Larkin, R. J., and P. G. Creel, 2008, Methodologies and Solutions to Remediate Inner-Well Communication Problems on the SACROC CO2 EOR Project: A Case Study, SPE Symposium on Improved Oil Recovery, Tulsa, Oklahoma, USA, Society of Petroleum Engineers.
Laubach, S. E., J. E. Olson, and M. R. Gross, 2009, Mechanical and fracture stratigraphy: AAPG Bulletin, v. 93, p. 1413-1426.
Longley, A. J., 1999, Differential compaction and its effects on the outer shelf of the Permian Capitan Reef Complex, Guadalupe Mountains, New Mexico.
Lozinsky, R., and P. Bauer, 1991, Structure and basin-fill units of the Tularosa Basin: New Mexico Geological Society Forty-second Annual Field Conference, p. 1991.
Machette, M. N., 1987, Preliminary assessment of paleoseismicity at White Sands Missile Range, southern New Mexico; evidence for recency of faulting, fault segmentation, and repeat intervals for major earthquakes in the region, US Geological Survey.
Marrett, R., J. F. W. Gale, L. A. Gómez, and S. E. Laubach, 2018, Correlation analysis of fracture arrangement in space: Journal of Structural Geology, v. 108, p. 16-33.
Mazzullo, S., and J. M. Cys, 1979, Marine aragonite sea-floor growths and cements in Permian phylloid algal mounds, Sacramento Mountains, New Mexico: Journal of Sedimentary Research, v. 49.
Meyers, W. J., 1974, Carbonate cement stratigraphy of the Lake Valley Formation (Mississippian) Sacramento Mountains, New Mexico: Journal of Sedimentary Research, v. 44.
Mondol, N. H., K. Bjørlykke, J. Jahren, and K. Høeg, 2007, Experimental mechanical compaction of clay mineral aggregates—Changes in physical properties of mudstones during burial: Marine and Petroleum Geology, v. 24, p. 289-311.
Osborne, M. J., and R. E. Swarbrick, 1997, Mechanisms for generating overpressure in sedimentary basins: A reevaluation: AAPG bulletin, v. 81, p. 1023-1041.
Narr, W., D. J. Fischer, P. Harris, T. Heidrick, B. Robertson, and K. Payrazyan, 2004, Understanding and predicting fractures at Tengiz–a giant, naturally fractured reservoir in the Caspian Basin of Kazakhstan: AAPG International Conference, Cancun, Mexico, p. 24-27.

Nikolinakou, M. A., P. B. Flemings, and M. R. Hudec, 2014, Modeling stress evolution around a rising salt diapir: Marine and Petroleum Geology, v. 51, p. 230-238.
Nolting, A., 2017, Syndepositional Deformation in Steep-Walled Carbonate Margins: Insights from Outcrop and Numerical Modeling of Carbonate Platforms in the Recent and Ancient Rock Record: Dissertation, The University of Texas at Austin, Austin, TX, 130 p.
Nolting, A., C. Zahm, C. Kerans, and D. Brooks, 2016, Spatial and Temporal Characterization of Mechanical Rock Properties from West Caicos, British West Indies: 50th US Rock Mechanics/Geomechanics Symposium.
Nolting, A., C. Zahm, C. Kerans, and M. A. Nikolinakou, in review, Effect of carbonate platform geometry on syndepositional deformation: insights from numerical modeling: Journal of Structural Geology.
Nygård, R., M. Gutierrez, R. K. Bratli, and K. Høeg, 2006, Brittle–ductile transition, shear failure and leakage in shales and mudrocks: Marine and Petroleum Geology, v. 23, p. 201-212.
Nygård, R., M. Gutierrez, R. Gautam, and K. Høeg, 2004, Compaction behavior of argillaceous sediments as function of diagenesis: Marine and Petroleum Geology, v. 21, p. 349-362.
Odling, N. E., P. Gillespie, B. Bourgine, C. Castaing, J. P. Chiles, N. P. Christensen, E. Fillion, A. Genter, C. Olsen, L. Thrane, R. Trice, E. Aarseth, J. J. Walsh, and J. Watterson, 1999, Variations in fracture system geometry and their implications for fluid flow in fractures hydrocarbon reservoirs: Petroleum Geoscience, v. 5, p. 373-384.
Otte, C., 1959, Late Pennsylvanian and Early Permian stratigraphy of the northern Sacramento Mountains, Otero County, New Mexico, State Bureau of Mines and Mineral Resources, New Mexico Institute of Mining & Technology.
Playford, P. E., 1980, Devonian" Great Barrier Reef" of Canning Basin: Western Australia: AAPG Bulletin, v. 64, p. 814-840.
Playford, P. E., N. F. Hurley, C. Kerans, and M. F. Middleton, 1989, Reefal platform development, Devonian of the Canning Basin, western Australia.
Pray, L. C., 1961, Geology of the Sacramento Mountains Escarpment: Otero County, New Mexico, State Bureau of Mines and Mineral Resources, New Mexico Institute of Mining & Technology.
Preto, N., M. Franceschi, G. Gattolin, M. Massironi, A. Riva, P. Gramigna, L. Bertoldi, and S. Nardon, 2011, The Latemar: A Middle Triassic polygonal fault-block platform controlled by synsedimentary tectonics: Sedimentary Geology, v. 234, p. 1-18.
Rankey, E. C., S. Bachtel, and Kaufman, 1999, Controls on Stratigraphic Architecture of Icehouse Mixed Carbonate-Siliciclastic Systems: A Case Study From the Holder Formation (Pennsylvanian, Virgillan), Sacramento Mountains, New Mexico.
Read, J., 1995, Overview of carbonate platform sequences, cycle stratigraphy and reservoirs in greenhouse and icehouse worlds.

Read, J. F., 1998, Phanerozoic carbonate ramps from greenhouse, transitional and ice-house worlds: clues from field and modelling studies: Geological Society, London, Special Publications, v. 149, p. 107-135.
Resor, P. G., and E. A. Flodin, 2010, Forward modeling synsedimentary deformation associated with a prograding steep-sloped carbonate margin: Journal of Structural Geology, v. 32, p. 1187-1200.
Rockfield, 2014, Elfen Training Manual, United Kingdom.
Roscoe, K. H., A. Schofield, and C. Wroth, 1958, On the yielding of soils: Geotechnique, v. 8, p. 22-53.
Rusciadelli, G., and S. Di Simone, 2007, Differential compaction as a control on depositional architectures across the Maiella carbonate platform margin (central Apennines, Italy): Sedimentary Geology, v. 196, p. 133-155.
Rush, J., and C. Kerans, 2010, Stratigraphic response across a structurally dynamic shelf: the latest Guadalupian composite sequence at Walnut Canyon, New Mexico, USA: Journal of Sedimentary Research, v. 80, p. 808-828.
Saller, A. H., 1996, Differential compaction and basinward tilting of the prograding capitan reef complex, Permian, west Texas and southeast New Mexico, USA: Sedimentary Geology, v. 101, p. 21-30.
Schatzinger, R. A., 1983, Phylloid algal and sponge-bryozoan mound-to-basin transition: A late Paleozoic facies tract from the Kelly-Snyder field, West Texas.
Schmoker, J. W., and R. B. Halley, 1982, Carbonate porosity versus depth: a predictable relation for south Florida: AAPG bulletin, v. 66, p. 2561-2570.
Seager, W. R., 1983, Laramide wrench faults, basement-cored uplifts, and complementary basins in southern New Mexico: New Mexico Geology, v. 5, p. 69-76.
Seager, W. R., and P. Morgan, 1979, Rio Grande rift in southern New Mexico, west Texas, and northern Chihuahua: Rio Grande rift: Tectonics and magmatism, v. 14, p. 87-106.
Shackleton, J. R., M. L. Cooke, and A. J. Sussman, 2005, Evidence for temporally changing mechanical stratigraphy and effects on joint-network architecture: Geology, v. 33, p. 101-104.
Shinn, E. A., D. M. Robbin, B. H. Lidz, and J. H. Hudson, 1983a, Influence of deposition and early diagenesis on porosity and chemical compaction in two Paleozoic buildups: Mississippian and Permian age rocks in the Sacramento Mountains, New Mexico.
Siemers, J., and W. Dreybrodt, 1998, Early development of karst aquifers on percolation networks of fractures in limestone: Water resources research, v. 34, p. 409-419.
Smart, K. J., D. A. Ferrill, and A. P. Morris, 2009, Impact of interlayer slip on fracture prediction from geomechanical models of fault-related folds: AAPG bulletin, v. 93, p. 1447-1458.
Soreghan, G. S., and K. A. Giles, 1999a, Amplitudes of Late Pennsylvanian glacioeustasy: Geology, v. 27, p. 255-258.

Soreghan, G. S., and K. A. Giles, 1999b, Facies character and stratal responses to accommodation in Pennsylvanian bioherms, western Orogrande Basin, New Mexico: Journal of Sedimentary Research, v. 69.
Stead, D., E. Eberhardt, and J. S. Coggan, 2006, Developments in the characterization of complex rock slope deformation and failure using numerical modelling techniques: Engineering Geology, v. 83, p. 217-235.
Stearns, D. W., 1968, Certain Aspects of Fracture in Naturally Deformed Rock: Rock Mechanics Seminar, p. 97-118.
Stefanizzi, S., G. Barla, and P. K. Kaiser, 2007, Numerical Modeling of Strain Driven Fractures Around Tunnels In Layered Rock Masses, 11th ISRM Congress, Lisbon, Portugal, International Society for Rock Mechanics and Rock Engineering.
Stevens, C. H., 1971, DISTRIBUTION AND DIVERSITY OF PENNSYLVANIAN MARINE FAUNAS RELATIVE TO WATER DEPTH AND DISTANCE FROM SHORE: Lethaia, v. 4, p. 403-412.
Thigpen, J. R., K. T. Ashley, and R. D. Law, 2017, Evaluating kinematic displacement rate effects on transient thermal processes in thrust belts using coupled thermomechanical finite-element models, *in* R. D. Law, J. R. Thigpen, A. J. Merschat, and H. Stowell, eds., Linkages and Feedbacks in Orogenic Systems: Geological Society of America Memoir v. 213, Geological Society of America, p. 1-23.
Toomey, D. F., J. L. Wilson, and R. Rezak, 1977, Evolution of Yucca mound complex, late Pennsylvanian phylloid-algal buildup, Sacramento Mountains, New Mexico: AAPG bulletin, v. 61, p. 2115-2133.
Underwood, C. A., M. L. Cooke, J. A. Simo, and M. A. Muldoon, 2003, Stratigraphic controls on vertical fracture patterns in Silurian dolomite, northeastern Wisconsin: AAPG bulletin, v. 87, p. 121-142.
Vahrenkamp, V. C., F. David, P. Duijndam, M. Newall, and P. Crevello, 2004, Growth architecture, faulting, and karstification of a middle Miocene carbonate platform, Luconia Province, offshore Sarawak, Malaysia.
Vyazmensky, A., D. Stead, D. Elmo, and A. Moss, 2010, Numerical Analysis of Block Caving-Induced Instability in Large Open Pit Slopes: A Finite Element/Discrete Element Approach: Rock Mechanics and Rock Engineering, v. 43, p. 21-39.
Walls, R. A., W. B. Harris, and W. E. Nunan, 1975, Calcareous crust (caliche) profiles and early subaerial exposure of Carboniferous carbonates, northeastern Kentucky: Sedimentology, v. 22, p. 417-440.
Webb, G. E., 1996, Was Phanerozoic reef history controlled by the distribution of non-enzymatically secreted reef carbonates (microbial carbonate and biologically induced cement)?: Sedimentology, v. 43, p. 947-971.
Wilson, D., R. Aster, and T. R. Team, 2003, Imaging crust and upper mantle seismic structure in the southwestern United States using teleseismic receiver functions: The Leading Edge, v. 22, p. 232-237.

Wilson, J., 1972, Influence of local structure in sedimentary cycles of Beeman and Holder Formations, Sacramento Mountains, Otero County, New Mexico: Cyclic sedimentation in Permian Basin, 2nd edn. West Tex Geol Soc Publ, p. 72-60.
Wilson, J. L., 1967, Cyclic and Reciprocal Sedimentation in Virgilian Strata of Southern New Mexico: Geological Society of America Bulletin, v. 78, p. 805-818.
Wood, D. M., 1990, Soil behaviour and critical state soil mechanics, Cambridge university press.
Yagiz, S., 2009, Predicting uniaxial compressive strength, modulus of elasticity and index properties of rocks using the Schmidt hammer: Bulletin of Engineering Geology and the Environment, v. 68, p. 55-63.
Zahm, C., C. Kerans, and X. Janson, 2009a, Integrating Fracture Systems into a Carbonate Sequence Stratigraphic Framework, AAPG Annual Convention and Exhibition, Denver.
Zahm, C., J. Lambert, and C. Kerans, 2016, Use of Unmanned Aerial Vehicles (UAVs) to Create Digital Outcrop Models: An Example from the Cretaceous Cow Creek Formation, Central Texas: CGACS Journal, v. 5, p. 180-188.
Zhang, Z., 2002, An empirical relation between mode I fracture toughness and the tensile strength of rock: International Journal of Rock Mechanics and Mining Sciences, v. 39, p. 401-406.